# COBRAS/SAMBA

## A Mission Dedicated to Imaging the Anisotropies of the Cosmic Microwave Background

## REPORT ON THE PHASE A STUDY

M. Bersanelli, F.R. Bouchet, G. Efstathiou, M. Griffin, J.M. Lamarre,
N. Mandolesi, H.U. Norgaard-Nielsen, O. Pace, J. Polny, J.L. Puget,
J. Tauber, N. Vittorio, S. Volonté

# COBRAS/SAMBA Mission Summary

| Main Scientific Objective | To image over the whole sky the temperature anisotropies of the cosmic microwave background radiation, with a sensitivity $\frac{\Delta T}{T} \lesssim 2\times10^{-6}$ and an angular resolution of $\sim$10 arcminutes. To achieve this objective, the whole sky will be mapped in nine frequency channels ranging between 30 and 900 GHz, with a sensitivity and an angular resolution which allow the separation of the cosmological signal from all other sources of confusion. |
|---|---|

| PAYLOAD | | | | | | | | | |
|---|---|---|---|---|---|---|---|---|---|
| Telescope | 1.5 m Diam. Gregorian; shared focal plane; system emissivity 1% Viewing direction offset 70° from spin axis. | | | | | | | | |
| Center Frequency (GHz) | 31.5 | 53 | 90 | 125 | 143 | 217 | 353 | 545 | 857 |
| Detector Technology | HEMT radio receiver arrays | | | | Bolometer arrays | | | | |
| Detector Temperature | $\sim$100 K | | | | 0.1-0.15 K | | | | |
| Cooling Requirements | Passive | | | | Cryocooler + Dilution system | | | | |
| Number of Detectors | 4 | 14 | 26 | 12 | 8 | 12 | 12 | 12 | 12 |
| Angular Resolution (arcmin) | 30 | 18 | 12 | 12 | 10.3 | 7.1 | 4.4 | 4.4 | 4.4 |
| Optical Transmission | 1 | 1 | 1 | 1 | 0.3 | 0.3 | 0.3 | 0.3 | 0.3 |
| Bandwidth ($\frac{\Delta\nu}{\nu}$) | 0.15 | 0.15 | 0.15 | 0.15 | 0.37 | 0.37 | 0.37 | 0.37 | 0.37 |
| $\frac{\Delta T}{T}$ Sensitivity per res. element (14 months, $1\sigma$, $10^{-6}$ units) | 7.8 | 7.5 | 14.4 | 35.4 | 1.2 | 2.0 | 12.1 | 76.6 | 4166 |

| SPACECRAFT | |
|---|---|
| Launcher | Ariane 5 (Dual- or triple-launch Configuration, SILMA Fairing) |
| Orbit | Lissajous around Sun-Earth L2 point |
| Stabilization | Spinner at 1 rpm |
| Pointing ($2\sigma$) | $2'5$ a posteriori |
| Lifetime | 1.5 yrs baseline, 5 yrs extended |
| Operations | 10-11 hr per day contact; one ground station |

| Mass & Power Breakdown | | |
|---|---|---|
| | Mass (kg) | Power (W) |
| Payload Module | 304 | 413 |
| Service Module | 413 | 196 |
| Fuel | 555 | |
| L/V Adapter | 92 | |
| Margin | 159 | 84 (10%) |
| Total | 1523 kg | 693 W |

figs/spacecraft/COSA.ps

# Contents

# List of Figures

# List of Tables

# Foreword

In late 1992 ESA issued a call for proposals for candidates to become the 3rd medium-sized mission (M3) of the Agency's Horizon 2000 Scientific Programme. In response to this call, two proposals devoted to the study of the anisotropies of the cosmic microwave background (CMB) were presented to ESA and evaluated by the Astronomy Working Group (AWG). In response to the recommendation of the AWG, and recognizing the fundamental importance of this problem, the Space Science Advisory Committee (SSAC) recommended that a study be carried out to assess the feasibility of a mission dedicated to map the primordial fluctuations. COBRAS (Cosmic Background Radiation Anisotropy Satellite) and SAMBA (Satellite for Measurement of Background Anisotropies) were both conceived as 1 meter class telescopes, each carrying broad-band detection systems at four different frequencies, in the case of COBRAS in the range 30 to 130 GHz, and in that of SAMBA 140 to 800 GHz. Several frequency bands were required in each of these experiments because of the need to remove foreground sources of emission from the observed signal to obtain the cosmological component; this separation is possible because the spectral signature of the foreground sources is different from that of the CMB. COBRAS and SAMBA together span a range of frequencies which, due to technical limitations, would be impossible to achieve for each of them alone. Thus, early in the assessment study, it was recognized that merging the two original (COBRAS and SAMBA) instruments into one payload would be the only way to obtain a definitive and credible answer to the scientific questions to be addressed.

The assessment study, carried out between December 1993 and May 1994, showed that the combined COBRAS/SAMBA mission could survey the large majority of the sky with an angular resolution better than $\sim$15', a sensitivity better than $\frac{(\Delta T)}{T} \sim 2 \times 10^{-6}$, and covering a frequency range wide enough to enable a reliable separation of all possible sources of foreground emission. In addition to its primary cosmological objective, the satellite would provide the community with data adequate to address a huge variety of astrophysical phenomena.

In June of 1993, ESA's AWG, endorsed by the SSAC, recommended that the Agency carry out a Phase A study of COBRAS/SAMBA . For this purpose, Matra Marconi Space (MMS - Toulouse) was selected in open competition to be the industrial prime contractor. With support from MMS (Bristol), MMS (Stevenage), and Fokker Space, MMS (Toulouse) developed a viable design concept for the COBRAS/SAMBA spacecraft between December of 1994 and February of 1996. In parallel and over the same period, the COBRAS/SAMBA Science Team (ST) considerably reinforced the scientific case for the mission, and developed detailed design options for the payload instruments and telescope.

The Phase A study has confirmed and enhanced the scientific case for COBRAS/SAMBA which was developed during the Assessment study, and in addition it has proven that the mission can be carried out within the technical and financial constraints of the M3 call for proposals.

This report summarizes the results of the scientific and technical study activities of the COBRAS/-SAMBA Phase A. The scientific case for the mission was written by the ST, in close collaboration with many members of the astrophysical community. The technical part was prepared by the Future Science Projects Office of ESA/ESTEC, with the support of the COBRAS/SAMBA team at Matra Marconi Space, and specialists from the ESA Technical Directorate at ESTEC and the Directorate of Operations (ESOC). More extensive credits are listed in the following page. We believe that the report reflects a very close and fruitful collaborative spirit between the scientific and technical teams.

# COBRAS/SAMBA

The members of the Science Team supporting this study at the Phase A level were:

| | |
|---|---|
| M. Bersanelli | Istituto di Fisica Cosmica - CNR, Milano, Italy |
| M. Griffin | Queen Mary and Westfield College, London, United Kingdom |
| J.M. Lamarre | Institut d'Astrophysique Spatiale - CNRS, Orsay, France |
| N. Mandolesi | Istituto TESRE-CNR, Bologna, Italy |
| H.U. Norgaard–Nielsen | Danish Space Research Institute, Lyngby, Denmark |
| J. Polny | Danish Space Research Institute, Lyngby, Denmark |
| J.L. Puget | Institut d'Astrophysique Spatiale - CNRS, Orsay, France |

From **ESA:**

| | |
|---|---|
| O.Pace | Study Manager |
| | ESA/ESTEC, Future Science Projects Office, Noordwijk, The Netherlands |
| J. Tauber | Study Scientist, Report Editor |
| | ESA/ESTEC, Space Science Department, Noordwijk, The Netherlands |
| S.Volonté | Astronomy Missions Coordinator |
| | ESA/HQ, Directorate of Scientific Programmes, Paris, France |

Extensive contributions to this report were prepared by:

| | |
|---|---|
| F.R. Bouchet | Institut d'Astrophysique de Paris - CNRS, Paris, France |
| G. Efstathiou | University of Oxford, Oxford, United Kingdom |

Additional scientific support was provided by:

| | | | | |
|---|---|---|---|---|
| N. Aghanim | A. Albrecht | F. Boulanger | L. Danese | J. Delabrouille |
| A. DeLuca | A. Franceschini | R. Gispert | B. Guiderdoni | M. Haehnelt |
| S. Hancock | E. Hivon | A. Lasenby | M. Linden-Vornle | R. Stompor |
| M. Tegmark | L. Toffolatti | N. Vittorio | S. White | and many others. |

# Executive Summary

Since the announcement in 1992 of the first results from the Cosmic Background Explorer (COBE), there has been an enthusiastic resurgence of interest in the study of the anisotropies of the cosmic microwave background (CMB), fueled by the realization that the CMB can set very significant constraints on our current cosmological paradigm. The main objective of the COBRAS/SAMBA mission is to build on the pioneering work of COBE and fulfill this potential.

The special status of CMB observations is well illustrated by one of COBE's major achievements, i.e. the absolute measurement of the spectrum of the CMB to an accuracy of $10^{-3}$ per spectral element. The CMB, which represents 99% of the electromagnetic content of the Universe, was generated at an early time when the Universe was nearly uniform and close to thermodynamic equilibrium, *a time when all the relevant physical processes are linear and well known.* Consequently, high precision measurements can be used to constrain cosmological parameters to correspondingly high accuracy.

Another major achievement of COBE was the detection of the anisotropies of the CMB on large angular scales at a level of $\frac{\Delta T}{T} \sim 10^{-5}$. This detection, although very important, was obtained with scant signal to noise ($\sim 1$) and angular resolution ($\sim 7^o$), and is still far from the fundamental limits to the precision achievable in such a measurement; limits which are set by confusion due to emission from other astrophysical sources (e.g. galactic foregrounds, and background levels due to extragalactic point sources). True imaging of the CMB fluctuations with a precision approaching the limits set by astrophysics still remains to be accomplished, but can be achieved by an experiment which combines high angular resolution, high sensitivity, wide frequency coverage, and excellent rejection of systematic effects. This combination of requirements cannot be met by either ground-based or balloon-borne observations, but rather demands a space mission such as COBRAS/SAMBA .

Detailed computations of the properties of the CMB anisotropies predict that most of the cosmological information in the CMB is contained in angular scales of order and larger than 10 arcminutes. Detailed analysis and simulations of the foreground contaminants show that it is possible to map the CMB fluctuations with a sensitivity in 10 arcminute pixels which is 10 times better than the one obtained by COBE. Thus *the basic scientific goal of the COBRAS/SAMBA mission is to measure the CMB anisotropies at all angular scales larger than 10 arcminutes, with an accuracy set by astrophysical limits.*

One immediate result of such a measurement is the determination of the angular power spectrum and of the statistical properties of the fluctuations originated in the early universe. Since particle physics at the extremely large energies involved ($10^{16}$ GeV) cannot be tested in any accelerator, this determination constitutes the most direct way of testing not only the physics of the early Universe, but also fundamental theories of high-energy physics. In particular, it will establish the nature of the primordial fluctuations, e.g. whether they are due to topological defects or quantum fluctuations.

In either case, fluctuations at angular scales larger than one degree depend primarily on the primordial spectrum, but as smaller angular scales are probed, the power spectrum depends more on physical processes which are sensitive to most of the fundamental cosmological parameters. Very accurate measurements of the CMB anisotropies at high angular resolutions can therefore be used to constrain strongly (to a few percent) basic parameters such as the Hubble constant, the geometry of the universe as characterized by the total density parameter $\Omega_o$, the cosmological constant $\Lambda$, the baryon content and the nature of the dark matter. Observational cosmology has been struggling for more than 50 years to constrain these parameters from local measurements, but the remaining uncertainties are still very large: e.g. the Hubble constant is uncertain by a factor of 2 and the density parameter by a factor of 10. The astrophysical processes involved in these local measurements are for the most part

nonlinear (evolution of galaxies, supernovae, giant HII regions, hot gas in clusters, cluster dynamical mass, etc), and they offer no hope of reaching the accuracies achievable with measurements of the CMB.

A critical issue that is extensively discussed in this report is the ability to separate the observed microwave signal into the various astrophysical components that contribute to it. The galactic foregrounds around 100 GHz are much weaker than the CMB in the cleanest 50 % of the sky. In this region, COBRAS/SAMBA will be able to determine the amplitude of CMB fluctuations to an uncertainty better than $\Delta T/T \sim 2 \times 10^{-6}$ at all angular scales larger than $\sim 10'$. To achieve this sensitivity level on the CMB measurements, the amplitude of the foregrounds has to be determined to a relatively low precision of $\sim 10$ %; this will be accomplished using the information on the spectral behavior of the foregrounds which is contained in measurements at frequencies where they are much stronger than the CMB. A major simulation effort has been carried out during this study that demonstrates the feasibility of the separation process with the required accuracy.

COBRAS/SAMBA will not only yield CMB anisotropies, but also near-all-sky maps of all the major sources of microwave emission, opening a broad expanse of astrophysical topics to scrutiny (see the accompanying Table). These maps will constitute a product which is comparable to the IRAS and COBE-DIRBE maps at shorter wavelengths. The IRAS data have been in use by the community for over 10 years with a scientific output which has remained roughly constant throughout this period. The COBRAS/SAMBA data set will have a similar impact on many areas of astrophysics. In particular, the physics of dust at long wavelengths and the relative distribution of interstellar matter (neutral and ionized) and magnetic fields will be investigated using dust, free-free and synchrotron maps. In the field of star formation, COBRAS/SAMBA will provide a systematic search of the sky for dense, cold condensations which are the first stage in the star formation process.

One specific and local distortion of the CMB which will be mapped by COBRAS/SAMBA is the Sunyaev-Zeldovich (SZ) effect arising from the Compton interaction of CMB photons with the hot gas of clusters of galaxies. The very well defined spectral shape of the SZ effect allows it to be cleanly separated from the primordial anisotropy. The physics of gas condensation in cluster-size potential wells is an important element in the quest to understand the physics of structure formation and ultimately of galaxy formation. The COBRAS/SAMBA data set will be an extremely useful complement to X-ray data from the XMM observatory for such studies: the COBRAS/SAMBA SZ measurements are in fact more sensitive than XMM for the detection of clusters at redshift larger than 0.5, and to detect the gas in the outskirts of the clusters, but X-ray data will be needed to determine the redshift, the gas temperature, and for studies of the physics of the central cores of clusters. From the SZ data can also be extracted a signal which is sensitive to deviations of cluster velocities from the Hubble flow: the sensitivity of COBRAS/SAMBA will allow the determination of the large scale peculiar velocity fields as traced by ensembles of clusters.

Finally the survey will detect several thousands of extragalactic sources in a frequency range little observed so far. It will certainly find many new sources and considerably increase our knowledge of the spectra of star burst galaxies, AGNs, radio galaxies and quasars in the millimetre and submillimetre wavelength range.

Achieving the scientific objectives of COBRAS/SAMBA presents a significant challenge to the design of its payload, but one that can be met. This study shows that technological progress since the time when the COBE satellite was defined allows the large required increase in both angular resolution and sensitivity. In addition, COBRAS/SAMBA can be developed within the boundary conditions of the call for proposals of the ESA's M3 mission.

It is now possible to achieve instrumental sensitivities of $\mu$K magnitude thanks to the recent rapid progress in detector technology and the resulting increase in their performance. Amplifiers using High Electron Mobility Transistors (HEMT) now operate above 100 GHz with good noise figures at temperatures which can be reached by passive cooling. New types of bolometers cooled to 100 mK have noise figures a thousand times better than e.g. those used in the COBE/FIRAS experiment, and

provide a total power output with negligible 1/f noise over time scales of minutes. A dilution cooler that can reach these very low temperatures in space is now available and can be coupled to active space-qualified cryocoolers. Low-mass high-accuracy reflectors made of carbon fiber epoxy material have been developed and fulfill the requirements of the mission.

The model payload consists of a 1.5 meter off-axis telescope with an optical design which minimizes off-axis distortions and two focal plane arrays of detectors sharing the focal plane. The low frequencies (30 to 125 GHz) are covered by 56 tuned radio receivers grouped into four channels and the high frequencies are covered by 56 bolometers divided among 5 channels. The straylight level as well as the thermal stability of the telescope are controlled by a system of optical baffles.

To minimize the contributions of the strong sources of radiation present in the sky (Earth, Sun and Moon), and to reach more easily the required temperature and thermal stability, the satellite will be placed into orbit around the outer Lagrange point of the Sun-Earth system. The technical requirements on the satellite are very moderate by today's standards, and can be implemented in a spin-stabilized spacecraft which minimizes its cost.

The sky scanning strategy is simple. The optical axis of the telescope is offset by $70^o$ from the rotation axis, and scans one full circle on the sky every minute. Near-full sky coverage is achieved by periodically displacing the rotation axis to remain within $15^o$ of the anti-solar direction. The nominal mission duration calls for two coverages of the sky, to be achieved within 14-15 months of routine operations. Very simple spacecraft operations will consist of a daily set of twelve preplanned manoeuvers automatically carried out by the on-board computer.

Planning of the science operations, as well as data reduction, will be carried out by a Science Team (ST). The ST will oversee and direct the work carried out by three Consortia of scientists, centered respectively around three hardware teams, one for each of the two focal plane instruments, and the third for the telescope. The Consortia will include subteams responsible for data processing and the production and delivery of the various scientific products which will be distributed to the astronomical community. Although conceived as a PI mission, the structure of the scientific operations scenario allows enough flexibility to include the active participation of the astronomical community in a wide range of activities, from hardware development to the generation of a large number of diverse scientific products.

The primary output of the mission will be 9 calibrated all-sky maps ranging in frequency from 30 GHz ($\lambda =1$ cm) to 900 GHz ($\lambda =350$ $\mu$m) and in angular resolution from 30 to 4.5 arcminutes. These maps will be made available to the astronomical community within one year after the end of the nominal 18-month mission. In addition to this basic product, the result of the first component separation analysis will be made available at the same time in the form of all-sky maps of the major physical processes: CMB anisotropies, Compton parameter, dust, free-free and synchrotron emission. Finally, the calibrated data stream and attitude reconstruction will also be made available for reanalysis by other groups.

**Scientific areas addressed by COBRAS/SAMBA**

| Component | Area | Highlights |
|---|---|---|
| CMB | Cosmology & origin of structure | • Initial conditions for structure evolution<br>• Constraints on particle physics at energies $>10^{15}$ GeV:<br>− Origin of primordial fluctuations<br>− Testing and characterizing inflation<br>− Testing and characterizing topological defects<br>• Constraints on the nature and amount of dark matter<br>• Determination of fundamental parameters:<br>− $\Omega_0$, $H_0$, $\Lambda$ to 1%<br>− $\Omega_b$, $Q_{rms}$, $n_s$ to a few % |
| SZ | Cosmology & structure evolution | • Measurement of y in $>10^4$ clusters<br>• Estimate of $H_0$ from y and X-ray measurements<br>• Cosmological evolution of clusters<br>• Bulk velocities (scales $>300$ Mpc) out to $z \simeq 1$ with $\Delta v \simeq 50$ km/s |
| Extragalactic sources | Cosmology & structure formation | • Source catalogues of<br>− IR and radio galaxies<br>− AGNs, QSOs, blazars<br>− inverted-spectrum radio sources<br>• Far-infrared background fluctuations<br>• Evolution of galaxy counts |
| Dust emission<br><br>Free-free and synchrotron | Galactic studies | • Dust properties<br>• Cloud and cirrus morphology<br>• Systematic search for cold cores<br><br>• Determination of spectral indices<br>• Cosmic ray distribution<br>• Magnetic field mapping |

# Chapter 1

# The Scientific Case

## 1.1 Introduction

These are exciting times for observational cosmology. In 1992, the Cosmic Background Explorer (COBE) satellite detected the existence of temperature irregularities in the cosmic microwave background (CMB) radiation field (Smoot *et al.* 1992). These irregularities (usually referred to as anisotropies) were imprinted on the CMB by primordial perturbations generated within $10^{-35}$ seconds of the Big Bang, and provide us with a probe of the ultra-high energy conditions in the early Universe. COBE has opened up the field of microwave background research, and propelled it into a state of hectic activity. Experimental groups are devoting much effort on the design of new ground-based, balloon-borne and satellite experiments to improve on the poor angular resolution and sensitivity of COBE. This effort has been complemented by theoretical calculations that have revealed a wide horizon of new science that can be extracted from high precision measurements of the CMB anisotropies, science that ranges in time and scope from the physics of the early Universe to that of our present astrophysical environment.

In this proposal, we summarize the case for a new satellite, COBRAS/SAMBA, that will provide a definitive high-angular resolution mapping of the microwave background over at least 95% of the sky and over a wide frequency range. COBRAS/SAMBA has been designed to have 10 times the sensitivity and more than 50 times the angular resolution of the COBE satellite. The simultaneous mapping of the sky over a wide frequency range by COBRAS/SAMBA will permit a separation of Galactic and extragalactic foregrounds from the primordial cosmological signal to exquisite precision over much of the sky. COBRAS/SAMBA will far exceed the performance of balloon-borne and ground-based experiments and will be superior to any other proposed satellite mission. COBRAS/SAMBA will operate in a survey mode, scanning at least 90% of the sky twice over in 14 months. High resolution ($\theta_{FWHM} \sim 4'$–$30'$) maps of the sky in 9 frequency bands in the range 30–1000 GHz will be made generally available within a year of the end of the survey, providing the community with near all-sky data of unprecedented quality at frequencies that have hitherto been little explored.

Very little is known about the Universe prior to the epoch of nucleosynthesis. For example, we do not yet know whether the large-scale uniformity of the Universe owes its origin to an early period of rapid expansion known as *inflation*. Neither do we know the origin of the primordial irregularities required to form galaxies and other structure in the Universe; *e.g.* are galaxies and clusters the product of quantum fluctuations generated during an inflationary phase or of topological defects, such as cosmic strings, created at an ultra-high energy phase transition? What is the spatial curvature of the Universe? What is the nature of the dark matter that dominates the present Universe? What is the relationship between primordial irregularities and the large-scale structure – the chains, filaments and voids – observed in galaxy surveys? These are some of the key scientific questions that COBRAS/SAMBA has been designed to answer. COBRAS/SAMBA will revolutionize our understanding of Cosmology, from fundamental questions concerning the origin and early phases of the

Universe to the astrophysics of galaxy formation. The unprecedented quality of the maps provided by COBRAS/SAMBA will, however, open an even wider range of scientific problems: *e.g.* with certain general assumptions we show that it is possible to determine the fundamental cosmological parameters, in particular, the total density $\Omega_0$, the baryon density $\Omega_b$ and the Hubble constant $H_0$ *to a precision of a few percent* – an accuracy that is far beyond what is possible with conventional astronomical techniques. Such high precision measurements will have a major impact on practically every aspect of astronomy, including the physics of the early Universe, determinations of the extragalactic distance scale, primordial nucleosynthesis, stellar ages, dynamical measurements of the mean mass density and the origin of large-scale structure in the Universe. Many thousands of individual extragalactic and Galactic sources will be detected by COBRAS/SAMBA via their spectral signature, including clusters of galaxies, infrared luminous galaxies and Galactic star forming regions. Furthermore, the COBRAS/SAMBA maps will revolutionize our understanding of diffuse background emissions, again with wide ranging implications extending from the contribution of primordial galaxies to the far-infrared background, to the origin of Galactic synchrotron emission and the nature of Galactic dust. It is important to emphasize that COBRAS/SAMBA, while primarily a mission designed to solve cosmological problems, will provide data that will be invaluable to an extremely wide astronomical community.

COBRAS/SAMBA will also have a strong impact on particle physics. Observations of the CMB anisotropies are one of the very few ways of testing physics at energies $\gtrsim 10^{15}$ GeV and are of crucial importance in developing fundamental theories of high energy physics (*e.g.* supersymmetry, superstrings and quantum gravity). Accurate investigations of the CMB anisotropies are thus complementary to the next generation of accelerator experiments such as those planned with the Large Hadron Collider (LHC) at CERN and provide a critical link between high energy physics and the formation of structures – quasars, galaxies, clusters and superclusters of galaxies – that can be observed by astronomers.

The key scientific objectives of COBRAS/SAMBA are as follows:

- Measurements of the CMB anisotropies to an accuracy of $\Delta T/T \sim 1 \times 10^{-6}$ over a wide range of angular scales ($\theta \approx 10'$–$180°$); this will allow a determination of fundamental parameters such as the spatial curvature, Hubble constant $H_0$ and the baryon density $\Omega_b$, to a precision of a few percent.

- Tests of inflationary models of the early universe; specifically the determination of the spectral index of the primordial fluctuation spectrum to high precision and the possible detection of a component of the CMB anisotropies induced by primordial gravitational waves, which would show conclusively that the Universe passed through an inflationary phase.

- The detection of characteristic signatures in the CMB created by topological defects, such as cosmic strings and textures, generated at a phase transition in the early Universe.

- To measure the amplitude of structures in the CMB with physical scales $\lesssim 100 h^{-1}$ Mpc [1] (requiring an angular resolution of better than $1°$) which have sizes comparable to the voids and filaments observed in the galaxy distribution today. By comparing COBRAS/SAMBA measurements with new redshift surveys of $\sim 10^6$ galaxies it will be possible to determine the evolution of cosmic structure and constrain the nature of the dark matter in Universe.

- Measurements of the Sunyaev-Zeldovich effect – temperature anisotropies which are caused by the frequency change of microwave background photons scattered by hot electrons in the gaseous atmospheres of rich clusters of galaxies. COBRAS/SAMBA will detect this effect in many thousands of rich clusters, providing information on the physical state of the intracluster gas

---

[1] where $h$ denotes the Hubble constant in units of 100 km s$^{-1}$ Mpc$^{-1}$.

and on the evolution of rich clusters. These measurements can also be combined with spatially resolved X-ray observations to estimate the Hubble constant $H_0$.

- Using the high sensitivity of COBRAS/SAMBA and the sub-mm bolometer channels it will be possible to disentangle the frequency dependent Sunyaev-Zeldovich effect in rich clusters of galaxies from temperature differences caused by their peculiar motions. It should be possible to measure cluster peculiar velocities for more than 1000 clusters to an accuracy of $\lesssim 250 \mathrm{kms}^{-1}$ providing powerful tests of theories of structure formation and on the mean mass density of the Universe.

- COBRAS/SAMBA will produce high sensitivity maps over 95% of the sky over a wide range of frequencies *which have never before been studied at such high resolutions and sensitivities*. These maps will have a large number of applications, from studies of synchrotron emission in our Galaxy, star-forming regions, Galactic dust and the interstellar medium to the origin of the far-infrared background and the evolution of infrared luminous galaxies at high redshifts. In particular,

  - the comparison of maps of the free-free emission and the dust emission will allow to study the relative distribution of the ionized vs the neutral interstellar medium;

  - the synchrotron emission at high frequency will constrain the cosmic ray electron and magnetic field distributions;

  - the anisotropies of the far infrared background, together with a survey of point sources, will constrain models of galaxy formation.

The main science goals of COBRAS/SAMBA are described in the rest of this Section. However Figure 1.1 shows one specific example of the dramatic impact on cosmology that we can expect from COBRAS/SAMBA. COBRAS/SAMBA will produce maps of the CMB anisotropies with about 4000 times as many resolution elements as the COBE maps and with more than an order of magnitude improvement in the sensitivity/pixel. From this vast increase in information, we show in Section 1.4.3 that it is possible to estimate fundamental cosmological parameters which determine the properties of the CMB anisotropies, in particular $\Omega_0$, $H_0$ and $\Omega_b$ to a precision of a few percent or better. There is enough information in the fine scale structure of the CMB anisotropies to remove degeneracies between these and other parameters, such as the cosmological constant, $\Lambda$, the residual optical depth to Thomson scattering, *etc*, which are also extremely uncertain at present. Figure 1.1 shows the joint probability distribution of $H_0$ and $\Omega_0$ derivable from COBRAS/SAMBA, illustrating that it will be possible to constrain these parameters to a precision of about a percent, independently of the values of other cosmological parameters. The only assumptions involved in deriving these constraints are that the CMB anisotropies arise from primordial adiabatic fluctuations (which can be verified from the COBRAS/SAMBA maps of the CMB) and that secondary CMB anisotropies, Galactic, and extragalactic foregrounds can be removed to an accuracy of $\Delta T/T \lesssim 2 \times 10^{-6}$ (which we demonstrate is feasible in Section 2). Such high accuracies are realistic, since the relevant physics describing the temperature anisotropies is linear and extremely well understood, a situation that is rare in astronomy. A high sensitivity CMB experiment thus offers the exciting prospect of determining fundamental cosmological parameters to accuracies unimaginable with conventional astronomical techniques.

## 1.2  Observations of the CMB

In 1992, the NASA COBE satellite detected small ($\Delta T/T \sim 1 \times 10^{-5}$) temperature irregularities in the microwave background radiation temperature on angular scale $\theta \gtrsim 7°$ (Smoot *et al.* 1992). The COBE results provided the first convincing detection of primordial temperature anisotropies, which had been
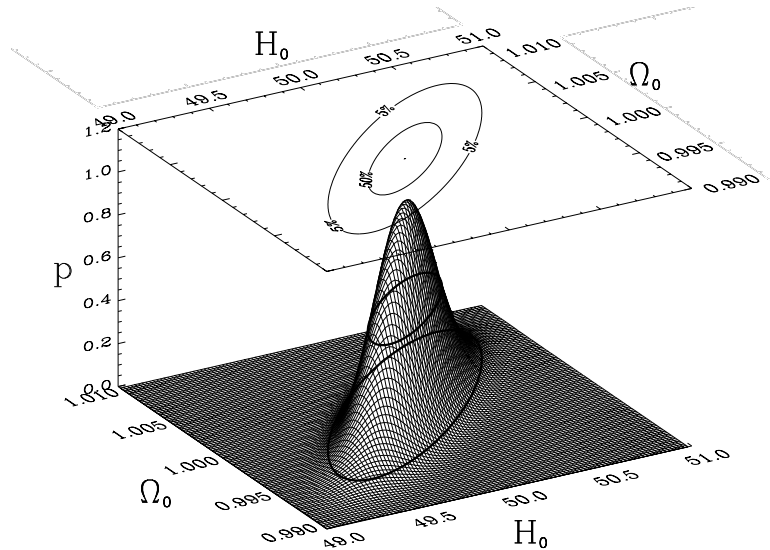
Figure 1.1: The joint probability distribution of the cosmological density parameter, $\Omega_0$, and the Hubble constant $H_0$, expected from fitting models of the primary CMB anisotropies to the COBRAS/SAMBA maps. The heavy lines show the 50% and 5% contours of the distribution, and have been projected into the $H_0$ and $\Omega_0$ plane in the upper part of the figure. These estimates are derived under the general assumption that the CMB anisotropies arise from adiabatic perturbations in the early universe. In this specific example, we have assumed that $\Omega_0 = 1$ and $H_0 = 50 \mathrm{kms}^{-1} \mathrm{Mpc}^{-1}$. (See Section 1.4.4 for further details.)

searched for earnestly by experimenters since the discovery of the microwave background by Penzias and Wilson in 1965. COBE has provided low resolution maps of the sky at three frequencies, 30, 53 and 90 GHz and with relatively poor sensitivity ($\Delta T/T \approx 3.4 \times 10^{-5}$ at 53 GHz) after four years of observation. The COBE measurements are consistent with ground based measurements from Tenerife at frequencies 10, 15 and 32.5 GHz (Watson *et al.* 1994) and with the balloon-borne Far-infrared Survey (Ganga *et al.* 1993). Thus at large angular scales ($\theta \gtrsim 5°$) there is strong evidence that the temperature irregularities are independent of frequency over the range 10–170 GHz, as expected if they are of primordial rather than of Galactic origin.

The COBE discovery has stimulated a concerted effort to detect primordial anisotropies on smaller angular scales $\theta \sim 1°$ (*e.g.* Fischer *et al.* 1992, Gaier *et al.* 1992; Schuster *et al.* 1993, Meinhold *et al.* 1993, Wollack *et al.* 1993, Cheng *et al.* 1994, de Bernardis *et al.* 1994, Gundersen *et al.* 1995, Ruhl *et al.* 1995). These experiments utilize either radio frequency techniques at dry, high altitude, sites such as the South Pole, or balloon-borne bolometers sensitive at frequencies $\gtrsim$ 150 GHz. Almost all of these experiments report detections of temperature anisotropies with an amplitude $\Delta T/T \sim 1 - 4 \times 10^{-5}$, but the limited sensitivity and frequency coverage of any single experiment, particularly those at radio frequencies, precludes any firm conclusion that the anisotropies are primordial. The present observational situation is summarized in Figure 1.4 below.

To meet the science goals of this proposal, an experiment with high angular resolution $\theta \sim 10'$, and high sensitivity $\Delta T/T \sim 1 \times 10^{-6}$ is required *that maps a large fraction of the sky over a wide frequency range*. As we will show in this proposal, the latter requirements are *essential* to measure the statistical properties of the CMB fluctuations to high accuracy and to monitor and remove Galactic and extragalactic foregrounds. These requirements are formidable, and can only be met by a satellite experiment.

It is important to emphasize that balloon-borne experiments planned for the next decade cannot achieve the comprehensive frequency and sky coverage of COBRAS/SAMBA. For example, the TopHat experiment of Kowitt *et al.* (1995) (frequency range 150–630 GHz, angular resolution of 0.5°)

will be mounted on top of a balloon to reduce ground and atmospheric emission, and is expected to measure temperature differences at 40 points on the sky in a single long duration flight of two weeks. The area covered by TopHat per flight is only *one four-thousandth* of the area of sky covered by COBRAS/SAMBA and would be observed with considerably lower resolution. Furthermore, it is exceedingly difficult to design a balloon-borne experiment free of spurious atmospheric and ground emissions to an accuracy of $\Delta T/T \approx 1 \times 10^{-5}$, which is an order of magnitude higher than the sensitivity required for the scientific goals of this proposal. Similar considerations apply to ground based experiments, including interferometric experiments such as the Cambridge Anisotropy Telescope (O'Sullivan *et al.* 1995). A satellite experiment is the only feasible way of simultaneously achieving a large sky coverage at high angular resolution and sensitivity over a wide frequency range, while eliminating atmospheric and sidelobe contamination. This has been widely recognized by the experimental community, both in Europe and the USA, with proposals for CMB anisotropy satellites under serious consideration by ESA and NASA.
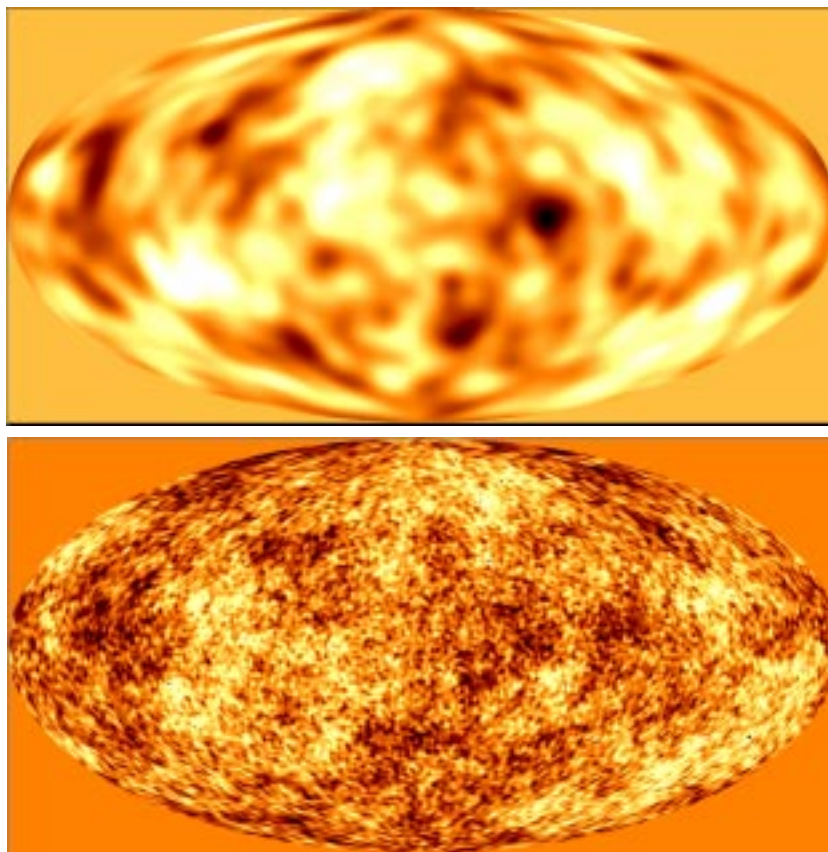


Figure 1.2: Simulated maps of the background radiation anisotropies expected in an $\Omega = 1$ CDM model. The upper picture shows a simulated COBE map with a resolution of $\theta_{FWHM} = 7°$ together with random noise as in the COBE two-year data. The lower panel shows the same realization of the sky at the much higher angular resolution and signal-to-noise of COBRAS/SAMBA.

How different will the CMB sky look to COBRAS/SAMBA compared to COBE? The maps in Figure 1.2 show simulations of the CMB anisotropies expected in an inflationary cold dark matter model. The upper figure is constructed at the angular resolution and signal-to-noise of the second year COBE maps (Bennett *et al.* 1994). The lower figure shows how the sky would appear at the much higher angular resolution and sensitivity of COBRAS/SAMBA. The individual hot and cold spots seen in the COBRAS/SAMBA simulation have physical sizes comparable to those of clusters and superclusters of galaxies observed in the present Universe. Evidently, we expect to see a wealth

of fine-scale structure in the microwave sky. The primary goal of COBRAS/SAMBA is to map these structures with high precision, free of foreground contamination, so enabling us to address the scientific questions described in the rest of this proposal.

## 1.3    The Origin of CMB Anisotropies

### 1.3.1    Statistical Description of the Anisotropies

The temperature pattern on the celestial sphere can be expanded in spherical harmonics

$$\frac{\Delta T}{T} = \sum_{\ell,m} a_\ell^m Y_\ell^m(\theta, \phi), \tag{1.1}$$

and the power spectrum of the temperature fluctuations, $C_\ell$, is defined by the mean square value of the coefficients $a_\ell^m$

$$C_\ell = \langle |a_\ell^m|^2 \rangle. \tag{1.2}$$

If the fluctuations in the early universe obey Gaussian statistics, as expected in most theories (see Section 1.4), each of the coefficients $a_\ell^m$ is independent and so the power spectrum $C_\ell$ provides a *complete* statistical description of the temperature anisotropies. The temperature power spectrum, $C_\ell$, is thus of fundamental importance in studies of the microwave background anisotropies. The temperature power spectrum can be estimated directly from observations by performing a spherical harmonic analysis, as has been done with the COBE data (Gorski *et al.* 1994, Bond 1995, Tegmark 1996). However there are other ways of analyzing observations which are closely related to the temperature power spectrum, *e.g.* the temperature autocorrelation function (see *e.g.* Banday *et al.* 1994, for an application to the COBE maps).

Figure 1.3 shows a calculation of the temperature power spectrum for a cold dark matter dominated universe with $\Omega_0 = 1$. These curves assume a scale-invariant initial fluctuation spectrum, as expected in the simplest models of inflation, a baryon density $\Omega_b = 0.05$ and a Hubble constant $h = 0.5$. The curve labeled 'density' shows the power spectrum from density perturbations; these are the small irregularities in the early universe that grow under the action of gravity to form the structure in the Universe that we see today. The curve labeled 'grav. waves' shows the power spectrum arising from gravitational waves generated during inflation (*e.g.* Starobinsky 1985, Davis *et al.* 1992, Crittenden *et al.* 1993). Notice the large differences in shape between the two curves which can be utilized to test models of inflation (see Section 1.4).

The multipole $\ell$ tells us about anisotropies on an angular scale $\theta \sim 1/\ell$, as indicated by the scale at the top of the Figure. Thus COBE, which has an angular resolution of $\theta_{FWHM} \approx 7°$ samples only low multipoles $\ell \lesssim 20$ (shown by the shaded bar in the upper panel). In contrast, the high angular resolution of COBRAS/SAMBA will allow measurements of multipoles up to $\ell \gtrsim 1000$, thus sampling almost the full multipole range of the theoretical predictions. The shapes of these curves, and the physics that determine them, are described in the next section.

### 1.3.2    Potential Fluctuations in the Early Universe

In the standard hot Big Bang model, the Universe is highly ionized until a redshift $z_R \sim 1000$, the so-called recombination epoch, when protons and electrons combine to make hydrogen atoms (*e.g.* Peebles 1990). Prior to this epoch, photons are tightly coupled to the radiation by Thomson scattering, but once recombination is complete the Universe becomes transparent to radiation. Provided there is no subsequent energy input in the intergalactic medium that can reionize the Universe at high redshifts[2],

---

[2]CMB anisotropy experiments probing angular scales $\sim 1°$ already set strong limits on early reionization, as described in Section 1.4.
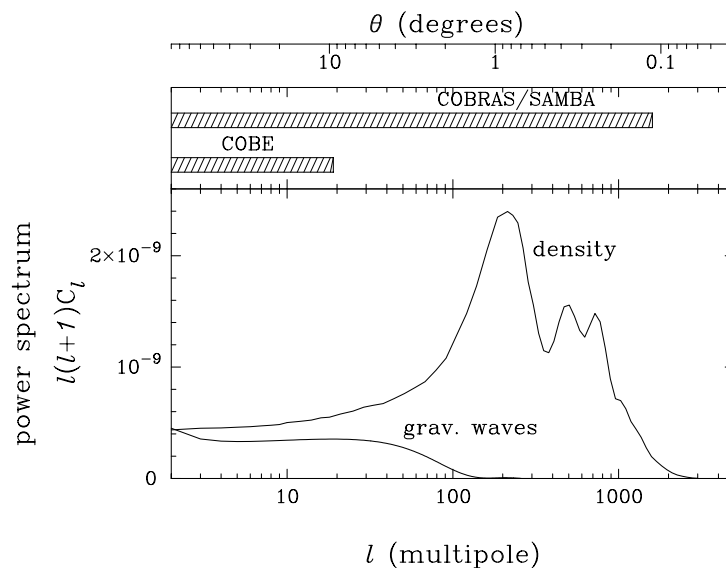
Figure 1.3: The power spectrum $C_\ell$ of the microwave background anisotropies plotted against multipole $\ell$ for an inflationary cold dark matter cosmology. The angular scale corresponding to a given multipole is indicated by the scale at the top of the figure. The curve labeled *density* shows the contribution to the temperature power spectrum from small density fluctuations in the early universe. The curve labeled *grav. waves* shows the contribution to the temperature power spectrum from gravitational waves generated during inflation. The relative amplitude of these two contributions depends on the specific details of the model of inflation, as described in Section 1.4. The bars show the range of multipoles (angular scales) probed by COBE and by COBRAS/SAMBA.

photons propagate towards us along geodesics, unimpeded by the matter. Maps of the microwave background radiation therefore provide us with a picture of irregularities at the 'last scattering surface' at $z_R \sim 1000$, when the Universe was about $300,000$ years old.

At redshifts $z \gg 1$ an irregularity with a comoving scale $\lambda$ subtends an angle

$$\theta_\lambda \approx (\lambda/\mathrm{Mpc})(\Omega_0 h) \ \text{arcminutes.} \tag{1.3}$$

Thus, an irregularity of scale $\lambda \sim 100 h^{-1} \mathrm{Mpc}$, comparable in scale to the largest structures detected in galaxy surveys, subtends an angle of $\sim 100'$ at the last scattering surface. The size of a causally connected region, $ct$ (the 'Hubble radius'), at the time of recombination subtends an angle

$$\theta_H \approx (\Omega_0/z_R)^{1/2} \ \text{radians} \approx 2(\Omega_0)^{1/2}(z_R/1000)^{-1/2} \ \text{degrees.} \tag{1.4}$$

Temperature fluctuations in the microwave background radiation on angular scales $> \theta_H$ therefore *cannot have been in causal contact* at the time of recombination. How could such causally unconnected fluctuations have been formed? The only plausible solution is to appeal to exotic physical processes in the very early Universe that extend well beyond the Standard Model of particle physics. The properties of the microwave background anisotropies, *e.g.* their amplitude, power-spectrum, high-order correlations, thus provide quantitative tests of physical theories applicable at energies $\gtrsim 10^{15}$ GeV when the Universe was less than $10^{-35}$ seconds old.

For example, the temperature power spectra in Figure 1.3 show predictions for an inflationary universe dominated by cold dark matter. Quantum fluctuations during inflation generate macroscopic fluctuations in the gravitational potential with mean square value that scales with the scale of the perturbation as a power law

$$\left\langle \Delta\phi^2 \right\rangle \propto \lambda^{(1-n)/2}, \tag{1.5}$$

(see Section 1.4 for further details) where $n$ defines the *spectral index* of the fluctuations. Most models of inflation predict a spectral index that is close to unity $n \approx 1$ ; if $n = 1$, the potential fluctuations are independent of scale and so this is often referred to as a 'scale-invariant' spectrum.

Variations in the gravitational potential along different lines-of-sight to the last scattering surface cause temperature fluctuations in the CMB (called the Sachs-Wolfe effect) with an *rms* amplitude

$$\frac{\Delta T}{T} \sim \frac{(\Delta\phi)_\lambda}{c^2} \propto \theta^{(1-n)/2}. \tag{1.6}$$

This effect dominates the anisotropy pattern at large angular scale ($> \theta_H$) and, since according to General Relativity the potential fluctuations $\Delta\phi$ are time-independent, a map of the CMB anisotropies *provides us with a picture of the potential fluctuations as they were at the time that they were generated in the early Universe.*

In the more technical language of the previous Section, the Sachs-Wolfe effect leads to a temperature power spectrum of the form

$$C_\ell \quad = C_2 \frac{\Gamma\left(\ell + \left(\frac{n-1}{2}\right)\right)}{\Gamma\left(\ell + \left(\frac{5-n}{2}\right)\right)} \frac{\Gamma\left(\frac{9-n}{2}\right)}{\Gamma\left(\frac{3+n}{2}\right)} \tag{1.7}$$

$$\propto \ell^{n-3}, \qquad \text{for } \ell \gg 1 \tag{1.8}$$

(Bond and Efstathiou 1987) and so for a scale-invariant spectrum, $\ell(\ell + 1)C_\ell$ is approximately independent of multipole at $\ell \lesssim 90$ (corresponding to angular scales $\theta > \theta_H \sim 2°$) as shown in Figure 1.3. A scale-invariant spectrum of potential fluctuations generated in the early Universe thus leads to a scale-invariant temperature fluctuation spectrum on the sky. An accurate determination of the spectral index from the CMB anisotropies provides an extremely powerful test of theories of inflation, as described in Section 1.4.

### 1.3.3   Fluctuations on Angular Scales $< 2°$

On smaller angular scales $\theta \lesssim 2°$, fluctuations were causally connected at the time of recombination and so the pattern of the temperature anisotropies is distorted from its primordial form. The main effect is an acoustic compression of the matter-radiation fluid which leads to a series of 'Doppler' peaks in the power spectrum (Bond and Efstathiou 1987, Hu and Sugiyama 1995) as shown in Figure 1.3. The positions and relative heights of these peaks are extremely sensitive to fundamental cosmological parameters, principally the spatial curvature of the Universe, the baryon density $\Omega_b$ and the Hubble constant $H_0$. With the high precision measurements of the CMB provided by COBRAS/SAMBA it will be possible to determine the values of these parameters to an accuracy of a few percent or better (see Section 1.4). It may even be possible to set constraints on the nature of the dark matter, *e.g.* whether it is predominantly cold dark matter (CDM) in the form of weakly interacting supersymmetric particles, or mixed dark matter (MDM), i.e. a mixture of CDM and neutrinos with masses of a few $eV$. The temperature power spectrum therefore provides a cosmic fingerprint which can be used to identify the parameters of our Universe to high precision.

As a consequence of the anisotropic nature of Thomson scattering, the CMB anisotropies are predicted to be linearly polarized at about the 5% level with a characteristic angular scale of $\sim 1°$ (see Bond and Efstathiou 1987). Such small levels of polarization would be difficult to detect and, since they contain little information that is not already present in the Doppler peak structure of the temperature power spectrum, we have decided not to compromise the primary science goals of COBRAS/SAMBA in an attempt to detect polarization.

Some specific examples of temperature power spectra for the inflationary CDM model are shown in Figure 1.4. The temperature power spectrum is plotted in Figure 1.4a for a constant value of the Hubble constant ($h = 0.5$) and for several values of $\Omega_b$; Figure 1.4c shows the dependence on the Hubble constant for a fixed baryon density $\Omega_b = 0.05$. Each of these curves has been normalized to

match the COBE observations and so they look indistinguishable at multipoles $\ell \lesssim 30$. However, the structure of the Doppler peaks at multipoles $\ell \gtrsim 100$ differs from model-to-model. The points in these Figures show the results of a number of recent anisotropy experiments mentioned in Section 1.2. The COBE observations are shown by the point with the small error bar at $\ell = 5$. At present, balloon and ground based experiments are just beginning to probe angular scales $\theta \lesssim 2°$ (multipoles $\ell \gtrsim 100$) where we expect to see the first Doppler peak. The experimental points suggest a rise in the power spectrum at $\ell \gtrsim 100$, consistent with the theoretical predictions (*e.g.* White *et al.* 1994) but the error bars are much too large to distinguish between the curves shown in the Figures. In Figures 1.4b and 1.4d, we plot the *rms* temperature variations measured in a Gaussian beam as a function of the beam width $\theta_s$. The curves in these figures are almost identical at angular scales $\theta \gtrsim 1°$, but the variations in the structure of temperature power spectra at $\ell \gtrsim 100$ lead to differences in $\Delta T/T$ of typically a few $\times 10^{-6}$ on angular scales $\theta \lesssim 1°$. Evidently, to detect the cosmic fingerprint imprinted on the CMB, high sensitivities of $\Delta T/T \sim 10^{-6}$ and angular resolutions $\sim 0.1°$ are required. *The principal goal of COBRAS/SAMBA is to achieve these high levels of precision and to provide a wide frequency coverage to allow accurate subtraction of Galactic and extragalactic foregrounds from the primordial cosmological signal.*
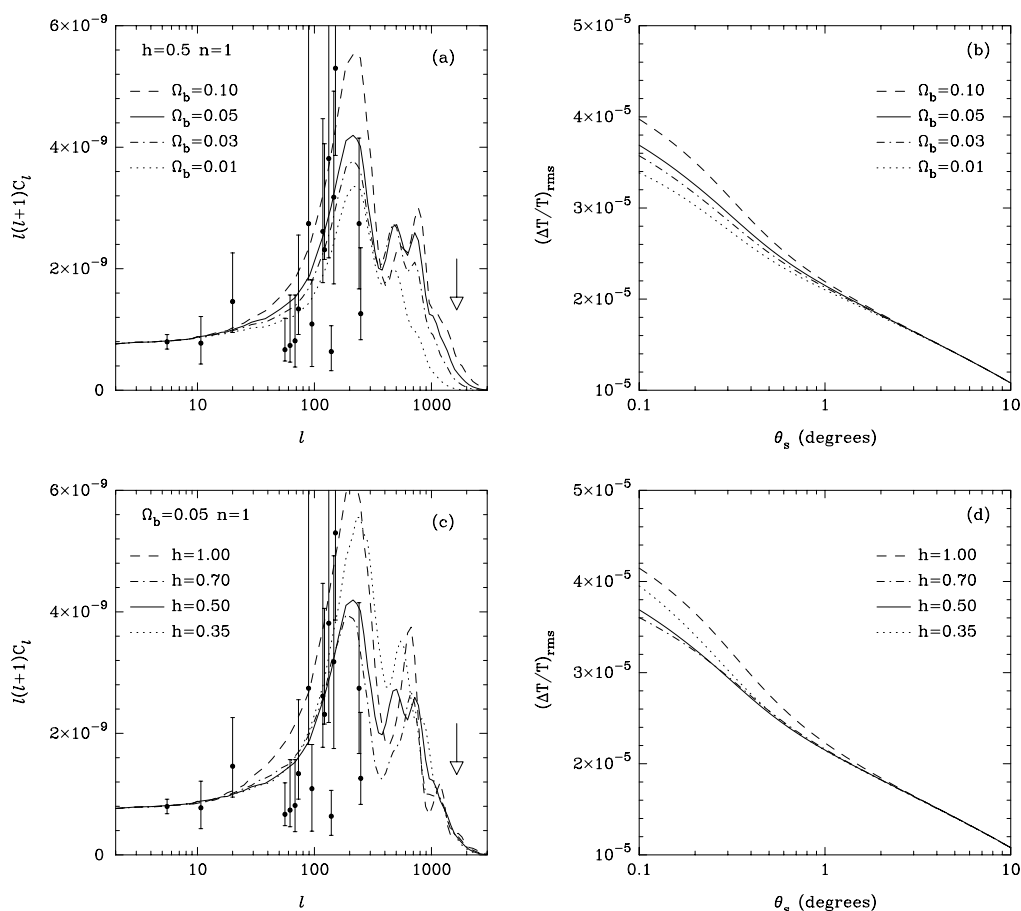


Figure 1.4: Figures 1.4a and 1.4c show how the temperature power spectrum of a scale-invariant CDM model depends on the baryon density $\Omega_b$ and the Hubble constant $h$. In 1.4a we show curves for several values of $\Omega_b$ with the Hubble constant fixed at $h = 0.5$. In 1.4c, we show curves for several values of $h$ with the baryon density fixed at $\Omega_b = 0.05$. The points with error bars show the results from a number of recent experiments (see the reviews by White *et al.* , 1994, and Bond, 1996). The point with the small error bar at $\ell = 5$ shows the two-year COBE results. The curves plotted in Figures 1.4c and 1.4d show the *rms* temperature fluctuations in a Gaussian beam of width $\theta_s$ illustrating how the the power spectra in 1.4a and 1.4c translate into a dependence of the *rms* temperature fluctuations on angular resolution.

### 1.3.4    Topological Defects

The inflationary model that we have discussed above has become a paradigm in modern cosmology (see Section 1.4). However, there exists a second set of theories for the origin of structure in the early Universe that leads to distinctly different predictions for the CMB anisotropies. These theories involve symmetry breaking in unified field theories. As the Universe expands from its hot dense state, symmetries are broken which can result in a disorderly phase containing topological defects such as cosmic strings, monopoles or textures (Kibble 1976; Turok 1989).

Defect theories differ fundamentally from the inflationary model. Whereas quantum fluctuations generated during inflation produce irregularities in the spatial curvature (and hence gravitational potential) of the Universe, topological defects are examples of *isocurvature* perturbations; no curvature fluctuations are generated at the symmetry breaking, but as the defects evolve they produce a time-dependent gravitational field which generates both irregularities in the matter distribution and temperature fluctuations in the microwave background radiation with a characteristic statistical signature (Bouchet *et al.* 1988, Pen, Spergel & Turok 1994; Coulson *et al.* 1994, Crittenden & Turok 1995). Measurements of the CMB anisotropies can therefore distinguish between inflation and defect theories and can even differentiate between different types of defect, as discussed in Section 1.4.

## 1.4    Tests of Cosmological Theories and the Estimation of Cosmological Parameters

### 1.4.1    Scientific Requirements: Sensitivity, Angular Resolution and Sky Coverage

In the preceding Section, we have listed several important scientific questions that can only be answered with high sensitivities of $\Delta T/T \sim 10^{-6}$ and high angular resolutions of $\lesssim 30'$. Only by achieving these requirements can we hope to measure the fine-scale structure in the CMB radiation that provides strong discrimination between competing theories for the formation of cosmic structure. It is also important to recognize that a wide frequency coverage, in addition to high sensitivities, is essential in order to subtract foregrounds (principally free-free, synchrotron and dust emission) at the $10^{-6}$ level. The accurate subtraction of foregrounds is crucial to the success of COBRAS/SAMBA and has been investigated in detail, as discussed in Chapter 2. There, we show that with the wide frequency coverage and high sensitivity of COBRAS/SAMBA *it should be possible to subtract Galactic and Extragalactic foregrounds to an accuracy of $\Delta T/T \sim 10^{-6}$ over an area of about 1/3–1/2 of the sky.* Furthermore, the wide frequency coverage, which is a unique feature of the COBRAS/SAMBA mission, will allow us to produce clean, high sensitivity maps of the primordial cosmological fluctuations over a frequency range of at least $\sim 50$–300 GHz, so providing unambiguous evidence of the reality of the fine-scale features of the background fluctuations, as well as a wealth of information on the foregrounds themselves (see Section 1.6).

To illustrate the power of COBRAS/SAMBA, Figure 1.5 shows simulated measurements of the temperature power spectrum for three experimental configurations. In the large panel Figure (1.5a) we have adopted a set of parameters similar to those expected for the high-frequency instrument on COBRAS/SAMBA, *i.e.* we have assumed a Gaussian beam width of $\theta_{FWHM} = 10'$, coverage of 1/3 of the sky and a sensitivity of $\Delta T/T = 2 \times 10^{-6}$ at the resolution limit. The solid line shows the theoretical power spectrum from Figure 1.3 convolved with the beam, and the filled circles with error bars show the mean and standard deviation of the temperature power spectrum derived from 50 simulated skies after subtraction of the instrumental noise. The key points of this Figure are easy to understand: in a Gaussian theory each of the spherical harmonic coefficients $a_\ell^m$ (equation 1) is statistically independent and Gaussian distributed, thus the power spectrum $C_\ell$ is $\chi^2$ distributed with variance

$$\mathrm{Var}(C_\ell) \approx \frac{2}{(2\ell + 1)} \frac{C_\ell}{f_{sky}}, \tag{1.9}$$

where $f_{sky}$ is the fraction of the sky covered. The errors are therefore a strong function of the multipole moment and sky coverage. At low multipoles, $\ell \lesssim 100$, the errors on $C_\ell$ are primarily determined by sky coverage rather than by sensitivity, but at higher multipoles systematic errors of $\Delta T/T \gtrsim 10^{-6}$ in the subtraction of foregrounds will exceed the theoretical variance of equation (1.9). *The high sensitivity and wide frequency of COBRAS/SAMBA is required to subtract foregrounds to the accuracy shown in Figure 1.5a* (see Chapter 2 for a detailed discussion). The remaining two panels show the effects of reducing the sky coverage and resolution. In Figure 1.5b we show an estimate of $C_\ell$ derived from a single $10° \times 10°$ patch of sky at the same angular resolution and sensitivity of the COBRAS/SAMBA simulation of Figure 1.5a. This is roughly ten times the area of sky that would be observed by a single flight of the TopHat long duration balloon experiment (Kowitt *et al.* 1995) and three times the angular resolution. Figure 1.5b is probably an over-optimistic estimate of what might be achieved by a concerted effort of CMB mapping with balloon borne instruments. However, Figure 1.5b shows that even if foregrounds and atmospheric emission can be removed to high accuracy, the sampling errors resulting from the reduced sky coverage (1/144th of the area of the COBRAS/SAMBA simulations) are larger than the subsidiary Doppler peaks in $C_\ell$ and so such an experiment cannot constrain the parameters of cosmological models to high precision. Figure 1.5c shows the effects of reducing the resolution to $\theta_{FWHM} = 1°$ while sampling 1/3 of the sky. The variances of the low order multipoles ($\ell \lesssim 100$) are almost identical to those of the COBRAS/SAMBA simulations, but there is very little useful information at higher multipoles.
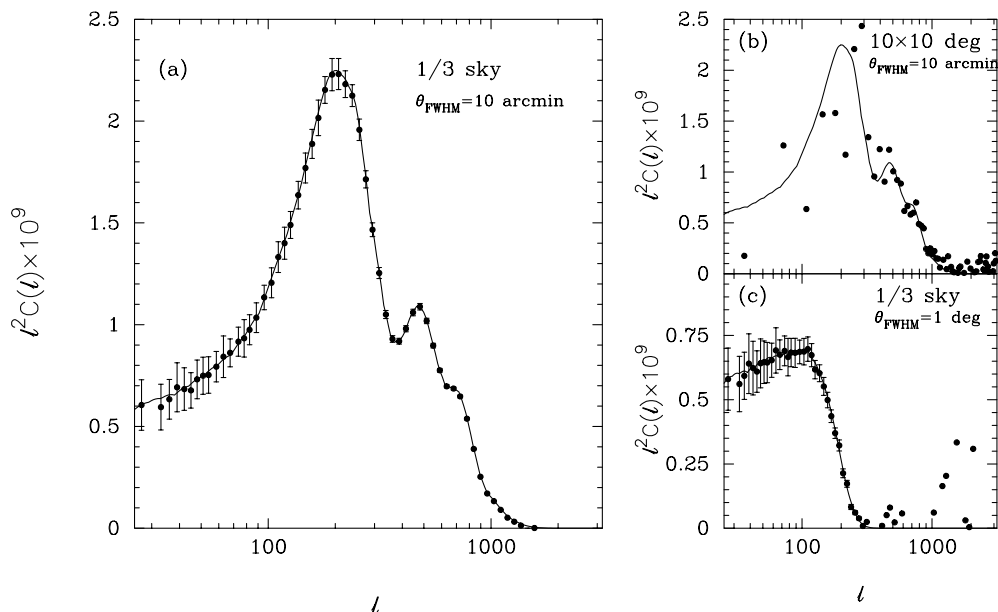


Figure 1.5: This figure illustrates the requirements of large sky coverage and high angular resolution in order to achieve an accurate measurement of the temperature power spectrum. The solid lines in each of the figures show the temperature power spectrum of an $\Omega = 1$ cold dark matter model. The error bars in Figure 1.5a show the $1\sigma$ errors on the power spectrum if 1/3 of the sky is mapped at an angular resolution of $10'$ with a sensitivity of $\Delta T/T = 2 \times 10^{-6}$ per resolution element. COBRAS/SAMBA should achieve at least the accuracy shown in Figure 1.5a. Figure 1.5b shows an estimate of the power spectrum if only $10° \times 10°$ of the sky is mapped at the same angular resolution and sensitivity. Figure 1.5c shows how accurately the power spectrum can be measured if 1/3 of the sky is mapped at an angular resolution of $1°$; at this resolution there is very little useful information on the background anisotropies at multipoles $\ell \gtrsim 100$. The instrumental noise has been subtracted from the simulated power spectra. An experiment with the accuracy of figure 1.5a is clearly required to distinguish between cosmological models with different cosmological parameters such as those shown in Figure 1.4.

In summary, high angular resolution such as that provided by COBRAS/SAMBA and a large

sky coverage are required to accurately probe the high multipole region $\ell \gtrsim 100$. Furthermore, a wide frequency coverage and high sensitivities are required to enable subtraction of foregrounds to an accuracy of $\Delta T/T \sim 10^{-6}$ at the resolution limit, as described in detail in Chapter 2.

### 1.4.2  Testing Theories of Inflation

In 1981 Guth proposed a radical new theory of the early universe, the inflationary model, which can explain a number of fundamental problems in Cosmology: *e.g.* why is the Universe so nearly homogeneous and spatially flat, and why are there no magnetic monopoles or other remnants of Grand Unified phase transitions? The inflationary model has since become a paradigm in modern cosmology (see *e.g.* Kolb and Turner 1990, Linde 1990). The key idea, common to all models of inflation, is that at some very early time after the Big Bang, the Universe underwent a rapid near-exponential expansion increasing in size by a factor $\gtrsim e^{60}$. The large expansion during the inflationary phase dilutes the abundance of remnant monopoles and smooths any initial spatial curvature leading to a Universe that is very nearly spatially flat at the present epoch. Furthermore, quantum fluctuations produced during inflation are stretched in scale by many orders of magnitude producing density fluctuations that can then grow by gravity to make the galaxies and clusters of galaxies seen in the Universe today (Guth and Pi 1982, Hawking 1982, Bardeen, Steinhardt & Turner 1983).



Figure 1.6: The table gives values of the spectral indices $n_s$ and $n_t$ of the density and gravitational wave spectra and the ratio $r$ of their amplitudes, for several common inflationary potentials $V(\phi)$. The box in the figure shows the range of $r$-$n_s$ consistent with inflationary models. Most models of inflation are constrained to lie along the grey lines. (Adapted from Steinhardt 1996).

By studying the CMB anisotropies we can determine the nature of the fluctuations as they were at the time that they were generated, less than $\lesssim 10^{-35}$ seconds after the Big Bang. The CMB anisotropies offer a direct test, not only of whether inflation took place, but also of the specific details of the inflationary mechanism. For example, in the simplest inflationary models, the energy density of the Universe is dominated by a single scalar field $\phi$ (called the inflaton field). The dynamics of the inflaton field is governed by an effective potential $V(\phi)$. In principle, the potential $V(\phi)$, the nature of the inflaton field and its couplings to other fields should be deducible from fundamental physics, but at present we have so few experimental constraints on physics at energies $> 10^{15}$ GeV that the parameters of inflationary models, which determine the amplitudes and spectra of the primordial fluctuations, are almost arbitrary. *Observations of the CMB anisotropies are thus one of the few ways of setting firm experimental constraints on theories at ultra-high energies of $\gtrsim 10^{15}$ GeV.* Nevertheless, successful inflationary models (*i.e.* models that produce sufficient expansion) lead to some predictions that

depend only weakly on specific details such as the shape of the inflaton potential. These are as follows:

- Spatial flatness: Most models of inflation lead to a Universe which is spatially flat with $\Omega = 1 \pm \epsilon$, where $\epsilon$ is exponentially small. Here $\Omega$ includes all contributions to the energy density including matter, radiation and any vacuum energy associated with a non-zero cosmological constant.

- Gaussian perturbations: Quantum fluctuations during inflation generate irregularities that obey Gaussian statistics. Any deviations from Gaussian statistics in the CMB temperature anisotropies would thus be difficult to reconcile with the inflationary model.

- Gravitational wave fluctuations: Quantum fluctuations of massless gravitons can lead to a spectrum of primordial gravitational waves after inflation is complete. These produce a special signature in the CMB radiation, unique to inflationary models, as illustrated in Figure 1.3.

- Nearly scale invariant fluctuation spectra: The spectra of the density and gravitational wave fluctuations resulting from inflation can be characterized by power law indices $n_s$ and $n_t$ respectively (for *scalar* and *tensor* modes). Most models of inflation predict nearly scale-invariant fluctuations (*cf* Section 1.3.2) with $n_s \approx 1$ and $n_t \approx 0$.

An exactly exponential (de Sitter) expansion during inflation would lead to precisely scale invariant density and gravitational wave spectra with indices $n_s = 1$ and $n_t = 0$ respectively. In order to match on to Friedman-Robertson-Walker models, the expansion rate must slow down at the end of inflation. This leads to small deviations from a purely scale invariant spectrum in any realistic inflationary model that depend on the precise shape of the potential $V(\phi)$. However, extreme fine tuning is required to produce inflationary models with spectral indices that lie outside the bounds $0.7 \lesssim n_s \lesssim 1.2$ and $0.3 \lesssim n_t \lesssim 0$ (Steinhardt 1996, Bond 1996) shown by the heavy box in Figure 1.6.

Furthermore, the ratio $r = C_2^t/C_2^s$ of the CMB quadrupoles from gravitational wave (tensor) and density perturbation (scalar) components depends on the shape of the potential and hence on the spectral indices $n_s$ and $n_t$. Inflationary models can be grouped into two categories, one in which $n_t = n_s - 1$ and the ratio

$$r = 7(1 - n_s), \qquad (1.10)$$

shown by the diagonal grey line in Figure 1.6, and another in which negligible gravitational waves are produced, shown by the grey line along the abscissa. *Any experimentally determined deviation of the CMB anisotropies from the grey lines in Figure 1.6 would be extremely problematic for inflationary models.*

Figure 1.7 illustrates the power of COBRAS/SAMBA for testing inflationary models. Here we have assumed a pure power law fluctuation spectrum with scalar spectral index $n_s = 1$ and we have estimated the error on the determination of the spectral index from an all-sky experiment as the number of multipoles is increased. The dotted lines show the limits on $n_s$ from an experiment with the same angular resolution and sensitivity as the 2 year COBE data; the $1\sigma$ error on $n$ approaches $\pm 0.3$ at multipoles $\ell \sim 20$ corresponding to the resolution limit of the COBE maps. The solid lines show the $1\sigma$ errors on $n_s$ from an experiment with the sensitivity of COBRAS/SAMBA. Here the error on $n_s$ is determined primarily by "cosmic variance" (equation 1.9) and decreases rapidly to $\delta n_s = 0.023$ at $\ell = 100$. An experiment with the sensitivity and resolution of COBRAS/SAMBA can therefore measure the spectral index with an accuracy that is much smaller than the width of the heavy box plotted in Figure 1.8 *and can therefore distinguish between different theories of inflation.* The ability to measure small deviations from a precise scale invariant spectrum will provide tight constraints on the form of the inflationary potential and hence on fundamental physics at energies $\gtrsim 10^{15}$ GeV.

In the next section, we extend the simple analysis of Figure 1.7 to the full range of multipoles accessible to COBRAS/SAMBA and to a wide range of cosmological parameters including the inflationary parameters $n_s$, $n_t$ and $r$.
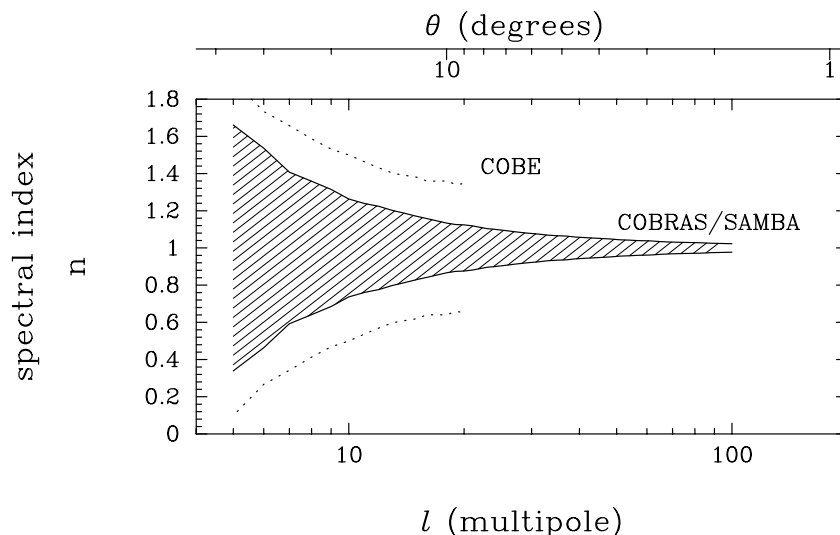
Figure 1.7: This figure illustrates the fundamental limits on the accuracy with which the scalar spectral index $n_s$ can be determined from observations of the CMB anisotropies at multipoles $\ell \lesssim 100$. The initial spectrum is assumed to be a scale-invariant power law with $n_s = 1$ and gravitational waves have been ignored. The lines show the $1\sigma$ scatter in $n_s$ from a maximum likelihood fit to the temperature power spectrum as the number of multipoles is increased. The dotted lines show the limits from the 2 year COBE data, which contain no useful information on multipoles $\ell > 15$. The shaded regions show the $1\sigma$ scatter in $n_s$ expected from COBRAS/SAMBA.

### 1.4.3   Determining Fundamental Cosmological Parameters

At multipoles $\ell \gtrsim 100$, the CMB anisotropies become sensitive to fundamental cosmological parameters, such as the spatial curvature of the Universe, the baryon density and the Hubble constant. Some specific examples have been shown in Figure 1.4. With the high sensitivity, angular resolution and large sky coverage afforded by COBRAS/SAMBA it is possible, with certain general assumptions, to determine these fundamental parameters *to a precision of a few percent*. This is illustrated in Figure 1.8. Here, we have computed maximum likelihood estimates in an eight dimensional parameter space defined by the parameters $\Omega_0$, $h$, $\Omega_b$, the scalar spectral index $n_s$[3], the amplitude $Q_{rms}$, the ratio of scalar to tensor components $r$, the cosmological constant $\Lambda$, and the residual optical depth $\tau$ arising from reionization of the intergalactic medium. In Figure 1.8, we have plotted the $1\sigma$ error in $\Omega_0$, $h$ and $\Omega_b$, irrespective of uncertainties in other parameters, attainable by an experiment with angular resolution $\theta_{FWHM}$ sampling $1/3$ of the sky with a sensitivity of $2 \times 10^{-6}$ per resolution element.

The CMB anisotropies are especially sensitive to the spatial curvature, $\Omega_0$, because the position of the first Doppler peak in the CMB power spectrum is determined by the angle subtended by the Hubble radius, $ct$, at the time of recombination (equation 1.5). The position of the first Doppler peak therefore provides a geometrical measurement of the spatial curvature of the Universe. For example, if $\Omega_0 = 1$, the first Doppler peak has a maximum at $\ell \approx 200$, but if $\Omega_0 = 0.2$ the maximum will occur at $\ell \approx 450$. As Figure 1.8 shows, a high sensitivity CMB experiment with a resolution of $\theta_{FWHM} = 1°$ is capable of determining $\Omega_0$ to an accuracy of about 10% and the accuracy increases to better than one percent for $\theta_{FWMH} = 0.1°$ (*cf* Jungman *et al.* 1996). Furthermore, with the high angular resolution of COBRAS/SAMBA it is also possible to estimate the Hubble constant and $\Omega_b$ *to a precision of a few percent or better*, accuracies far beyond those possible with traditional astronomical techniques. The high angular resolution of COBRAS/SAMBA eliminates the degeneracies between these and other cosmological parameters and, with the ability afforded by COBRAS/SAMBA to remove foregrounds

---

[3] The spectral index of the gravitational wave (tensor) perturbations is assumed to be $n_t = n_s - 1$.

and discrete sources (Chapter 2), the high accuracies of Figure 1.8 should be achievable.
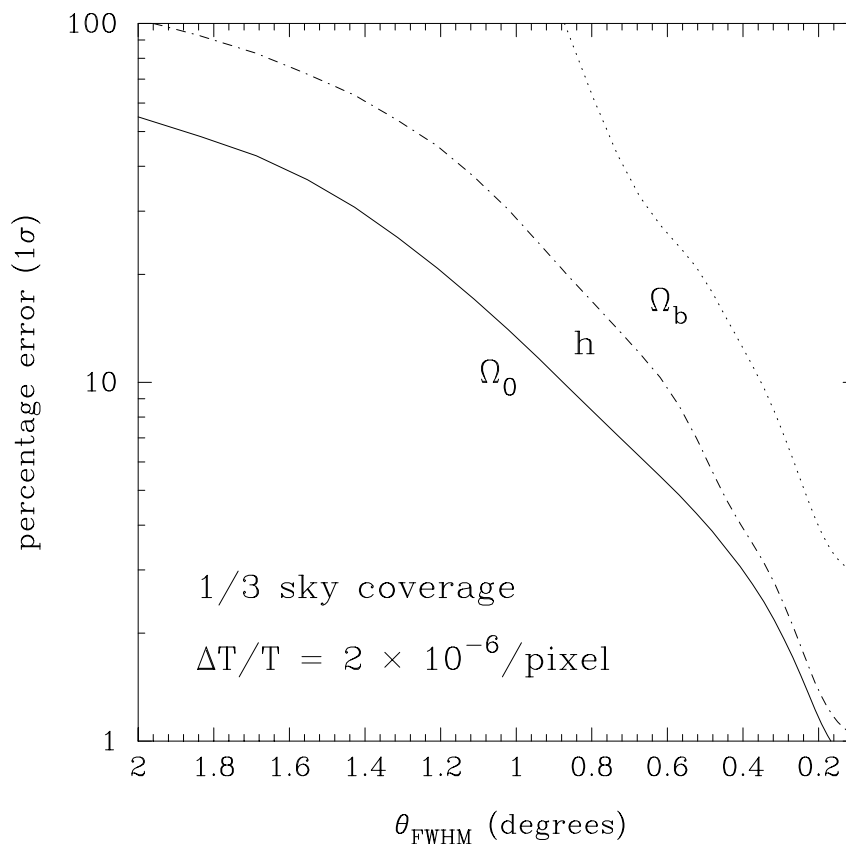


Figure 1.8: The accuracy with which the three fundamental cosmological parameters $\Omega_0$, $h$ and $\Omega_b$ can be determined from measurements of the microwave background fluctuations plotted as a function of the angular resolution of the experiment. We have assumed that 1/3 of the sky is observed at a sensitivity of $\Delta T/T = 2 \times 10^{-6}$ per resolution element.

Such high accuracies for fundamental cosmological parameters would lead to a profound change in our understanding of cosmology. For example:

- COBRAS/SAMBA promises the first accurate geometrical estimate of the spatial curvature of the Universe. Will it be compatible with the inflationary prediction of $\Omega_0 = 1$? How will it compare with dynamical estimates of the mean mass density derived from galaxy peculiar velocities?

- Will CMB estimates of the Hubble constant be compatible with estimates from more traditional techniques, such as from Cepheid distances to galaxies in the Virgo cluster (e.g. Freedman et al. 1994) or from Type Ia supernova light curves (Riess et al. 1995)? Will the values of $\Omega_0$ and $H_0$ be compatible with the ages of stars in globular clusters?

- COBRAS/SAMBA can set tight limits on the value of a cosmological constant $\Lambda$. With an angular resolution of $10'$, the $1\sigma$ error on the dimensionless quantity $\lambda = \Lambda/(3H_0^2)$ is expected to be $\approx 0.02$, well below the dynamically interesting values of $\lambda \gtrsim 0.5$ proposed by some authors (e.g. Ostriker and Steinhardt) to solve the age-Hubble constant problem and observed large-scale structure in the Universe. Such a stringent limit on $\lambda$ (or perhaps a detection of a non-zero value), will be of fundamental significance to particle physics since there is, at present, no

accepted theoretical explanation of why the cosmological constant is 120 orders of magnitude smaller than the natural value set by the Planck scale.

- Will estimates of the baryon density and Hubble constant be compatible with the predictions of primordial nucleosynthesis? The COBRAS/SAMBA limits on $\Omega_b h^2$ will be about 30 times smaller than the range derived from primordial nucleosynthesis (*e.g.* Walker *et al.* 1991), and will serve as a stimulus for more accurate measurements of primordial element abundances and for theoretical investigations of deviations in the predicted abundances caused by physics beyond the Standard Model of particle physics (*e.g.* massive $\tau$ neutrinos, singlet neutrinos *etc*).

- Do we require dark baryonic matter in the present Universe? Luminous stars in galaxies contribute only $\Omega_* \approx 0.003$ to the density parameter in the Universe. The net baryon content is very poorly constrained at present and it is not known, for example, how much remains as hot ionized gas, or whether a significant fraction of the baryons are locked up in low-mass stars below the nuclear burning threshold of $0.08 M_\odot$.

These and many other questions will, for the first time, be open to quantitative analysis. CO-BRAS/SAMBA would truly revolutionize cosmology, turning it from a qualitative science fraught with systematic errors and uncertainties, into a quantitative science in which most of the key parameters are constrained to high precision.

Figure 1.9 shows examples of the correlations between some of these parameters. In Figure 1.9 we have assumed a universe with $\Omega_0 = 1$, $h = 0.5$, $\Omega_b = 0.05$, spectral index $n_s = 1$, $r = 1$, $\tau = 0$, and a normalization of $Q_{rms} = 20\mu$K to match the amplitude of the second year COBE measurements at large angular scales. The figure shows likelihood contours for representative pairs of parameters marginalized over all other parameters for CMB experiments at two angular resolutions, $\theta_{FWHM} = 10'$ and $\theta_{FWHM} = 1°$. In both cases we have assumed that 1/3 of the sky is mapped at a sensitivity of $\Delta T/T = 2 \times 10^{-6}$ per resolution element.

This figure shows that: (1) the parameters $\Omega_0$, $h$ and $\Omega_b$ are relatively weakly coupled with each other and that the accuracy with which these parameters can be measured is strongly dependent on angular resolution; (2) some parameters are strongly coupled, for example the amplitude $Q_{rms}$ and spectral index $n_s$, but again with the angular resolution of COBRAS/SAMBA the uncertainty on each parameter can be reduced to a few percent; (3) the uncertainty on the amplitude of the gravitational wave component of the fluctuations, $r$, depends only weakly on angular resolution because it is determined by low order multipoles (*cf.* e.g. Knox, 1995).

In summary, the analysis of this section shows that observations of the CMB anisotropies with COBRAS/SAMBA are capable of determining fundamental cosmological parameters to high precision. The only assumptions involved are that the primordial fluctuations are adiabatic and characterized by an approximately power-law spectral index, assumptions which themselves can be verified from the COBRAS/SAMBA maps of the CMB anisotropies. The physics underlying these predictions is extremely well understood, involving only linear perturbation theory, and hence the theoretical predictions presented here should be realistic. The analysis of Chapter 2 shows that the frequency coverage and high sensitivity of COBRAS/SAMBA will allow subtraction of foregrounds and discrete sources, so that the CMB anisotropies should be retrieved over at least 1/3 of the sky with a sensitivity of $\Delta T/T \lesssim 2 \times 10^{-6}$, as assumed in this Section. No other technique is capable of yielding results of such precision for parameters that have yet to be measured reliably, despite many decades of research.

### 1.4.4    The Nature of the Dark Matter

The nature of the dark matter that dominates the present mean mass density of the Universe remains enigmatic. Searches for microlensing in the direction of the Large Magellanic Cloud have set strong constraints on the possibility that the halo of our Galaxy is composed of low mass stars (*e.g.* Alcock
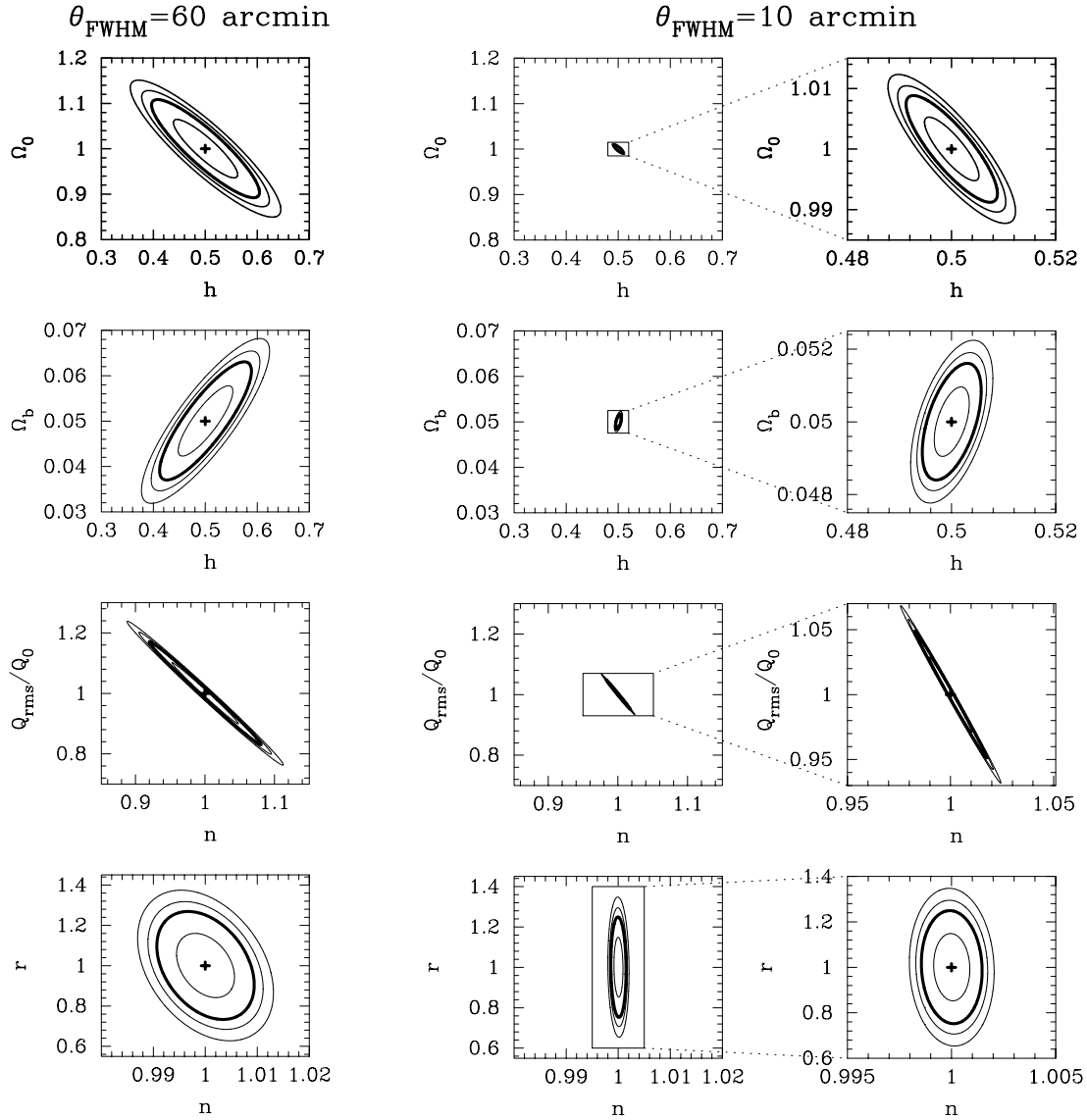
Figure 1.9: The contours show $50, 5, 2$ and $0.1$ percentile likelihood contours for pairs of parameters determined from fits to the CMB power spectrum. The figures to the left show results for an experiment with resolution $\theta_{FWHM} = 1°$. Those to the right for a higher resolution experiment with $\theta_{FWHM} = 10'$ plotted with the same scales (central column) and with expanded scales (rightmost column). Notice how the accuracy of parameter estimation increases dramatically at the higher angular resolution. In these examples, we have assumed that $1/3$ of the sky is observed at a sensitivity of $\Delta T/T = 2 \times 10^{-6}$ per resolution element. (See Figure 1.5 for simulations of the CMB power spectra for these experimental configurations.)

*et al.* 1995). It is unlikely, therefore, that the bulk of the dark matter is composed of baryonic material. The most popular candidate for the dark matter is a weakly interacting massive supersymmetric particle (see *e.g.* Ellis 1990). Many groups around the world have initiated experiments to search for such cold dark matter by the laboratory detection of nuclear recoil (see e.g. Smith and Lewin 1990).
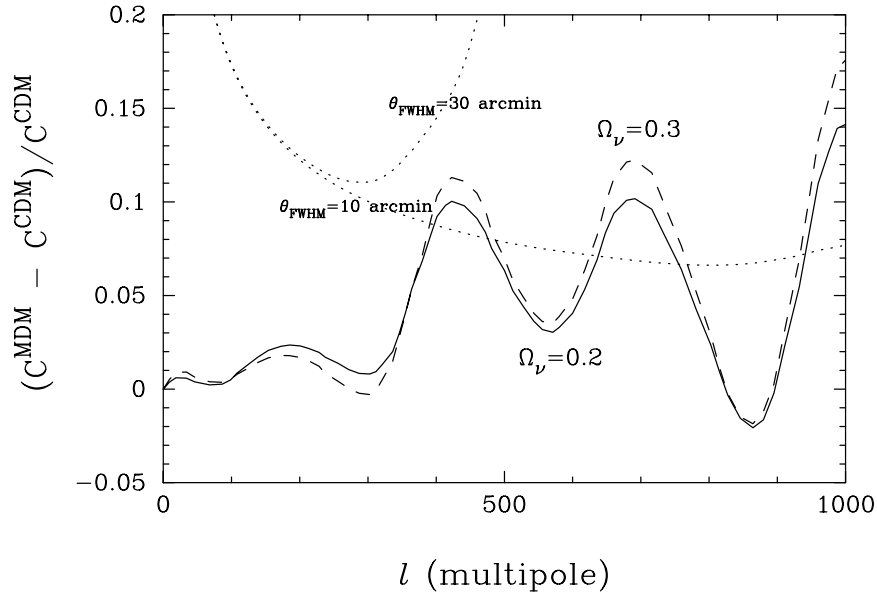


Figure 1.10: The solid and dashed lines show the fractional difference in the CMB power spectrum for mixed dark matter models compared to a scale-invariant cold dark matter model with $\Omega_0 = 1$, $\Omega_b = 0.05$ and $h = 0.5$ (adapted from Dodelson *et al.* 1996). In the mixed dark matter models, light neutrinos contribute $\Omega_\nu = 0.3$ (dashed line) and $\Omega_\nu = 0.2$ (solid line); in both cases $\Omega_0 = 1$ and $\Omega_b = 0.05$. The dotted lines show th fractional error in the CMB power spectrum attainable by an experiment that surveys one-third of the sky with resolutions $\theta_{FWHM}$ of 30′ and 10′ at a sensitivity of $\Delta T/T = 2 \times 10^{-6}$ per resolution element.

However, studies of large-scale structure in the Universe are inconsistent with the simplest versions of the CDM model (see *e.g.* Maddox *et al.* 1990, Park *et al.* 1994). One way of resolving this discrepancy is to postulate that the dark matter consists of a mixture of cold dark matter and light neutrinos (*e.g.* Davis *et al.* 1992, Klypin *et al.* 1993), a possibility that is extremely difficult to test directly in laboratory experiments. However, even a small admixture of light neutrinos leads to systematic differences of typically 10% in the spectrum of CMB anisotropies compared to a model consisting only of cold dark matter and baryons (*e.g.* Dodeleson *et al.* 1995). The differences in the CMB anisotropies arise primarily from differences in the equation of state of the Universe at the time of recombination. An example is shown in Figure 1.10. These small differences in the CMB power spectrum can be detected by an experiment with sufficient angular resolution, sky coverage and sensitivity. High angular resolution is particularly crucial, however. The dashed lines in the figure show the fractional error in the power spectrum attainable by a CMB experiment with 1/3 sky coverage, sensitivity of $\Delta T/T = 2 \times 10^{-6}$ per resolution element and angular resolutions of $\theta_{FWHM} = 30'$ and 10′. An experiment with the high angular resolution of COBRAS/SAMBA is therefore capable of detecting the small difference in the power spectrum at multipoles $\ell \gtrsim 400$ and hence of setting constraints on the *nature* of the dark matter, in addition to its contribution to the total mean mass density.

### 1.4.5    Signatures From Topological Defects

Each type of topological defect produces a characteristic signature in the CMB − for example, cosmic strings would produce line-like discontinuities on the sky (Kaiser and Stebbins 1984), while cosmic textures produce distinct hot and cold spots (Coulson *et al.* 1994). This is illustrated in Figure 1.11 which compares the CMB anisotropies expected in a cosmic string model with the inflationary cold dark matter described in the previous section. Notice the step-like discontinuities in the string model − generally the fluctuations produced by topological defects are non-Gaussian, unlike the Gaussian noise predicted by inflationary models. The non-Gaussianity can be measured in a number of different ways, *e.g.* by testing for correlations between the spherical harmonic coefficients $a_\ell^m$ (Magueijo 1996), by calculating higher moments of the temperature maps such as the skewness $\langle \Delta T^3 \rangle / \langle \Delta T^2 \rangle^{3/2}$ and kurtosis $(\langle \Delta T^4 \rangle - 3\langle \Delta T^2 \rangle^2)/\langle \Delta T^2 \rangle^2$, which are zero for a Gaussian distribution, or by designing statistics to test for specific features such as discontinuities. However, detailed numerical calculations (Coulson *et al.* 1994) show that high sensitivities $\Delta T/T \sim 10^{-6}$, large sky coverage, and angular resolutions of much less than a degree are required to detect the non-Gaussianities arising from topological defects. High resolution is particularly crucial − for example, the line-like discontinuities of the cosmic string model shown in Figure 1.11 would be smeared out by a beam of width $\gtrsim 1°$ and so the anisotropy pattern would be difficult to distinguish from the Gaussian fluctuations predicted by inflation. For this reason, statistical tests of Gaussianity applied to the COBE CMB maps (Kogut *et al.* 1995) do not provide strong constraints on topological defect models.
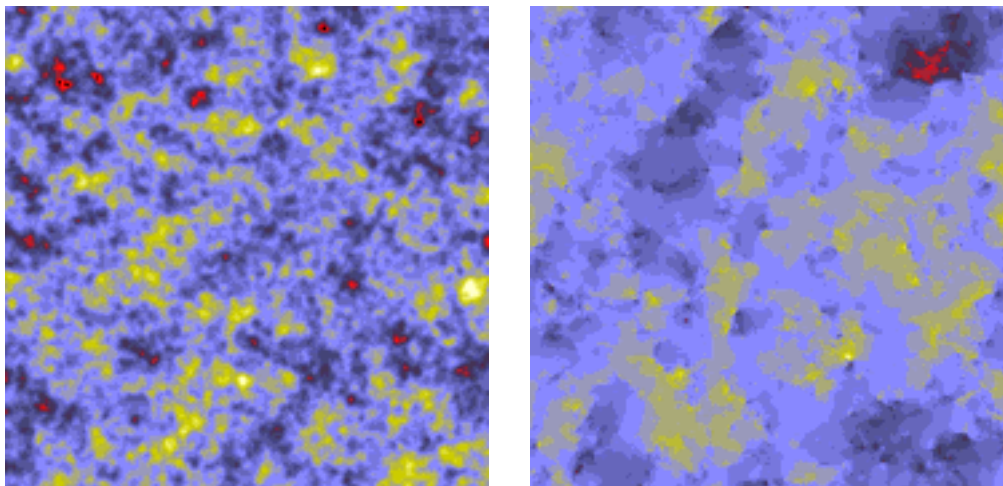


Figure 1.11: The picture on the left shows a simulated map of the sky of area $12.8° \times 12.8°$ for an inflationary CDM model. The picture to the right shows the anisotropy pattern in a $12.8° \times 12.8°$ patch of sky in a universe seeded by cosmic strings.

The temperature power spectrum can also be used to distinguish between topological defect models and inflation. Figure 1.12 shows a calculation of the power spectrum in a cosmic string model compared to an inflationary cold dark matter model (Magueijo *et al.* 1996). At low multipoles the curves are quite similar − topological defect models predict a nearly scale invariant fluctuation spectrum as expected in the simplest models of inflation. At multipoles $\ell > 100$, the power spectra differ significantly. The Doppler peak is much broader in the string model and the secondary peaks characteristic of the inflationary models are absent in the string model. Similar conclusions apply to the CMB power spectra in cosmic texture theories (Crittenden and Turok, 1995). In summary, the non-Gaussian signatures in the CMB arising from topological defects can distinguish between these models and the inflationary theories described above. Furthermore, the locations and shapes of the Doppler peaks in the temperature power spectrum would allow a clear distinction between these two classes of theories.
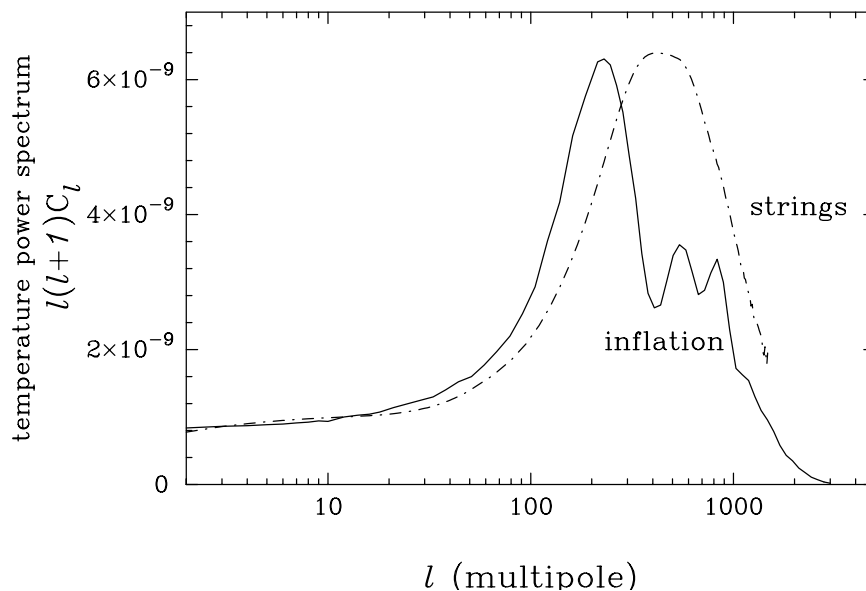
Figure 1.12: The dot-dashed line shows the temperature power spectrum of a cosmic string model with $\Omega_b = 0.05$ and $h = 0.5$. The solid curve shows a scale invariant inflationary CDM model with $\Omega_b = 0.1$ and $h = 0.4$, which matches the height of the first Doppler peak predicted in the string model, but has additional structure at high multipoles.

High resolution and high sensitivities, such as those provided by COBRAS/SAMBA are required to apply these tests.

In the previous section, we showed how cosmological parameters could be determined with high accuracy if the CMB anisotropies were generated by adiabatic perturbations. Would the same be true if the CMB fluctuations arose from topological defects (*i.e.* isocurvature perturbations)? Certainly, the CMB power spectrum in topological defect theories at high multipoles is sensitive to cosmological parameters such as $\Omega_0$, $\Omega_b$, $H_0$ *etc* in a similar way to the adiabatic fluctuations described above. However, theoretical computations of the CMB anisotropies in defect theories are inherently much more complex than for adiabatic fluctuations and calculations with the precision achievable by CO-BRAS/SAMBA have not yet been made. It is therefore, not yet possible to compute the accuracies of cosmological parameters expected in defect theories, though we expect that comparable accuracies to those presented in the previous section are probably achievable.

### 1.4.6   CMB Anisotropies and Large-Scale Structure in the Universe

By comparing CMB anisotropies with spatial distribution of galaxies, we can learn how fluctuations have evolved from the time of last scattering when the Universe was about 300,000 years old to the present day. The evolution of irregularities depends on the cosmological parameters, principally $\Omega_0$, $\Lambda$, and also on the matter and radiation content of the Universe, *i.e.* the precise mix of cold dark matter, baryonic material, massive neutrinos and relativistic components.

At present, however, large errors in both the CMB measurements and in the values of the cosmological parameters, lead to poor constraints on the form and evolution of the matter power spectrum. The situation will be improved dramatically by COBRAS/SAMBA as illustrated in Figure 1.13. The points in the Figure show constraints on the matter power spectrum from various galaxy redshift surveys, assuming that galaxies trace the matter fluctuations. The boxes in the left hand panel show constraints on the matter power-spectrum at the present day inferred from various CMB experiments, assuming that the Universe has a critical density ($\Omega = 1$); COBE provides constraints on fluctuations with physical scales $\lambda \gtrsim 1000\,\mathrm{h}^{-1}\,\mathrm{Mpc}$, *i.e.* about ten times larger than the largest structures that

have been observed in galaxy surveys. The boxes in the wavenumber range $k = 0.01$–$0.1 h \text{Mpc}^{-1}$, sampling scales 100–1000 $h^{-1}$ Mpc, show results from a number of balloon and ground based experiments with angular resolution of $\sim 1°$ (see Section 1.3); these suggest a positive signal on such scales but with an uncertainty in the inferred matter power spectrum $P(k)$ of nearly two orders of magnitude (since the matter power spectrum is proportional to $(\Delta T/T)^2$). The panel to the right shows the enormous improvement in accuracy that will be achieved by COBRAS/SAMBA, especially on physical scales of 100–1000 $h^{-1}$ Mpc. Furthermore, since COBRAS/SAMBA will constrain the cosmological parameters to unprecedented precision, it will be possible to extrapolate the spectrum of irregularities to the present day modulo small residual uncertainties concerning the nature of the dark matter.

Over the next decade, we can expect dramatic improvements in our knowledge of the large-scale distribution of galaxies. At present, the largest redshift survey contains about 30,000 galaxies (Schectman *et al.* 1995). However, two large galaxy surveys, the Sloan Digital Sky Survey (Gunn and Weinberg 1995) and the Anglo-Australian 2-degree field survey (Efstathiou 1996), are about to begin which aim to measure redshifts of more than $10^6$ galaxies over the next few years. By combining the results of these new surveys with COBRAS/SAMBA it will be possible to establish a consistent theory of the formation of cosmic structure and so elucidate the nature of the dark matter that dominates the present Universe.
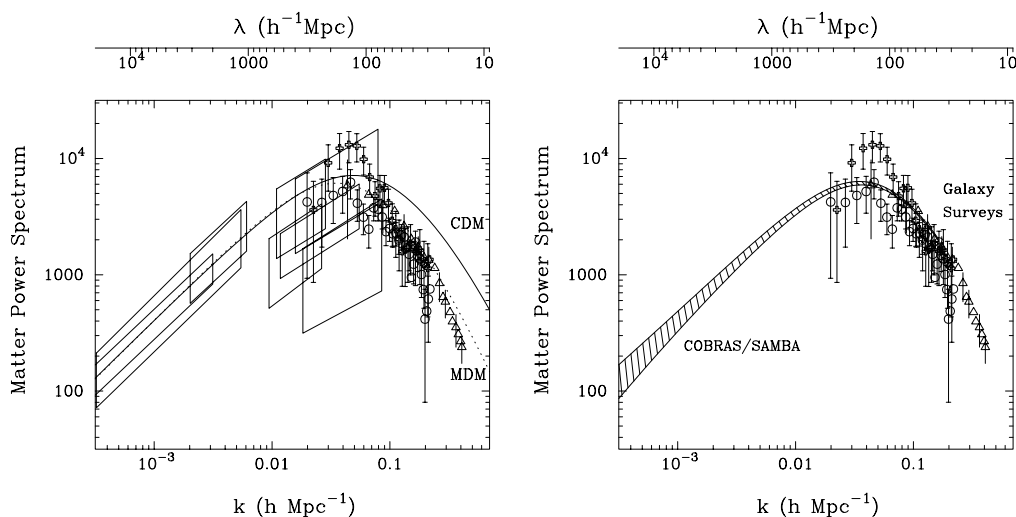


Figure 1.13: The boxes in the left hand panel show constraints on the power spectrum $P(k)$ of the matter distribution in an $\Omega = 1$ universe implied by observations of the microwave background anisotropies (adapted from White *et al.* 1994). The points show the power spectrum of the galaxy distribution determined from various galaxy surveys (see Efstathiou 1996). The right hand panel illustrates the accuracy with which COBRAS/SAMBA will be able to determine the power spectrum. The solid curve shows the matter power spectrum expected in an inflationary cold dark matter (CDM) universe. The dotted curve shows a theoretical prediction for a 'mixed dark matter' (MDM) universe consisting of a mixture of CDM (60%), massive neutrinos (30%) and baryons (10%).

## 1.5 Clusters of Galaxies

In addition to the primary CMB anisotropies generated in the early Universe, secondary anisotropies can be generated between the epoch of decoupling and the present epoch. The most important of these are caused by the Sunyaev-Zeldovich effect (Zeldovich & Sunyaev 1969) in which CMB photons are scattered by free electrons in the hot gaseous component of rich clusters of galaxies. The temperature of the CMB in the direction of a rich cluster of galaxies is modified in a way which depends on both the spatial distribution and temperature of the hot cluster gas, and the relative velocity of the cluster

with respect to the rest frame defined by the CMB. The Sunyaev-Zeldovich (hereafter SZ) effect has been observed unambiguously in a small number of rich clusters in ground based observations (see *e.g.* Rephaeli 1995 for a recent comprehensive review). However, as we show in this Section, the high angular resolution and sensitivity of COBRAS/SAMBA should lead to the detection of the SZ effect in several thousand rich clusters of galaxies and to valuable statistical information on cluster peculiar motions.

### 1.5.1 Thermal Sunyaev-Zeldovich Effect from Clusters of Galaxies

The thermal Sunyaev-Zeldovich effect arises from the frequency shift when CMB photons are scattered by the hot electrons in the intra-cluster gas. The frequency dependence of this effect (see Figure 1.14), results in a temperature decrement in the Rayleigh-Jeans region of the CMB spectrum and to a temperature excess at high frequencies. As described in Section 2.4.4, the central frequencies of the COBRAS/SAMBA bolometer bands have been carefully chosen to straddle the regions of negative and positive decrement, with one channel centered at 217 GHz, where the thermal SZ flux is zero. This arrangement has been chosen to optimize the separation of the thermal SZ effect from the frequency independent primary anisotropy pattern, as described in more detail in Section 2.4.5.

The amplitude of the SZ effect in a particular direction can be characterized by the Compton parameter $y = \int n_e \sigma_T (kT_e/m_e c^2) \, dl$, where $\sigma_T$ is the Thomson cross-section and the integral is taken along the line-of-sight. The net SZ flux from a cluster can therefore be written

$$S_\nu = A g_\nu \, Y, \tag{1.11}$$

where $g_\nu$ describes the frequency dependence of the Compton distortion (see figure 1.14.a), $A$ is a normalization constant and $Y = \int y \, d\Omega$, where the integral extends over the solid angle subtended by the cluster. The integral $Y$ is proportional to the total gas mass within the cluster times the mass-weighted temperature.

Observations of the SZ effect provide information on the hot intra-cluster gas that is complementary to that derived from observations at X-ray wavelengths. A key difference between the SZ and X-ray fluxes of clusters arises from their different scaling with the electron density ($n_e^2$ for X-rays, and $n_e$ for SZ): while the X-ray emission is strongly peaked near the centre, the signal-to-noise in the SZ signal remains roughly constant in logarithmic rings around the centre. This remains true insofar as the gas is approximately isothermal (*i.e.* within the virialized region of the cluster) defining a characteristic radius $R_{SZ} \approx 10 r_c$, where $r_c$ is a typical cluster core radius.

Figure 1.15 shows the differences between the X-ray and $y$ profiles of a typical rich cluster of galaxies at two different redshifts. The scales correspond to typical sensitivities for an X-ray mission such as XMM and for the COBRAS/SAMBA mission.

The net SZ flux from a cluster is insensitive to cluster redshift, due to the increase of the CMB temperature with $z$. Hence we expect distant clusters ($z \approx 1$) to be observable with COBRAS/SAMBA, although these will not be resolved. Figure 1.14.b shows the ratio of the expected X-ray brightness to the SZ brightness at $\lambda = 2$mm, which decreases strongly with $z$ for different central temperatures of cluster. The main effect is the $z$ dependence: the ratio has decreased by a factor of ∼30 at $z = 1$. Therefore, the SZ effect provides a powerful tool with which to study the evolution of clusters, as described in further detail below. The sensitivity of COBRAS/SAMBA to high redshift clusters can be utilized to complement X-ray and optical/near-IR investigations. For example, high $z$ clusters detected by COBRAS/SAMBA can be selected as targets for XMM observations and for ground based/HST spectroscopy and imaging.

Observations of the SZ effect with COBRAS/SAMBA will circumvent a further problem of X-ray observations. The peaked character of the X-ray emissivity allows gas mass determinations in a very limited radius, of a few $r_c$ only (except for very long integrations possible only on a small sample of clusters). However, COBRAS/SAMBA observations will probe the gas properties far beyond a few
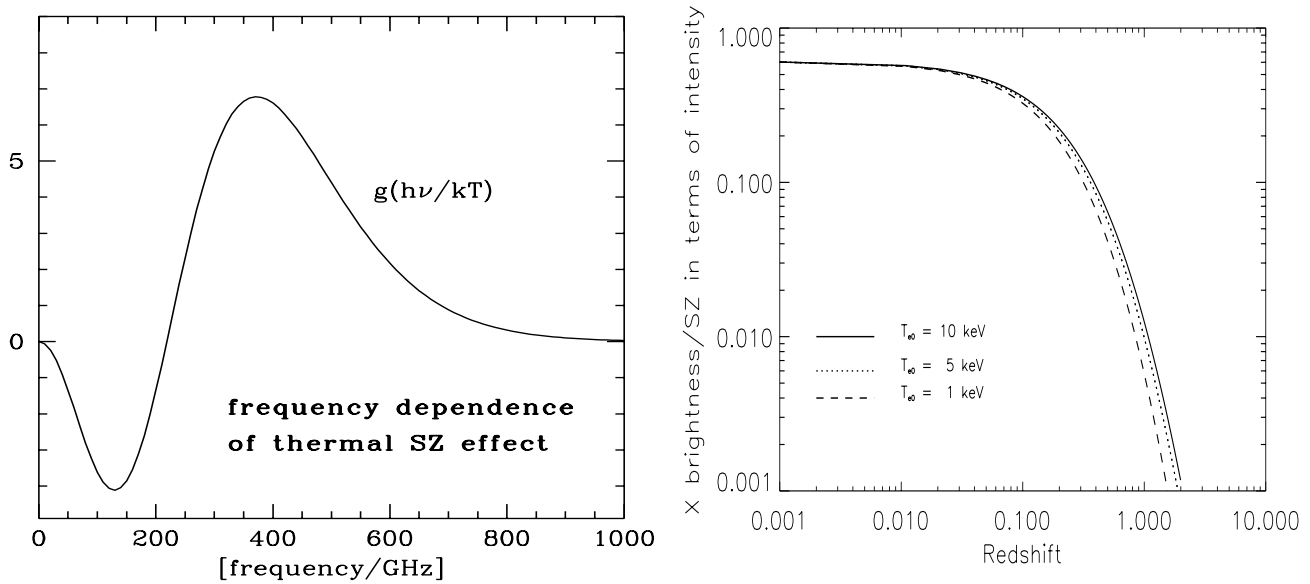
Figure 1.14: (Left) The spectral dependence of the SZ-flux (thermal effect). (Right) X-ray brightness (within 0.3-10 keV) versus y as a function of redshift for 3 central temperatures of the cluster.
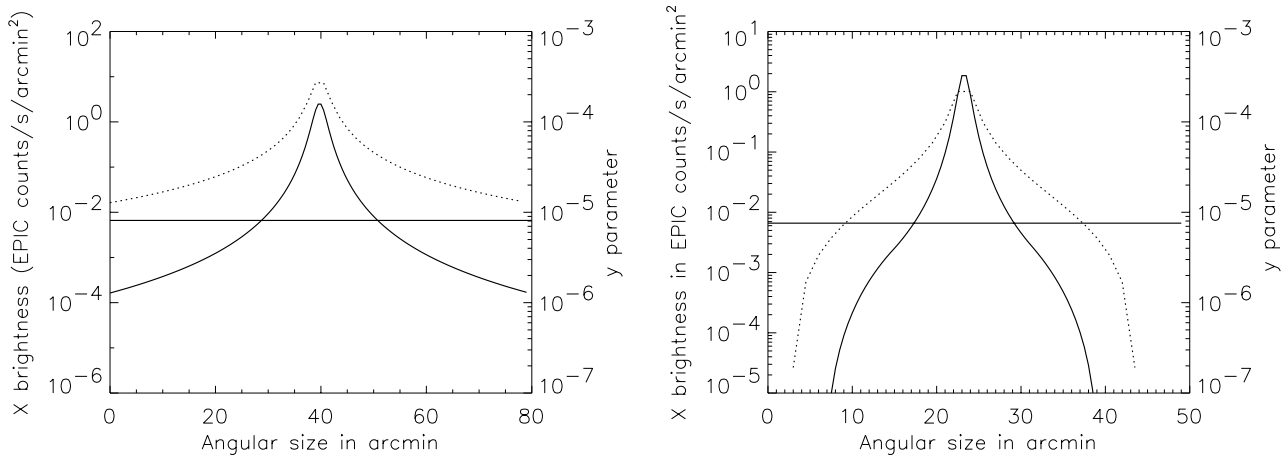


Figure 1.15: Profiles of a 4 keV cluster in X-ray brightness (solid, with scale on the left axis in counts in 0.3-10 keV for the XMM–EPIC instrument) and in the Compton $y$ parameter (dashes with scale on the right axis) for clusters with a King-type profile, a core radius $r_c = 0.3$ Mpc, and a central electron density $n_{e0} = 2\,10^{-2}{\rm cm}^{-3}$. This Abell 496-like cluster is viewed at a redshift $z = 0.1$ (left) and $z = 0.2$ with in addition a cut-off for the virialized gas at $20\,r_c$ (right). The horizontal line shows the level of the diffuse X-ray background.

core radii. This is illustrated in figure 1.15 which shows X-ray brightness and $y$ profiles for typical rich clusters at two different redshifts. The COBRAS/SAMBA sensitivity allows the detection of $y$ values of $3 \times 10^{-7}$ within rings of order one degree (Section 2.4). The SZ effect is thus sensitive enough to observe the temperature drop which defines the limit of virialization.

The EPIC instrument, on the XMM observatory, in a 20-hour observation, will be able to map the same cluster up to about $7 \, r_c$. This shows that the most powerful strategy for learning about the properties and evolution of the gas in clusters will be to combine COBRAS/SAMBA observations with X-ray brightness profiles and X-ray temperature measurements.

The combination of spatially resolved X-ray temperature and flux profiles, and measurements of the thermal SZ effect in the CMB, can be used to estimate the true spatial dimensions of rich clusters of galaxies and hence to estimate the Hubble constant (Gunn 1978, Silk and White 1978). Ground based SZ measurements already provide useful constraints on the Hubble constant, suggesting a value of $H_0 \sim 60 \mathrm{kms}^{-1} \mathrm{Mpc}^{-1}$ (Rephaeli 1995). COBRAS/SAMBA will produce spatially resolved thermal SZ maps for nearby rich clusters which will be complementary to those of purpose-designed ground based experiments such as the submillimetre SUZIE experiment (Wilbanks *et al.* 1994), covering a wider spectral range and with better control of systematic sources of error. COBRAS/SAMBA SZ measurements of the many thousands of more distant, unresolved, clusters can also be used to estimate $H_0$ and to constrain the deceleration parameter $q_0$. The main limitation in this case is likely to arise from the difficulty of the X-ray observations, which must have good spatial resolution, rather than from the CMB measurements where all that is required is a high signal-to-noise measurement of the integrated SZ effect.
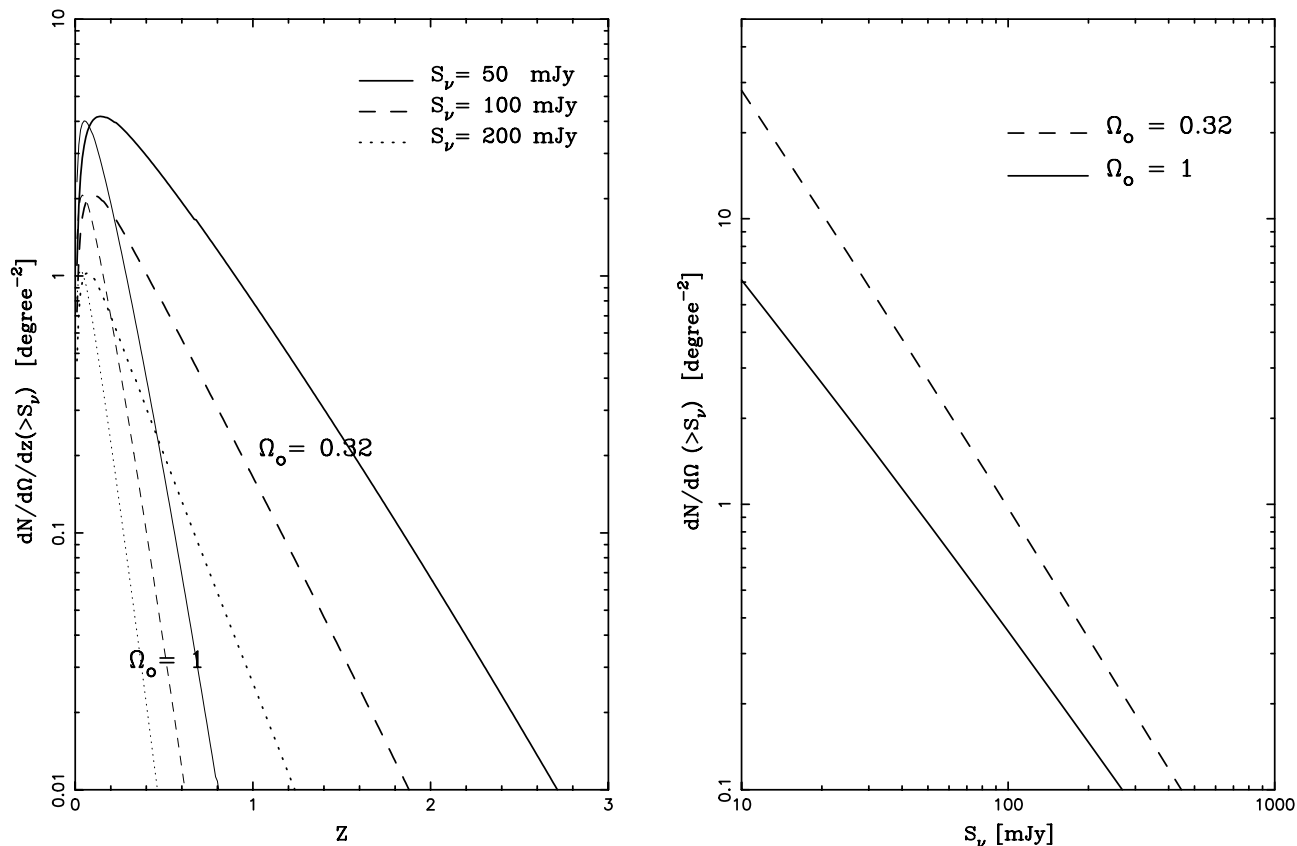


Figure 1.16: (Left) Differential number counts versus redshift for different flux limits and $\Omega$. (Right) Number counts per square degree versus flux limit for two values of $\Omega$.

To evaluate the number of clusters detectable by COBRAS/SAMBA, we refer again to our sim-

ulations which have shown (see Section 2.4.5) that COBRAS/SAMBA will detect clusters with $Y > 5 \times 10^{-4}$ when they cover more than one pixel (70% detection rate for a one year mission), or $Y > 3 \times 10^{-4}$ if $r_c$ subtends less than 0.5′. The integrated value is $Y = 64 y_0 \theta_C^2$, where $y_0$ stands for the central value and $\theta_C$ in expressed in arcmin.

The exact number of clusters detectable through the SZ effect, as a function of $z$, depends on

- the cosmological parameters,

- the shape of the present mass and temperature distributions of galaxy clusters, and

- the cosmological evolution of the mass and temperature distributions (which in turn depends on the model for galaxy and structure formation).

Analytic estimates based on the Press-Schechter (1974) mass function suggest the presence of about 15 000 such clusters over the whole sky (assuming $\Omega_0 = 1$), or up to 3 times higher for lower values of $\Omega_0$ (figure 1.16.b). This dependence on $\Omega_0$ is a consequence of the earlier formation of clusters of galaxies in a low density universe. Figure 1.16.a shows the corresponding redshift distribution. Since these estimations are strongly model dependent, measurements of the SZ effect will provide sensitive tests of theories of structure formation.

In summary, COBRAS/SAMBA will detect many thousands of rich clusters of galaxies via the SZ effect, and significant numbers are expected to lie at redshifts $z > 0.2$ and perhaps as high as $z \sim 1$. The observed counts of clusters will provide a powerful test of models of structure formation and evolution. Clusters observed by COBRAS/SAMBA can be selected as targets for X-ray observations with new satellites such as XMM, to study the properties and evolution of the intracluster gas and as targets for optical and near-infrared observations to study galaxy evolution and gravitational lensing.

### 1.5.2 Peculiar Velocities of Clusters

Peculiar velocities of the hot intra-cluster gas lead to a Doppler shift of the scattered photons which is proportional to the product of the radial peculiar velocity $v_{pec}$ and the electron density $n_e$ integrated along the line of sight through the cluster. For small optical depths, the relative change in intensity of the CMB is given by

$$\frac{\Delta I}{I} = \frac{\sigma_T}{c} \int_{los} v_{pec}\, n_e d\ell \left[ \frac{x\, e^x}{e^x - 1} \right], \qquad x = \frac{h\nu}{kT}, \tag{1.12}$$

where $T$ is the temperature of the microwave background and $\sigma_T$ is the Thompson cross section. For a typical cluster, the kinematic SZ effect at the cluster center is of order

$$\Delta T \sim 30 \left( \frac{n_e}{3 \times 10^{-3}\, \mathrm{cm}^{-3}} \right) \left( \frac{r_c}{0.4\, \mathrm{Mpc}} \right) \left( \frac{v_{pec}}{500 km s^{-1}} \right) \mu K, \tag{1.13}$$

where $n_e$ is the electron density in the core, $r_c$ is the core radius and we have scaled to the values of the Coma cluster. Since this effect is independent of frequency, the maximum attainable signal-to-noise ratio for a typical cluster is determined primarily by confusion with the primordial CMB fluctuations. It is therefore essential to use information on the statistical properties of the primordial CMB anisotropies and the gas distributions of the individual clusters which will be given by the high precision $y$ determinations derived from the COBRAS/SAMBA mission itself. This knowledge makes it possible to analyze the CMB maps with a spatial filter optimized for individual clusters. An improvement in signal-to-noise by a factor of two is easily achievable with this technique, and even a factor of 10 is possible if the gas mass distribution is well known. The final signal-to-noise ratio depends sensitively on the angular resolution of the instrument and on the temperature power spectrum of the primordial CMB anisotropies (and hence on the cosmological parameters), thus the precise accuracy

of peculiar velocity measurements for individual clusters depends on parameters which are poorly known at present (see Figure 1.17). Simulations of the COBRAS/SAMBA data analysis discussed in Section 2.4.5 show that the estimates of Figure 1.17 are realistic. Prime candidates for accurate peculiar velocity measurements ($\Delta v_{pec} \lesssim 200$ km/s) are clusters at intermediate redshifts with core radii slightly smaller than the angle subtended by the first Doppler peak in the primordial CMB power spectrum.
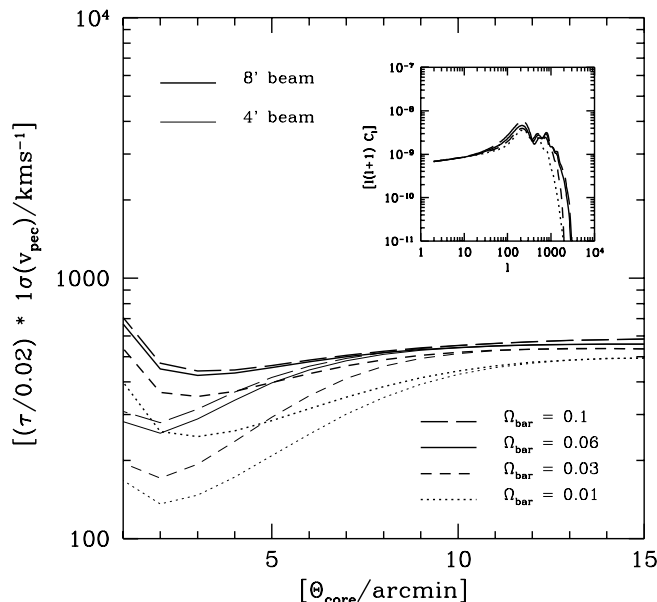


Figure 1.17: The $1\sigma$ error in the determination of the peculiar velocity as a function of the core radius of the cluster using an axisymmetric optimal filter function for a standard CDM scenario ($\Omega_{tot} = 1$, $H_0 = 50 \mathrm{kms^{-1}Mpc^{-1}}$) with varying baryonic fraction. The pixel noise is fixed and corresponds to $7\,\mu$K in a $4'$ (FWHM) beam. Thick curves are for a beam size of $8'$ and thin curves are for a beam size of $4'$. The inset shows the angular power spectra of temperature fluctuations for the three cosmological models.

In addition to estimates of peculiar velocities for individual clusters, it will be possible to extract statistical information on the bulk motion of clusters on scales of $\gtrsim 100h^{-1}$Mpc. So far, not much is known about bulk velocities on such large scales. The measurement of the bulk velocity of a volume-limited sample of 119 Abell clusters out to a distance of $15000\mathrm{kms^{-1}}$ has yielded a high value of $700 - 800\mathrm{km\ s^{-1}}$ (Lauer and Postman 1994). This is considerably larger than the $400 - 500\mathrm{km\ s^{-1}}$ expected in most cosmological scenarios currently favored. Detailed calculations show that COBRAS/SAMBA is capable of determining bulk motions to an accuracy of between 100 and 300 km/s within a sphere of radius $100h^{-1}$Mpc, depending on the statistical properties of the primordial CMB anisotropies (Haehnelt and Tegmark 1996). COBRAS/SAMBA can therefore provide unique statistical information on bulk motions, which can be used to constrain the power spectrum of matter fluctuations on large scales and to elucidate the relationship between irregularities in the galaxy and mass distribution (Dekel 1994).

## 1.6   Extragalactic Sources

In the spectral range covered by COBRAS/SAMBA , we can identify three regions characterized by the predominance of drastically different classes of *extragalactic* sources.

1. In the low frequency channels ($\nu = 30$ to 90 GHz), we expect to detect mainly radio–loud, flat–spectrum radiogalaxies and QSOs, blazars, and possibly some inverted–spectrum radiosources.

2. In the millimetre channels (90 to 300 GHz), the predominant extragalactic sources will be rich clusters of galaxies detected via the SZ effect.

3. In the sub–millimetre channels (300 to 900 GHz), we expect to detect many thousands of infra-red luminous galaxies (both normal and starbursting) and (mostly radio–quiet) AGNs, and a few high–redshift galaxies and QSOs.

In addition, studies of the anisotropies of the diffuse background at these wavelengths will constrain galaxy counts to faint flux levels and, consequently lead to strong constraints on models of galaxy evolution.

### 1.6.1   Radio–loud Active Galactic Nuclei

The highest frequency at which radio continuum sky surveys have been made is $\nu \simeq 8$ GHz. Since the beam area of a given radio telescope scales as $\nu^{-2}$, a large, ground–based, extragalactic survey at higher frequencies would require expensive multi–channel receivers and huge amounts of telescope time. Above 30 GHz, ground–based observations are in any case extremely difficult, and only very small areas can be surveyed.

In the large area of sky surveyed at the three COBRAS/SAMBA radio frequencies (30, 53 and 90 GHz), we expect to find several thousand flat–spectrum radiogalaxies, QSOs and blazars above the overall noise level. This prediction is based on high–frequency extrapolations of radiogalaxy counts at centimetre wavelengths (see Table 1.1).

Given the large fraction of blazars among flat–spectrum radiosources, the all–sky COBRAS/SAMBA survey will provide the most complete and richest catalogue of such objects, suitable for comparison with X–ray selected samples (e.g. as produced by ROSAT). A great advantage of such a radio–selected sample will be its common detailed spectral information over a wide frequency interval.

Another important outcome will be to check for the existence of strongly inverted–spectrum millimetre–peaked radiosources, i.e. very compact, radio–loud AGNs, which is a matter of speculation at present.

### 1.6.2   Infrared Galaxies and Radio–quiet AGNs

Optical searches are biased towards unobscured, active and/or starbursting galaxies (including low–mass galaxies in an active phase). Near–infrared surveys, in turn, detect primarily photospheric emission of late–type stars (red giants) and hence are biased towards early–type (E/S0/Sa) galaxies. Dust, which is found in most galaxies, includes a substantial fraction of all metals and strongly affects the observability of galaxies at different wavelengths. In this context, a major breakthrough in our understanding of galaxies has been made by the IRAS survey. Nevertheless, because the longest wavelength observed was $100\mu$m, IRAS detected primarily the warm dust component in low redshift galaxies, heated by the intense radiation fields from star–forming regions. IRAS was not sensitive to either cold dust or high–redshift galaxies.

Only future extensive sub-millimetre surveys, such as the one planned in the COBRAS/SAMBA mission, can determine how much of the stellar radiation in galaxies is either reprocessed by cold dust or redshifted to submillimetre wavelengths. COBRAS/SAMBA is expected to provide broad–band spectral information for several thousands of optical– and IRAS–selected galaxies (see Table 1.1), and also to test for the existence of galaxies optically obscured by cold dust. The observations will reveal the spectral behavior in this poorly–known frequency range. In addition to the study of energy balance in normal and starbursting galaxies, the multi–frequency sample will set constraints on dust properties (temperature, emissivity).

Statistical information on the various classes of objects will allow the definition of templates for modeling galaxy formation and evolution. Furthermore, a large sample of local sub-mm galaxies is required for precise and unbiased estimates of the local luminosity functions, a crucial step when interpreting the evolution of galaxies at infrared wavelengths. Studies of the angular correlation function will complement the analyses made from optical or IRAS surveys, and could help to test the

| $\nu_{eff}$ (GHz) | $\lambda_{eff}$ (mm) | Beam (arcmin) | $\sigma_{noise}$ (mJy) | $\sigma^1_{conf}$ (mJy) | $\sigma^2_{CMB}$ (mJy) | No. sources[3] (8 steradians) |
|---|---|---|---|---|---|---|
| 31 | 10 | 30 | 40 | 50 | 60 | $350 - 2500$ |
| 53 | 6 | 18 | 40 | 50 | 57 | $250 - 2000$ |
| 90 | 3 | 12 | 80 | 50 | 90 | $130 - 1000$ |
| 125 | 2.4 | 10 | 210 | 40 | 81 | $50 - 300$ |
| 150 | 2 | 10 | 24 | 6 | 114 | $-$ |
| 217 | 1.4 | 7.5 | 15 | 5 | 66 | $400 - 2000$ |
| 353 | 0.85 | 4.5 | 20 | 16 | 15 | $3000 - 15000$ |
| 545 | 0.55 | 4.5 | 32 | 40 | 3 | $7000 - 50000$ |
| 857 | 0.35 | 4.5 | 190 | 100 | - | $5000 - 20000$ |

[1] Standard deviation of the pixel brightness fluctuations due to galaxies, after removal of the brightest pixels, i.e. those with signal $D > 5\sigma_{conf}$.
[2] Sky variance induced by CMB anisotropies corresponding to $\Delta T/T = 10^{-5}$.
[3] Expected number of sources with flux $S > 4\sigma$ in 70% of the sky. The lower value is without evolution, the upper one for the RG and PLE models.

Table 1.1: Instrumental and confusion noise estimates for COBRAS/SAMBA , and number of extragalactic sources anticipated without evolution (NE), and in a particular evolutionary model (radiogalaxies and galaxies respectively evolve according to the RG and PLE models, see Appendix A).

evolution of galaxy clustering with cosmic time over a fraction of the Hubble time corresponding to $z \sim 0.2$.

Figure 1.18 summarizes some specific results about the predicted galaxy counts and redshift distributions relevant to the sub–mm observations of COBRAS/SAMBA, based on IRAS luminosity functions and theoretical FIR/submm/mm spectra designed to fit IRAS colors. There is a large uncertainty on dust emission at sub–mm wavelengths. In order to bracket the uncertainties, two extreme evolutionary models have been assumed based on pure luminosity evolution (PLE) and density plus luminosity evolution (DLE) which are described in more detail in Appendix A. The DLE model includes only the warm dust seen by IRAS while the PLE model also includes a cold dust component consistent with the 1.25 mm observations of Franceschini & Andreani (1995). The counts and redshift distributions are estimated with reference to the $\lambda_{eff} = 550\mu$m channel which, given the combination of sensitivity and angular resolution, gives the largest sample of infrared galaxies. The large difference in the predictions of these two models at $550\mu$m, given that they agree with the IRAS counts at $60\mu$m, illustrates how crucial submillimetre observations are in constraining models of galaxy evolution. These models show that a significant fraction of galaxies detected by COBRAS/SAMBA are expected to lie at $z > 0.2$, in marked contrast to the low median redshift ($z \leq 0.1$) of galaxies detected by IRAS. Note that Figure 1.18 shows that the behavior of the counts depart from an Euclidean law even for weakly–evolving galaxies (e.g. the normal spirals).

The conclusion, although model dependent to some extent, is that COBRAS/SAMBA surveys would give access to an intermediate redshift range that is complementary to other existing all–sky catalogues.

### 1.6.3   The Infrared Background due to Unresolved Sources

A peculiarity of galaxy spectra in the mm and sub–mm region is the very steep rise to shorter wavelengths following the strong spectral dependence of dust emissivity. This is the only spectral region where such a steep spectral shape is observed. The effect of the redshift on the location of the peak implies that it is possible to select high–redshift galaxies at a given flux level.

Figure 1.19 compares the diffuse background for the 2 extreme models of figure 1.18, together with
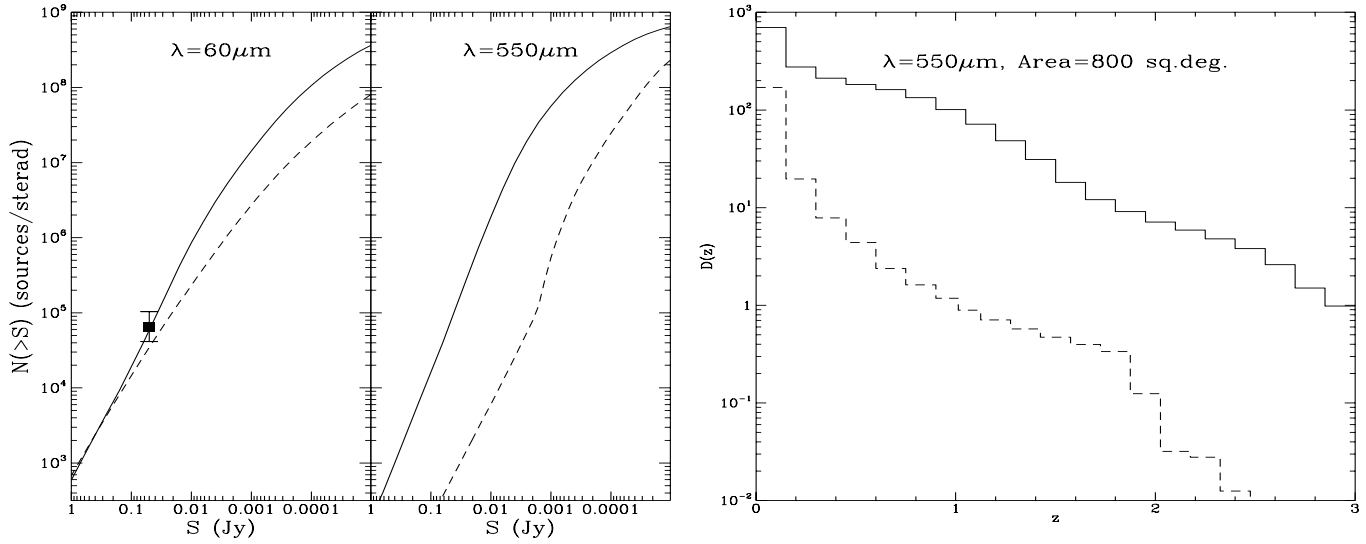
Figure 1.18: (Left) Estimates of integrated counts of galaxies at $\lambda = 60$ $\mu$m (IRAS) and at $\lambda = 550\mu$m; the latter is the optimal wavelength for source selection according to our two extreme models, PLE (solid line) and DLE (dashes) - see Appendix A. Both models reproduce IRAS data. The solid square shows the counts by Hacking & Houck (1987) with their Poisson errors. (Right) Predicted redshift distributions for a flux limit of $S = 150$ $mJy$ at $\lambda = 550\mu$m, over 800 square degrees. The dashes give the PLE no–evolution model based on the IRAS luminosity functions and theoretical FIR/submm/mm spectra fitting IRAS "colors" and observations of a sample of galaxies at 1.25 mm (Franceschini & Andreani 1995). The solid line gives the prediction for the PLE scheme.
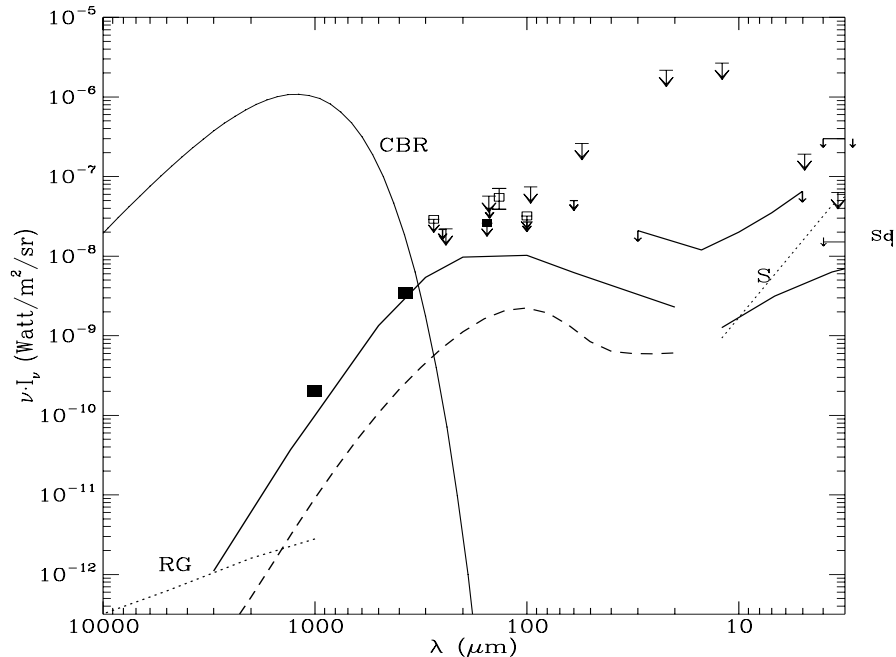


Figure 1.19: Extragalactic background in the FIR/submm/mm region. The predictions of two evolutionary schemes (PLE, pure luminosity evolution and DLE, density and luminosity evolution) fitting the IRAS data are respectively given by the solid line and the dashes. The predictions for a model of evolving radiosources (RG) is drawn with a dotted line. The Cosmic Microwave Background is also shown (CBR). Various observational upper limits are shown, as well as the predicted extragalactic background in the NIR (solid line) and the predicted Galactic starlight (dots). The solid squares show the isotropic component measured by Puget *et al.* (1995) from FIRAS observations.

other observational information about the FIR/sub-mm/mm backgrounds. We see that the isotropic sub–mm component found by Puget *et al.* (1995) in the COBE/FIRAS data is fitted by a PLE model, where the bulk of star–formation activity is confined to $z \geq 3$. In contrast, galaxy formation is assumed to be a continuous process in the DLE model, with giant galaxies forming at $z \sim 2$. As a result of the decrease in the number density of galaxies with increasing redshift, and of the absence of cold dust in the ISM, the predicted sub-mm background is much smaller.

**Fluctuations in the Diffuse Infrared Background**

It has been shown (Maffei 1996) that, owing to the steep submillimetre spectrum of galaxies, the background fluctuations due to unresolved sources can be dominated by sources much weaker than the detection limit. Based on the models described above, the variance of the fluctuations of the extra-galactic background are lower by about an order of magnitude than that of dust even for the maximal model (PLE) which reproduces the isotropic component. The multi–frequency information will allow an accurate subtraction of this small component from the millimetre wavelength COBRAS/SAMBA maps, in order to measure CMB anisotropies. Nevertheless, integrated information on fainter, high–redshift objects could be extracted from the all–sky COBRAS/SAMBA survey by means of an analysis of the small–scale anisotropies at $\lambda 550\mu$m, in clean regions of the sky where Galactic dust does not mask this information. This sample will set stringent constraints on the source counts to flux levels $S_{550\ \mu m} \sim$ a few mJy. At these flux levels, we may test, in particular, the anisotropy signal expected from a population of high–redshift, dusty primeval spheroids, which may be responsible for the rather high isotropic background in the COBE–FIRAS data (Puget *et al.* 1995). The presence or absence of such a signal will provide a further strong constraint on models of galaxy formation and evolution.

## 1.7   Galactic Studies

### 1.7.1   Interstellar Medium

COBRAS/SAMBA will provide all-sky maps of the emission from Galactic dust at sub-mm and mm wavelengths. At the two shortest wavelengths the COBRAS/SAMBA maps will have the same resolution as those from IRAS with an order of magnitude better sensitivity in terms of gas column density: N(H) of a few times $10^{18}$ H cm$^{-2}$. At longer wavelengths the detection limit is 1 to $2 \times 10^{19}$ H cm$^{-2}$. This sensitivity allows the detection of emission from Galactic dust over the whole sky in all of the bolometric bands. One can thus expect that COBRAS/SAMBA will have an even more significant impact on Galactic studies than the successful IRAS mission. Within the Galactic plane the sub-mm data will allow a decomposition of the IR emission from the different gas components and, in particular, the detection of emission from cold clouds that are not heated by active star forming regions. The fraction of gas in such clouds is still a matter of debate, and an estimate of its value is essential in establishing the efficiency of star formation in our Galaxy.

The IRAS data have been used to derive the size distribution of interstellar grains (Desert *et al.* 1990). An important result of this work was the discovery that the abundance of small particles emitting in the mid-IR varies by one order of magnitude within nearby molecular complexes, such as Taurus or Chamaeleon, and among high latitude cirrus clouds (Boulanger *et al.* 1990). The abundance of small particles has been observed to drop over physical sizes of about 0.1 pc where dense molecular gas is present (Laureijs *et al.* 1991). The COBE mission has provided data on the overall emission spectrum of dust from the near-IR to mm wavelengths which allows a better characterization of the evolution of dust. However at the sub-mm wavelengths, the low angular resolution of FIRAS (7 degrees) smooths out most of the spatial variations revealed by IRAS. The analysis of the high latitude COBE data shows that the emission spectrum from dust associated with HI gas is well fitted by a single temperature grey body with an emissivity scaling as $\nu^2$ and a temperature $T = 17.5$ K. However

it is clear from the spectra within the Galactic plane and in the direction of molecular complexes that a colder emission component is present there. The nature of this colder component is controversial. Is it a particular type of grain or does it only correspond to a change in dust emissivity? Is the cold dust component correlated with variations in the abundance of small particles and physical conditions in the gas? The angular resolution provided by COBRAS/SAMBA will allow a detailed investigation of these questions.

Hints suggesting a correlation between cold dust emission and dense gas opens the prospect of using the COBRAS/SAMBA data to systematically search for dense condensations in nearby clouds. Such a condensation with $T_d = 10$ K has recently been found in Orion with the Pronaos experiment (Ristorcelli 1996). For $T_d = 10$ K, the COBRAS/SAMBA detection limit at $350\mu$m corresponds to a gas mass of $10^{-2}M_\odot$ at a distance of 150 pc.

Dispersion measurements towards pulsars show that about a quarter of the gas in the nearby interstellar medium is ionized gas outside classical HII regions. The presence of such a large amount of ionized gas far away from ionizing stars is not understood (Reynolds 1990). The diffuse ionized gas is the dominant gas component at distances higher than 1kpc above the Galactic plane. Studies of this gas are important in establishing the physical processes responsible for expelling gas from the Galactic disk and in developing general models of the evolution of interstellar matter.

The wide frequency range of COBRAS/SAMBA will allow studies of this gas component from two distinct points of view: (1) the infrared emission from dust associated with this gas and (2) the free-free emission from the electrons. Attempts to identify dust emission from the diffuse ionizing gas using IRAS and COBE data have so far been unsuccessful. The difficulty here is to separate the emission from the HI and HII gas since the two are known to be spatially correlated to a significant extent (Reynolds *et al.* 1995). The free-free maps which will be extracted from the longer wavelength maps will help to spatially separate the two gas components. Dust in the low density HII gas is likely to have been processed by shocks. Detection of this dust would thus open the possibility of testing models of dust destruction in shocks.

### 1.7.2 Star Formation

Studies of the star formation process have concentrated, on the one hand, on determining the density and kinematics of the cold interstellar medium and, on the other hand, on understanding and observing the physics of protostellar sources when the accretion energy of the protostellar core makes them detectable in the near infrared.

It has become understood in the last few years that turbulence and magnetic fields stabilize the cold interstellar medium on large scales and that gravitational instability begins on small scales. Nevertheless the complicated interplay between gravity, supersonic turbulence, magnetic field and thermodynamics of the gas is poorly understood and there is, as yet, no theory that can predict with any accuracy the star formation rate as a function of a few critical parameters of the interstellar clouds.

To understand the physical mechanisms which control star formation, detailed investigations are required of the critical phase when a *small* region of the ISM becomes gravitationally unstable. The detection with large ground-based millimeter and sub-millimeter telescopes of a small number of dense and cold condensations in star forming regions (Mezger, 1994) provides a few tentative glimpses of the onset of gravitational instability. Nevertheless, large scale surveys are impossible with these techniques. COBRAS/SAMBA will provide the first systematic search for cold condensations in the ISM over a large fraction of the Galaxy and will provide a unique way of finding regions forming cold dense cores which have not yet produced stars detectable in the near infrared.

### 1.7.3    Interstellar Magnetic Fields and Cosmic Ray Electrons

The synchrotron emission at frequency $\nu$ is dominated by electrons of energy

$$E = 3 \left( \frac{\nu}{1\ GHz} \right)^{1/2} \text{GeV} \tag{1.14}$$

The intensity is proportional to the product of the magnetic field intensity and the density of cosmic ray electrons. The simulations described in Chapter 2 have shown that COBRAS/SAMBA will be able to map the synchrotron emission accurately at Galactic latitudes below 30 degrees and to derive useful information even in the lowest brightness regions at high Galactic latitudes. The synchrotron emission as detected in the COBRAS/SAMBA frequency range, when combined with lower frequency data, will lead to new information on the spatial distribution of the spectrum of cosmic ray electrons in the energy range 10 to 20 GeV.

The high frequency data will have other major advantages over lower frequency maps obtained from the ground: a significantly higher angular resolution (typically 15 arcminute instead of 51 arcminute for the 408 MHz Haslam survey) and a homogeneous coverage of the whole sky. An important unresolved question of interstellar medium physics is the distribution of magnetic field with respect to the matter distribution. In recent years, interstellar matter has been found to be structured on all scales observed (see for example Falgarone 1992). The physics of the very small scale structure is still not understood. It is known that on large scales the magnetic field is correlated with matter, probably as a result of gravitational instability in a medium where gas and magnetic fields are well coupled. On very small scales where gravity is not important, it has been proposed that matter and magnetic fields could be anticorrelated (Tagger & Falgarone, 1995). Theories of this nature could be tested through the investigation of the correlations between the synchrotron emission and the dust emission in the COBRAS/SAMBA data.

# Chapter 2

# From Observations to Scientific Information

## 2.1 Introduction

A major obstacle to a precise measurement of the CMB anisotropies by any experiment is the fact that other sources of radiation emit in the same range of frequencies as the CMB. This and other technical complications pose practical problems to a mission such as COBRAS/SAMBA which must be addressed early in the design phase to ensure that its ambitious goals can be met. The approach that we have taken here is to carry out detailed analysis and numerical simulations of the complete mission, starting from our best knowledge of the microwave sky, convolving it with the measurement process, and finally separating the simulated observations into maps of each physical component present.

   Using this approach, we demonstrate in this chapter that the technical characteristics of the COBRAS/SAMBA model payload (number and position of wavebands together with their angular resolution and sensitivity) will enable CMB maps to be generated *with the very high accuracy required* to obtain the scientific results anticipated in Chapter 1.

   This demonstration was achieved through a major study carried out specifically for this Phase A document; since it is much more sophisticated than any previously available analysis, many aspects are treated in detail. The full demonstration is rather technical, but the salient points are simple and summarized in the conclusions. The demonstration proceeds as follows.

1. We first determine what is the magnitude of the "contamination" problem. To do this we review (Appendix A) the current knowledge on the various sources of radiation (other than the CMB itself) which are relevant in the frequency range of COBRAS/SAMBA . In particular we shall estimate, for each source of emission, its spectral behavior, and the distribution across the sky of the amplitude of the fluctuations versus their angular scale. On the basis of this knowledge (see a partial summary in Table 2.1), we will construct a realistic model of the sky (Section 2.2) which can later be used to assess the relevance of any proposed strategy of measurement and analysis.

2. We generate with this model a full-sky map of the fluctuations around the degree scale (see Figure 2.3) and show that, over the best (cleanest) half of the sky, there is a frequency range where the fluctuations at all scales but the largest (quadrupole) are weak compared to the expected CMB anisotropy signal. What this means in practice is that over one half of the sky we expect to be able to detect the CMB fluctuations directly by simply selecting the optimum frequency channel, to an accuracy of order 10% in the relative amplitude of the angular spectral modes ($\Delta C(\ell)/C(\ell)$, see Figure 2.6).

3. Using the foreground levels derived earlier (Fig. 2.4), we simulate maps of small patches of the sky, and the data collection process. We then apply to the simulated data an inversion algorithm, and finally judge the quality of the procedure by comparing input and recovered components. In Section 2.3.4, we describe the assumptions that we use for the sky and data collection simulations; the outcome of this first step can be seen in Figure 2.7, which shows small patches of the sky, as would be seen by the COBRAS/SAMBA instruments. We then discuss and propose an inversion technique (Section 2.4) which is based on the idea of Wiener filtering. When applied to the problem of extracting the CMB anisotropies from the observed data, the technique yields the required accuracy, as illustrated in Figures 2.9, 2.10, and 2.11.

4. We develop (Section 2.4.4) a quantitative measure of the "quality" of the extraction which can be achieved by any particular experiment. This measure summarizes accurately many of the simulation results (Figure 2.12). It is used to quantify (i) the effect of an unresolved foreground of point sources (Table 2.3), (ii) the increase in accuracy brought by the COBRAS/SAMBA design as compared to a simpler mission with a much more restricted frequency range (Table 2.4), and (iii) the performance degradation in the event of detector noise excess

   at some of the more critical frequencies (Table 2.5).

5. We extract galaxy clusters from the data using the SZ effect (Section 2.4.5) and derive the detection rate as a function of the integrated Compton parameter $Y$ (Figure 2.14); we establish that COBRAS/SAMBA will be extremely efficient at detecting low $Y$ clusters. Moreover we determine that COBRAS/SAMBA will accurately determine the radial profiles of SZ clusters to large distances, even for central $y_0$ values as low as $3 \times 10^{-6}$ (Figure 2.13).

6. Finally, we discuss a number of specific topics (striping of the maps by $1/f$ noise, calibration offsets, determination of the beam shape, Section 2.5) which have a potentially degrading effect on the mission results, and show that they can be handled adequately, either by technical design or by means of specialized data processing.

While much of this chapter is generic, i.e. it does not depend on the characteristics of a given CMB experiment, in some instances we refer specifically to the characteristics of the COBRAS/-SAMBA mission, in particular when we evaluate the accuracy achievable in the final scientific products. Although the model payload is introduced later (Chapter 3), we here refer the reader to the Mission Summary located at the beginning of this report, in which the main parameters of COBRAS/SAMBA are briefly described.

## 2.2 Models of the Microwave Sky

Many detailed studies have been devoted to analyzing the sources of emission that may confuse the signature of the primordial CMB anisotropies. It is well established that the dust, free-free, and synchrotron emission of our own galaxy, those of radio-sources and infrared galaxies, and the Sunyaev-Zeldovich effect of clusters of galaxies all contribute detectable microwave anisotropies, at a variety of frequencies and angular scales. The current state of knowledge of these sources is reviewed in Appendix A and is used here to create a realistic model of the microwave sky.

### 2.2.1 Galactic Emission

Using the available information reviewed in Appendix A and briefly summarized in Table 2.1, we have created a model of galactic emission at microwave frequencies. We shall use that model to (1) generate full-sky maps with moderate resolution (typically greater than one degree) to assess global levels and the sky distribution of the fluctuations (see also Bouchet *et al.* 1995c); (2) generate maps

of small patches of the sky ($12.5° \times 12.5°$ ) to be used for detailed simulations of the process of data acquisition and analysis (Bouchet *et al.* 1995a, 1996). In all cases, maps are generated using existing observations as spatial templates of the galactic emission.

| Galactic Component | Spectral[a] Dependence | Angular Dependence | Spatial template $\theta > 1°$ | Spatial template $\theta < 1°$ |
|---|---|---|---|---|
| Dust | $I_\nu \propto \nu^2 B_\nu(18K)$ | $C(\ell) \propto \ell^{-3}$ | DIRBE 240 $\mu$m (42') | IRAS (4') |
| Free-free | $I_\nu \propto \nu^{-0.16}$ | $C(\ell) \propto \ell^{-3}$ | DIRBE[b] 240 $\mu$m | IRAS |
| Synchrotron | $I_\nu \propto \nu^{-0.9}$ | $C(\ell) \propto \ell^{-3}$ | Haslam  408MHz (51') | Haslam "extended"[c] |

[a] For the dust emission, $B_\nu(T)$ stands for a blackbody spectra at a temperature $T$; the free-free emission is normalized such that each components (HI-correlated and uncorrelated) yields 5.3 $\mu$K at $\nu = 53$GHz for a template value of 2.45 MJy/sr at 240$\mu$m.

[b] North/South inverted map in galactic coordinates.

[c] Haslam maps to which artificial small scale structure has been added, smoothly extending the angular power spectrum measured at larger scales.

Table 2.1: Summary of the present state of knowledge of high-latitude galactic emissions between $\sim$30 and 1000 GHz.

At scales $\gtrsim 1°$, we use the 408 MHz full-sky map of Haslam et al. (1970) as a template for the *synchrotron* emission, extrapolated to other frequencies with a spectral index of $\alpha = -0.9$. We use the DIRBE 240 $\mu m$ map as a template for the HI-correlated dust and the free-free emission. Comparisons with other tracers of the free-free emission show that the H-I correlated free-free emission accounts for most (at least 50%), and maybe all, of that component. We conservatively assume that there may be a second, uncorrelated, component accounting for 5% of the total dust and 50% of the free-free emission. There is of course no known template for such a component, but we assume that it should have the same "texture" as the correlated component: we simulate it by using again the DIRBE 240$\mu m$ map, but North/South inverted (in galactic coordinates). While arbitrary, this choice preserves the expected latitude dependence of the emission, and the expected angular scale dependence of the fluctuations. The dust spectral behavior is modeled as a single temperature component with $T_d = 18$K and $\nu^2$ emissivity. We assume that the free-free emission will behave according to $I_\nu \propto \nu^{-0.16}$, and normalize it to give a total *rms* fluctuation level of 6.2 $\mu$K at 53 GHz. The spectra of the three galactic components are summarized in Figure 2.1.

At smaller angular scales, there is no template available for the synchrotron emission, even over relatively small areas of the high latitude sky. We instead use patches of the 408 MHz radio map of Haslam with its 0.85° resolution and add to them small scale structure with a $C(l) \propto l^{-3}$ power spectrum[1], thereby extrapolating to small scales the observed behavior of the spatial spectrum. For the dust and free-free emissions, the DIRBE data lacks the proper resolution (42'), but we can use instead 100$\mu$ IRAS maps as spatial templates. The IRAS sky was divided into 300 maps, which were then sorted according to their *rms* level, so that we could check for systematic effects related to the foreground level. When we pick a map as a template for the HI correlated component, we used a contiguous map for the uncorrelated component.

## 2.2.2   Radio-sources and Infrared Galaxies

Our models for the contribution of point sources emitting in the centimetric to sub-millimetric range (detailed in Appendix A) were used to generate a large number of realizations of portions of the sky

---

[1] To do so, the map is Fourier transformed (which is equivalent to a spherical harmonics decomposition if the size of the map is much smaller than a radian) and its spectrum till the cutoff is computed. New harmonics are then generated at larger $l$, and globally normalized so that their spectrum smoothly extends the measured one. The results are then transformed back.

at many different frequencies. The angular power spectra were then computed (Toffolatti 1996) at each frequency and their amplitude in temperature units were found to be well fitted by

$$[\ell(\ell+1)C(\ell)/2\pi]^{1/2} = 0.3 \, \frac{\sinh^2(\nu/113.6)}{(\nu/1.5)^{4+\alpha_l}} \, \ell \text{ K}, \quad \text{with} \quad \alpha_l = 0.75 - 0.185 \log_{10}\left(\frac{\nu}{1.5}\right) \qquad (2.1)$$

for the radio-sources, if $\nu$ is expressed in GHz. This level assumes that bright resolved sources will be excised or subtracted from the observed data by specialized algorithms or by using existing point sources catalogs, but fluctuations from unresolved (or unsubtracted) sources will remain. The threshold[2] used was 100 mJy at 1.5 GHz. At high frequencies, the formula

$$[\ell(\ell+1)C(\ell)/2\pi]^{1/2} = 2.6 \times 10^{-11} \, \frac{\sinh^2(\nu/113.6)}{(\nu/857)^{4-\alpha_h}} \, \ell \text{ K}, \quad \text{with} \quad \alpha_h = 1.8 + 0.8\left(1 - \frac{\nu}{1000.}\right) \quad (2.2)$$

provides an adequate fit. In this case, no removal of resolved sources was assumed.

The corresponding fluctuation levels are shown in Figure 2.5 and they are quite low as compared to the expected CMB fluctuations, or those of the galactic foregrounds.
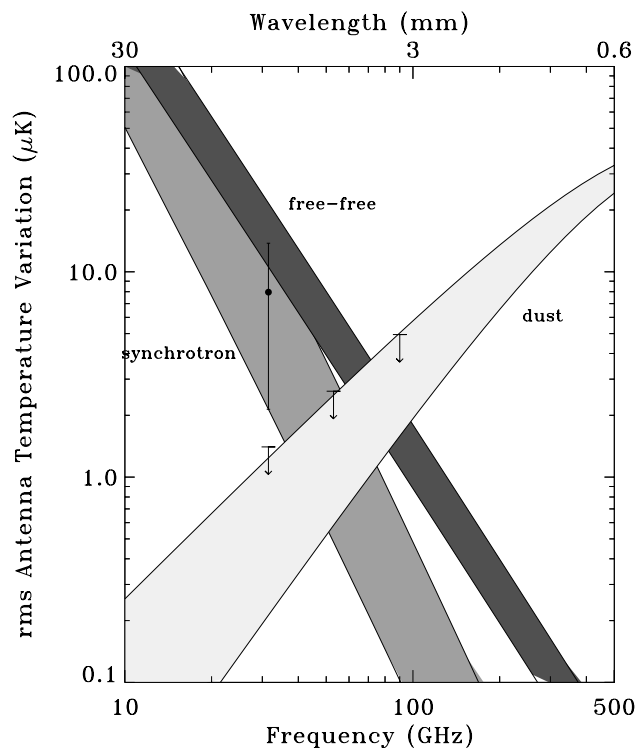


Figure 2.1: Amplitude of the galactic *rms* fluctuations at latitudes $|b| > 30°$ as a function of frequency, for a 7° FWHM beam (Kogut *et al.* 1995). The dipole and the quadrupole components have been subtracted out. This Figure summarizes the information extracted from the DMR-DIRBE and DMR-Haslam cross-correlations. The arrows show the upper limits on the dust derived from this analysis only. More recent analysis (see Appendix A) indicates that the spectral dependence of the dust at high galactic latitudes is close to the lower line delimiting the corresponding shaded area. Thus measurements around 100 GHz should be optimal for determining fluctuations on this angular scale (at smaller scales, the optimal frequency is higher, due to the increasing contribution from unresolved sources - see text).

---

[2]This corresponds to the removal of about 70000 sources over the sky. A lower threshold would entail removing more than 12 times more sources, for a decrease of the fluctuations by about 4.

### 2.2.3   Clusters of Galaxies

The mass function of clusters of galaxies at low redshift has been inferred from X-ray and optical surveys (Bahcall and Cen 1993) and models based on the Press-Schechter formalism have been used to predict the evolution of their mass function (Bartlett and Silk 1994). On the basis of such models a minimum contribution of the Sunyaev-Zeldovich effect to the fluctuations of the CMB on 10 arcminute scale, including the kinematic effect due to peculiar velocities, has been estimated and is shown in Figure 2.2 (De Luca *et al.* 1995). It shows that measurements of the CMB fluctuations at a sensitivity of $\delta T/T \simeq 2.\,10^{-6}$ require the removal of the S-Z component (Colafrancesco *et al.* 1994). Fortunately, the Sunyaev-Zeldovich effect has a unique spectral signature (see Fig. 1.14a) which makes it relatively easy to identify, if the experiment covers the range 500 $\mu$m to 2 mm with high sensitivity and good angular resolution (better than 10 arcminute), as is the case of COBRAS/SAMBA .
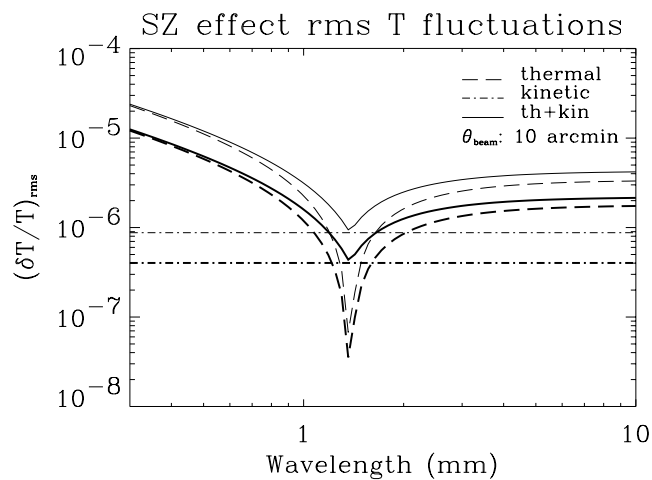


Figure 2.2: An estimate (see text) of the *rms* contribution as a function of wavelength of the Sunyaev-Zeldovich effects of a cluster background at the 10' scale. The bold set of lines corresponds to the contribution of all sources weaker than 100mJy for the thermal part and 30 mJy for the kinetic part. The light set of lines corresponds to the contributions of sources weaker than 1 Jy.

By using the same Press-Schecter approach, we have created actual realizations of small patches of the sky. This procedure yields the number density of clusters per unit redshift, solid angle and flux density interval. Thus we simply lay down in each redshift slice the appropriate number of clusters. Here we have used a King model for the gas profile in the clusters. To generate temperature maps, the radial peculiar velocities $v_r$ of each cluster were drawn randomly from an assumed initial Gaussian velocity distribution with standard deviation at $z = 0$ of $\sigma_0 = 400\,km/s$. A $\Delta T/T$ profile was then computed for each of the resolved clusters. The resulting maps (Aghanim *et al.* 1996) were found to agree reasonably well with a more sophisticated algorithms which we have also used (the "peak-patch" method, Bond & Myers 1996).

## 2.3   Simulations

### 2.3.1   Distribution and Amplitude of Galactic Fluctuations

The galactic emission is strongly concentrated toward the galactic plane. But what is the geography of the galactic fluctuations? Do we expect large connected patches with low levels of fluctuations? What is the amplitude of fluctuations typical of the best half of the sky?

To answer these questions, the DIRBE and Haslam spatial templates were first brought to the same 1° FWHM resolution. This relatively small angular scale was chosen to preserve the geography of the fluctuations on the smallest possible scale at the expense of overestimating the galactic fluctuations

(due to the substantial remaining noise in the maps at that resolution). Using the spectral models of the components described earlier, we can now create full sky maps of the total galactic emission converted to an equivalent thermodynamical temperature at any chosen frequency. Note that at this resolution, extragalactic point sources and the SZ effect would contribute negligible signal (see below, Figures 2.5 & 2.8).
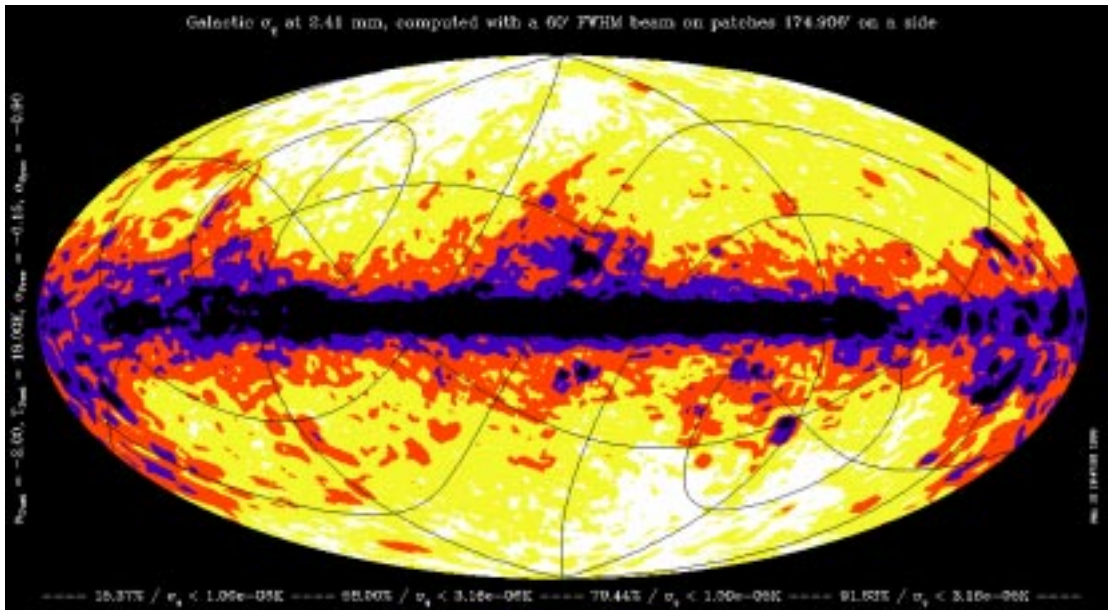


Figure 2.3: Map of the temperature fluctuations due to the galactic foregrounds at $\lambda = 2.4$ mm. The fluctuation levels, denoted by 5 different color levels, are obtained by computing the local variance over square patches with 3 degrees on a side (see text). From the lightest (small $\sigma_T$) to the darkest regions close to the galactic plane, the levels correspond to $\sigma_T = 1.0, 3.16, 10.0$ and $31.1$ $\mu$K. CMB fluctuations would correspond to blue and black regions. The galactic fluctuations will thus contribute less than 10% (at this frequency) of the total (CMB+galaxy) over the best half of the sky. More quantitatively, over 15.4% of the sky the galactic fluctuations are at a level $\sigma_T < 1$ $\mu$K, over 58% $\sigma_T < 3$ $\mu$K, over 79% $\sigma_T < 10$ $\mu$K, and over 92% $\sigma_T < 32$ $\mu$K.

In order to obtain *local* estimates of the level of fluctuations, we have computed their *rms* amplitude ($\sigma_T$), over square patches of 3 degrees on each side (i.e. containing about 11 beams of 1 degree FWHM). Thus, this estimator only retains perturbations at angular scales roughly between 1 and 3 degrees, equivalent to restricting the contribution to the variance to a range of angular modes[3] with $\ell$ between $\sim 20$ and 60. Figure 2.3 shows an example of such a map at $\lambda = 2.4$ mm. The darkest regions (black, $\sigma_T > 31.1\mu$K) are the areas where galactic fluctuations would exceed those of a COBE-normalized CDM model. This map provides direct graphical evidence that a large fraction of the sky is quite "clean" around the degree scale (Bouchet *et al.* 1995b, 1995c).

Analyzing Figure 2.3 more quantitatively, Figure 2.4.a shows the fraction of the sky for which the *rms* fluctuations of each of the foregrounds and of their total contribution are less than a given value at $\lambda = 2.4$ mm. These curves are steep for low fluctuation levels; the best half of the sky (median value) is only a factor of $\sim 4$ noisier than the best regions. The high level "plateaus" correspond to low galactic latitude regions. Indeed the maps tell us that that the "clean" sky essentially corresponds to the areas at high galactic latitudes, excepting only a few "hot spots" due to sources such as the Magellanic clouds. Figure 2.4.b, which plots the median fluctuation values as a function of frequency, shows a clear minimum around 100 GHz (as could be expected from Figure 2.1). Thus measurements restricted to that frequency would already be sufficient to achieve better than 10% accuracy around the degree scale (provided hot spots are flagged out using higher and lower frequency channels).

---

[3] $\ell$ indexes the order of the spherical harmonics $Y_{lm}$, see Ch. 1
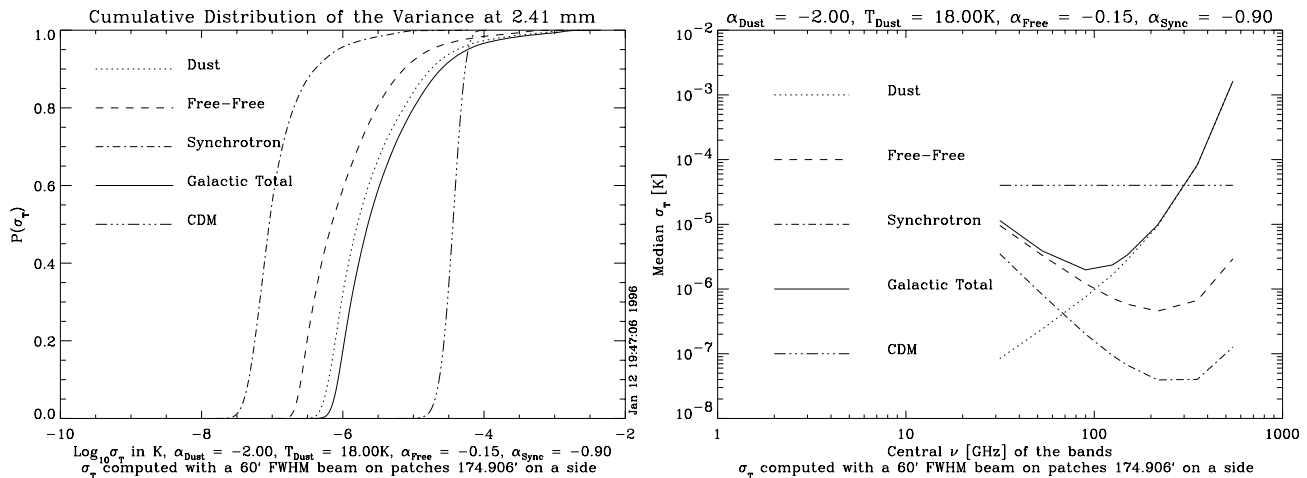
Figure 2.4: (Left) Cumulative distribution functions of the galactic foreground fluctuations at $\lambda = 2.4$ mm in 3 degree patches for a 1 degree FWHM Gaussian beam, showing directly the fraction of the sky in which the *rms* fluctuation level is lower than a certain value. The CDM curve shows for comparison the expected range of fluctuations for a COBE normalized CDM model. (Right) Median fluctuation values (i.e. corresponding to 50% of the sky) for the galactic components around the degree scale as a function of frequency.

## 2.3.2   Angular Scale Dependence of the Fluctuations

The previous analysis was limited to a single angular scale, but the fluctuation levels vary both as a function of frequency and of scale. In particular point sources will become much more significant at very small angular scales. We can initially evaluate these effects statistically using power spectra.

As was shown in Appendix A, the angular power spectra $C(l)$ of the galactic components all decrease strongly, approximately as $C(l) \propto l^{-3}$. Smaller angular scales thus bring increasingly small contributions per logarithmic interval of $\ell$ to the variance, $l(l+1)C(l)$: the galactic sky becomes smoother on smaller angular scales. We set the normalization constants of the spectra to obtain a level of fluctuations representative of the best half of the sky: i.e. the local fluctuations in regions of interest for CMB measurements would actually be even lower[4]. The square root of the resulting spectra at 3.3 and 1.4 mm are compared in Figure 2.5 with our standard CMB model.

The Figure also shows the power contributed by unresolved radio and infrared sources, as estimated from eqs. 2.1 & 2.2. Since point processes have flat ("white noise") angular power spectra, their logarithmic contribution to the variance, $l(l+1)C(l) \propto l^2$, increases and becomes dominant at very small scales. These levels must now be compared with the detector noise, in order to evaluate what is measurable in practice.

The detector noise is added to the total signal *after* the sky fluctuations have been convolved by the beam pattern. Its level depends on the details of the observing strategy, e.g. the total integration time per sky pixel. When the time-ordered data is converted into a map, the pixel noise will depend on the size of the map pixels, which must in practice be at least a factor of two smaller than the beam FWHM to preserve all the angular information available. We assume at this stage that the detector noise can be modeled as isotropic white noise, leaving aside the effect of low frequency $1/f$ noise. If uncorrected, the latter translates into "striping" of the maps; our strategy for removing this effect down to adequate levels is described in Section 2.5.1.

In order to directly compare the astrophysical fluctuations with those arising in the detectors, it is convenient to derive a fictitious noise field "on the sky" which, once convolved with the beam

---

[4]In practice, this was achieved by generating an artificial map with $C(l) = l^{-3}$, and then measuring its $\sigma_T$ using our previous procedure of measuring the variance in 3 degree patches after convolving with a one degree beam. This yields the required normalization factor of the power spectra by comparison with the median values plotted in Fig. 2.4.b.
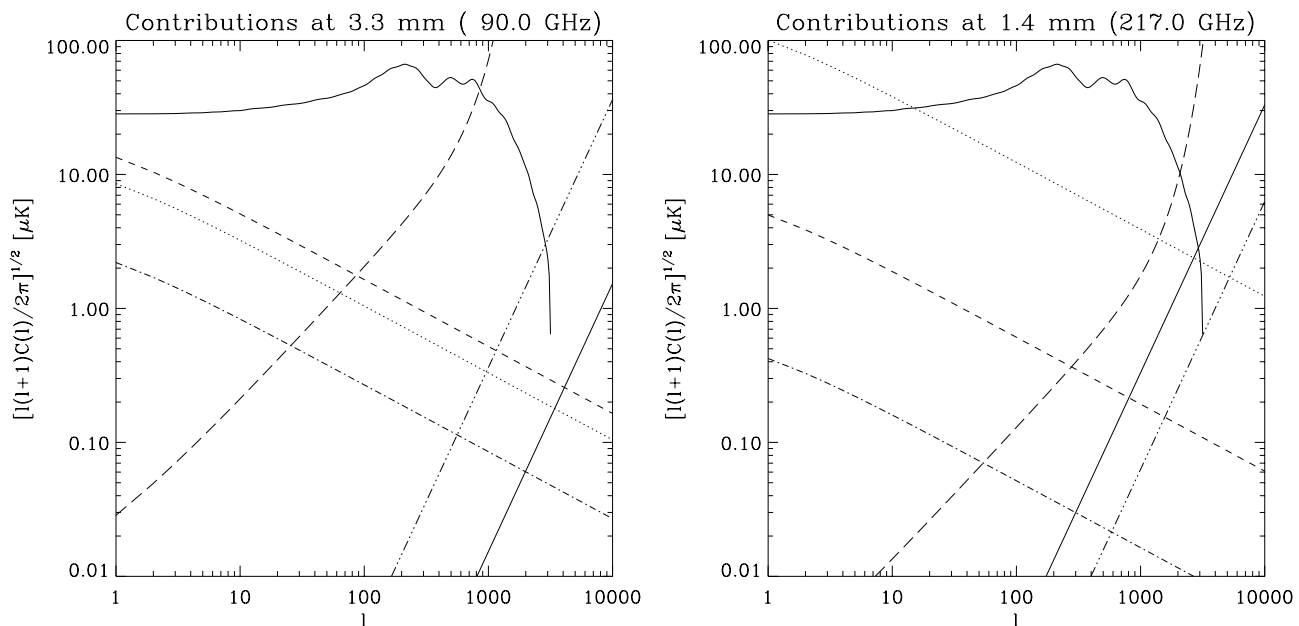
Figure 2.5: Contributions to the fluctuations of the various components, as a function of angular scale. The wiggly solid line corresponds to a COBE normalized CDM model. The dots, dashes and dot-dashes refer respectively to the dust, free-free and synchrotron galactic emissions. Long dashes show COBRAS/SAMBA "unsmoothed" noise level. The triple-dot-dashed lines display the contribution of unresolved radio sources (i.e after sources with flux > 100mJy at 1.5 GHz have been removed), while the solid line on the right is an estimate for all infrared galaxies.

pattern and pixelized, will be equivalent to the real one (Knox, 1995). Modeling the angular response of channel $i$, $w_i(\theta)$, as a Gaussian of FWHM $\theta_i$, the sky or "unsmoothed" noise spectrum is then

$$C_i(l) = C_i \ exp(l^2\theta_i^2/8\ln 2), \quad \text{with} \quad C_i^{1/2} = \theta_i\sigma_i,$$

if $\sigma_i$ stands for the $1\sigma$ $\Delta T/T$ sensitivity per field of view. The long dashes in Figure 2.5 correspond to detector noise at the level of the COBRAS/SAMBA specifications (see the Mission Summary).

### 2.3.3    Angular-Frequency Dependence of the Fluctuations

An extensive series of angular power spectra at many frequencies (such as those in Figure 2.5), or of amplitudes of fluctuations at different angular scales as a function of frequency (e.g. Figure 2.4), can provide a detailed picture of the behavior of the various components. However, it proves convenient to consider the fluctuation amplitudes as simultaneous functions of frequency and angular scale ($\ell$) to build a more synthetic view of the fluctuation "landscape".

The contours in Figure 2.6.a show the location in the $\nu - \ell$ plane where the fluctuations, as estimated from $\ell(\ell + 1)C(\ell)/2\pi$, reach the large scale COBE level ( $[\ell(\ell + 1)C(\ell)/2\pi]^{1/2} \simeq 28\mu K$). These contours map the three dimensional topography of the fluctuations of individual components in the $\nu - \ell$ plane. Tick marks show the "downhill" directions. The synchrotron component (when expressed in equivalent temperature fluctuations) defines a valley which opens towards large $\ell$ (since $\ell^2 C(\ell)$ decreases with $\ell$ as $1/\ell$). The free-free component defines a shallower and gentler valley (see also Fig. 2.4.b), while the dust emission creates a high frequency cliff. The large $\ell$ end of the valley is barred by the radio and infrared sources, together with the very steep (exponential) wall of the COBRAS/SAMBA noise[5].

---

[5]The discontinuity seen between 125 and 140 GHz is due to the change of technology between the low and the high

The solid black line (no ticks) shows the path followed by a stream lying at the bottom of the valley, i.e. it traces the lowest level of total fluctuations (except for detector noise). Its location confirms that $\nu \simeq 100\,\mathrm{GHz}$ is the best frequency for low-$\ell$ measurements. At $\ell \gtrsim 200$, the optimal frequency moves to higher values and is determined by the minimum of the fluctuations from unresolved sources; its exact value depends on the uncertain modeling of the infrared galaxies background for which, conservatively, no separation of resolved sources has been assumed (any removal of resolved source would tend to move to higher frequencies the locus of minimum foregrounds).
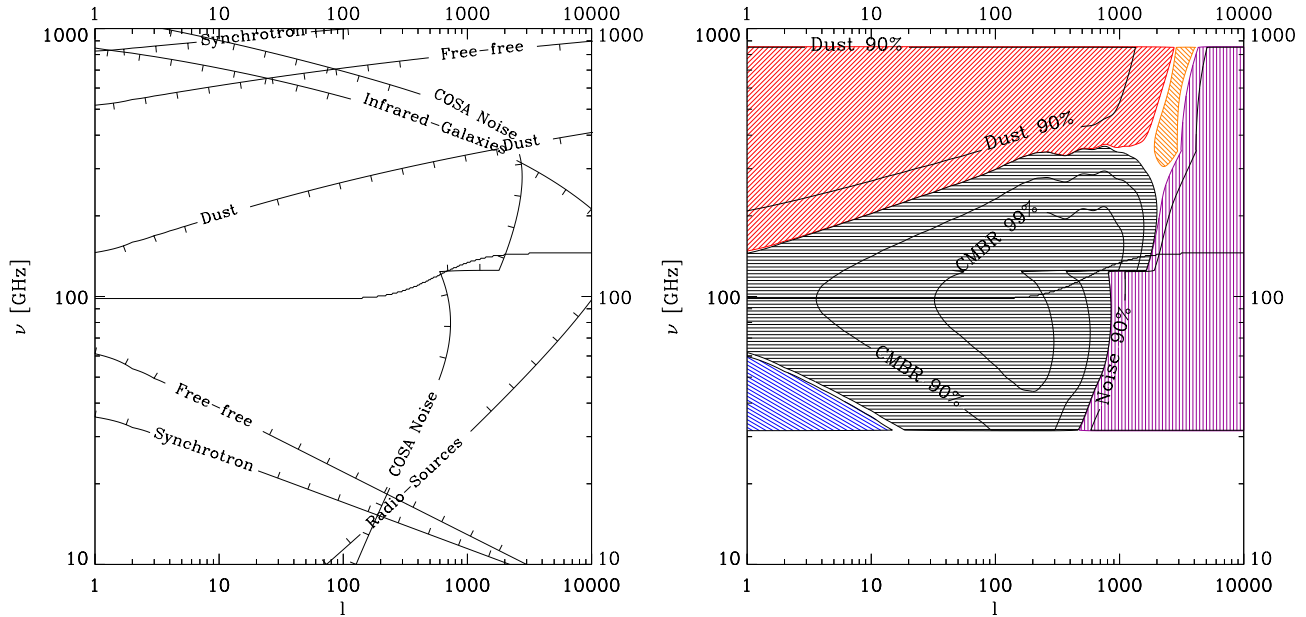


Figure 2.6: Contour levels of the different components in the angular scale–frequency plane. (a) On the left, the levels indicate where the power spectra of the various components reach $\sim (28\,\mu\mathrm{K})^2$ - the level of the COBE detection; tick marks show the downhill direction. Thus the central area is the region where the CMB signal will dominate over all other components. The central line (no ticks) marks the locus of weakest overall contamination by foregrounds. (b) On the right, each hatched area corresponds to the region where a given component accounts for 50% of the total variance, including detector noise (see text). The triangular area in the lower right corner corresponds to free-free emission, and the "tongue" at the upper left to point sources. Inner contours show where a component accounts for 90% of the signal – for the CMB only, the 99% contour is also shown. This figure has been restricted to the frequency range effectively covered by COBRAS/SAMBA .

In order to identify more clearly the dominant processes, Figure 2.6.b shows the regions where the contribution from a given process accounts for half of the variance of the measurements (the total including the noise); the inner contours show where that process accounts for 90% of the total (the 99% level is also marked for the CMB). This figure thus shows the areas in the $\nu$-$\ell$ plane where a given component will be sampled directly by the measurements. Note that the figure has been restricted to the frequency range covered by COBRAS/SAMBA ($\nu \simeq 30 - 1000$ GHz). Clearly, the COBRAS/SAMBA experiment will have no problem reaching 10% accuracy on the CMB anisotropies (i.e. $\Delta C(\ell)/C(\ell) < 0.1$) over all modes between a few and a thousand in the cleanest 50% of the sky. 1% accuracy levels can only be obtained in a much smaller angular range, if no foreground subtraction is performed. However, all the spectral and angular information can be used to enable the extraction of the fluctuations of the CMB component to a much higher accuracy (of order 1% in $\Delta C(\ell)/C(\ell)$) over all scales $l \lesssim 1100$. This we shall demonstrate in the following sections.

Finally, Figure 2.6.b shows clearly that the large frequency coverage of the experiment will allow

an accurate determination of the large scale behavior of the free-free emission and give very detailed information on the dust emission. Infrared galaxies will be detectable only at the highest frequencies in typical regions, but detailed studies should still be possible in the cleanest regions of the sky.

### 2.3.4   Simulations of Observed Maps

In order to determine what level of accuracy can be reached in practice when separating the various components, we now construct actual simulations of patches of the sky as observed by COBRAS/-SAMBA (Bouchet *et al.* 1995a, 1995c, 1996). We include the three galactic components, the primary fluctuations, and the Sunyaev-Zeldovich effect from clusters. The only astrophysical source of fluctuations missing from the simulation is that arising from the background of unresolved sources, which is very faint where the CMB contribution is strongest (see Figure 2.5). We do however include galaxy clusters, to allow an assessment of how well faint extended clusters can be recovered through their Sunyaev-Zeldovich effect. This type of recovery cannot be evaluated analytically, since the corresponding fluctuation field is highly non-Gaussian, and a description in terms of power spectrum would be misleading.

We have chosen to construct $12.5° \times 12.5°$ fields with $1.5' \times 1.5'$ pixels, and have created spatial templates for all the components. For the primary $\Delta T/T$ fluctuations, the realizations generated correspond to a COBE-normalized CDM model. Realizations of the thermal and kinetic effects of clusters (stored respectively as maps of the $y$ parameter and of $\Delta T/T$) were generated using the Press-Schecter formalism, as described in Section 2.2.3. To simulate galactic emissions, we have used the small-scale galactic model outlined in Section 2.2.

The measurement process of the COBRAS/SAMBA instruments was simulated in the following way. We have assumed constant transmission T across each spectral channel (with T=1, $\Delta \nu/\nu = 0.15$ for the LFI, and T=0.3, $\Delta \nu/\nu = 0.37$ for the HFI, see Mission Summary), and integrated across each waveband the different spectral components. The angular response of each channel was assumed to be Gaussian (of the corresponding FWHM width, see Mission Summary), and the sky maps were convolved with these beams. Finally, we have added isotropic noise maps, assuming a spatial sampling at 1/2.4 of the beam FWHM. That is we assumed that the destriping procedure (cf. Section 2.5.1) was efficient enough to be negligible.

Figure 2.7 shows an example of (simulated) "observed" maps in a region with median foregrounds; what we mean here by median is that for a spatial template we have picked IRAS map No. 151 in our series of 300 ordered by increasing variance. The power spectra of the various components included can be seen in Figure 2.8.a. Their amplitude is similar to those of the models in Figure 2.5 at low $\ell$; the difference at high-$\ell$ arises from the fact that the spectra in Fig. 2.7 correspond to the signal detected (i.e. after convolution with COBRAS/SAMBA beams) while those of Fig. 2.5 are "on the sky". The corresponding *rms* contributions in $\Delta T/T$ units of the various components are shown in Figure 2.8.

Having created simulated observations, we now turn to the problem of separating the "observed" data into component maps.

## 2.4   Separation of Components

### 2.4.1   Linear Inversion

As was shown earlier, it is possible to reach 10% accuracy (in $\Delta C(\ell)/C(\ell)$) on the CMB anisotropies over $\sim 50\%$ of the sky, by simply monitoring the lowest and highest frequency channels to flag and remove the regions with high foregrounds, and then using the least polluted channel to measure directly the CMB fluctuations. However, with a larger number of spectral channels, more information
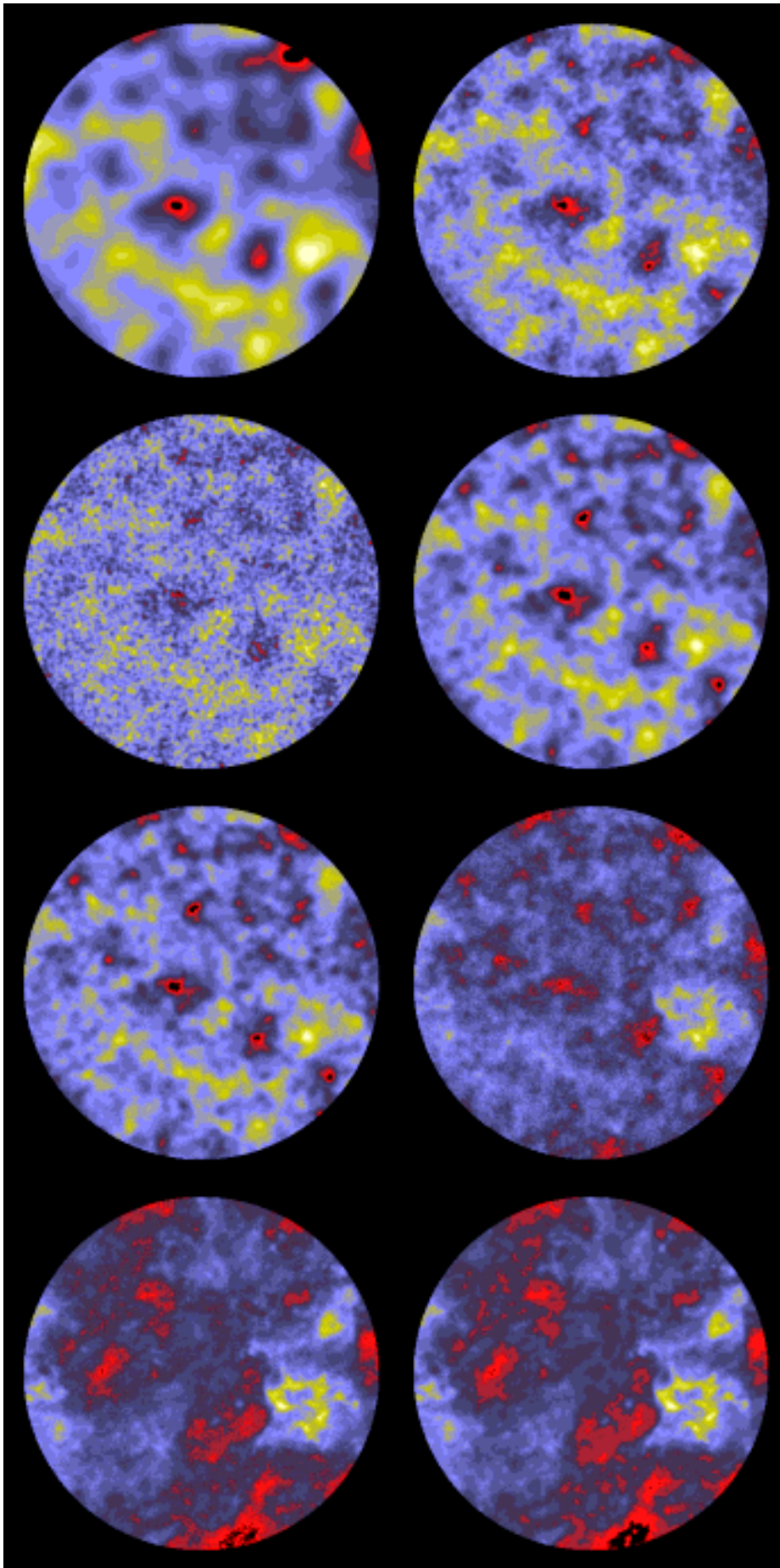
Figure 2.7: Simulated maps of 9 degree diameter, as observed by COBRAS/SAMBA . From left to right and from top to bottom are displayed the first three channels of the LFI instrument followed by the 5 channels of the HFI instrument (see Mission Summary). The *rms* level of the foregrounds is displayed in Figure 2.8 and corresponds approximately to the median levels shown in Figure 2.4.
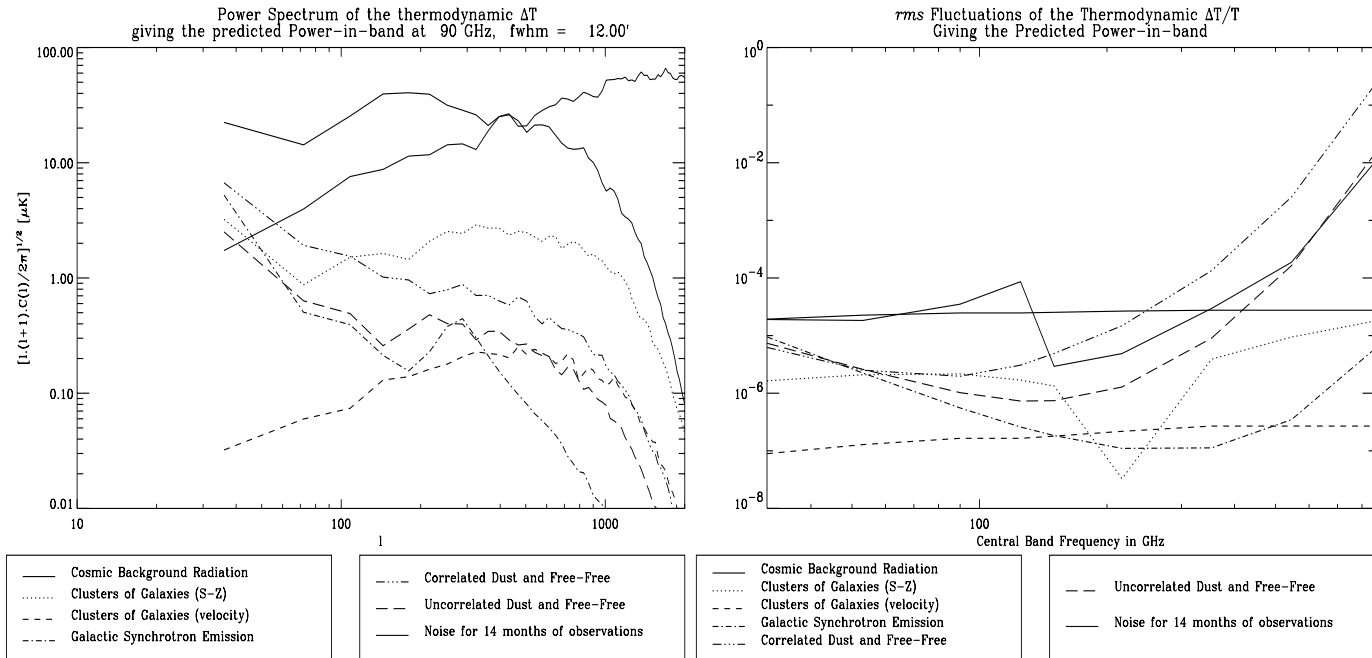
Figure 2.8: Characteristics of the "observed" maps of Figure 2.7: (left) power spectra at 90 GHz (note that of the two solid lines, the one that drops towards high $\ell$ is the spectrum of the CMB fluctuations); (right) *rms* contribution of the various components as compared to the nominal noise level of COBRAS/SAMBA (the horizontal solid line is the assumed CMB level). Note the discontinuity in detector noise at $\sim$100 GHz, due to the transition in detector technology.

is available that can be used to achieve higher accuracy. We start by describing a simple linear approach to this "inversion problem".

We make the hypothesis that the flux $f(\mathbf{r}, \nu)$ measured in the direction $\mathbf{r}$ and at a frequency $\nu$ is a superposition of $n_p$ processes (physical components) whose contributions can be factorized[6] as a spatial template $x_j(\mathbf{r})$ times a spectral coefficient $s_j(\nu)$

$$f(\mathbf{r}, \nu) = \sum_{j=1}^{n_p} s_j(\nu) x_j(\mathbf{r}). \qquad (2.3)$$

Note that this assumption does not restrict the analysis to components with a spatially constant spectral behavior. Indeed, these variations are expected to be small, and can thus be linearized too[7].

If there are $n_c$ channels, each with a spectral transmission $t_i(\nu)$, the observation in each direction can be arranged as an $n_c$ component vector $\mathbf{y}(\mathbf{r})$ given by

$$\mathbf{y}(\mathbf{r}) = P\mathbf{x}(\mathbf{r}) + \mathbf{B}(\mathbf{r}), \qquad (2.4)$$

where $\mathbf{x}$ is an $n_p$ elements vector, $\mathbf{B}$ is a vector whose $n_c$ elements are the noise contributions in each channel, and the $n_c \times n_p$ design matrix P describes the "projection" of each component on each channel:

$$P_{ij} = \int_0^{\infty} t_i(\nu) s_j(\nu) d\nu. \qquad (2.5)$$

---

[6] This is unlikely to be realistic for the unresolved contribution from galaxies, since at different frequencies different redshift ranges dominate, and thus different sources. But as shown above, this contribution should be rather weak, and we defer a discussion of the contribution of point sources to Section 2.4.2.

[7] For instance, in the case of a varying spectral index whose contribution can be modeled as $\nu^{\alpha(\mathbf{r})} x_j(\mathbf{r})$, we would decompose it as $\nu^{\overline{\alpha}}[1 + (\alpha(\mathbf{r}) - \overline{\alpha}) \ln \nu] x_j(\mathbf{r})$. We would thus have two spatial templates to recover, $x_j(\mathbf{r})$ and $(\alpha(\mathbf{r}) - \overline{\alpha}) x_j(\mathbf{r})$ with different spectral behaviors, $\propto \nu^{\overline{\alpha}}$ and $\propto \nu^{\overline{\alpha}} \ln \nu$ respectively. But given the low expected level of the high latitude synchrotron emission, this is unlikely to be necessary.

If all the observations are at the same angular resolution, equation (2.4) applies also to spatially smoothed quantities.

Since COBRAS/SAMBA operates at or near the diffraction limit in each channel, it becomes more convenient to work in Fourier space (or with spherical harmonics for larger maps) where convolutions reduce to products. Then[8]

$$\mathbf{y}(\ell) = A(\ell)\mathbf{x}(\ell) + \mathbf{B}(\ell), \tag{2.6}$$

with $A_{ij}(\ell) = P_{ij} \, w_i(\ell)$, if $w_i$ is the angular response of channel $i$. Every pixel in Fourier space is then independent and it is natural to define a Figure of merit

$$\chi^2(\ell) = |\mathbf{y} - A\mathbf{x}|^2 \tag{2.7}$$

for each mode $\ell$. The matrix inversion algorithm by singular value decomposition is precisely designed to solve the problem of finding the vector $x$ that minimizes this Figure of merit.

We have found that this method works well for values of $\ell \lesssim 300$. For instance, when applied to the "observations" of Figure 2.7 (not a particularly "clean" region), it recovers each *individual* mode of the CMB power spectrum ($\ell \lesssim 300$) with an accuracy close to the 1% level. However, the errors quickly increase for higher $l$. Better results can be obtained, for a given mode, by including only those channels for which the beam weight $w(\ell)$ is not too small. Nonetheless, it seems pointless to try to fine-tune this method since, as we show in the next section, there are other methods that automatically make the best compromise in a statistical sense.

## 2.4.2    Improving the Separation

The inversion scheme described above is really only a first guess which can be considerably refined. One can for instance apply "Wiener" filtering techniques (Tegmark & Efstathiou 1995, Bouchet *et al.* 1995c). Any *linear* recovery procedure may be written as an $n_p \times n_c$ matrix $W$ which applied to the $y(\ell)$ vector yields the $x(\ell)$ vector, i.e.

$$W(\ell)\mathbf{y}(\ell) = \mathbf{x}(\ell) \tag{2.8}$$

The simple inversion of Section 2.4.1 was designed to best reproduce the observed data set by minimizing the residuals between the observations and the model (eq. [2.7]). Another possibility is to require a *statistically minimal* error in the recovery, when the method is applied to an ensemble of data sets with identical statistical properties. One then obtains the "Wiener" matrix $W$, by demanding that the difference between the initial and recovered *processes* be of minimal variance

$$\varepsilon_i^2(\ell) \equiv < |W\mathbf{y} - \mathbf{x}|_i^2 > = < |W(A\mathbf{x} + \mathbf{B}) - \mathbf{x}|_i^2 > = < |W_{ij}(A_{jl} - \delta_{il})x_l + W_{ij}B_j|^2 > . \tag{2.9}$$

The solution of this equation leads to an "optimal linear recovery", with the input data weighted according to a generalization of the usual signal-to-noise ratios in Fourier space. In addition to the spectral weights, these ratios involve the expected typical amplitude of a given mode $\ell$, estimated through the power spectra $C_j(\ell)$ of the processes and of the noise.

One can think of Wiener filtering as a "polishing" stage of a first inversion yielding an estimate of the power spectra. Note though that the "typical amplitude" $\sqrt{C(\ell)}$ of a component at scale $\ell$ might be a rather poor indicator for a non-Gaussian process like the Sunyaev-Zeldovich effect from clusters. Other methods for that particular case might then be more accurate. An obvious approach would be to first use optimal filters for localized sources, among which wavelet transforms may be good candidates. This step will in any case be necessary to remove all point sources due for instance to resolved galaxies or radio-sources.

When we apply the Wiener filtering method to our simulated maps, we indeed find considerable improvement over the results of the simple linear inversion. Figures 2.9 and 2.10 show a comparison

---

[8]Here, as in the simulation part, we assume an isotropic noise.
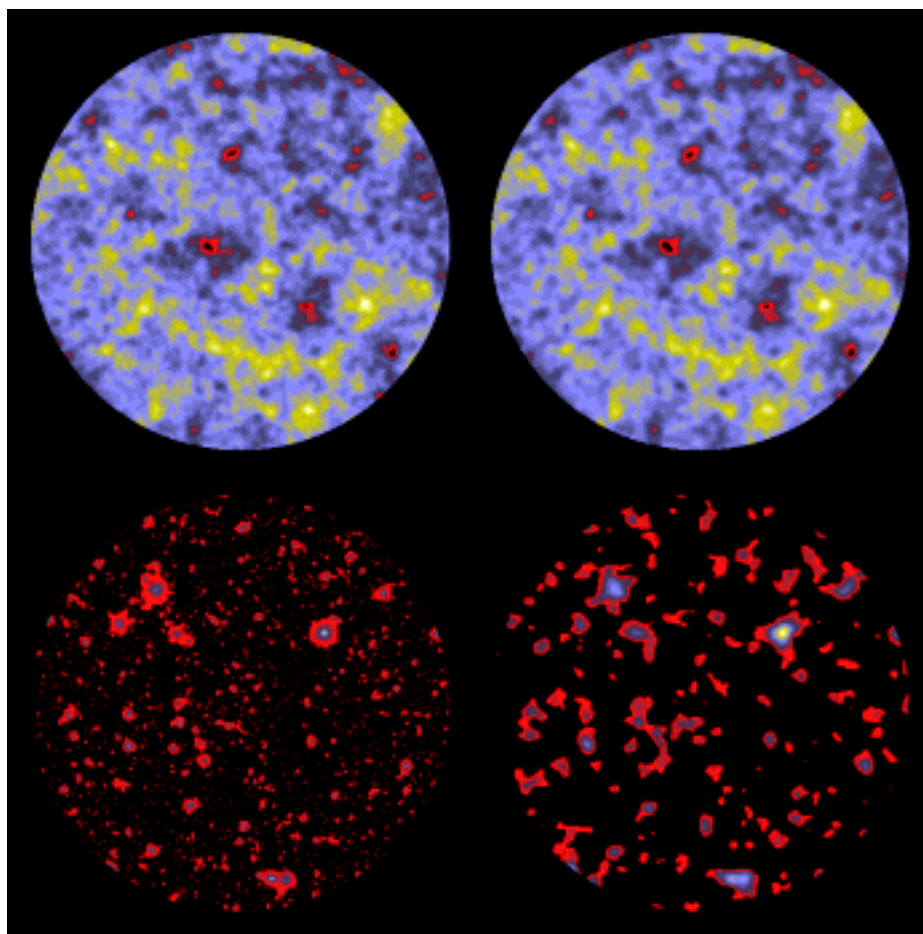
Figure 2.9: An example of component separation of the "observations" of Figure 2.7. The left column shows the maps used in the simulation while the right column shows the recovered maps of the $\Delta T/T$ primary anisotropies (top row) and of the $y$ parameter of the Sunyaev-Zeldovich effect (bottom row).
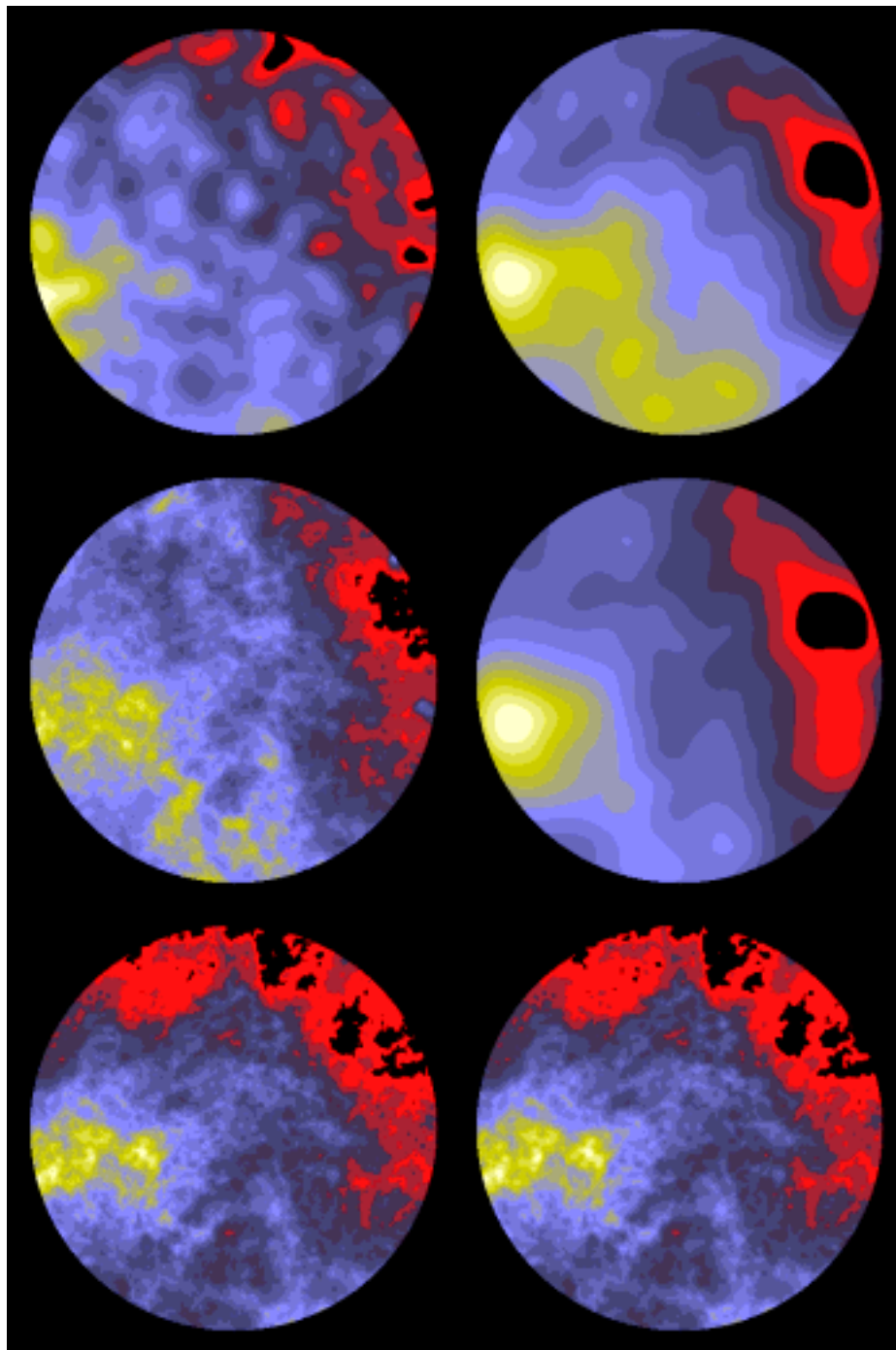
Figure 2.10: An example of component separation of the "observations" of Figure 2.7. The left column shows the input maps of the galactic components used in the simulation while the right column shows the recovered maps for the synchrotron, the free-free and the dust emissions taken at $\lambda = 1$ mm for illustration (from top to bottom).

between the input templates of the simulated maps of Figure 2.7, and those recovered after Wiener analysis. All processes are adequately recovered, even in this region with foregrounds fluctuations amplitudes exceeding the expected one in (the best) half of the sky.

In the following section we quantify more rigorously the "quality" of the recovery process.

### 2.4.3    Accuracy of the Recovery of the CMB Anisotropies

By comparing the input and recovered maps, we have computed the mean relative error $\Delta C(\ell)/C(\ell)$, and found an average value of 1.8% in the range $30 < \ell < 1000$. This was done assuming negligible errors in the assumed spectral behavior of the foregrounds. In addition, we have checked that these Figures would not be significantly degraded by different input assumptions. Table 2.2 shows that this is indeed the case. In the worst case, when we assumed a 10% positive error on the dust emissivity index, the accuracy on $C(\ell)$ remained below 2.2 %, up by less than 0.4% from the best case. However, such a large error on the dust emissivity is quite unlikely, given the high frequency information which will be available by combining together IRAS and COBRAS/SAMBA data. In addition, relatively large errors on the synchrotron and free-free spectral index have very low impact on the final CMB accuracy.

| $\alpha_{Sync}$ | $\alpha_{Free}$ | $\alpha_{Dust}$ | $\Delta C(\ell)/C(\ell)$ |
|:---:|:---:|:---:|:---:|
| 0.9 | 0.15 | 2.0 | 1.80 % |
| 0.7 | 0.15 | 2.0 | 1.90 % |
| 1.1 | 0.15 | 2.0 | 1.80 % |
| 0.9 | 0.10 | 2.0 | 1.80 % |
| 0.9 | 0.20 | 2.0 | 1.82 % |
| 0.9 | 0.15 | 1.8 | 1.81 % |
| 0.9 | 0.15 | 2.2 | 2.14 % |

Table 2.2: The last column of this table shows the mean relative error on the recovered CMB spectra in the range $30 < \ell < 1000$ for different assumed spectral behaviors of the foregrounds. These numbers correspond to analysis of the simulated observations of Figure 2.7, i.e. for strong foregrounds. The value $\alpha_{Dust}$ of the third column corresponds to the dust emissivity index. The first line in the Table is the accuracy obtained without spectral errors; the other lines demonstrate that the CMB recovery is not very sensitive to reasonable spectral errors.

Because the simulated maps are very small in spatial extent compared to the area to be observed by COBRAS/SAMBA , we have analyzed the variation in accuracy as a function of sky coverage. We have done this numerically by generating many realizations (maps) of patches of the sky, and by comparing the input CMB maps to the extracted ones. Figure 2.11.a compares the average input CMB spectrum over 128 maps with the average recovered spectrum, and displays the corresponding error $\Delta C(l)/C(l)$ (on a different scale, at left). This error is the overall "inversion noise" which depends in a complicated fashion on a combination of the detector noise and of the beam width at all frequencies (the obtained $C(\ell)$ are "on the sky"), as well as the varying amplitudes of the foregrounds with scale and location (see below). In any case, if we assume that this noise spectrum remains flat toward low $\ell$, by summing over $\ell$ from $\ell = 1$ to $\ell \sim 1100$ this inversion noise, we find an *rms* of $\Delta T/T \sim 1.6 \ 10^{-6}$ on a scale $\theta \sim 10'$. This already exceeds the requirements set in Chapter 1.

The maps used to obtain Figure 2.11 correspond to the first 128 in our series of IRAS maps (see Section 1.2.1). We found that the error on the $C(l)$ of each individual map is nearly constant, i.e. it does not depend strongly on the level of the foregrounds. Figure 2.11.b shows how the mean error $\Delta C(l)/C(l)$ within different $l$ ranges *decreases* as the average is taken over an increasing number of maps. Note that the combined area of these 128 maps amounts to only $\sim 20\%$ of the sky (albeit the

Comparaison of input and recovered CMB spectra     Comparaison of input and recovered CMB spectra
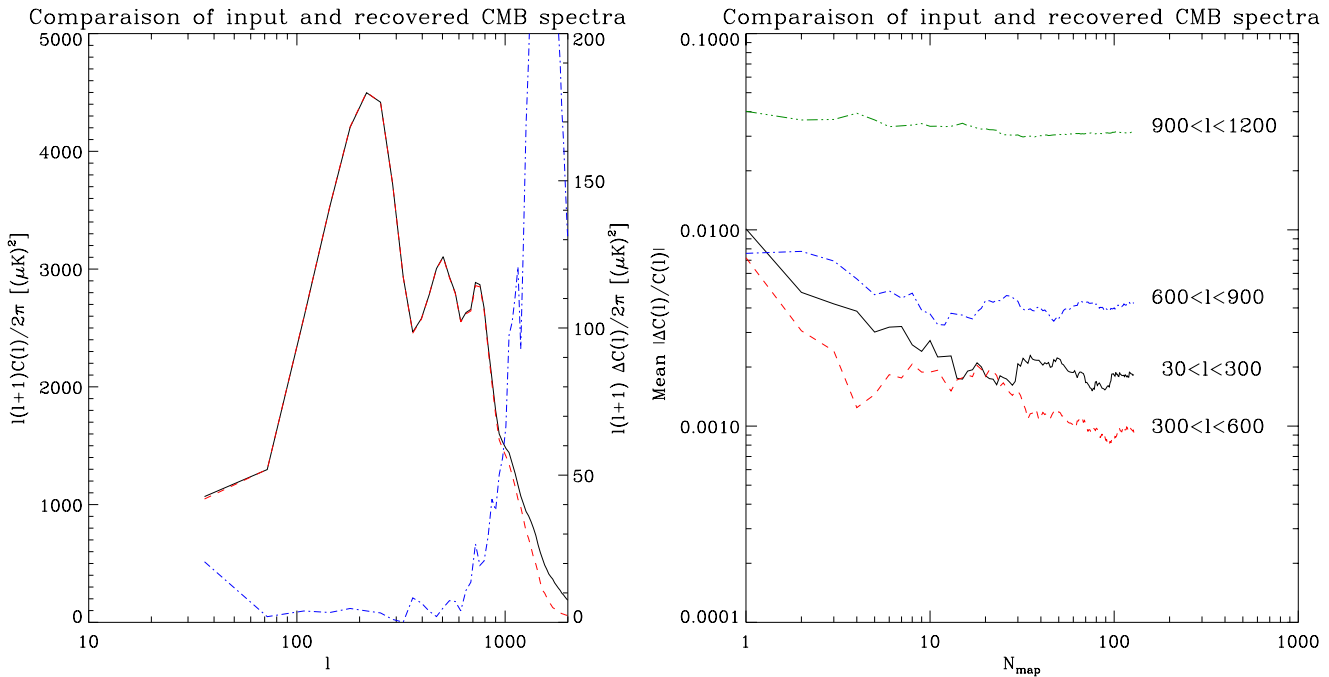


Figure 2.11: Errors in the recovery of the mean CMB spectrum (an average over 128 maps). (a) In the left panel, we show the input (solid) and recovered (dashes) average CMB spectrum (scale on the left), and the error $\ell(\ell+1)\Delta C(\ell)/2\pi$ (scale on the right). The accuracy on individual modes is $\lesssim 5\mu K$ up to $l \sim 800$, and is still $\lesssim 8\mu K$ at $\ell = 1000$. (b) In the right panel, we show the mean relative error on the power spectrum recovery, binned within ranges of $\ell$, when an increasing number of maps ($N_{map}$) is taken into account.

cleanest 20% of the IRAS sky). Thus analyzing the best half of the sky should lead to an even more accurate determination of the high $\ell$ part of the CMB power spectrum.

The analysis outlined above (e.g. Figure 2.11) demonstrates that it will be possible for CO-BRAS/SAMBA to achieve accuracies on the $C(\ell)$ better than 1 % for $\ell \lesssim 1000$ in the recovery of the spectrum of CMB anisotropies.

In addition, we have used the Kolmogorov–Smirnoff test to check to what extent the input and derived *distributions* of fluctuation amplitudes are consistent with each other. This test involves the overall shape of the distribution; i.e. not only its variance, but also its skewness, kurtosis, and higher moments. We have applied the test to 64 pairs of input and recovered distributions, and find on average a probability greater than 0.99 that the two distributions are identical (with a pair to pair dispersion smaller than 0.02). In other words, irrespective of the specific shape of the CMB fluctuations (e.g. Gaussian or not), the recovered distribution will mimic the original one accurately. This is a prerequisite to an investigation of the underlying physics.

In the following section we derive an analytical measure of the quality of the inversion, which not only confirms Figure 2.11, but also provides us with a relative measure of the performance of any particular experiment.

## 2.4.4   Overall Quality of the Inversion

Wiener filtering is designed to statistically minimize the residuals between the real process and the recovered one, given the information available (eq. 2.9). Once obtained, the Wiener matrix can be put back into eq. (2.9) to estimate the residual variance to be expected, yielding

$$\varepsilon_i^2(\ell) = C_i(\ell)\left[1 - Q_i(\ell)\right]. \tag{2.10}$$

A value of $Q_i$ equal to unity indicates that enough information has been collected by the experiment, and that the initial and recovered process number $i$ have the same power spectrum. Contrariwise, if $Q_i$ is close to zero, the information collected is not sufficient, and the Wiener filter sets the mode of this process to nearly zero. In other words, $1 - Q_i(l)$ yields the expected $\Delta C(l)/C(l)$ of the process $i$, and $Q_i(l)$ may be used as a "quality factor" which evaluates the ability of a given experiment to recover process $i$ at scale $l$. This indicator (Bouchet *et al.* 1996) generalizes the real space "Foreground Degradation Factor" introduced by Dodelson (1995).
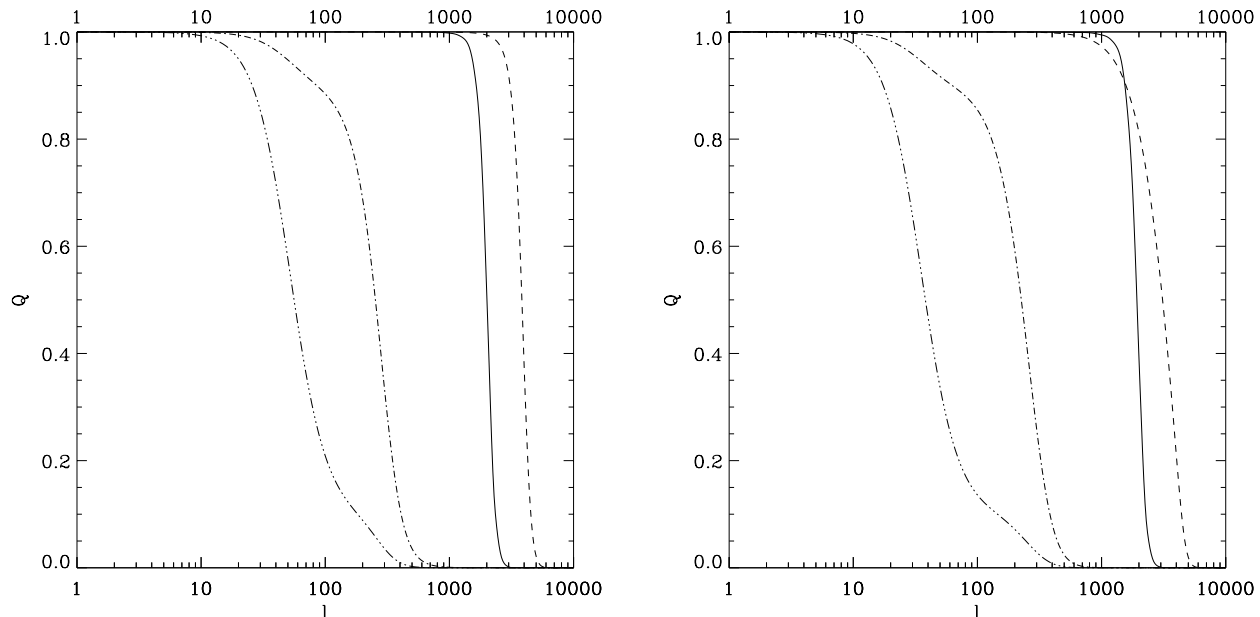


Figure 2.12: Quality factor (see text) of the COBRAS/SAMBA experiment, for the model described in Section 2.2, i.e. for foreground levels typical of the best half of the sky (this $Q$ is thus overly optimistic at $\ell \lesssim 5$). The solid line corresponds to the CMB, while dashes, dot-dashes, triple dots-dashes refer respectively to the dust, the free-free and the synchrotron. (Left) In this case, the fluctuations from unresolved point sources were neglected. (Right) Case when the unresolved fluctuations are treated as uncorrelated noise: the degradation is weak, because the unresolved background has a weak amplitude at scales $\ll 1000$.

We have carefully checked that the numerical inversions described above, even in the presence of a non-Gaussian component such as galaxy clusters, yield results in agreement with *a priori* analytical calculations of the quality factor, for all components, and at all angular scales probed by the simulations ($l > 30$). Consequently, the quality factor for COBRAS/SAMBA shown in Figure 2.12.a is a good description of the simulation results and can be used directly to gauge the effect of foreground sources, as well as that of changing specific experimental parameters. This we do in the rest of this Section.

### Effect of a Background of Unresolved Sources

We first use the quality factor formalism to assess the degrading effect of unresolved sources. Since the fluctuations at different frequencies may not be well correlated, we have performed the calculation under two extreme assumptions, cf. that fluctuations are either totally correlated between different frequencies, or totally uncorrelated. In the first case, the effect amounts to adding two more processes (for the radio-sources and the infrared galaxies), while in the second case, unresolved sources are treated as noise and added to the detector noise. Even in the most pessimistic case shown in Figure 2.12.b, the CMB recovery is essentially unaffected. On the other hand, the high precision determination of the galactic foregrounds, in particular that of the dust, is now restricted to lower $\ell$ than previously. Table 2.3 gives the numerical values of the angular scale $\ell$ when the quality of the

recovery drops below a given threshold. One sees that even in the worst case, the CMB anisotropies are recovered with an accuracy (1-Q) better than 1% up to values of $\ell$ exceeding 1100.

| Q | $\ell_{CMB}$ | $\ell_{Dust}$ | $\ell_{Free}$ | $\ell_{Sync}$ |
|------|------------------|------------------|----------------|---------------|
| 0.99 | 1288/1230/1148 | 2238/1023/724 | 25/21/17 | 12/11/8 |
| 0.95 | 1548/1513/1445 | 2818/1584/1258 | 49/41/34 | 20/18/14 |
| 0.90 | 1659/1621/1584 | 3090/1905/1584 | 86/66/64 | 26/24/18 |
| 0.66 | 1905/1862/1862 | 3630/2691/2630 | 208/173/181 | 45/40/30 |

Table 2.3: Angular scale $\ell$ at which the quality of the recovery drops below Q. The first number gives the value when the contribution of sources is not taken into account, the second number is when they are considered as just another foreground with a well defined spectral behavior, while the third corresponds to this contribution being treated as pure noise (i.e. no correlations between frequencies). The latter two values should bracket practical expectations for COBRAS/SAMBA .

**The effect of the available frequency range**

As has been stressed throughout this report, the frequency range over which a given CMB experiment carries out measurements has an important effect on the accuracy achievable on the final scientific products. Qualitatively, it is straightforward to see why the spectral placement of the COBRAS/- SAMBA channels is nearly optimal. One clearly wants measurements at frequencies close to the minimum of the foregrounds at low $l$, i.e. near 100 GHz (thus justifying the 90 and 125 GHz channels), and 3 others at the minimum, maximum and at the null of the Sunyaev-Zeldovich effect (143, 353, 217 GHz), the latter being also close to the minimum of the foregrounds at high $l$. This range in frequency is then complemented by two additional channels on either side of the frequency range, e.g. at 31.5 and 53 GHz to monitor the free-free and synchrotron emission, and at 545 and 857 GHz to monitor the dust emission and the background of unresolved infrared galaxies.

More quantitatively, the quality factor formalism can be used to compare different experimental concepts. In particular, table 2.4 illustrates the effect of increasing the top end of the experimental frequency range from that achievable with HEMT-based receivers only (corresponding to the LFI instrument in COBRAS/SAMBA , see Ch. 3), to a much larger value (achievable only with bolometer technology, as in COBRAS/SAMBA 's HFI instrument). While low frequency measurements are adequate to reach an accuracy level on the CMB of 10% at angular scales up to $\ell \simeq 700$, or of 1% at scales up to $\ell \simeq 330$, the combination of the LFI and HFI brings about accuracy levels of 1% up to scales of $\ell \simeq 1150$! In addition, the recovery of the dust is greatly enhanced, while the improvement on the other galactic foregrounds is only modest.

| Q | $\ell_{CMB}$ | $\ell_{Dust}$ | $\ell_{Free}$ | $\ell_{Sync}$ |
|------|-----------|---------|---------|-------|
| 0.99 | 338/1148 | 7/724 | 7/17 | 4/8 |
| 0.95 | 588/1445 | 14/1258 | 13/34 | 6/14 |
| 0.90 | 691/1584 | 20/1584 | 22/64 | 8/18 |
| 0.66 | 870/1862 | 39/2630 | 144/181 | 14/30 |

Table 2.4: Increase in quality achieved by combining COBRAS/SAMBA 's LFI and HFI instruments. The table lists the angular scales $\ell$ at which the quality of the recovery drops below Q. The first number gives the value if only the LFI is considered, while the second number shows the improvement obtained with a measurement using both LFI and HFI. In both cases, the contribution of point sources was included as an additional source of noise (worst case scenario).

**Required performance level at high frequencies**

Finally, we investigate the performance degradation in the event of detector noise excess at high frequencies, which has been shown above to be crucial for the accurate determination the high–$\ell$ part of the CMB spectrum. In the case of COBRAS/SAMBA , high frequencies are covered by the HFI instrument. As table 2.5 shows, a uniform increase of the noise level of the HFI by factor of two would still allow us to meet the scientific objectives, and demonstrates the existence of a reasonable margin with respect to the nominal performance of COBRAS/SAMBA . However, further increases in the noise level would lead to a very significant negative impact on the scientific return. This fact has a very clear consequence in terms of the physical temperature at which the bolometric detectors in the HFI have to be operated (see Section 3.5).

| Q | Nominal $\sigma$ | $2\,\sigma$ | $4\,\sigma$ | $8\,\sigma$ | $16\,\sigma$ |
|------|------|------|------|------|------|
| 0.99 | 1148 | 977 | 831 | 588 | 416 |
| 0.95 | 1445 | 1288 | 1071 | 870 | 741 |
| 0.90 | 1584 | 1412 | 1202 | 977 | 831 |
| 0.66 | 1862 | 1659 | 1479 | 1230 | 1047 |

Table 2.5: Angular scale $\ell$ at which the quality of the recovery of the CMB drops below Q. The first column gives the value when the HFI bolometers are assumed to be nominal, and adjacent columns show the impact of degradation by successive factors of two. While an increase of the HFI noise by a factor of 2 would still bring about the recovery of the CMB power spectrum with $Q = 0.99$ up to scales $\ell \simeq 1000$, any further decrease would begin to compromise significantly the scientific objectives set out in Chapter 1.

We now turn to the simulation results concerning the accuracy of the extraction of galaxy clusters.

## 2.4.5  Sunyaev-Zeldovich Effect of Clusters

As mentioned previously, because the SZ effect from clusters has a non-gaussian distribution, measuring the accuracy of the recovery in terms of the power spectrum is not adequate. For this reason, we present below a separate analysis (Aghanim *et al.* 1996).
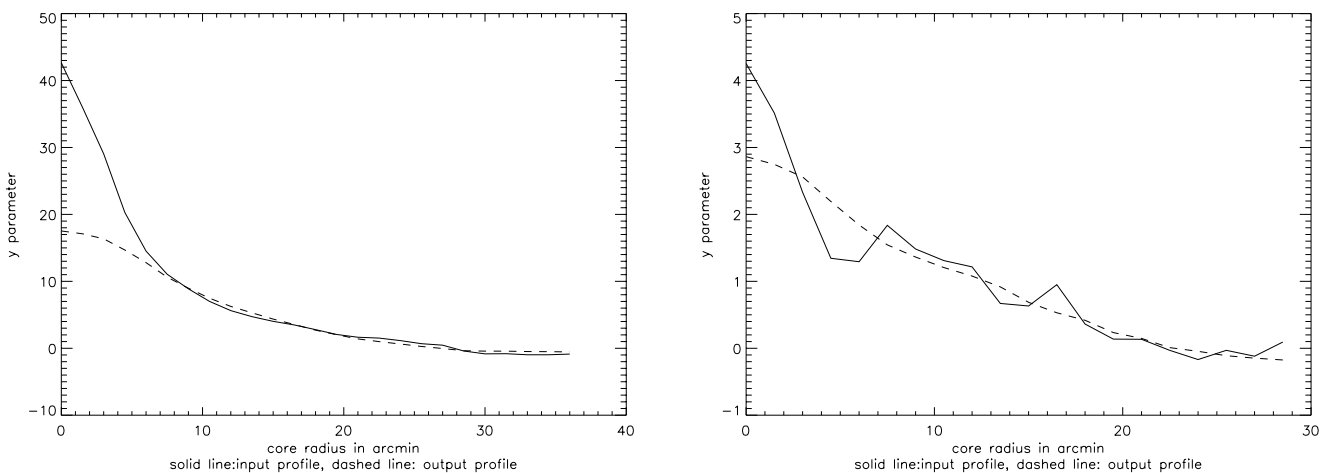


Figure 2.13: Initial (solid) and recovered (dashes) profiles for a strong cluster with an integrated $Y \simeq 3.5\,10^{-3}$ (left), and a weak cluster with $Y \simeq 2.7\,10^{-4}$ (right).

Starting from one recovered map of $y$ (e.g. Figure 2.9), we have searched for local maxima. For each peak found, we have built a radial $y$ profile, assuming circular symmetry, and computed the

integrated Y parameter (defined in Section 1.5.1). A comparison with the input to the simulation yields an estimate of the sensitivity and the quality of the recovered profiles. Figure 2.13 shows typical initial and recovered $y$ radial profiles for two cases. The first case corresponds to a cluster with a strong central $y$ in a small unresolved core. It illustrates well the capacity of COBRAS/SAMBA to resolve the wings of such clusters down to a sensitivity level of $y \approx 0.5 \times 10^{-6}$. In this case, the cluster is detected out to a diameter of about one degree. The second case shows recovered profiles for a cluster near the sensitivity limit.
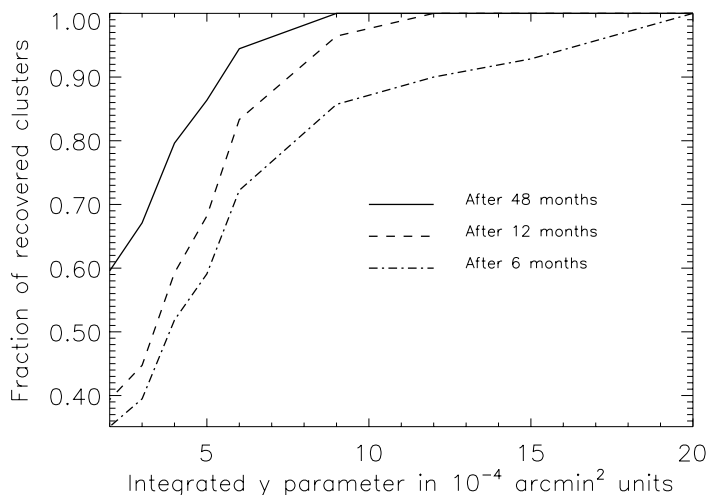


Figure 2.14: Fractional number of clusters recovered from a typical simulated map (solid line) for three sensitivity levels as a function of the integrated $Y$ parameter. The nominal COBRAS/SAMBA mission requires at least 14 months of observations.

Figure 2.14 shows the fraction of clusters detected in the recovered map as a function of Y. Fig. 2.13.b for a cluster with $Y \simeq 3 \times 10^{-4}$ exemplifies the type of accuracy to be expected close to the detection limit. Approximately 70% of the clusters with $Y > 5 \times 10^{-4}$ arcmin$^2$ are recovered after one year of observations, or 40% if the threshold is set at a very low Y~ $2 \times 10^{-4}$ arcmin$^2$. These percentages increase rather steeply as the detector noise level is decreased. However, the sensitivity for the nominal duration of the COBRAS/SAMBA mission is such that it will be possible to use the observed cluster density variation with limiting flux as a sensitive cosmological test.

## 2.5  Other Data Analysis Aspects

The previous sections have shown that the scientific goals of the mission can be met, provided one is able to produce calibrated maps with the nominal sensitivity per pixel, and well defined beams. However, a number of undesirable features are often present in the data collection process which result in systematic effects (e.g. map striping, etc.). In this section we show appropriate ways to deal with the most severe of these features, namely, the presence of $1/f$ noise, the consequences of poorly defined angular responsivity, absolute and relative calibration, and the existence of "glitches" in the data stream. Since these problems are specific to the experiment, we again refer the reader to the Mission Summary to review the main characteristics of COBRAS/SAMBA , and for more details to Chs. 3 and 4.

### 2.5.1 Removal of Striping due to 1/f Noise

As in any experiment, the COBRAS/SAMBA instruments will be subject to gain drifts and $1/f$ noise. In the simplest way, the effective signal measured by the instruments before digitization can be written as :

$$s(t) = G(t)(u(t) + 2.7K + B(t) - C) + n(t), \tag{2.11}$$

where $G(t)$ is the gain, $u(t)$ the useful astrophysical signal of a few mK (mainly due to the dipole and the galaxy), $B(t)$ the thermal background of a few K (mainly from the telescope and shield), $C$ a stable reference source (for the LFI only) which is adjusted so that $(2.7K + B(t) - C)$ is small, and $n(t)$ the noise.

Thermal stability requirements on the reflecting surfaces insure that the contribution due to the fluctuations of the thermal background $B(t)$ is smaller than the noise (see Section 3.7.1), so that equation 2.11 reduces to

$$s(t) = G(t)u(t) + n(t), \tag{2.12}$$

where now $n(t)$ contains the part of $G(t)(2.7K + B(t) - C)$ that is due to gain fluctuations. Since the nature of the mission is such that the telescope will scan successively over given strips of the sky, the low frequency noise and the instabilities in the gain will appear in the final maps in the form of "stripes".

Low-frequency noise removal can be achieved by taking advantage of the scan strategy. In the case of COBRAS/SAMBA , the sky scanning strategy proposed (see Section 4.4) consists of sweeping the sky in circles of diameter 140°, so that the same annular strip of the sky is scanned 120 times over two hours, before a new annulus (displaced by 5′ from the previous) is observed.

Drifts with periods longer than the scan period (1 minute) and shorter than two hours will be removed by requiring that the average signal over each rotation period remain constant over the two hour dwell time. As an illustration, Figure 2.15 shows 1 hour of simulated signal for the 150 GHz HFI channel before and after subtraction of low frequency drifts due to low frequency noise for periods between 1 minute and 2 hours. For this simulation, a critical frequency[9] of 0.1 Hz was assumed, which is an extremely conservative (high) value for COBRAS/SAMBA 's HFI.

In addition to the basic two hour dwell time, the observing strategy of COBRAS/SAMBA ensures that there also is redundancy at longer periods. Since each data circle (obtained from 120 superimposed scans) crosses 3360 other such circles in two spots for a 1 year mission (see Figure 2.16 for illustration), the next step, which is to remove drifts for periods longer than two hours, is achieved by requiring that the differences between signal over the same sky pixels but observed with a different spacecraft attitude are minimized.

The problem of the removal of long term drifts corresponds to the determination of $\sim 5000$ arbitrary constants for each detector (corresponding to one offset $A_i$ for each two hour period), for a 14 month mission. These constants are constrained by more than $8 \times 10^6$ independent equations. For all pairs of circles $i$, $j$ having at least some pixels in common, we can write

$$A_i - A_j = \delta S_{ij} - n_{ij}, \tag{2.13}$$

where $A_i$ and $A_j$ are the constants to be determined for circles $i$ and $j$ respectively, $\delta S_{ij}$ is the difference between the average of measurements made on common pixels, and $n_{ij}$ is a noise term corresponding to the (high frequency) noise in the measurement of $\delta S_{ij}$.

The rms value of the noise term $n_{ij}$ depends on the actual area on the sky that scan circles $i$ and $j$ have in common. For any two circles that cross each other, there are at least two common pixels, and thus the rms value of the noise term $n_{ij}$ is at most $\sqrt{2}$ times the mission rms noise per detector for any pair of circles (but can be as much as 10 times lower than this value for consecutive circles). Because of the number of equations involved (more than 1000 times more independent equations than

---

[9]the frequency at which the 1/f noise power spectral density is equal to the white noise power spectral density
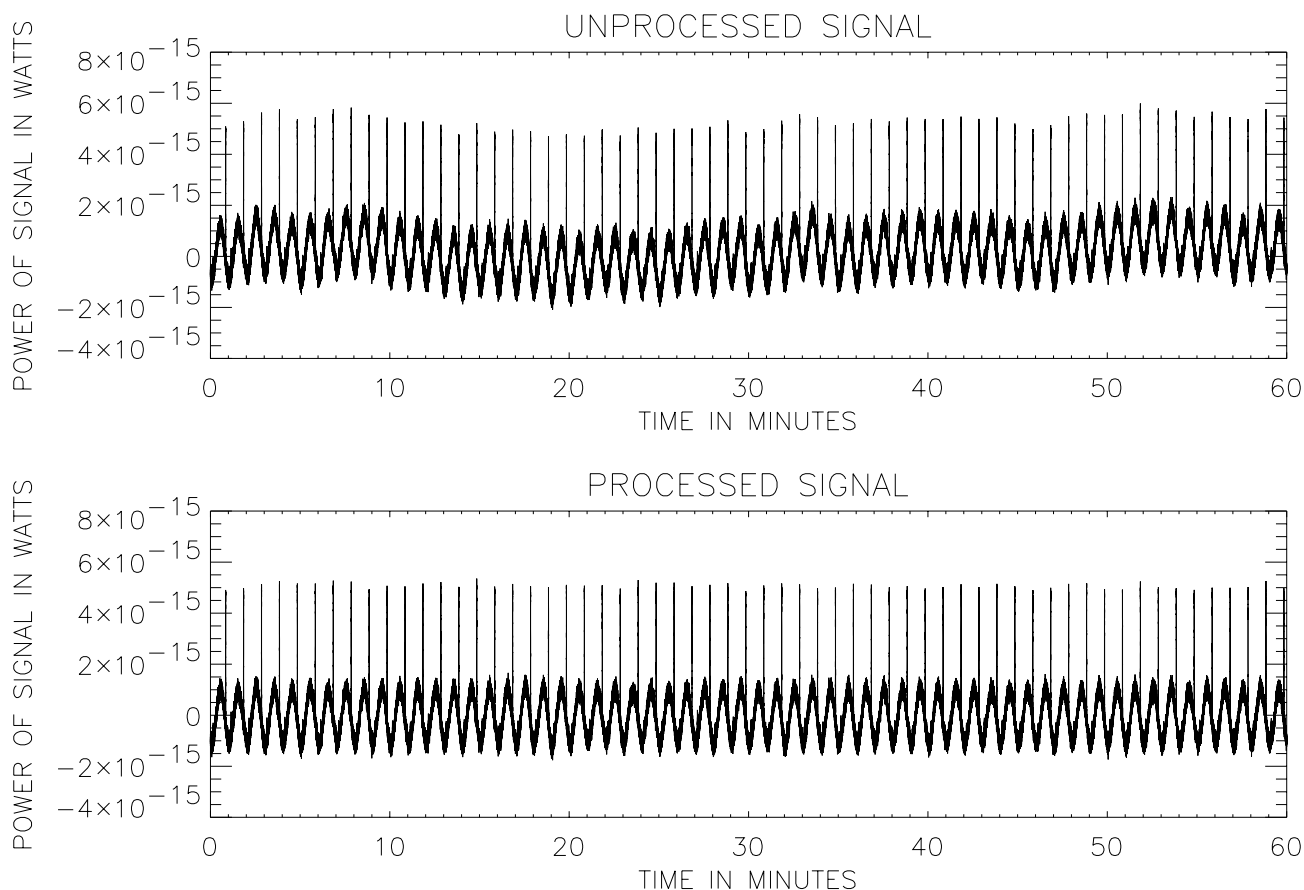
Figure 2.15: Comparison of a simulated unprocessed signal in the 150 GHz waveband, and of the same signal after processing (see text). In the processed signal, low frequency drifts with time periods greater than 1 minute have been removed. Besides low frequency noise, patterns due to the dipole and the galactic plane can clearly be seen: a smooth oscillation for the dipole, and a sharp peak for the galactic ridge, the ratio of which depends strongly on the channel. Here in the 150 GHz channel, both are much stronger than the high frequency part of the noise. Smaller scale fluctuations (such as those of the CMB) are lower than the noise, and cannot be seen at all before all the scans are superimposed.

the number of constants to be determined), the accuracy on the determination of the $A_i$ that can be obtained by a global least mean squares method is better than $\sim 3\%$ of the final sensitivity per detector.

## 2.5.2  Calibration and Control of Thermal Drifts

Proper reconstruction of the COBRAS/SAMBA maps requires accurate calibration, i.e., conversion of the signal strength from raw telemetry data into physical units. In principle, each detector $i$ is characterized by a calibration factor $G_i$ which is constant in time. In practice, variations of the physical temperature or intrinsic instrumental effects may produce drifts or time fluctuations in the value of $G_i$.

The stability of the gain depends on detector technology. For the HFI bolometers, gain drifts are very small ($\Delta G/G \sim 10^{-5}$-$10^{-4}$) and have negligible effects for periods shorter than one minute even in a much less advantageous thermal environment, as demonstrated by recent ground-based experiments (Désert *et al.* 1996). The LFI detectors do not exhibit such stability and are thus used in a differential mode, with a reference source stable on periods shorter than one minute, which restricts the dynamic

AITOFF PROJECTION OF COBRAS/SAMBA SCAN CIRCLES
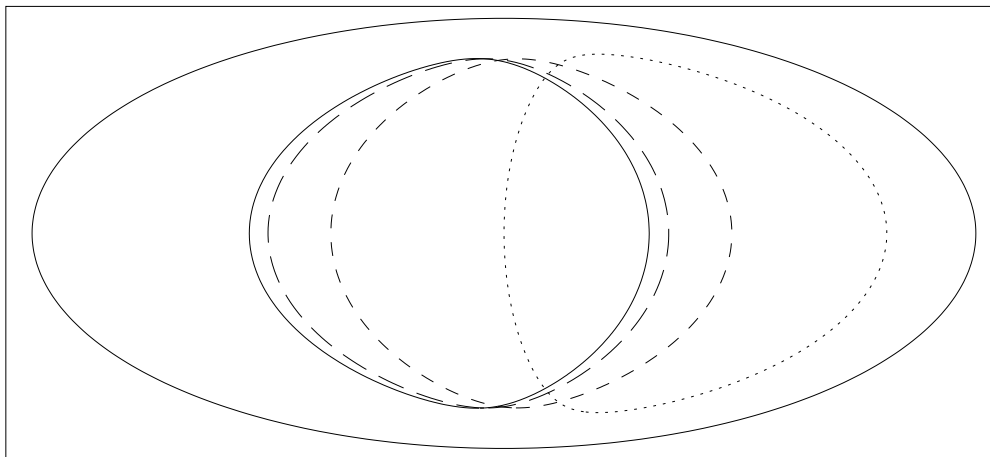


Figure 2.16: Aitoff projection of four COBRAS/SAMBA scans. The second, third and fourth scan from the left are obtained 1 week (long dashes), 1 month (short dashes) and 3 months (dots) respectively after the first.

range of the fluctuations due to gain drifts. In any case, in order to recover the useful physical signal, it is necessary to measure the calibration constants as accurately as possible and, for the LFI, as frequently as possible during the mission. In principle, relatively large calibration signals produce better accuracies for a given integration time and sensitivity. However, the useful signal amplitude is limited by the linearity of the receiver which is usually set by saturation effects occurring in the amplification chains or in the detectors.

The COBRAS/SAMBA detectors will be calibrated exploiting the observation of stable celestial sources of known, adequate intensity which will naturally fall in the field of view if the instrument during the mission. The main calibration source will be the CMB dipole. The amplitude ($\Delta T_D = 3.357 \pm 0.023$ mK) and direction ($[l, b] = [264.33° \pm 0.14°, 48.05° \pm 0.09°]$) of the CMB dipole have been accurately measured by the COBE–DMR instruments[10](Lineweaver *et al.* 1996), and confirmed by the COBE/FIRAS instrument. The dipole signal is a particularly attractive calibrator for COBRAS/SAMBA since it provides a continuous, accurately known modulation of the signal with a convenient amplitude, and it can be used without reducing the efficiency of the observation time. The CMB dipole signal will appear in the COBRAS/SAMBA data as an offset sine–wave. Available freedom in the observing strategy will be used to avoid the spin axis being pointed close to the dipole axis (in which case the dipole signal would be significantly decreased). The voltage modulation detected by each channel can then be fit to the known dipole signal across the observed sky region in order to derive $G_i$. Detailed simulations show that calibration accuracies of order 1–2% can be obtained at a rate of few hours to $\approx 1$ day for most of the mission lifetime (Bersanelli *et al.* 1996). Results for the 90 GHz channels are shown in Figure 2.17.

However, it must be noted that the amplitude of the dipole signal decreases rapidly as the frequency increases, so that it has insufficient strength to adequately calibrate the highest frequency channels. At $\sim 500$ GHz, the dipole signal is only $\approx 40\mu$K, but it can still be used to calibrate the corresponding HFI channel with high signal to noise ratio if the dipole signal is fitted on a large number of pixels. For higher frequencies, the dipole signal is very small, but good calibration can be achieved using the FIRAS calibrated maps of the Galactic plane. In addition, because of the higher angular resolution achieved for high frequency channels, a large number of IR sources will be detected, which will provide

---

[10]The small dipole seasonal component due to the Earth's revolution was used to provide an overall calibration of the COBE–DMR maps (Bennett *et al.* 1992).
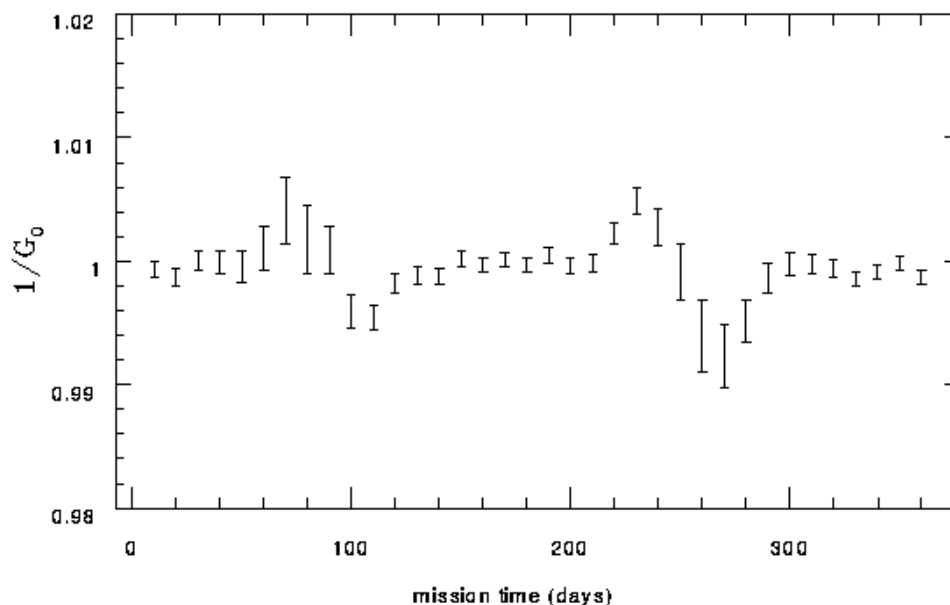
Figure 2.17: Accuracy expected for calibration using the CMB dipole as a calibrating source in the 90 GHz channels during 1 year mission. The plot shows the estimates of $A = G'/G$, where $G'$ is the reconstructed calibration constant and $G$ is its true value. Two peaks in the uncertainties are expected every year, corresponding to the periods where the observed dipole modulation happens to have a minimum.

independent control on calibration.

Additional calibration "point sources" at all frequencies will be external planets. After correction for slowly varying seasonal effects, they provide a highly stable signal with suitably detected intensities (0.1 to 100 mK, depending on the planet, frequency and angular resolution). Even if occurring occasionally (about twice per year per planet) planetary calibration will yield a valuable cross-check of the estimates of $G_i$ routinely obtained with the CMB dipole and Galactic plane. The expected accuracy ($\approx 3\%$ to $5\%$) is limited by the uncertainty in the planets' brightness temperatures at millimeter and sub–mm wavelengths (e.g. De Pater 1990), and it is subject to improvement as progress is made in this field.

It is worth noting that the comparison of calibration on point sources (e.g. planets) and extended sources (e.g. the CMB dipole) will provide a useful cross-check of the measurements of radiation patterns (see Section 2.5.3).

The COBRAS/SAMBA mission is designed so that thermal effects which may perturb the performance of the instruments are controlled and reduced below significance level. The most stringent instrument requirements concern temperature stability (of the focal plane for the LFI, of the telescope for the HFI). These requirements translate into the (stringent) limits described in Section 3.7.1, and the mission study demonstrates that those levels will be achieved, both by proper choice of the thermal architecture of the spacecraft (e.g., insuring large thermal constants), and by using an orbit and observing strategy which provide the best possible thermal environment (Section 3.7.3).

Furthermore, residual instability and slow drifts can be checked a posteriori by exploiting the closure pattern of the proposed scanning technique, as is for instance shown in Section 2.5.1. Indeed, simulations have shown that thermally induced baseline drifts can be removed with an accuracy of $\sim 1\%$ (Bersanelli *et al.* 1996).

### 2.5.3    Beam Pattern Measurements

An important systematic effect that could severely hinder the overall performance of the experiment if not well understood is due to stray signals from bright astrophysical sources, entering the detectors through the sidelobes of the telescope. Sources to be considered are the Sun, the Earth and Moon, the planets, and the galactic plane. Since the positions of these bright sources relative to the telescope change as the beam scans the sky, there is a change in the level of rejection of signals from these sources from pixel to pixel. In spite of the smoothing due to the frequency width of the frequency band, it is expected that the beam pattern may feature significant sharp discontinuities (due to reflections, edges, baffling, spillover and so on), and numerical simulations of the telescope pattern do indeed show such discontinuities. In the near sidelobes, the level of rejection varies rapidly with the distance to the main axis. Because of this rapid variation and because of the existing discontinuities, the fluctuations of the stray signals from pixel to pixel could be of the same order of magnitude as the signals themselves. Figure 2.18 shows a comparison of the absolute level of some straylight signals in normal COBRAS/SAMBA operating conditions at the L2 Lagrange point, assuming simple diffraction by an 1m aperture. This estimate does not take into account spillover and the effects of baffling, so that the actual straylight signals will probably be much larger (typically by a factor of $\sim 100$) in the near to intermediate sidelobes because of spillover radiation entering directly the feed horns, and somewhat smaller in the far sidelobes, due to the effect of the baffling. Nevertheless, if one keeps in mind that the plotted estimated straylight signals for the galaxy and outer planets might be underestimated by one or two orders of magnitude (if there is an important spillover off the mirrors), Figure 2.18 illustrates reasonably well what the sidelobe effects might be.
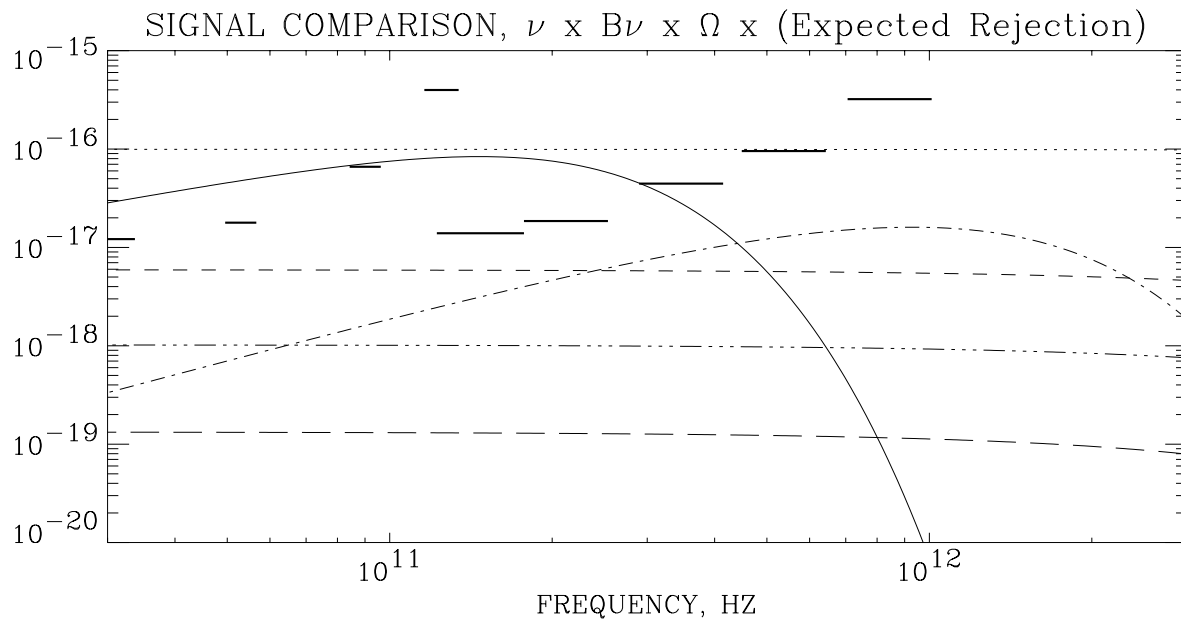


Figure 2.18: Detectable signal ($\nu B_{\nu} \Omega_{useful} R(\theta)$ in W/m$^2$, where $R(\theta)$ is the expected rejection for a given source assuming simple diffraction by a 1 m. aperture) induced by the Sun and planets versus the CMB anisotropy at the level of 30 $\mu$K. The curves refer to the Sun at 90° from the main beam (dots), the Earth at 80° (dashes), an estimate of the galactic dust sidelobe signal at 20° on the average, (dash-dot), the Moon at 70° (dash-dots), and Jupiter at 20° (long-dashes). For comparison, the expected COBRAS/SAMBA sensitivities in the same units for the nine channels are also shown as horizontal bars.

The selected orbit and scan strategy (see Section 4.4) guarantee that the brightest sources remain in the very far lobe and behind the shield during the whole nominal mission, and thus contamination

by sources in the sidelobes is reduced to a minimum. However any sharp discontinuity in the back-lobe pattern may result in a non-negligible parasitic signal (depending on the performance of the baffling system). Thus, it is possible that the total flux from the Sun, the Earth or from the galaxy be above the full mission nominal sensitivity for some channels (see Figure 2.18).

Over the nominal duration of the COBRAS/SAMBA mission, the signals detected in the far sidelobes of the telescope from the Sun, the Earth, and the galactic plane are comparable to the ultimate sensitivity for beam rejections from $3 \times 10^{-8}$ to $2 \times 10^{-11}$ for the Sun (depending on the channel), from $10^{-7}$ to $9 \times 10^{-9}$ for the Earth and from $10^{-4}$ to $4 \times 10^{-8}$ for the galactic ridge (these numbers vary according to the particular channel, because fluxes are frequency dependent, and because the sensitivity depends on the channel, see details in table 2.6).

|  | 32 GHz | 53 GHz | 90 GHz | 125 GHz | 150 GHz | 217 GHz | 353 GHz | 545 GHz | 857 GHz |
|---|---|---|---|---|---|---|---|---|---|
| Sun | 3.0e+08 | 9.2e+08 | 1.2e+09 | 6.1e+08 | 2.9e+10 | 6.3e+10 | 1.1e+11 | 2.0e+11 | 2.3e+11 |
| Earth | 1.3e+07 | 3.9e+07 | 5.2e+07 | 2.5e+07 | 1.2e+09 | 2.6e+09 | 4.7e+09 | 7.9e+09 | 8.9e+09 |
| Moon | 1.5e+06 | 4.4e+06 | 5.9e+06 | 2.9e+06 | 1.4e+08 | 3.0e+08 | 5.4e+08 | 9.1e+08 | 1.0e+09 |
| Jupiter | 4.5e+03 | 1.3e+04 | 1.8e+04 | 8.7e+03 | 4.2e+05 | 8.9e+05 | 1.6e+06 | 2.7e+06 | 2.9e+06 |
| Gal. ridge | 1.2e+04 | 7.8e+04 | 2.2e+05 | 1.7e+05 | 1.1e+07 | 3.6e+07 | 1.1e+08 | 2.9e+08 | 4.0e+08 |

Table 2.6: This table shows the level of the observed flux from bright astrophysical sources, in units of the sensitivity in each channel (assuming the nominal duration of the COBRAS/SAMBA mission). Thus, the tabulated values correspond to the inverse of the beam rejection required for the "stray" signal from each source to be equal to the final sensitivity. Note however that it is not necessary that the absolute flux from these sources be rejected to a level lower than the final sensitivity, since only unknown variations of these fluxes are of any relevance.

One can design the payload for these levels of rejection (as shown by the detailed straylight calculations, Section 3.7.2), but verifying that the requirements are met would be practically impossible in a controlled environment. Of course, such requirements would anyway be extremely conservative, since only unknown variations of the straylight signals need to be rejected at a level smaller than the final sensitivity for a given channel. The galactic ridge, for instance, is a very extended source, so that its sidelobe contribution is averaged over a large fraction of the radiation pattern. Thus, the variations of the galactic signal are expected to be significantly smaller than the signal itself.

In general, in addition to absolute sidelobe rejection, one can minimize sidelobe effects when CMB measurements are performed by keeping the variations of the sidelobe signals to a minimum. The orbit and scan strategy of COBRAS/SAMBA were chosen accordingly, with all the brightest sources roughly in a fixed direction away from the line of sight. In addition it is possible to *estimate the level of the variations*. As an example, we have shown by numerical simulations that it is possible to evaluate the sidelobe contribution of bright sources using the data collected by COBRAS/SAMBA during routine observations and during the transfer to its final orbit, thus correcting for the effect of straylight with an accuracy at the level of the detector noise or better. The principle of the method is to average the signals detected when a given bright source (e.g. planets and sun) is in the same position with respect to the spacecraft; this measure provides an estimate of the directivity of the telescope in that particular direction. In particular, during parts of the transfer cruise towards its final orbit, COBRAS/SAMBA will observe the Earth and the Moon as they move from the front to the back of the telescope beam. The redundancy of the positions occupied by all the strong sources in the far sidelobes is such that an estimate of both the sky brightness and the antenna pattern can be obtained simultaneously via an iterative algorithm, correcting for the effect of sidelobes with an increased precision at each step of the iteration.

For the actual simulation of the method (Delabrouille 1996), we have used a qualitatively reasonable 2-D model for the radiation pattern, featuring estimated discontinuities due to baffling and diffraction edges (see Figure 2.19.a). This corresponds to the 353 GHz COBRAS/SAMBA channel, for which
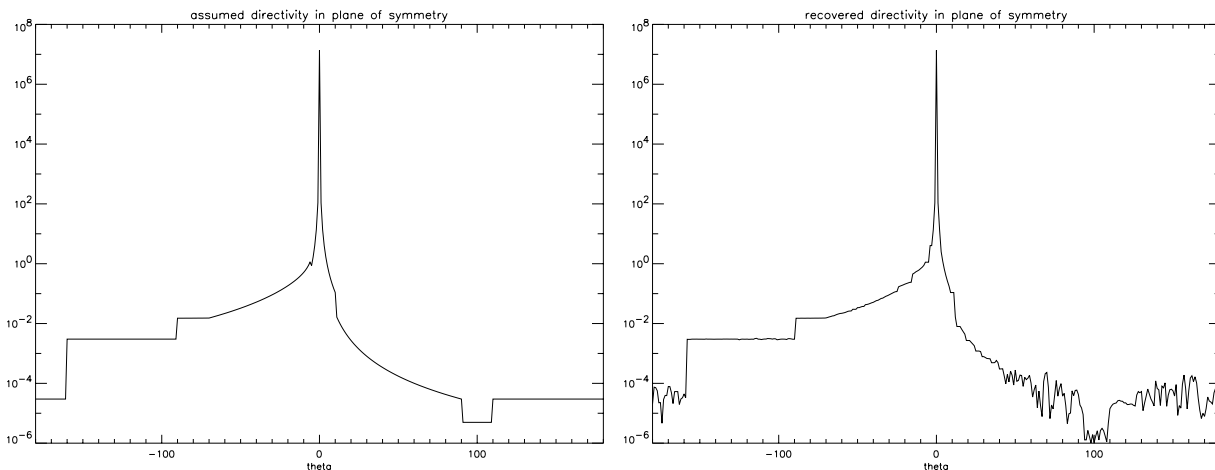
Figure 2.19: (Left) A cut through the input model of the beam pattern for the 353 GHz channel. (Right) Recovered pattern (see text).

both the contributions from the sun and the galaxy were expected to be significant. The fact that the actual radiation pattern of the COBRAS/SAMBA telescope may significantly differ from this model, even by an order of magnitude for some directions, does not alleviate the demonstrative results of the simulation. The beam pattern in the plane of symmetry of the spacecraft, recovered using the simulated data, is shown in Figure 2.19.b. The comparison shows that this method allows the measurement of the overall angular response of the telescope with an excellent relative accuracy, for rejection levels as low as $\sim 10^{-12}$. The method can be further improved by correcting in a self consistent way for the galactic plane contribution, by devising an adapted observing strategy during the transfer phase to map the near to intermediate sidelobes, and by improving the interpolation methods in the directions of the radiation pattern where there is no data.

### 2.5.4   Removal of Glitches due to Cosmic Rays

Cosmic rays may interact with the bolometers of the HFI, depositing some of their energy in the material, which can be seen on the bolometer signal as "glitches". However, the volume of the sensitive part of the COBRAS/SAMBA bolometers is small (less than $10^{-6}$ cubic centimeters) and thus the expected rate of cosmic rays is small (less than one per second). The characteristic signature of the cosmic rays, combined with the redundancy of the data during the 120 turns, allows for efficient removal of the corresponding affected data samples. This corresponds to a loss of 10% at most of integration time on a given pixel, with negligible effect on the final sensitivity and no effect on the completeness of the maps.

## 2.6   Summary and Conclusions

Thanks to detailed estimates of the magnitude of the contaminating foregrounds (cf. Fig. 2.6), we have shown in this chapter that the COBRAS/SAMBA mission will yield maps of the CMB fluctuations which will be faithful to the true statistical nature of the distribution (whether Gaussian or not, Section 2.4.4), with an accuracy better than 1% on the amplitude of individual modes of the recovered power spectrum at all angular scales $\ell < 1100$; in integrated form, this accuracy is equivalent to $\Delta T/T \lesssim 2. \ 10^{-6}$ on 10 arcminute angular scale (cf. Fig. 2.11). These maps meet the requirements set out in Chapter 1 to fulfill the far-reaching cosmological goals of the mission.

    This demonstration has been based on elaborate simulations of the overall data collection and analysis. In addition to showing that the foregrounds can be removed with the required accuracy, the

analysis has shown that these conclusions are very robust:

- the accuracy of the derived CMB spectrum is insensitive to the assumptions made on the spectral behavior of the galactic foregrounds (see table 2.2);

- the confusing effect of point sources will not impair the process of component separation, even when the most pessimistic assumptions are made (see table 2.3).

In terms of the specific technical characteristics of the COBRAS/SAMBA model payload, this exercise has confirmed the following conclusions:

- its frequency range (30–900 GHz) is adequate to separate the foreground contributions to the required accuracy.

- The sensitivity of its detectors is similarly adequate. The noise Figure at frequencies larger than ∼150 GHz (i.e. of the HFI) could be degraded by up to a factor of two without a significant loss of the science output (see table 2.4). However, further degradation would not be tolerable.

- Three spectral bands of COBRAS/SAMBA have been chosen to best isolate the Sunyaev-Zeldovich effect. The simulations have confirmed that COBRAS/SAMBA will not only remove this contribution to the CMB fluctuations, but also provide a nearly full–sky map of the Compton parameter $y$, with a very low detection threshold (see Fig. 2.9 & 2.14).

Finally, we have developed data processing schemes which will allow us to (i) determine to high accuracy the detector radiation patterns, using mostly the Earth, Sun and Moon during the transfer phase to the final orbit; (ii) remove the striping of the maps due to $1/f$ noise down to the levels assumed in the separation analysis; and (iii) calibrate the detectors using mainly the cosmic dipole and the galactic ridge. We here note that there is still ample room to improve on the algorithms used at this stage, which have been kept simple to demonstrate the feasibility of the mission.

# Chapter 3

# The Model Payload

## 3.1 Scientific Requirements

The scientific objectives of COBRAS/SAMBA (Ch. 1) require that the payload instruments fulfill three essential requirements:

1. The **angular resolution** achieved must be of order $10'$ or better at the frequencies where the CMB signal is dominant. This requirement sets the size of the effective aperture of the telescope to be of order 1 meter in diameter.

2. The **frequency coverage** must be wide enough to provide robust removal of the foregrounds. Simulations (Ch. 2) indicate that the range $30 - 800$ GHz is adequately large. To achieve this large range requires two technologically different types of detectors: tuned radio receivers at low frequencies and bolometers at high frequencies. While it seems possible to use bolometers at frequencies as low as $\sim$50 GHz, achieving the sensitivity levels required (see below) at 30 GHz appears very difficult with bolometers; similarly, the most sensitive applicable radio techniques (High Electron Mobility Transistor, or HEMT, amplifiers) cannot presently be pushed to frequencies higher than $\sim$150 GHz (although experimental prototypes now exist up to 210 GHz). Thus it is quite clear that the optimum anisotropy experiment should include two instruments. In addition to the scientific gain, when compared to a single-instrument payload COBRAS/SAMBA will present two significant advantages: the reliability of the mission will be much enhanced (yielding results even in the event of failure of one of the instruments), and a pre-designed frequency overlap between the two techniques will contribute a very useful cross-check of the instrumental sensitivity to systematic effects.

3. The **sensitivity** must be sufficient for adequate detection of the CMB anisotropy. Note that the uncertainty in the determination of the CMB anisotropy will be larger than the instrumental sensitivity at any observed frequency, due to the presence of foreground confusion sources (a problem discussed in detail in CH. 2) and potential systematic effects. A useful criterion on the instrumental sensitivity is that it should be smaller than the confusion noise level contributed by sources of foreground emission in the "cleanest" regions of the sky, guaranteeing the best possible signal-to-noise level over the whole sky. Contaminating foreground fluctuations in the cleanest 20% of the sky are expected to contribute a signal larger than $\sim$5 $\mu$K at $\sim$90 GHz (though this depends both on frequency and angular scale, see Ch. 1 and 2). We thus set a goal of achieving an instrumental sensitivity level better than $\Delta T/T \sim 2 \times 10^{-6}$ in the channels where the CMB is the dominant signal, and as close to this value as technically possible at all other channels.

In addition to these basic requirements, the payload is designed with the goal to reduce its sensitivity to systematic effects, mainly those due to straylight and thermal modulation. In particular,

systematic effects which produce signals at frequencies larger than that of the observing pattern, cannot be easily distinguished from real signals and thus introduce an additional uncertainty which must be minimized.

## 3.2  Payload Architecture

There are three basic payload components: (1) a telescope and baffling system, providing the angular resolution and rejection of straylight; (2) the Low Frequency Instrument (or LFI) – an array of tuned radio receivers, based on HEMT amplifier technology, and covering the frequency range ~30 - 135 GHz; and (3) the High Frequency Instrument (or HFI) – an array of bolometers covering the frequency range ~116 - 1000 GHz. The LFI and HFI are both placed in the focal plane formed by the telescope, and share the focal area equally. This arrangement maximizes the optical throughput to each instrument, while keeping off-axis aberrations to an acceptable level.

The temperature requirements of the two types of detector are very different, the HEMTs giving adequate performance at 100 K (achievable by passive cooling), while the bolometers must operate at temperatures between 0.1 and 0.15 K to achieve adequate performance. Thus, while the LFI will simply consist of an array of corrugated horns feeding miniaturized receivers, the bolometers must be located inside a "cold box" consisting of a series of nested radiation shields, and cooled by an open-cycle dilution refrigerator coupled to a mechanical 4 K cooler. A schematic overview of the arrangement of the payload is shown in Figure 3.1. In the remaining sections of this Chapter we describe each of the three main elements (telescope, LFI, HFI) in turn, their integration into a working payload, and the constraints the payload sets on the technical design of the spacecraft.
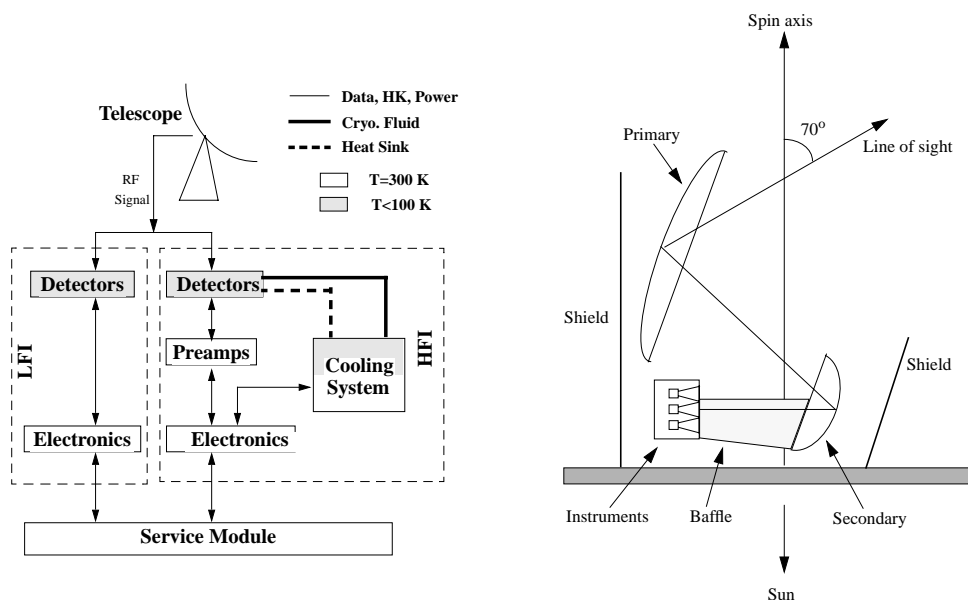


Figure 3.1: A subsystem-level block diagram of the model payload, and a sketch of the geometric architecture of the payload.
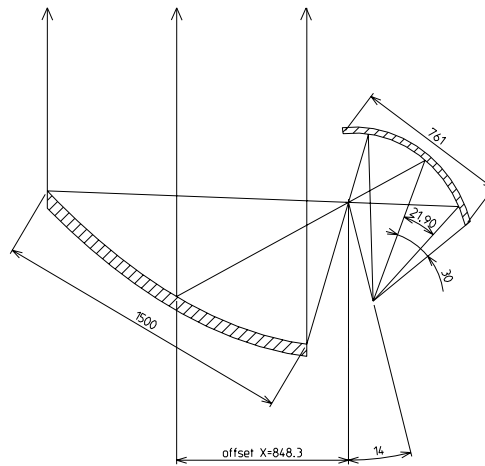
Figure 3.2: A sketch of the configuration of the telescope main and secondary mirrors. Linear dimensions are in mm and angular dimensions in degrees. The offset of the main mirror is marked in the direction perpendicular to the telescope boresight.

## 3.3  The Telescope and Baffling System

The optical design of the telescope has been carefully studied, and the resulting parameters are summarized in Table 3.1. One of the main goals is to obtain diffraction limited performance at wavelengths longer than $\sim$800 $\mu$m. Achieving this goal requires that the (on-axis) in-flight wavefront error (WFE) be less than $\sim$60 $\mu$m; this requirement sets the accuracy which must be achieved by the reflector surfaces (see Tables 3.1 and 3.6). At wavelengths shorter than $\sim$800 $\mu$m the beam size will be set by the detector size rather than the diffraction limit (Section 3.5); the detectors at these wavelengths are oversized (with respect to the diffraction pattern) in order to collect efficiently the flux of the degraded image.

A second goal is to achieve good control over the shape of the radiation patterns at all frequencies (in order to reject straylight effectively, see Section 3.7.2). In order not to degrade the far side-lobes (which are the main causes of straylight contamination), the micro-roughness of the reflector surfaces must be kept below 1 $\mu$m (rms), implying that the total integrated scatter produced by the mirrors will be less than 0.2% at $\lambda$ =350 $\mu$m. Finally, due to the multi-beam nature of the payload, careful attention must be paid to the minimization of off-axis aberrations. The mapping nature of the mission requires that the beam pattern shapes for all array pixels within each frequency channel be as uniform as possible. As shown in more detail in Section 3.6.2, these goals can be met by the COBRAS/SAMBA payload.

The design (see Figure 3.2) consists of an off-axis tilted Gregorian system, offering the advantages of no blockage and compactness. The eccentricity and tilt angle of the secondary mirror, and the off-axis angle obey the so-called Dragone-Mizuguchi condition, which allows the system to operate without significant degradation in a large focal plane array, while simultaneously minimizing the polarization effects introduced by the telescope.

The baffling system is composed of two elements. The first (the "shield") is a large, self-supporting, and roughly conical structure covered with MLI, which surrounds the telescope and focal plane instruments. Together with the optical bench, it defines the payload (or optical) "enclosure". It has an important function both in reducing the level of straylight (which at the chosen orbit - see Ch. 4 - is in large part due to the spacecraft itself) and in promoting the radiative cooling of the enclosure towards deep space. The second element (the "baffle") consists of one half of a conically shaped surface that links the focal plane instruments to the bottom edge of the subreflector; its function is to shield the detectors from thermal radiation originating within the enclosure.

Table 3.1: Telescope Parameters

| Main reflector (M1) | |
|---|---|
| shape | off axis paraboloid |
| physical size | $1.5 \times 1.292$ m |
| focal length | 0.72 m |
| surface accuracy[†] | <10 $\mu$m rms |
| roughness[‡] | <1 $\mu$m rms |
| Sub-reflector (M2) | |
| shape | off axis ellipsoid |
| physical size | $0.761 \times 0.719$ m |
| focal length | 0.514 m |
| f-number | 1.36 |
| surface accuracy[†] | <10 $\mu$m rms |
| roughness[‡] | <1 $\mu$m rms |
| Telescope | |
| focal length | 1.8 m |
| main- to sub-reflector axis angle | 14° |
| central feed to sub-reflector axis angle | 34°.129 |
| Total Wavefront[§] Error | <40 $\mu$m rms |
| Total emissivity | 0.01 |

[†] Deviation from best paraboloid/hyperboloid

[‡] Average over spatial scales up to 0.8 mm

[§] Not in-flight

### 3.3.1   Mirror Technology

The primary and secondary mirrors will be fabricated using Carbon Fibre (CFRP) technology, and taking advantage of the experience accumulated in the design and development of the FIRST (the Far Infrared and Submillimetre Telescope, an ESA cornerstone mission) telescope. The FIRST program has already achieved the manufacture of a 1.1 meter-diameter mirror with specifications similar to those required by COBRAS/SAMBA .

The baseline design for the COBRAS/SAMBA mirrors consists of an all-CFRP honeycomb sandwich structure designed to exhibit isotropic behavior and was chosen because it satisfies the requirements of low mass, high stiffness, high dimensional accuracy, and can be tailored to have a very low coefficient of thermal expansion. The sandwich concept consists of a thick (4-10 cm) honeycomb-like core, whose surfaces have been machined to the desired shape, and to which are bonded two thin (1-1.5 mm) skins. The core is fabricated by winding CFRP filaments around individual aluminum mandrels; these "cells" are integrated to create a large (machinable) honeycomb core panel. The face skins are manufactured by laying CFRP "tows" (i.e. flat bundles of carbon filaments wetted with epoxy) directly on the surface of the pre-treated mould; the mould is made of a dimensionally and thermally stable material, which can be easily machined and polished to the surface accuracy and roughness levels required (e.g. monolithic graphite). The reflecting properties of the mirror surface are achieved by metalization of the concave side of the sandwich. Several techniques are currently available for this process; the present baseline is to use replication. In this technique a protective layer (of $MgF_2$ or $SiO_2$) and a $\sim$5000 Å layer of metal (e.g. aluminum) are evaporated onto the mould; a thin (10-100 $\mu$m) layer of epoxy is created between the evaporated metal and the finished CFRP sandwich. Once the epoxy has cured, the sandwich is lifted, stripping and carrying away the evaporated layers and the top protective coating with it. The existence of the latter allows the implementation

of a cleaning procedure before launch; the ability to clean the mirror surfaces insures the required in-flight cleanliness level without the need to keep the payload in expensive high-quality clean rooms during the integration and test phases.

The 1.1 m reflector built by Dornier as a technology demonstrator for FIRST achieved an rms surface accuracy of $\sim$5.7 $\mu$m. The specification for the 3 meter-diameter main mirror of FIRST calls for a surface accuracy better than 5 $\mu$m. Thus, the specification of 10 $\mu$m set on the surface roughness of each of the COBRAS/SAMBA mirrors is comparatively much looser than those for FIRST and should be straightforward to achieve. This specification yields a WFE of $\sim$40 $\mu$m on the full telescope; inclusion of other sources of WFE (see Section 3.6.2) shows that the requirement of diffraction-limited performance at $\lambda 800$ $\mu$m can be met.

The mirror mounting structures will also be made of CFRP. The primary and secondary mirrors will be independently mounted via three attachment points in each case. The optical bench will be fabricated from a sandwich panel consisting of CFRP skins on an aluminum honeycomb. The all-CFRP design ensures that no significant dimensional changes due to temperature variations will occur during assembly, alignment and testing, and simplifies the testing and mounting scheme.

## 3.4    The Low Frequency Instrument

The LFI (Figure 3.3) is designed to cover the 30 - 135 GHz band, with an array of 56 detectors split into 4 channels, centered at 31.5, 53, 90, and 125 GHz. The three lowest center frequencies were chosen to match the COBE-DMR channels, to facilitate the comparison of product maps. Table 3.2 summarizes the characteristics of the LFI receivers. The total number of detectors is a compromise between the high sensitivity desired, and the requirement to cool the enclosure passively to $\sim$100 K (the LFI amplifiers are the dominant heat input into the focal plane). The number of detectors in each band was chosen as a trade-off between the instrumental sensitivity (which varies with frequency), and the desire to obtain the highest final sensitivity at $\sim$90 GHz. Table 3.2 illustrates the instantaneous and final (i.e. after achieving two full coverages of the sky) sensitivity expected to be achieved with state-of-the-art receivers.

Radiation will be coupled from the telescope to the detectors via conical corrugated feedhorns exploiting the two orthogonal polarizations at a given frequency. Thus, each horn feeds two receivers. The design of the feedhorns, though straightforward, must be optimized to provide low sidelobe level, low loss, and good stability. The feedhorns will be oriented so as to minimize beam pattern aberrations: a good first approximation places the feed apertures on a spherical surface centered on the subreflector apex.

Each receiver consists of a pair of amplification/detection chains connected in parallel via so-called hybrid rings (Figure 3.4), and constitutes a "continuous-comparison" device (Bersanelli *et al.* 1996). In this scheme, the difference between the inputs to each of the chains (the signal from the telescope and that from a reference blackbody respectively) is continuously being observed. To achieve this, it is necessary to modulate periodically the sign of the inputs via solid-state phase-shifters. This design was chosen over a much simpler total-power scheme (consisting of one of the two parallel chains) because the latter exhibits inadequate gain stability at time scales larger than a few seconds. The differencing receiver improves the stability considerably if the two input signals are almost equal (at a cost of a factor of $\sqrt{2}$ in sensitivity); in this case the reference is a blackbody at $\sim$100 K while the signal is at $\sim$3–5 K, but they are effectively equalized by modulating the gain. The blackbody reference itself must remain at a very stable temperature ($\Delta T < 100$ $\mu$K); this, together with the $\sim$100 K temperature which must be achieved passively at the focal plane, are the most significant requirements placed by the LFI on the design of the spacecraft.

Each amplification stage will be provided by High Electron Mobility Transistors (HEMTs). This technology offers at present the best compromise between sensitivity and ease of implementation in the frequency range of the LFI. Total power receivers based on Monolithic Microwave Integrated Circuit
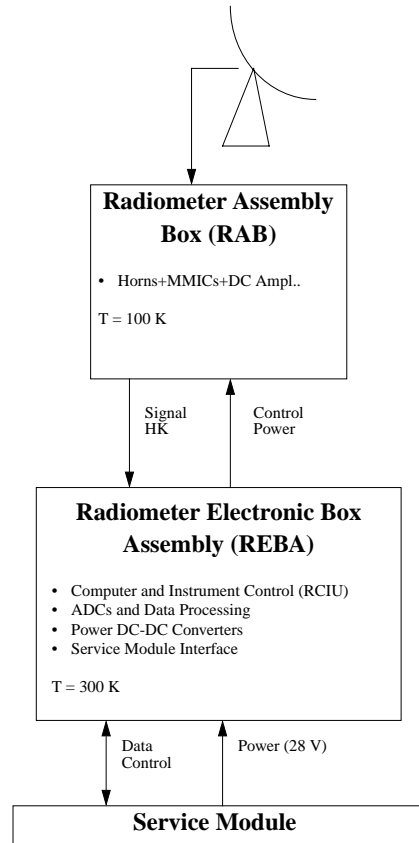
Figure 3.3: (a) A unit-level block diagram of the LFI. Each box in this diagram represents a single physical unit in the instrument.
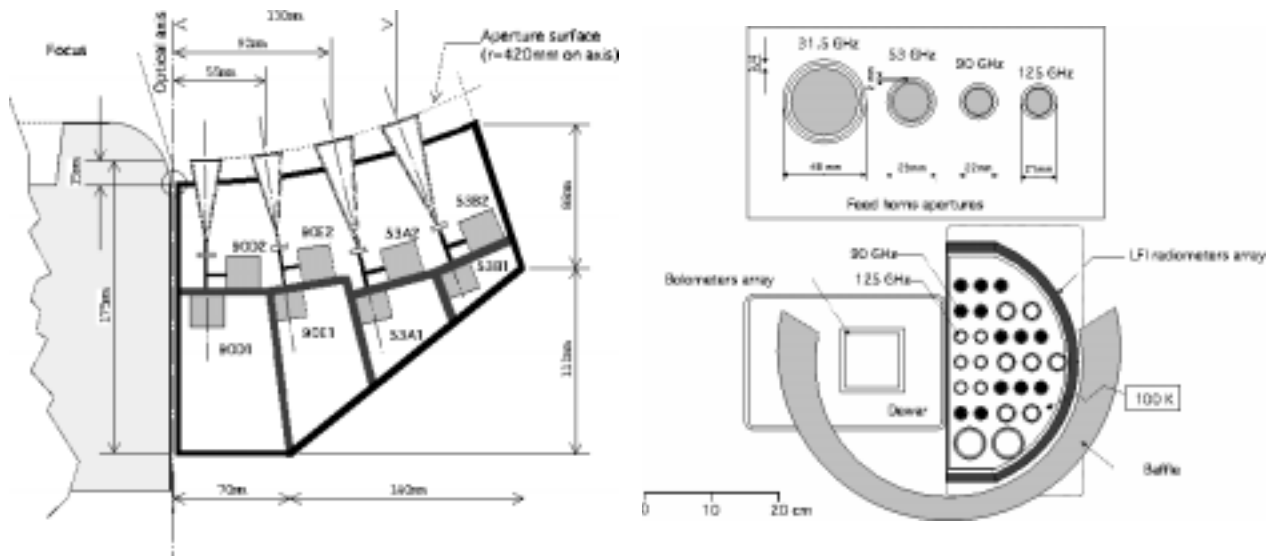


Figure 3.3: (b) Side and top view of the LFI, the former showing the horn/receiver arrangement, and the latter the layout of the feed apertures in the focal plane.
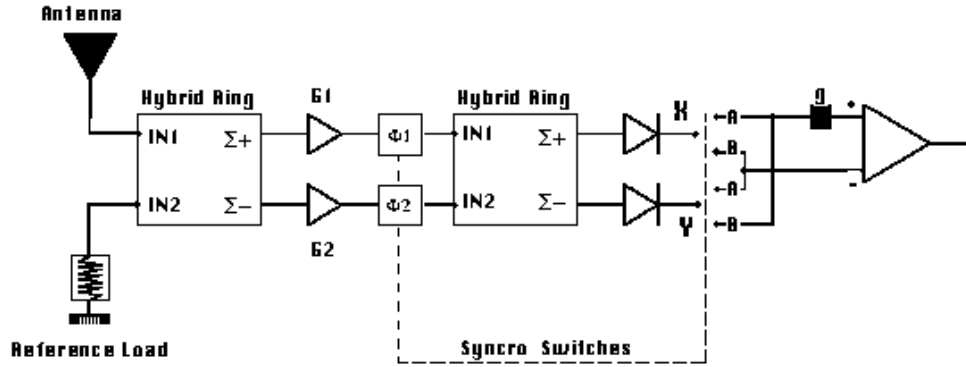
Figure 3.4: A conceptual description of the "continuous-comparison" receiver, two of which are fed by each (dual-polarization) horn. All of the elements in this figure can be packaged into a single MMIC only a few cm$^3$ in volume, with one input (radiation) connected to the feedhorn, and one output (the detected signal).

Table 3.2: Characteristics and Sensitivity of the LFI

| Center Frequency (GHz) | 31.5 | 53 | 90 | 125 |
|---|---|---|---|---|
| Wavelength (mm) | 9.5 | 5.7 | 3.3 | 2.4 |
| Detector Temperature (K) | 100 | 100 | 100 | 100 |
| Bandwidth ($\Delta\nu/\nu$) | 0.15 | 0.15 | 0.15 | 0.15 |
| Bandwidth (GHz) | 4.7 | 8.0 | 13.5 | 18.8 |
| Number of Detectors | 4 | 14 | 26 | 12 |
| Angular Res. (FWHM, arcmin) | 30 | 18 | 12 | 12 |
| Beam crossing time (ms) | 90 | 54 | 36 | 36 |
| No. pixels on sky | 165012 | 458366 | 1031320 | 1031320 |
| $T_{sys}$ (K) (Diff. Rec.) | 30 | 40 | 80 | 130 |
| Nominal mission* ($1\sigma$ sensitivities, per pixel*) | | | | |
| Average integ. time per det.(sec.) | 223 | 80.5 | 35.6 | 35.6 |
| Array $\Delta\text{T}^\S$ (mK$\sqrt{s}$) | 0.311 | 0.169 | 0.191 | 0.387 |
| $\Delta T$ per pixel$^\S$ ($\mu$K) | 20.8 | 18.9 | 31.9 | 64.5 |
| $\Delta T/T$ Sensitivity$^\dagger$ ($\times 10^{-6}$) | 7.8 | 7.5 | 14.4 | 35.4 |
| Flux Sensit. per pixel (mJy) | 37.8 | 35.1 | 76.1 | 297.6 |

[*] 14 months of observations, or two full sky coverages

[*] A pixel is a square whose side is the FWHM extent of the beam

[§] Antenna temperature

[†] Thermodynamic temperature.

(MMIC) technology, in which the whole receiver is packed into a device a few centimeters across, are state-of-the-art but already available commercially with characteristics close to those required by COBRAS/SAMBA . The next step, consisting of building a complete continuous-comparison receiver into a single MMIC is currently in progress, and should be relatively straightforward.

As noted before, the dominant heat input into the focal plane is due to power dissipation in the MMICs; since this fact drives the thermal design of the payload module significantly, it is desirable to reduce it as far as possible. During the course of this study significant improvements have already been made in this direction (partly by switching from GaAs to InP technology), converting the initial assumptions into extremely conservative ones. Present developments indicate that a reduction by a factor of two in the assumed dissipated power is reasonable, and further reductions may soon be possible. These reductions, which can only be taken into account in succeeding stages of the development of the mission, should lead to substantial simplifications in the thermal design of the spacecraft.

Beyond the signal detection level, the LFI consists of electronics, data processing and interfacing software, all of which are packed into a single room-temperature box which is placed outside the optical enclosure.

## 3.5 The High Frequency Instrument

The HFI (Figure 3.5) will cover the high frequency part of the COBRAS/SAMBA range. The heart of the HFI − the detectors − are bolometers, solid-state devices in which the incoming radiation dissipates its energy as heat that increases the temperature of a thermometer. For a bolometer with a given time constant, the temperature increase (on time scales longer than the time constant) is inversely proportional to the heat capacity of the bolometer. The cooling of these detectors to very low temperatures provides for the low heat capacity needed for high sensitivities. Models of bolometer performance indicate that in practice, allowing for non-ideal effects, to obtain a useful speed of response and the highest sensitivity, the maximum allowable physical temperature of the bolometer heat sink is $T_{max} \simeq \frac{0.2}{\lambda\ (mm)}$ K. Thus, the HFI bolometers must be cooled to temperatures below 0.15 K. As an indication, if the temperature were increased to 0.3 K, the sensitivity at the most interesting frequencies would be degraded by a factor of $\sim 10$ - a degradation which is unacceptable in terms of the expected scientific return (see Section 2.4.4). The goal set for the HFI bolometers is that they should operate at a temperature of 0.1 K. With this assumption, and using the current best detector technologies (e.g. spider-web bolometers, Bock *et al.* 1995, Gear & Cunningham 1995) it is possible to reach Noise Equivalent Powers (NEPs) of the order of $10^{-17}$ W Hz$^{-1/2}$ (see Table 3.3).

The total number of bolometers will be 56, split into 5 channels at central frequencies of 143, 217, 353, 545, and 857 GHz. The placement of the channels in frequency space has been optimized (see Section 2.4.4), not only to remove the foregrounds (mainly dust emission at these high frequencies) and recover the CMB, but also for the detection of the Sunyaev-Zeldovich effect. Filters provide the necessary frequency selectivity for each channel, and also block the thermal radiation coming from the telescope itself. Light from the telescope will enter the cold box through an initial blocking stage at 4 K, proceed through a second bandpass filter at 1.6 K made from interfering cross-shaped grids embedded in a polyethylene matrix, and will finally be concentrated on the detectors by Winston cones. The entrance apertures of the cones define the fields of view of the detectors; they are sized to the diffraction pattern in the three low frequency channels, and oversized in the two highest frequency channels in order to cope with the aberrations of the telescope. The total number of detectors in each channel is limited by the area of the focal plane in which aberrations remain acceptable, and determine the size of the filters selecting each band. The detector arrangement with respect to the scan direction gives a fully sampled image of the sky, and partial redundancy.

The bolometers are read out via J-FETs located very close to them, in a box which is physically located inside the cold box of the HFI (the "BOB", see Figure 3.5), but thermally insulated from it.

Figure 3.5: (a) A unit-level block diagram of the HFI. Each box represents a single physical unit.
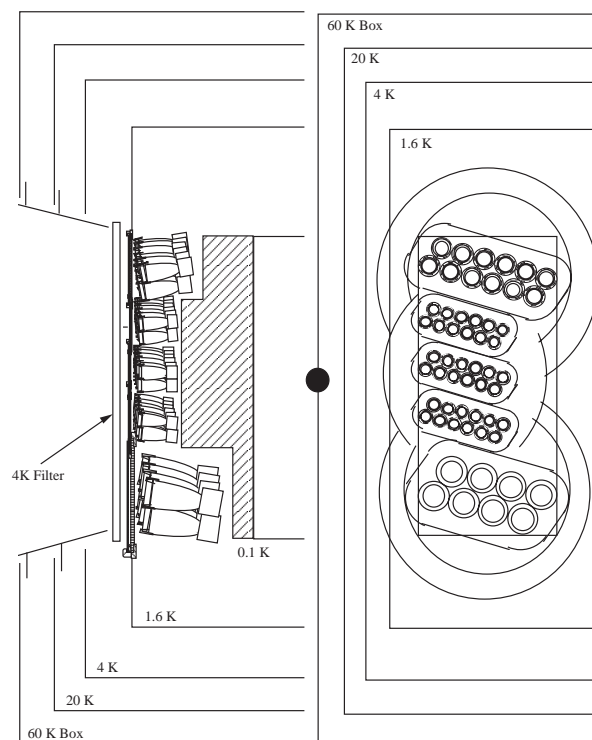
Figure 3.5: (b) A conceptual view of the HFI "cold box", which consists of nested radiation shields maintained at various temperatures by the active cooling system. The side view shows the optical arrangement, including the 4 K blocking and 1.6 K bandpass filters, and the Winston cones. The top view shows the detector layout and filter outlines.

The cryogenically-cooled J-FETs provide for the impedance matching with the following stages of the preamplifiers located farther from the detectors. The readout electronics are based on the principle of AC bias that has successfully demonstrated (in ground-based experiments, Wilbanks *et al.* 1990) its capability to detect signals at very low frequency without sky-chopping. The rotation of the satellite at 1 rpm (see Chapter 4) will provide signals in the range 0.016 Hz to 94 Hz, though little power remains above 70 Hz; in terms of spherical harmonic orders (see Chapter 2), these frequencies correspond to the range $l = 1$ to 4000, very suitable to the measurement sought.

Table 3.3 summarizes the characteristics of the HFI channels and the instrumental sensitivities that will be achieved after the nominal observation period.

### 3.5.1 Cooling System

The low temperature required by the bolometers must be provided by an active cooling system, which will consist of a number of Stirling-cycle mechanical coolers coupled to an open-cycle He dilution refrigerator. The mechanical coolers will provide precooling of $^3$He and $^4$He cryogen down to 4 K, as well as control of the temperature of the outermost radiation shield of the HFI to ∼65 K (Figure 3.6a); the dilution system (consisting of an initial Joule-Thompson stage followed by the $^3$He/$^4$He dilution refrigerator) carries the cooling down to 0.1 K (Figure 3.6b). The overall system is very similar to that which will be used by FIRST (an approved ESA cornerstone mission).

The basis of the COBRAS/SAMBA mechanical cooler technology is the development by Oxford University and Rutherford Appleton Laboratory (RAL) of an 80 K cooler that was space quali-fied for the ISAMS instrument, and the further development at RAL of a two stage Stirling Cycle Cooler achieving 20-50 K, and a closed cycle Joule-Thomson Expansion Cooler achieving 4 K. British Aerospace (now Matra Marconi Space), funded by ESA, has successfully transferred this technology

to an industrial level and can provide space qualified 4 K coolers. The long life and high reliability of these systems result from the use of a frictionless compressor that has demonstrated successful space operation for periods of years. A 4K cooler would provide for cooling power both at about 20 K ($\sim$50 mW) and at 4.4 K ($\sim$10 mW).

Table 3.3: Characteristics and Sensitivity of the HFI

| Center Frequency (GHz) | 857 | 545 | 353 | 217 | 150 |
|---|---|---|---|---|---|
| Center Wavelength (mm) | 0.35 | 0.55 | 0.85 | 1.38 | 2.0 |
| Detector Temperature (K) | 0.1 | 0.1 | 0.1 | 0.1 | 0.1 |
| Bandwidth ($\Delta\nu/\nu$) | 0.37 | 0.37 | 0.37 | 0.37 | 0.37 |
| Bandwidth (GHz) | 317 | 202 | 131 | 80 | 56 |
| Number of bolometers | 12 | 12 | 12 | 12 | 8 |
| Angular Res. (FWHM, arcmin)[♯] | 4.37 | 4.37 | 4.37 | 7.11 | 10.29 |
| No. pixels[*] on sky ($\times 10^6$) | 7.76 | 7.76 | 7.76 | 2.93 | 1.40 |
| $NEP_{bol}$ ($10^{-17}$ W/$\sqrt{Hz}$) | 8.5 | 4.6 | 2.6 | 2.1 | 2.0 |
| $NEP_{phot}$ ($10^{-17}$ W/$\sqrt{Hz}$) [♣] | 14.0 | 5.9 | 2.6 | 1.8 | 1.4 |
| $NEP_{tot}$ ($10^{-17}$ W/$\sqrt{Hz}$) | 16.4 | 7.5 | 3.7 | 2.8 | 2.5 |
| Nominal mission[*] (1$\sigma$ sensitivities, per pixel[*]) | | | | | |
| Average integ. time per bol. (sec.) | 4.7 | 4.7 | 4.7 | 12.5 | 26.2 |
| Array Sensit.[§] ($\mu$K) | 0.72 | 1.31 | 2.55 | 1.84 | 1.83 |
| $\Delta T/T$ Sensit.[†] ($10^{-6}$) | 4166 | 76.6 | 12.1 | 2.0 | 1.2 |
| Flux Sensit. (mJy) | 26.4 | 19.3 | 15.8 | 11.4 | 11.3 |
| ySZ[‡] ($10^{-6}$) | 254 | 9.3 | 3.6 | 173.7 | 0.8 |
| N(H)[♭] ($10^{20}$ H/cm$^2$) | 0.025 | 0.057 | 0.14 | 0.13 | 0.15 |

[*] 14 months of observations, or two full sky coverages

[♯] Diffraction limited at frequencies below 350 GHz (effective telescope diameter = 1 m)

[*] A pixel is defined as a square whose side is the FWHM extent of the beam

[♣] Telescope temperature = 100 K; total emissivity = 0.01

[§] Rayleigh-Jeans temperature

[†] Thermodynamic temperature

[‡] Sensitivity to the Sunyaev-Zeldovich $y$ parameter

[♭] Sensitivity to gas column density

The Open Cycle Dilution/Joule-Thomson Refrigerator has been developed at the Centre de Recherches des Très Basses Températures (CRTBT) in Grenoble (France) (Benoit *et al.* 1994). It uses a new dilution principle based on friction that does not need gravity to operate. Its cooling power depends on the gas flow, which is very low and thus allows sufficient gas storage to achieve long mission life. For a total ($^3$He and $^4$He) flow rate of 12 $\mu$mole/s, a cooling power of 100 nW at 0.1 K has been demonstrated. In the same process, the mixture is expanded in a Joule-Thomson valve, producing a cooling power of several hundreds of $\mu$W at 1.6 K. This is enough to insure a proper insulation of the 0.1 K stage from the radiative and conductive thermal loads coming from the 4 K stage. The principle of this cryogenic architecture and its $\pm1$ g operation have been successfully proven with a demonstration model, and qualification of this system for space operation is in progress. Astronomical observations have been performed with bolometers cooled at 85 mK with this system at the focus of the 30 m IRAM telescope.

Bolometric detectors of the type to be used in the HFI are known to be sensitive to microphonic noise induced by mechanical vibrations. Since the instrument will operate in conjunction with mechanical coolers, it is important to verify that the cooler vibration does not cause degradation of
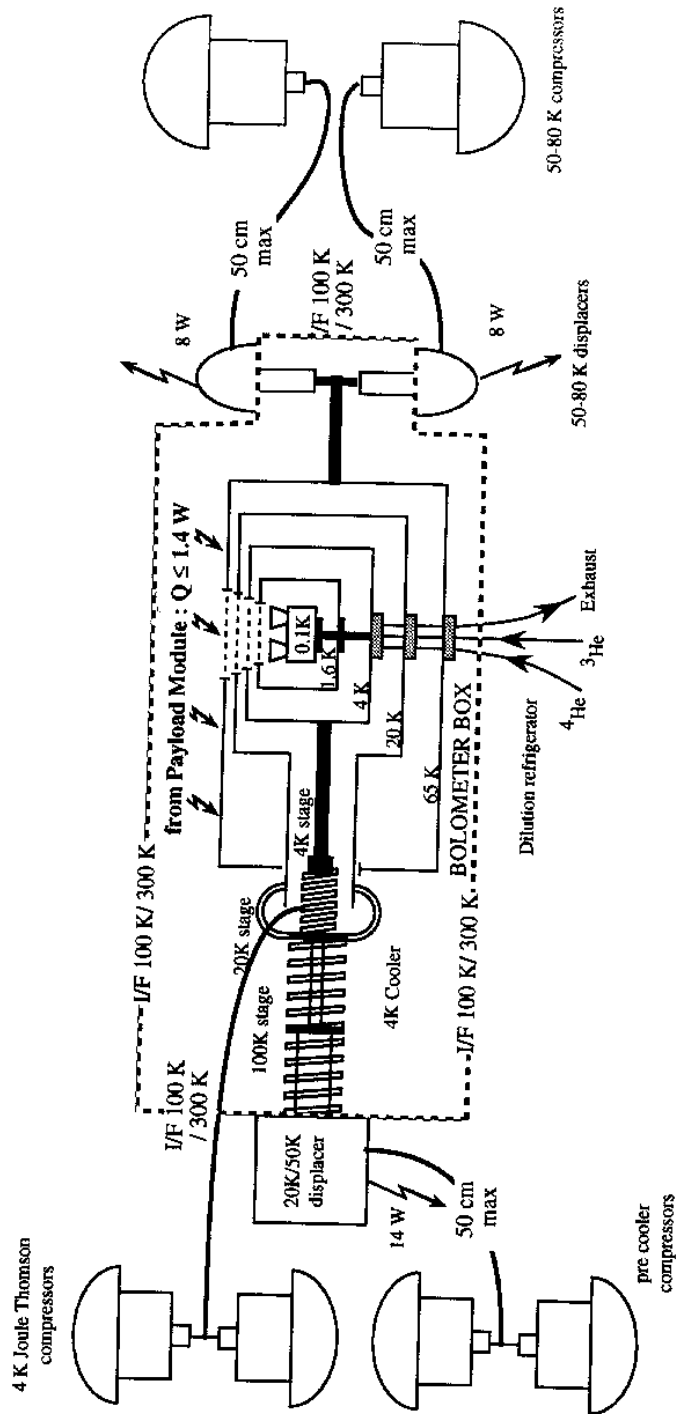
Figure 3.6: (a) The thermal layout of the mechanical cryocoolers and their links to the HFI "cold box".
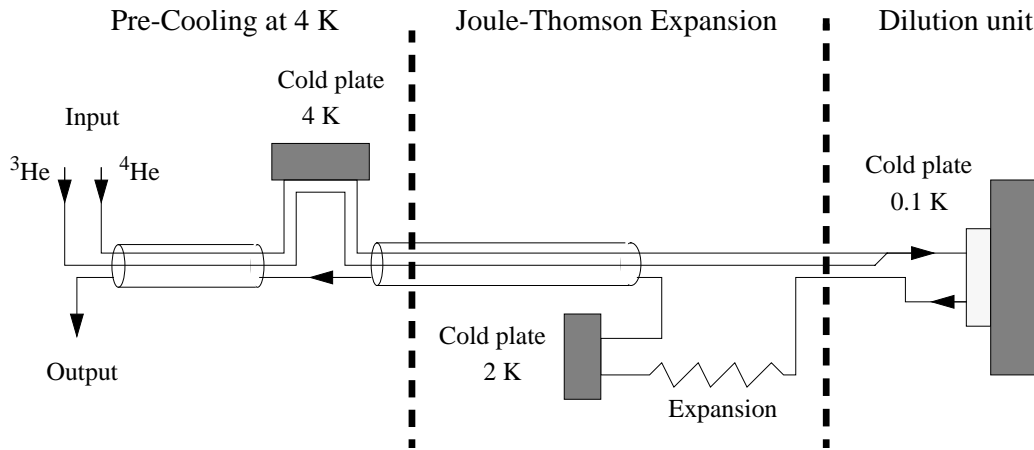
Figure 3.6: (b) The principle of operation of the cryogenic dilution system.

the performance of the detectors. As initial measures, the coolers and displacers will be mounted back-to-back (in the case of the 50-80 K cooler resulting in the addition of one completely redundant cooler), and driven with electronic circuits especially designed to minimize vibrations. Secondly, the mechanical design of the platforms which support the coolers can be optimized to an extent where the transfer of vibrations from the platforms to the focal plane is suppressed to levels of order 10 times lower than what is normally considered acceptable. If any transmission of vibrations exists, it will occur through the thermal link rather than the structure. However, thermal links can also be designed to adequately suppress microphonic transmission, as demonstrated for FIRST.

In any case, an experimental programme is underway to investigate the microphonic effects and to develop methods for minimizing them at the bolometer level. The results of this continuing programme will be used to determine whether a releasable clamping/damping mechanism is required to ensure minimal mechanical coupling between the coolers and the HFI in flight. Initial results have been very encouraging, and demonstrate that the problem of detector microphonics can be contained at a level where it does not affect the performance of the HFI significantly. It is worth noting here that the mechanical excitation by the coolers -if at all present- occurs at frequencies higher than 35 Hz, which would only contaminate the measurement of spherical harmonics higher than $\ell \simeq 2000$.

## 3.6 Payload System Engineering

As will be shown in more detail in Section 3.7.3, the optimal payload configuration has the telescope line-of-sight oriented at an angle of 70° with respect to the axis of symmetry of the spacecraft. Figures 3.7a and b show how the elements of the payload (telescope, baffling, LFI, HFI) are brought together into this configuration (see also Chapter 5).

The mass and power budgets of the COBRAS/SAMBA model payload are summarized in Table 3.4. The design of the payload and service modules (PLM/SVM) has been shown by simulation to comply with all mechanical and thermal requirements at the baseline orbit around the L2 Lagrangian point of the Earth-Sun system, and fits into the relevant launcher constraints. In the following sections, we discuss system engineering issues which are of importance in determining the final performance of the payload.

### 3.6.1 Thermal and Mechanical Interfaces

Thermal aspects are among the main drivers of the design of the Payload Module (PLM), most significantly the requirement to radiatively cool the focal plane to a temperature near 100 K. This requirement leads to the existence of two thermal environments on the PLM, one at ∼100 K (the
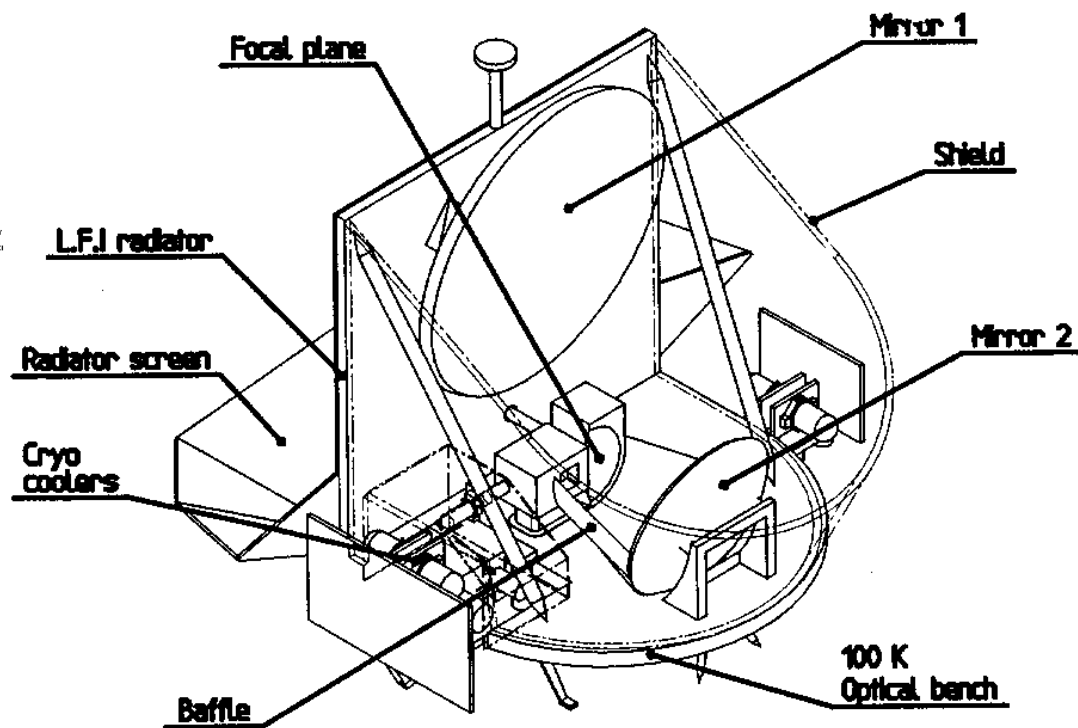
Figure 3.7: (a) A three-dimensional view of the fully assembled payload module.

Table 3.4: Payload Mass & Power Breakdown

| Item | | Mass (kg) | Power (W) |
|---|---|---|---|
| Telescope | | 28 | |
| Structure | | 42 | |
| Shield & Baffle | | 48 | |
| LFI | RAB | 14 | 10 |
| | REBA | 16 | 45 |
| | Total | 30 | 55 |
| HFI | BOB | 6 | 0.03 |
| | PRE | 8 | 20 |
| | CCS | 75 | 305 |
| | CDS | 30.5 | 3 |
| | BEBA | 7 | 30 |
| | Total | 126.5 | 358 |
| Harness | | 10 | |
| Thermal Control | | 40 | |
| Total | | 304.5 kg | 413 W |

SHIELD

OPTICAL BENCH
SUPPORTING DETECTORS
AND TELESCOPE

100 K

SVM UPPER FLOOR
ACCOMMODATING
DILUTION SYSTEM
CRYOCOOLERS
PREAMPLIFIERS

P.L.M. ELECTRONICS
ACCOMMODATED IN S.V.M.

S.V.M.
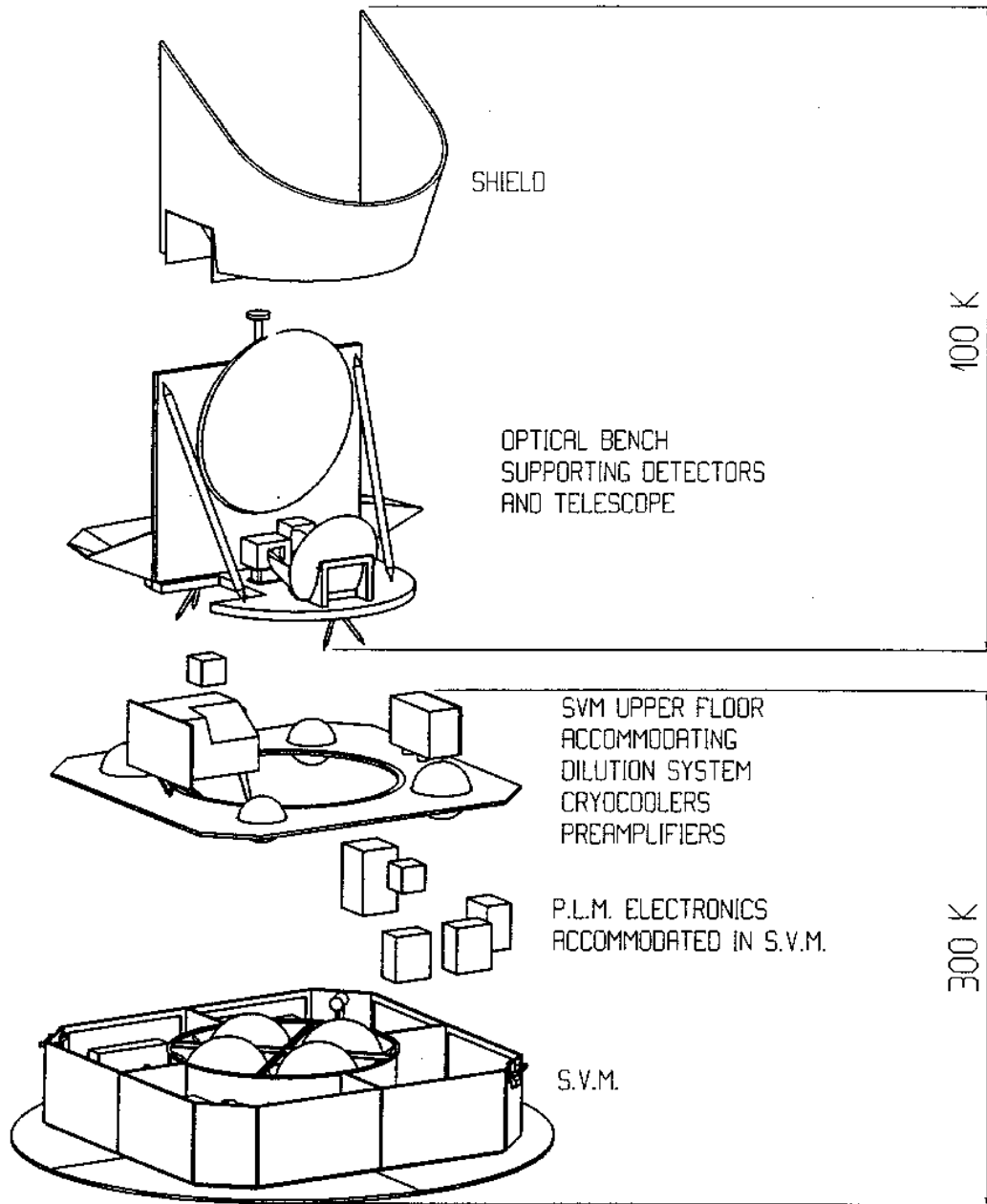
300 K

Figure 3.7: (b) A three-dimensional exploded view of the payload module.

telescope enclosure), and one at ~300 K (which holds the cooling systems and the payload electronics). This particularity is most conveniently accommodated by thermally decoupling the two environments. The PLM thus includes two "platforms" linked by a low thermal conductance interface structure (see Fig. 3.7b). The 100 K platform is in fact the optical bench on which the LFI and HFI are supported, and forms the baseplate of the telescope enclosure. The radiation shield and a vertical radiator constitute the remaining walls of the 100 K enclosure. The radiator evacuates to deep space the heat dissipated in the enclosure by the LFI, and also serves to support the main mirror. The 300 K platform supports the active cooling system (divided into two groups to improve the overall mass balance) and constitutes the interface to the Service Module (SVM, Ch. 5), which holds all the instrument electronic units. The SVM walls which house the instrument electronics can be directly attached to the PLM, which then becomes a completely independent unit for assembly and testing purposes.
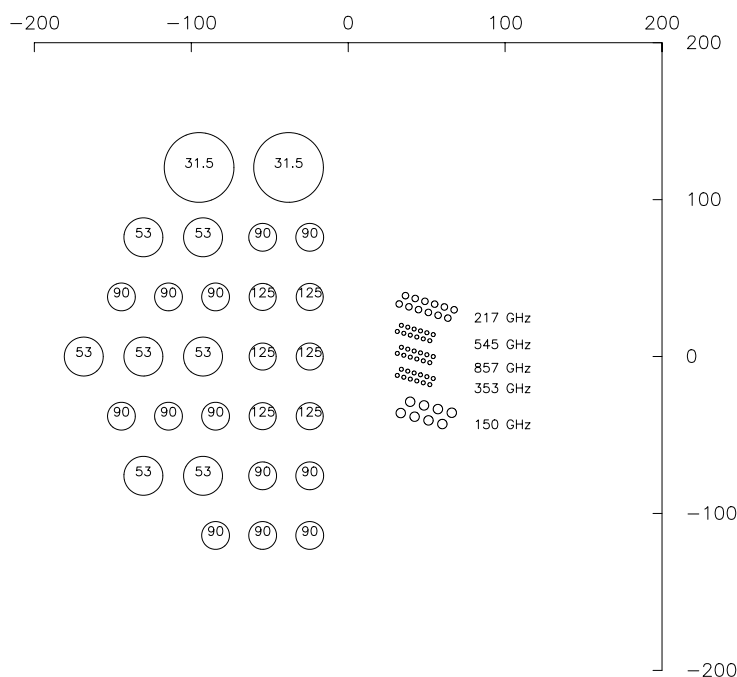
Figure 3.8: A top view of the layout of detectors in the focal plane, reflecting also the location (but not the relative separation) of the arrays of beams on the sky. Each circle corresponds to one feed aperture. Note that each LFI horn feeds two detectors. The axes are in millimetres relative to the optical focus.

### 3.6.2   Optical Quality

The optical quality of the system is affected not only by the telescope and the off-axis location of the detectors in the focal plane (See Fig. 3.8), but also by other sources of degradation such as alignment errors, cool-down distortions, etc. The impact of these sources on the WFE along the optical axis of the system, and on the depointing of the nominal line-of-sight has been evaluated numerically using the Nastran software, which incorporates the thermoelastic properties of the reflectors and payload elements. The results of this evaluation are summarized in Table 3.5, which shows only the displacements remaining after rigid body motions and telescope pure expansion effects have been removed (since these do not affect the image quality). This conservative calculation indicates that the on-axis system WFE is better than the goal of 60 $\mu$m (Section 3.3); since the assumed mirror manufacturing errors (which dominate the overall budget) are larger than what can in practice be achieved, it is expected that the final WFE will be well within the goal. It is also worth noting that

Table 3.5: On-axis Wavefront Error and Pointing Budget

| | WFE ($\mu$m rms) | LOS depointing (mrad) | |
|---|---|---|---|
| | | Scan angle | Spin Phase angle |
| Reflector Manufacturing Errors | | | |
| Main reflector surface accuracy (10 $\mu$m rms) | 20 | 0 | 0 |
| Subreflector surface accuracy (10 $\mu$m rms) | 20 | 0 | 0 |
| Alignment Errors | | | |
| Adjustment accuracy of 0.2 mm * | 30 | 0.4 | 0.4 |
| Adjustment accuracy of 1 arcminute * | 25 | 0.6 | 0.6 |
| Launch and In-orbit Distortions | | | |
| Launch effects | 5 | 0.1 | 0.1 |
| Gravity release [†] | 10 | 0.15 | 0.01 |
| Moisture release [‡] | 1.5 | 0.035 | 0 |
| Cooling down (300 K $\rightarrow$ 100 K) | 21 | 0.03 | 0.02 |
| Temperature gradients * | 0.5 | 0.015 | 0.003 |
| Thermal fluctuations in orbit | 0 | 0 | 0 |
| Long term aging | 5 | 0.1 | 0.1 |
| **Total** | **54** | **0.8** | **0.8** |

[*] Includes reflectors and instruments

[†] Assumes on-ground compensation during tests

[‡] Assumes CME=$10^{-4}$, 30% desorption

[*] Assumes 5 K/m on mirrors

the total expected depointing is low, and permits that on-ground alignment activities between the reflectors and detector boxes be carried out via mechanical means only. Finally, the WFE errors due to cool-down of the telescope to cryogenic temperatures do not dominate the overall budget, so that the optical quality of the telescope need only be verified at ambient temperature, thus simplifying considerably the testing activities.

While Table 3.5 considers only wavefront errors along the optical axis, it is clear that off-axis aberrations decrease the optical quality for pixels located near the edges of the focal plane. The layout of the detectors (see figure 3.8) has been designed with this in mind. Detailed analysis of the optical quality at all detector locations and frequencies has shown that the present design is acceptable in terms of the mapping goals of the mission. For example, for the worst pixel at $\lambda$850 $\mu$m, intrinsic aberrations due to off-axis effects contribute a WFE of $\sim$40 $\mu$m. Adding all other sources of WFE (see Table 3.5) lead to a total value for this pixel of $\sim$63 $\mu$m, just at the limit of what is deemed acceptable.

### 3.6.3   Data Management

The instrument electronic units independently interface the LFI and HFI to the spacecraft. The science data is packetized and transferred by the electronics to the spacecraft computer, which stores the data into a solid state recorder (SSR). All the data in the SSR will be downlinked to the ground during visibility windows. The instrument real-time data acquisition rates are summarized in Table 3.6, and add up to a total of $\sim$194 kbit/s, dominated by the higher frequency channels. To this must be added an allowance for instrument housekeeping data, estimated at a total of 0.4 kbit/s.

The amount of data which can actually be downlinked is strongly limited by the TM/TC link budget to an equivalent acquisition rate of $\sim$30 kbit/s (averaged over 24 hrs). Thus, the real–time data rate must be reduced by a factor of $\sim$6.9. This goal is achievable using a two-step strategy,

Table 3.6: Real–time Science Data Acquisition Rates

| Inst. | Band (GHz) | No. Det. | Beam (arcmin) | Rate/Det. (wrd/s) | Rate/Band (kbit/s) | Rate/Inst. (kbit/s) |
|-------|------------|----------|---------------|-------------------|--------------------|--------------------|
| LFI   | 31.5       | 4        | 30            | 27.5              | 1.8                |                    |
|       | 53         | 14       | 18            | 45.8              | 10.3               |                    |
|       | 90         | 26       | 12            | 68.7              | 28.6               |                    |
|       | 125        | 12       | 12            | 68.7              | 28.6               | 69.3               |
| HFI   | 150        | 8        | 10.5          | 78.5              | 10.1               |                    |
|       | 217        | 12       | 7.5           | 110               | 21.1               |                    |
|       | 353        | 12       | 4.5           | 183.3             | 35.2               |                    |
|       | 545        | 12       | 4.5           | 183.3             | 35.2               |                    |
|       | 857        | 12       | 4.5           | 183.3             | 35.2               | 136.7              |

the first part of which will be the use of a classical noiseless data compression algorithm (likely to be a variant of Differential Pulse Code Modulation, which in its simplest implementation consists of downlinking sample-to-sample differences rather than absolute values). Simulations indicate that this first step will achieve a compression factor of $\sim$4. The signal resulting from this initial stage will be dominated by noise and can thus no longer be compressed in a lossless fashion. The remaining factor of $\sim$1.7 in compression can be achieved with either one of two strategies, lossy (transform) compression of large sets of data, or the averaging of data acquired on successive spin revolutions (to achieve a reduction in the amount of data of a factor of 1.6, only 2 successive circles need be averaged). The implementation of the latter requires the on-board availability of continuous pointing information, which can be achieved in practice by synchronizing the data acquisition to the signal emitted by the star mapper when it crosses the brightest star in its field of view (i.e. once every spin period). Although averaging successive circles is a straightforward possibility, it has two undesirable side effects: (1) random events (such as cosmic-ray hits) will lead to the rejection of a larger fraction of data; and (2) the ability to detect spin-synchronized systematic effects will be reduced. For this reason, the option of using lossy compression is also being investigated, via analysis of realistic, simulated data streams.

### 3.6.4    Assembly, Test and Verification

The COBRAS/SAMBA payload is very sophisticated and adequate facilities must be planned in advance for the Assembly, Integration and Verification (AIV) phases. The configuration of the telescope and instruments is such that testing of the payload under operating conditions will be very difficult to achieve. The philosophy will be to test and measure the performance of individual units separately as fully as possible; subsequently the emphasis will be on *verification* rather than *measurement* of performance. For this purpose, the instruments will be outfitted with special circuitry to provide a "detector life" test, which can be carried out to monitor instrument health throughout AIV.

The stringent nature of the straylight rejection requirements (see Section 3.7.2) implies that special attention must be given to verifying that the radiation patterns meet the sidelobe level design goals. It is presently not possible to measure radiation patterns with the dynamic range required by the specified sidelobe levels or over the large frequency range of COBRAS/SAMBA . However, it is foreseen that prior to integration into the PLM, qualification models of the telescope and LFI will be brought together to measure radiation patterns down to the $\sim$50 dB level. The aim of this test will be to verify the mathematical model(s) used to predict the optical properties of the system. The patterns will be measured in-flight to the required dynamic range using celestial sources (see Sections 2.5.3 and 4.5.1).

The telescope itself requires special handling to avoid damage and contamination by dust particles. The philosophy in this area will be to use covers over all sensitive optical surfaces during AIV, and minimize to the utmost the time periods for which ultra-clean (i.e. Class 100) environments are required. The availability of a cleaning procedure for the mirror surfaces will ensure that contamination does not jeopardize the project schedules. The vast majority of AIV activities will be carried out in normal satellite assembly halls.

The telescope mirrors will be aligned on the PLM using light at NIR wavelengths (e.g. using the Shack-Hartman technique). The alignment of the focal plane instruments will subsequently be carried out using mechanical and/or optical means (i.e. utilizing pre-planned mechanical references and integral engraved and/or reflective patterns).

Because of their cryogenic nature, the HFI detectors cannot normally be operated after integration into the PLM. However, during thermal-vacuum tests, the PLM will be in a chamber such that the focal plane temperature will be close to nominal operating conditions, and the telescope will view a cooled wall at a low temperature. End-to-end verification tests on the HFI and LFI will be carried out at this time.

During transport to the launch site, and integration into the launcher, the outermost radiation shield will be outfitted with a cover to protect the focal plane and telescope against damage and contamination by dust, water, etc. The cover will only be removed at the latest possible stage.

## 3.7   Payload Requirements

To achieve the scientific objectives outlined in Ch. 1, the model payload sets a number of requirements on the mission, which in turn determine an appropriate observing strategy (Section 4.4):

1. The **sky coverage** must be very large, and a goal of observing at least 90% of the sky has been set (see Ch. 1).

2. The **pointing accuracy** must be compatible with the angular resolution of the final CMB anisotropy maps ($\sim 10'$). The spacecraft sensors must allow a-posteriori recovery of each individual observation with a $2\sigma$ uncertainty of $2'.5$.

3. The **observing pattern** must be periodically repetitive, to enable adequate control of systematic instrumental effects such as gain drifts. The periodicity replaces the more traditional sky-chopping used in ground-based observing. The shortest time-scale for periodicity should be of order one minute, which results as a compromise between drift rates in the LFI (which favor shorter time-scales) and response times in the HFI (which favor longer time-scales). Periodicity at longer time-scales (month, year) is also desirable to remove systematic effects.

4. **Systematic effects** must be maintained at a level such that they do not limit the sensitivity of the observations. The main sources of deleterious signals are: straylight, thermal variations, and interference due to the TM/TC system.

The requirements for large and periodic sky coverage indicate a solution in which the telescope line of sight sweeps large areas of the sky repetitively with a period of $\sim 1$ minute. This situation is most naturally arrived at with a spinning spacecraft where the telescope line-of-sight is offset from the spin axis by an angle (the so-called "scan angle", see Fig. 3.1 and Fig. 3.11), and thereby describes a circle on the sky. A spinning period of 1 r.p.m. fulfills the one minute periodicity requirement.

The control of straylight and thermal variations imposes severe constraints on the payload. Variations can be either random or systematic (e.g. synchronized with the observing pattern); the latter are the most severe since their effect does not average out by integration.

Table 3.7: Thermal Stability Requirements for Systematic Signals

| Element | Component | Required | Goal | Comment |
|---------|-----------|----------|------|---------|
| FPA | LFI Receivers | <0.1 mK | <0.05 mK | Set by LFI Ref. Loads |
| | LFI horns | <5 mK | | |
| | HFI 4K Filters | <0.1 mK | | |
| Reflectors & Shield | | <0.2 mK | <0.05 mK | Set by HFI |

### 3.7.1   Thermal Stability

Simulation of the instrumental sensitivity to temperature fluctuations of critical components results in the stability requirements listed in Table 3.7.

The main source of systematic temperature variations within the payload enclosure is spin-synchronized modulation of solar illumination on the spacecraft. The optimal situation is encountered when the payload is permanently maintained in solar shadow, and the spin axis points toward the Sun. This condition can be met if the payload is pointed in the anti-Sun direction and thus protected from direct solar illumination by the rest of the spacecraft, and in addition, if the motion of the spin axis is restricted to comply with the shadow condition. From the latter, it follows that to obtain the required sky coverage the scan angle must be large (e.g. 90° corresponds to tracing meridian circles on the sky, and achieving full sky coverage). Secondary sources of thermal modulation of the focal plane are caused by passages of the Earth and Moon through the field of view. These must be reduced by the choice of orbit.

### 3.7.2   Straylight Rejection

One of the most significant issues in the payload design is to achieve adequate rejection of unwanted radiation, which include local (satellite) sources and Solar System sources. The requirements in this area are met not only by appropriate optical design, but also by specifying the allowed orientation of the spacecraft with respect to the major sources of straylight.

The rejection required of the brightest source, the Sun, is 93 dB at the most critical frequency (31.5 GHz). For the next brightest sources, Earth, Moon and Jupiter, the rejection requirements are 79 dB, 67 dB and 43 dB, respectively (assuming a sensitivity of order $\Delta T/T \sim 10^{-6}$). Due to the orientation possibilities of the spin axis (see Sections 3.7.3 and 4.4), these requirements mean that the radiation suppression should be better than $\sim$-93 dB for $\theta > 165°$ and better than $\sim$-67 dB for $\theta > 150°$ ($\theta$ being the angle from the spin axis). The required rejection is best achieved if the enclosure is continuously pointed diametrically away from the Sun. This orientation of the spin axis towards deep space is also the most favorable to achieve passive cooling of the enclosure, and the required temperature stability (see Section 3.7.1).

Detailed electromagnetic simulations of the optical enclosure, which take into account the angular response of individual detectors have been performed at 31.5 GHz (see Figure 3.9). This is considered the most critical channel both because diffraction contributions decrease with frequency, and because it is the channel at which the telescope is the least under-illuminated. The simulations show that in the worst case 98% of the power will propagate from the feed to the subreflector and further on to the main reflector, where it is reflected again into the antenna boresight direction. The remaining 2% of the power is scattered in a complicated way into the half space region defined by the top rim of the shield. This half space corresponds to the region between -60° and 120° on Fig. 3.9b.

Careful analysis, which includes the presence of the baffle and shield, has quantified the effect of radiation which does not impinge on the main mirror. Two per cent of the power scattered evenly into a half space corresponds to an average level which is $\sim$-64 dB below the peak gain, as indicated by the horizontal line in Fig. 3.9b. Representative rays not hitting the main reflector are sketched

on Fig. 3.9a and their direct contributions to the radiation pattern are shown in Fig.3.9b. From the latter we conclude that the rejection requirements for the Sun, Earth and the Moon can be met with the current design of the optical enclosure. The requirement for Jupiter will be met when Jupiter is located at angles larger than ∼5° from the boresight.

It is important to realize that it is the stray signal *variations* which must be removed from the data rather than its absolute value. Most of the time, the change in stray signal will have a much lower amplitude than its absolute value, so that our requirements are actually extremely conservative. In addition it will be modulated by the 1 rpm spinning rate, which may help to identify and remove this component. Furthermore, every sky pixel will be observed at different times during the mission with different relative payload orientations; this fact can also be used to identify the stray signals. Lastly, it has been demonstrated (Section 2.5.2) that it will be possible during the commissioning and operational phases to measure the beam patterns to great accuracy using the observations themselves. Altogether, by combining an appropriate optical design and observing strategy, it will be possible to cope with the straylight problem adequately.
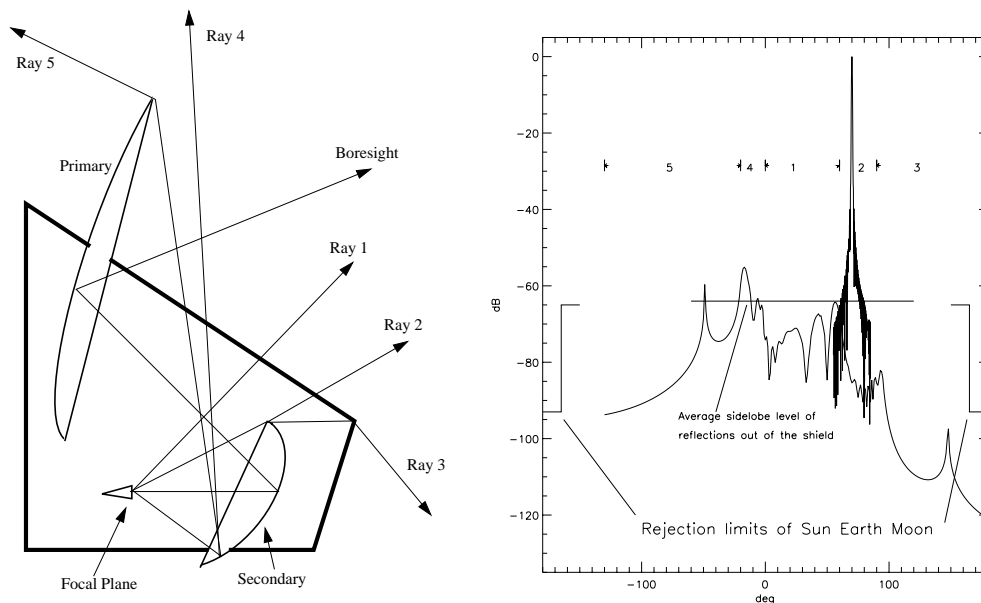


Figure 3.9: (a) Drawing of the telescope and shield, showing representative rays not impinging on the main reflector. (b) Radiation patterns showing the main reflector field at 30 GHz (heavier line centered at 70° ), as well as the direct contribution from the rays identified on (a) (simulations provided by TICRA). The spin axis is at zero degrees. The labels show the region corresponding to each type of ray sketched in panel (a). Ray 5 is followed to -130° , beyond which the radiation is shadowed by the left edge of the shield. The average level of the unpredictable field not hitting the main reflector (-60 to 120° ) is shown. The rejection requirements for the Sun, Earth and Moon are also indicated.

### 3.7.3   Choice of Scan Angle and Orbit

A compromise between achieving large sky coverage, maintaining thermal stability, and rejecting solar straylight, results in a scan angle of 70° . The geometry of the spacecraft (constrained by the launcher fairing) is such that the payload will remain in the shadow of the Sun for spin-axis to Sun-vector angles of up to 15° . Thus, ecliptic latitudes as large as ±85 degrees will be available for observation, or more than 99% of the whole sky.

The basic anti-Sun pointing strategy reduces the effects of solar radiation to a minimum; however, the Earth and Moon can also be intense sources of both straylight and thermal modulation, and
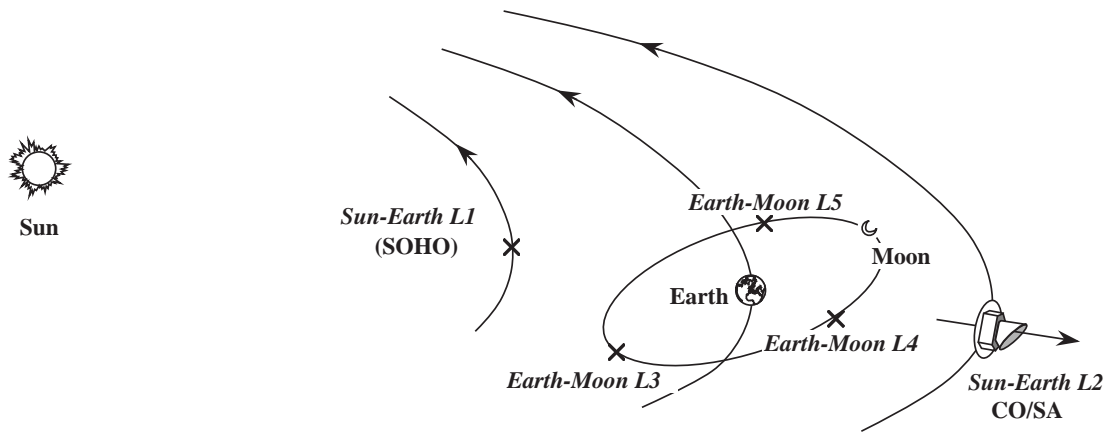
Figure 3.10: Far-Earth orbit options for COBRAS/SAMBA . The L4 and L5 Lagrangian points of the Earth-Moon system are located at ~400000 km from the Earth, while the L2 point of the Earth-Sun system is at a distance of ~$1.5 \times 10^6$ km. The baseline is a Lissajous orbit around the L2 Lagrangian point of the Earth-Sun system.

reducing their effects drives the choice of orbit. Near Earth orbits are eliminated mainly because the large thermal influx renders it extremely difficult to reach temperatures near 100 K in the focal plane, or to achieve the required thermal stability. The nearest far-Earth orbit possible is that around one of the Lagrangian points of the Earth-Moon system (L4 or L5, see Figure 3.10); this orbit (which shares the Lunar motion around the Earth) suffers from the fact that the Earth or the Moon are often not very far from the telescope line-of-sight. Simulations indicate that if this orbit were chosen, at least 35% of the acquired data would have to be discarded due to poor thermal or straylight conditions, leading not only to lower sky coverage but also to a less efficient removal of systematic effects. The optimal choice of orbit, resulting from a tradeoff of the various payload requirements, several spacecraft technical constraints (most importantly related to telecommunications to ground), and the transfer-to-orbit cost, is a Lissajous orbit around the L2 Lagrangian point of the Earth-Sun system. At this location (see Figure 3.10), the Sun, the Earth, and the Moon are all located behind the payload, where their undesirable effects are at the lowest possible level, both in terms of location and of flux. In addition, this is the only orbit in which the antennas which provide telemetry and telecommand (TM/TC) for the spacecraft are also continually pointed away from the payload, thereby minimizing the potential effects of RF interference. The main elements of the baseline L2 orbit (described in more detail in Ch. 5) are shown schematically in Figure 3.11.
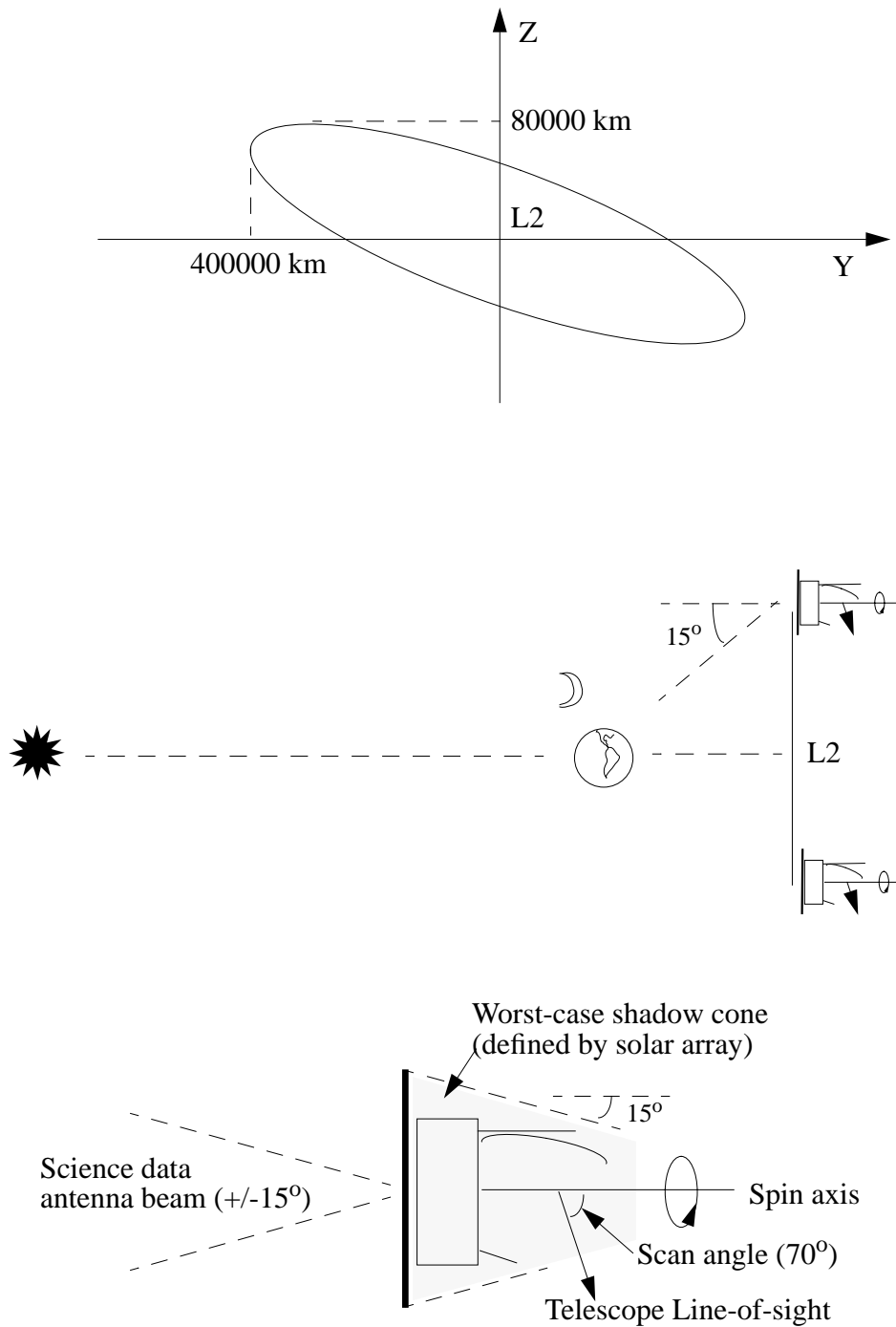
Figure 3.11: The baseline orbit chosen for COBRAS/SAMBA is a Lissajous orbit around the L2 point of the Earth-Sun system. A typical projection of the orbit on the plane perpendicular to the ecliptic and to the Earth-L2 vector has a maximum elongation from L2 of ~400000 km along the ecliptic plane (axis Y); the period of revolution is ~6 months. A projection from the ecliptic pole is also sketched, showing the occurrence of the maximum value of the spin-axis to Earth-vector angle (15$^o$). Finally, a sketch of the spacecraft outlines the main constraints related to payload shadowing and telecommunications.

# Chapter 4

# The Mission

## 4.1 Launch

COBRAS/SAMBA is designed to fit into the lowest cost launch scenario available in the year 2003 for ESA space science missions, i.e.:

- it will be one of two (or three, if this option is available) passengers on an Ariane 5 vehicle;

- the launch window and target transfer orbit are dictated by the most likely co-passenger(s) - telecommunications satellites in geostationary orbits - rather than by COBRAS/SAMBA itself.

The latter condition implies that:

- the launch is compatible with the standard daily launch window for geostationary spacecraft imposed by Ariane; thus, the launch will take place around midnight (UT) with a minimum daily window of 45 minutes

- it must be possible to launch COBRAS/SAMBA at any time of the year

- the Ariane vehicle will inject COBRAS/SAMBA into the standard Geostationary Transfer Orbit (GTO, see Table 4.1)

- transfer and injection into the final operational orbit will be accomplished using the on-board propulsion system of the spacecraft.

## 4.2 Operational Orbit

The operational orbit for COBRAS/SAMBA has been selected to maximize the scientific return within the technical constraints, and is a Lissajous orbit around the L2 point of the Earth/Sun system. The

Table 4.1: Ariane 5 Standard Geostationary Orbit

| Orbit Parameter | Injection Orbit (GTO) |
|---|---|
| Perigee height (km) | 620 |
| Apogee height (km) | 35883 |
| Inclination | 7° |
| Argument of perigee | 178° |
| Period (hr) | 10.5 |

L2 libration point (also known as the L2 Lagrangian point) is a point collinear with the Sun and the Earth-Moon barycentre, at a distance of about 1.5 million km from the Earth, and in opposite direction to the Sun in relation to the Earth (see Figure 3.9). This orbit offers the best possibilities to satisfy the stringent requirements imposed by the scientific instruments on stray light suppression, and on low and stable heat input to achieve the required low temperature in the focal plane assembly (see Section 3.7.3). In addition, the sky coverage of the telescope is maximized without disturbances by the Earth, Moon or Sun.

## 4.3  Mission Analysis

### 4.3.1  Operational Orbit

In the Lissajous orbit COBRAS/SAMBA will move around the L2 point with a period of about 180 days. The amplitudes of the motion have been selected as $A_y$= 400000 km (in the ecliptic plane and normal to the Earth-Sun direction) and $A_z$=100000 km (normal to the ecliptic plane). The $A_y$ amplitude is dictated by the fixed mounted medium gain antenna performances used for communications. The $A_z$ amplitude is selected to optimize the visibility conditions from a ground station.

Figure 4.1 shows the evolution of the orbit around L2 for a period of 5 years. The x-axis is in the direction Earth-Moon barycentre toward the Sun, and the z-axis is pointing to the north ecliptic pole.
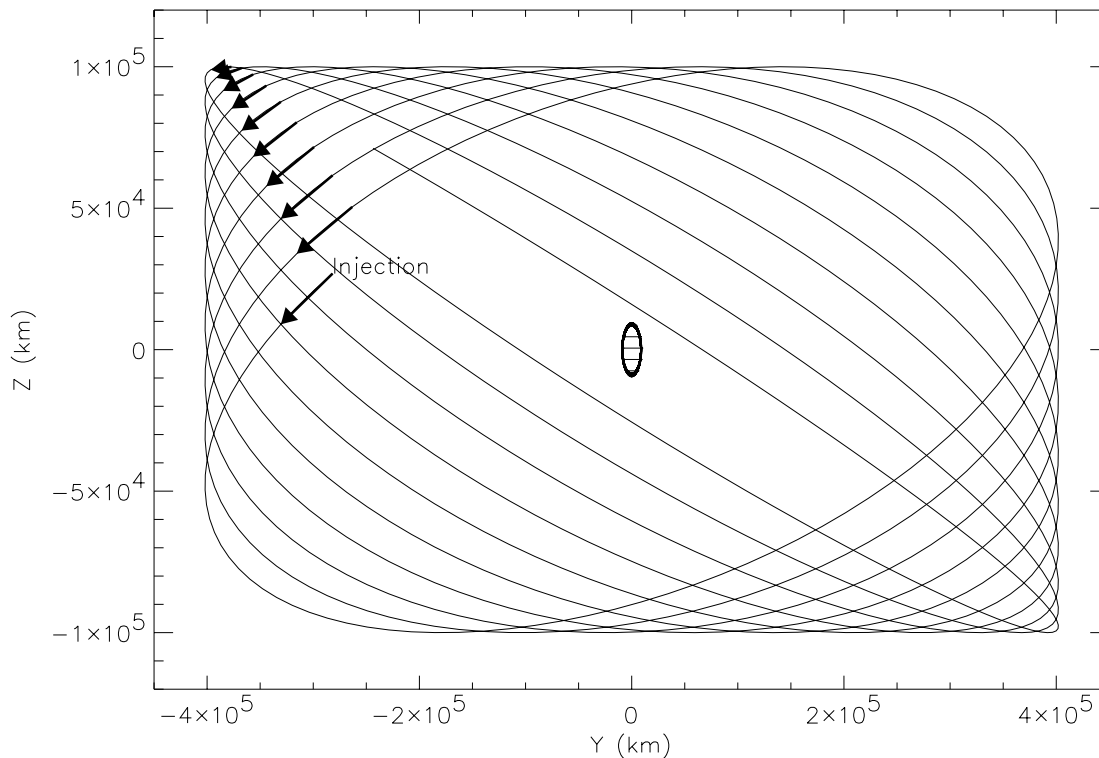


Figure 4.1: 5 years of Lissajous orbit around L2. The axes are in the plane perpendicular to the ecliptic. Arrows are plotted at six-month intervals. The hatched ellipse in the center indicates the zone of penumbra of the Earth: for at least 5 years eclipses can be avoided.

### 4.3.2   Transfer Orbit

The transfer from the GTO to the Lissajous orbit requires execution of apogee raising manoeuvers to bring the apogee to about 1 million km. Because of the finite thrust available (400 N), in order to reduce the gravity losses below 3 %, apogee raising to the final altitude requires 3 separate manoeuvers at perigee. These manoeuvers must furthermore be executed at solar aspect angles greater than 120 degrees, to prevent direct solar illumination of the payload enclosure. The first two manoeuvers of about 250 m/s each raise the apogee to about 58000 km, and 115000 km, respectively. The third perigee manoeuver requires between 250 m/s and 270 m/s and brings the apogee to about 1 million km from the Earth. The perturbation of the Sun raises the perigee of the orbit and near the fourth or fifth apogee an inclination change manoeuver is performed. The manoeuver $\Delta V$ ranges from 57 m/s, for launch in February, to 211 m/s for launch in April. In most cases this manoeuver is performed either 30 or 90 days after launch. The final injection into the operational orbit occurs about 170-184 days after launch and the manoeuver requirement ranges from 56 m/s, for launch in November, to 220 m/s for launch in July. The total $\Delta V$ needed for the transfer from GTO to the Lissajous orbit varies as a function of launch date between a minimum of ~970 m/s (March, November) and a maximum of ~1060 m/s (January, July). Figure 4.2 shows the projection onto the ecliptic plane of the transfer trajectory for launch on March 3, 2003, whereas Table 4.2 presents the sequence of events for a non-optimal trajectory with launch on July 1, 2003.
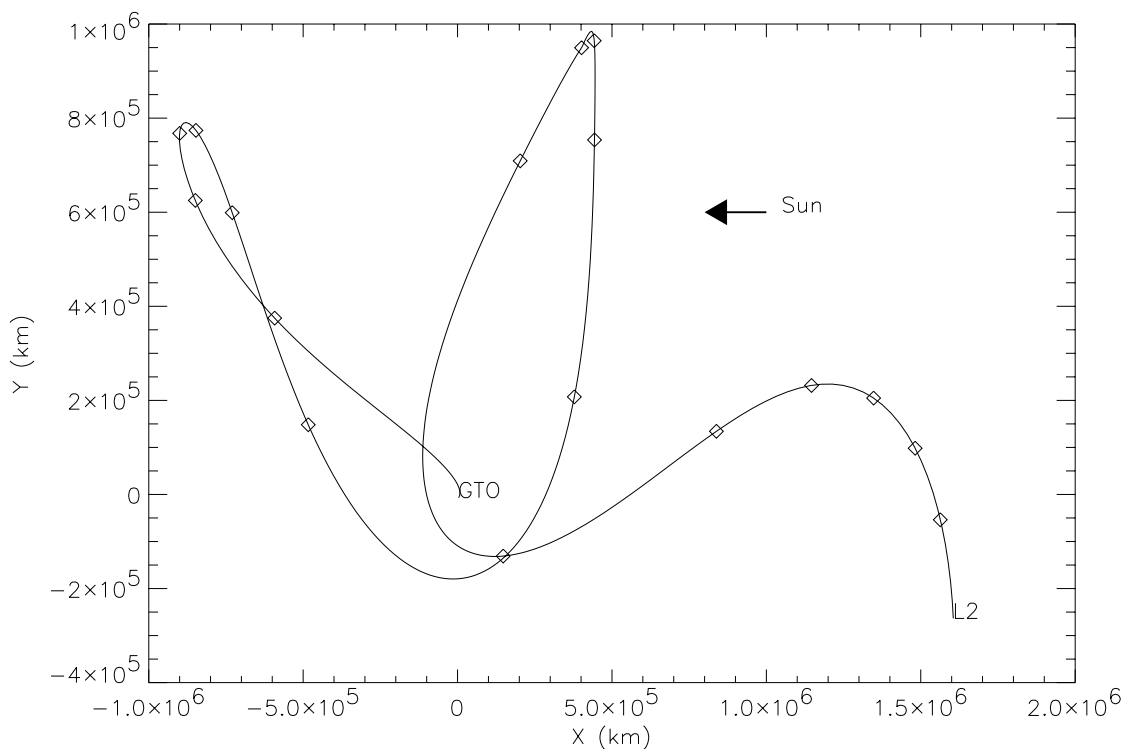


Figure 4.2: Best case transfer trajectory from GTO to L2 Lissajous orbit (projection onto ecliptic plane, launch on 3 March 2003). Ticks are marked along the trajectory at 10 day intervals, starting at launch. Orbital motion within GTO is not shown in this plot. In most cases, the inclination change manoeuver occurs about 30 days after launch, and the final injection manoeuver about 6 months after launch.

The performance of the motor for the apogee raising manoeuver can be calibrated so that the required navigation manoeuvers add to about 30 m/s.

Table 4.2: Sequence of events during transfer to L2

| Launch date: 2003/ 7/ 1 23: 0:30 | | | |
|---|---|---|---|
| | Date (days after launch) | $\Delta V$ (km/s) | Solar Aspect Angle* (degrees) |
| Launch | 0.00 | | |
| First Perigee | 0.44 | 0.250 | 120.0 |
| Second Perigee | 1.22 | 0.250 | 120.0 |
| Third Perigee | 3.17 | 0.256 | 120.0 |
| Inclination Man. | 48.52 | 0.070 | 82.9 |
| Injection Man. | 177.51 | 0.220 | 111.0 |
| Total | | 1.047 | |

\* The angle between the direction to the Sun and the required direction of thrust.

### 4.3.3  Launch Window

The standard launch window of 45 minutes near midnight required by ARIANE 5 in multiple launch configuration leads to an acceptable sequence of manoeuvers and corresponding solar aspect angle for the transfer from GTO to the operational orbit. The Lissajous orbit is not affected by seasonal variations. Thus, in principle, the launch window is open the complete year.

### 4.3.4  Sky Coverage

In operational orbit the spacecraft orientation must be such that the Sun direction is always within a cone centred around the -X-axis with a semi-angle of 15° . The line of sight of the telescope is at 70° of the +X-axis and because of the spin motion it will describe arcs that will cover 90% of the full sky in about 7.3 months (though note that a larger fraction can be covered by following and appropriate observing strategy).

### 4.3.5  Eclipses

The motion in the Lissajous orbit is such that after at most 7.5 years the spacecraft will enter an eclipse of several days of duration. As the extended lifetime of the COBRAS/SAMBA mission is of 5 years, it is possible to inject into the operational orbit with conditions such that there is no eclipse during the mission duration. If required, it is also possible to skid from one orbit just before entering eclipse to another orbit where eclipses will occur 7 years later. The skid manoeuver requires a $\Delta V$ of about 70 m/s.

### 4.3.6  Ground Station Coverage

The baseline ground station proposed for COBRAS/SAMBA is the station at Kourou in French Guyana, supported by the station at Villafranca in Spain, and Perth in Australia. With a minimum ground station elevation of 5 degrees, and for launch in January 2003, the ground contact time with Kourou is about 11 hours per day without seasonal variations. From Perth the ground contact time varies along the year from 8.5 to 13 hours per day, while for Villafranca the values are 9 to 14 hours.

### 4.3.7  Orbit Maintenance

The Lissajous orbit as any other libration orbit near the L2 point is highly unstable; if the orbit of the spacecraft is not controlled, after a few months it will leave the neighborhood of the L2 point. However, it is possible to perform small manoeuvers at intervals of 20-70 days to correct for residual

errors and maintain the orbit, at a total cost of less than 2-4 m/s year. The technique for orbit maintenance of libration orbits has already been used with ISE-C and it is used with SOHO.

## 4.4   The Observing Plan

The basic observing strategy is based on the antisolar orientation of the spin axis, as outlined at the beginning of this Chapter. To maintain this orientation, the spin axis must be displaced along the ecliptic plane by 1° every day. This is done in individual steps for ease of operations. An appropriate value for the amplitude of each step is 5′, given the layout of the detector arrays, the FWHM of the smallest beam (4.5′), and that it is desired to cover the sky as completely as possible. Thus, the basic plan consists of one 5′ displacement of the spin axis along the ecliptic plane every 2 hours. This basic scheme, together with the circular scanning motion of the telescope line-of-sight, results in a non-uniform distribution of the integration time across the sky. The solid line in Figure 4.3 shows the fractional area of the sky which is covered with a given integration time after one year of observations following this simple scan strategy, while Figure 4.4(a) shows the corresponding distribution on the sky.

The scan angle of 70° implies that one (>90%) sky coverage can be achieved after ∼7.3 months of observations. The need to control systematic effects requires that at least two full sky coverages be achieved. This sets the minimum mission duration as that allowing routine observations of more than ∼15 months, although clearly a longer duration of operations is desirable as it would lead to increased sensitivity, and better control of systematics.
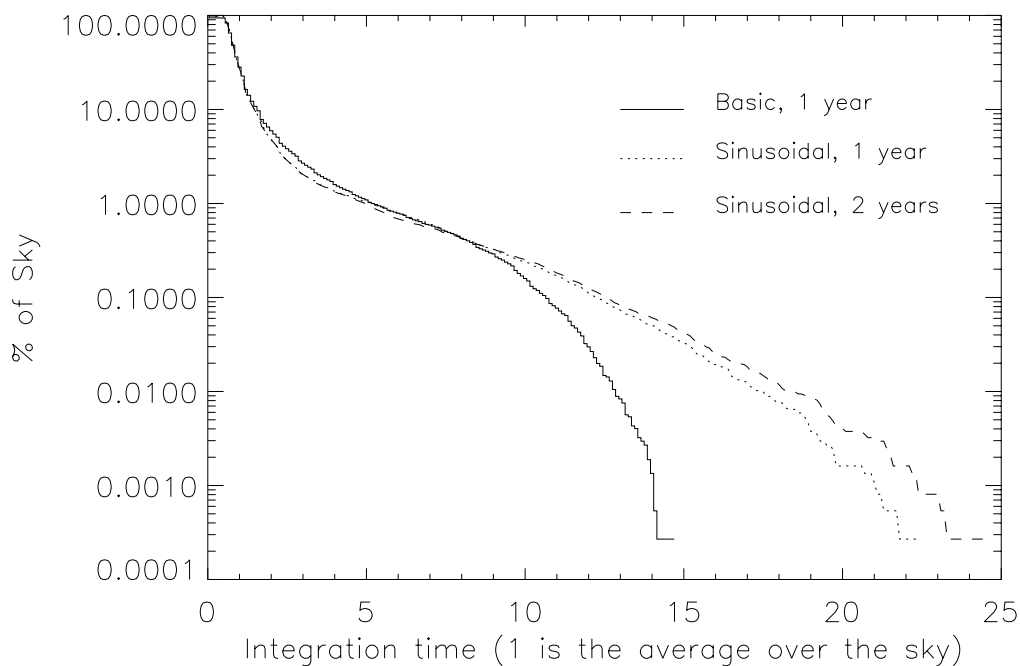


Figure 4.3: Histograms of the percentage of sky area achieving a given integration time, for the three maps of Figure 4.4 (rendered here as solid, dotted, and dashed lines respectively). In each case the integration time is normalized to the average time per pixel over the whole sky (which varies with frequency, see Tables 3.2 and 3.3). Note that the sensitivity varies as the square root of the integration time. In all three cases, the integration time over ∼30% of the sky is larger than the average value. In the simplest strategy (case a), ∼0.2% of the sky is covered with 10 times the average integration time. In the more optimized cases, this value is ∼0.3% (or about 100 square degrees); in addition, a smaller fraction (∼0.03%) is covered with 20 times the average value.

A perturbation to the basic motion along the ecliptic plane will be purposely introduced to optimize
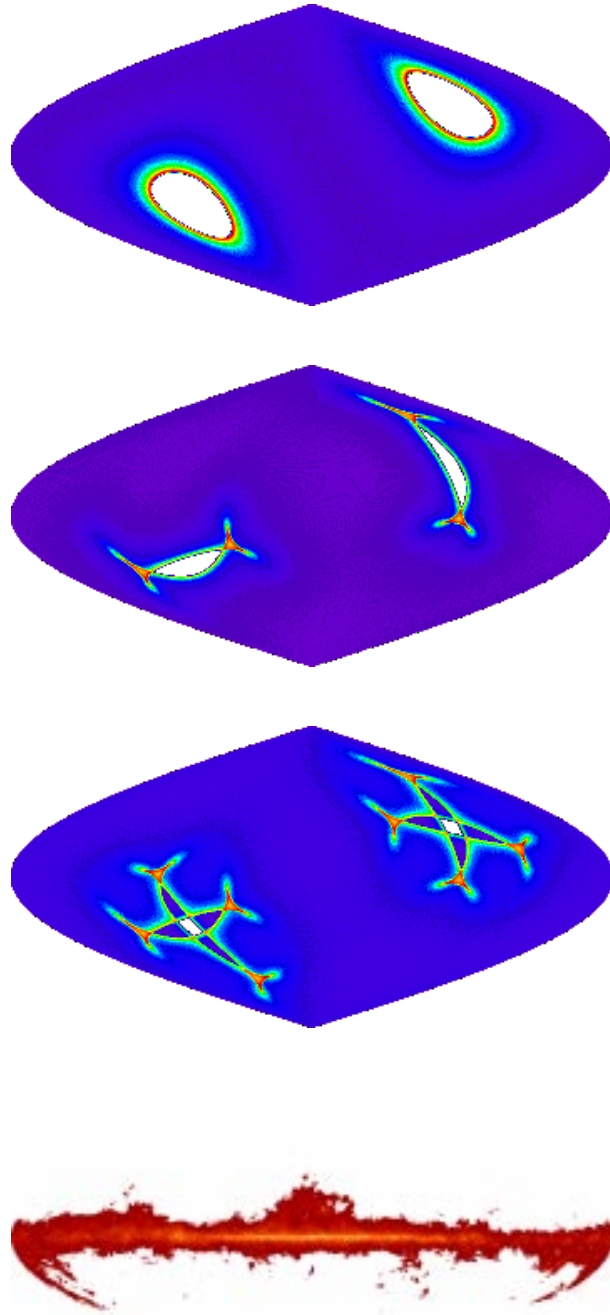
Figure 4.4: From top to bottom: (a) A map of the integration time obtained per pixel after one year of observations following the basic (in-the-ecliptic) scanning pattern outlined in the text. The maps are shown in galactic coordinates (sinusoidal projection). The linear color scale indicates the integration time per pixel relative to the all-sky average (see Fig. 4.3). (b) This map shows the effect of tilting the spin axis perpendicularly out of the ecliptic plane, with an amplitude varying between $\pm 15°$ sinusoidally in time, with a 6 month period. The sine is phased with the orbital motion so that the maximum out of the ecliptic motion occurs when the spacecraft is closest to L2 ($Y = 0$, see Fig. 4.2). This strategy achieves both near-all-sky coverage, and concentration of high integration times into small areas. (c) A possible 2-year strategy consists of combining (b) with its mirror image, i.e. in the second year the tilt amplitude has the opposite sign from the first year. (d) DIRBE map at $\lambda 240$ $\mu$m, showing the galactic plane. Histograms of the integration time for maps (a) to (c) are shown in Fig. 4.3.

the distribution of integration time (and thus of achieved sensitivity level) over the sky. Figure 4.4(a) shows that the maximum integration times are concentrated at high ecliptic latitudes, roughly uniformly with longitude. In fact it would be extremely interesting scientifically to obtain, in addition to the all-sky survey, observations of small regions with much higher than average sensitivity; these regions would have to be selected carefully to be as free as possible of foreground signals. It would be most useful if the regions of highest integration time could be concentrated in smaller areas than what is afforded by the basic strategy (Fig. 4.4), especially because not all of the high ecliptic latitude regions are as clean of foreground emission as required. It is in fact possible to use the ($\pm 15°$) ability to incline the spin axis to obtain an integration time coverage which fulfills the twin objectives of mapping the whole sky, and concentrating sensitivity into several small high-latitude spots. The strategy is to add to the basic ($5'$) ecliptic-plane manoeuver a component which brings the spin axis out of the ecliptic plane, by an amount which is to first order sinusoidal with time, with a period of order months.

The motion described by the (anti-Sun pointing) spacecraft in the L2 Lissajous orbit implies that the angle between the Sun- and Earth- vectors varies between -15° and +15° over a three-month period (see Fig. 4.2). Any additional tilt out of the ecliptic plane increases the spin-axis to Earth-vector angle over and above that imposed by the Sun-pointing attitude. However, there is a time-varying constraint on the magnitude of this angle, based on the fact that the satellite will transmit data to the ground via a fixed directional antenna, which is oriented along the spin axis and has a useful beam size of $\pm 15°$ (Fig. 4.2). The amplitude of the allowed out-of-the-ecliptic tilt will consequently be less than the theoretically possible $\pm 15°$ at all times, and may be as low as 0° (at the extremes of the orbital trajectory). The optimal strategy must thus synchronize the intentional tilt with the orbital motion, implying that the out-of-the-ecliptic motions must return to null at approximately three-month intervals. Sinusoidally varying motions which obey this condition result in an even number of small spots on the sky where high integration times are concentrated.

Figure 4.4 shows maps of integration time resulting from a simulation which includes the perturbative motions described above, and Figure 4.3 shows histograms of the area of the sky covered to a given level of integration time for each case. With an optimized strategy, an area of $\sim 100$ square degrees will be observed with an integration time 10 times larger than the average over the whole sky, implying a sensitivity $\sim 3$ times better.

## 4.5 Scientific Operations

### 4.5.1 Commissioning

Routine scientific operations will commence during transfer to L2, approximately 3 months after launch, or 4 months before insertion into the Lissajous orbit. However, commissioning of the instruments will begin earlier. The criterion for starting operations will be the ability to turn on the HFI, which depends on having reached in the focal plane the final temperature achievable passively ($\sim 100$ K). This will not occur until after the inclination change manoeuver ($\sim 30$ days after launch) is performed, because boosts require re-orientation to Sun illumination configurations which do not favor radiative cooling. In addition, the spacecraft will not be spun down (from 5 rpm) to its nominal rotation speed (1 rpm) until after this manoeuver occurs. Since the passive cool down time is of order 7 days, it is foreseen that the HFI will be turned on between 40 and 55 days after launch. Normally, routine operations can only be carried out once the angle between the spin axis and the Earth-vector is within $\pm 15°$, thus enabling high-rate science data telemetry (this condition will be fulfilled for brief periods during transfer, and continuously some $\sim 130$ days after launch). However, during commissioning the on-board low gain antennas can also be used with a more restricted data handling capability.

As soon as both instruments reach their nominal thermal environment, commissioning will begin.

This period will include sensitive measurements of the near lobes of the radiation patterns: during transfer the spacecraft must swing by the Moon and Earth, and at these times they will constitute a convenient source for these measurements (see Section 2.5.2). Proper (routine) observations of the sky will begin once the Earth and Moon are placed at a large enough angle from the telescope line-of-sight and the science telemetry is enabled.

### 4.5.2   Routine Operations

Once routine operations are initiated, the observing mode will be unique. However, a number of instrumental modes will be preprogrammed to support various levels of uncompressed data downlink (as noted in Ch. 3, in the normal mode the telemetered science data is heavily compressed); these modes will be used during commissioning and emergency situations as instrument diagnostics.

Routine operations will be tied to the period of visibility afforded by one ground station (Kourou), which varies according to the season between 10.1 and 11 hours. During the visibility period, the data of the preceding obscuration period will be telemetered to ground, interleaved with the ongoing observations. The capability of the TM link (see Section 5.3.8) guarantees a real-time science data rate of ∼30 kbit/s (averaged over 24 hrs), which will correspond to a compressed fraction of the scientific data acquisition ratio (see Section 3.6.3).

During routine operations, the spacecraft will operate in a pre-programmed, automatic manner. The observing pattern (consisting of a series of manoeuvers to be carried out at 2 hour intervals) will be known far in advance. However, the open-loop[1] nature of the spacecraft pointing system is such that both random and systematic deviations from the nominal pattern are expected (e.g. monotonic drift due to solar pressure). These must be corrected for on a daily basis, as follows. At the opening of the visibility window, the housekeeping (HK) information of the previous obscuration period will be downlinked first, a process which will have a duration of at most 1 hour. The attitude of the spin axis will be reconstructed from this data. Based on the past behavior of the pointing, corrections to the nominal pattern must be predicted for the following 24-hour period, and uplinked to the spacecraft before the close of the visibility window. The objective of this daily exercise is to maintain the attitude errors within the requirements of the payload.

### 4.5.3   Calibration

Calibration of the science data (both absolute and relative) will not require a special mode of operation, but will be an ongoing process during sky observations. Various sources will be used for this purpose, most notably the well-known dipole component of the CMB, passages through the galactic plane, extragalactic point sources, and planets present in or near the field of view (Jupiter, Saturn, Mars). The strength of the signal from these sources depends strongly on the frequency, and each of the COBRAS/SAMBA channels will rely on only a subset of the available sources for calibration. A more detailed discussion of the achievable calibration accuracy can be found in Section 2.5.3.

## 4.6   Management of Scientific Operations

COBRAS/SAMBA is a survey-type project which will be developed and operated as a PI mission. ESA will be responsible for the overall spacecraft and mission design, instrument integration into the experiment module and its integration onto the spacecraft bus, system testing, spacecraft launch and operations, and acquisition and transmission of the data to the science data centers. The payload instruments will be provided by PI teams, funded by ESA's member states, and selected via an Announcement of Opportunity (AO). The AO will cover the two focal plane instruments covering

---

[1] By this we mean that the attitude of the spacecraft is maintained from the ground by adding daily corrections to the uplinked thruster commands. No corrections are made autonomously on board, thereby simplifying the pointing system.

the frequency range 30 to 900 GHz; the active cooling system is considered a part of the HFI. The telescope system will be procured via international collaboration.

The AO will request proposals from Consortia which will provide both the instruments (one per Consortium) and the manpower and facilities needed for their development, as well as for processing of the scientific data. Each of the two selected Consortia will adhere to the following characteristics:

- it will be led by a single PI, who will act as interface to ESA

- it will be composed of interlinked teams of people responsible for specific tasks, and led by Team Leaders

- at the very least there will be teams responsible for the following tasks:

  - development and delivery of an instrument (LFI or HFI)
  - daily processing of the payload data
  - reduction, distribution, and archiving of the scientific data

- additional teams may be included to provide specific scientific products, e.g. a Point Source Catalog

- a central location will be provided where the bulk of the data reduction activities will be carried out (a Data Processing Center, or DPC)

A Science Team (ST) will be formed after selection of the Consortia through the AO process. It will include the ESA Project Scientist (PS) as its Chairman, one representative of the telescope provider, and two representatives from each of the selected Consortia: the PI, and one Data Reduction Scientist. Other scientists, representing the additional teams, may be included in the ST. The ST will be responsible for:

- insuring that the development of the mission remains compatible with the main scientific objectives

- formulating the sky observation and calibration strategies

- preparing for and overseeing the analysis of the data

- recommending updates to the observing plan during the operational phase, and requesting their implementation by the MOC

- delivering the final data products to the community

- organizing the data archive(s)

The satellite will be operated by the ESA Mission Operations Center (MOC) at ESOC via one ground station (presently assumed to be Kourou). In addition to the usual tasks of preparing for and carrying out spacecraft operations and mission analysis, the MOC will be responsible for:

- supporting the ST on all aspects concerning spacecraft operations

- maintaining a database containing the long term spacecraft pointing plan, on the basis of ST inputs

- converting ST requests into spacecraft commands and uplinking them

- daily stripping of the payload data and housekeeping from the telemetry stream, ordering them by time, and making them available to the DPCs electronically

- daily conversion of spacecraft housekeeping into the previous day's pointing history, prediction of pointing corrections for the next obscuration period, uplink of a corrected series of manoeuvers valid for the next 3 days, and provision of the pointing information to the DPCs

- checking the health and performance of the payload, by ensuring that payload housekeeping data remains within predetermined limits

- alerting the ST of all significant anomalies and/or deviations from the expected behavior of the spacecraft

- archiving the raw payload telemetry for a predetermined time
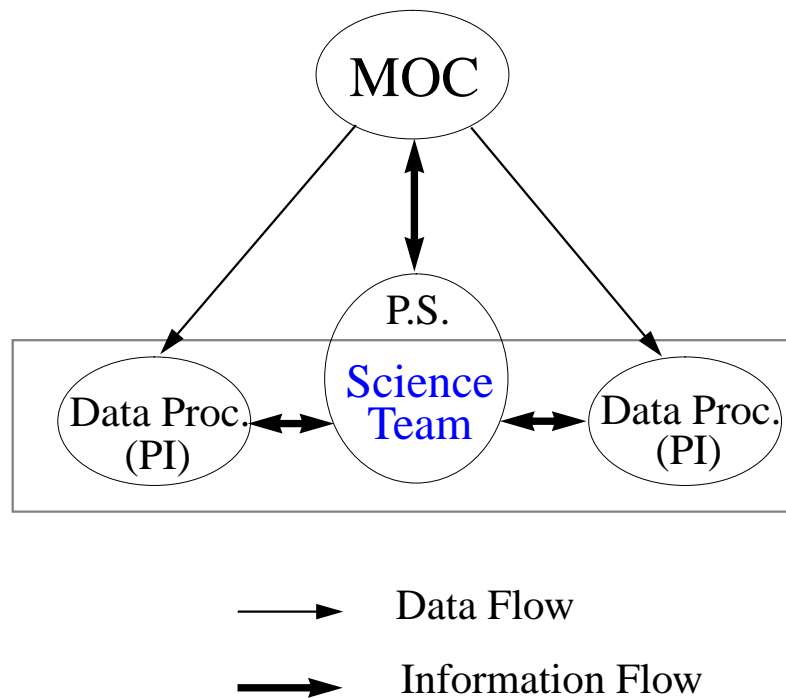


Figure 4.5: A schematic view of the various elements supporting COBRAS/SAMBA during its operational phase, and the flow of data and information among them.

The PS will act as interface between the ST, the MOC, and the DPCs (see Figure 4.5). All of the data output from the payload will be piped daily from the MOC to each of the two DPCs. Independent data processing will be carried out by each of the DPCs, in order to maintain redundancy and a good level of cross-checking, as well as the expertise provided by the instrument development teams. The DPCs will be responsible for:

- on a daily basis, acquiring the (time-ordered) payload scientific and housekeeping data, and the past (reconstructed) pointing information from the MOC

- carrying out a daily analysis of instrument health and performance (for this function, each DPC will be responsible for its associated instrument)

- carrying out a daily quick-look analysis of the current scientific data

- continuous data processing during operations, which will include monitoring of the data quality, calibration, cleaning, etc

- regular reporting to the ST on the data processing activities, and in particular of any anomalies detected

- supporting the MOC in all areas regarding payload hardware and software, and interpretation of the data generated by it

- maintaining a capability to support the ST and the MOC during emergency situations

- the final reduction of the data into the science products of the mission

- archiving and distribution of the science products to the astronomical community at large and to ESA

## 4.7   Scientific Data Products

In spite of the presence of two DPCs, the mission is conceived as an integrated one aimed at the fundamental cosmological and astrophysical measurements described in Chapter 1, and thus there will only be one final set of data, derived optimally under ST supervision from all the products of the individual DPCs.

Final data processing consists mainly of two steps: generation of maps of the surveyed area from the raw data, and separation of the various components from the maps to obtain both the cosmological signal, and the foreground emissions. The DPCs will be responsible for both steps.

There will be three levels of scientific data products:

1. time series of the data acquired by each detector, after basic calibration, removal of systematic features, and attitude reconstruction

2. maps of the sky in nine frequency bands

3. maps of the sky for each of the main underlying components (CMB, SZ, dust, free-free, and possibly synchrotron)

The first of these products will be of interest to astronomers seeking refinements on the basic scientific products, or alternative data reduction schemes. It consists of a large amount of data (50-100 Gbyte), but can easily be maintained as an EXOSAT-type electronic data base[2]. The second is the main product of the mission and will be available for distribution to the community 1 year after completion of the nominal mission, in accordance with ESA policy (as laid down in ESA-C 89 95 Rev.1); the quantity of data (0.5-1.0 Gbyte) is such that distribution by CD-ROM is both appropriate and inexpensive. The third product constitutes the main scientific result of the mission and will most likely require many iterations to achieve maturity. However a "first-generation" set of component maps will be distributed to the community simultaneously with the main product (the sky maps).

## 4.8   Ground Segment and Operations

The overall responsibility for the implementation of COBRAS/SAMBA rests with the ESA Directorate of Scientific Programs. The responsibility for mission operations, however, will be delegated to the Directorate of Operations (ESOC). The COBRAS/SAMBA operational scenario follows the lines of a survey-type project which will be developed and operated as a PI mission. Mission operations, performed by ESOC from the time of separation from the launcher, consist of mission planning, spacecraft monitoring and control, and all orbit and attitude determination and control. The instrument operations proper will be under the responsibility of the PIs. The coordination of payload operations

---

[2]A single workstation connected to an optical storage jukebox, accessible via public networks

and the interface between the PIs and the mission control centre will be under the responsibility of the Project Scientist (PS), at the head of a Science Team which is in turn supported by two PI-provided Data Processing Centres (DPCs, see Section 4.7). The ESOC task in support of the instrument operations is confined to routing of payload telemetry packages to the DPCs and processing instrument telecommand and mission planning requests from the PS.

### 4.8.1 Mission Operations

The mission operations activities for COBRAS/SAMBA will be conducted according to the following concept:

- All operations will be executed according to a Mission Timeline, Flight Control Procedures and Contingency Recovery Procedures laid down in the Flight Operations Plan, a comprehensive document drawn up by ESOC operations staff based on project/industry deliverables (User Manual and Database). With respect to the payload, operations support will be given according to the input from the PIs specified in the Payload Operations Plan.

- Nominal spacecraft control during the routine mission phase will be "off line". The contacts between the Mission Control Centre (MCC) at ESOC and the spacecraft, except for collecting payload and housekeeping telemetry, will be primarily used for pre-programming of the autonomous operations functions on the spacecraft (uplink of master schedule), and for data collection for off line status assessment. Anomalies will normally be detected with a delay. A limited number of time tag commands will be available for spacecraft safety operations. The master schedule will be prepared by a dedicated Mission Planning System, using inputs defined by the PIs on a weekly basis.

- Orbit determination will use two-way range and coherent Doppler tracking data; it also provides calibration of the main engine and the thrusters. The transfer orbit manoeuvers and the Lissajous orbit maintenance manoeuvers will be optimized to minimize propellant consumption under all operational conditions (e.g. sun aspect angle).

- The spacecraft attitude and spin rate will be determined to the required accuracy using star mapper and accelerometer data. During the transfer attitude manoeuvers will be implemented to satisfy the orbit manoeuver requirements and the spacecraft constraints. During payload operations the pointing plan prepared by the Science Team will be implemented and corrected to compensate for random perturbations on a daily basis.

- In routine operations only one Ground Station (Kourou) will be used. Contact with the spacecraft will occur over 10 to 11 hours per day. In conjunction with the 15m station at Kourou, the 15m station at Perth - Australia will be used to guarantee the required reliability throughout critical mission phases (LEOP - first 10 days, transfer orbit manoeuvers and Lissajous orbit injection), complemented by the ESA 15m station at Villafranca for the first 10 days of the mission.

- COBRAS/SAMBA mission operations will be conducted in shifts of spacecraft operations staff covering the ground station contact periods. In the critical mission phases (first days after launch and around orbit manoeuvers), 24 hours operations per day will be conducted.

### 4.8.2 Ground Segment

ESOC will prepare a Ground Segment which comprises all facilities (hardware, software, documentation, trained staff) required to conduct the operations. All ground facilities established for COBRAS/-SAMBA support will be based on extensions of existing ground segment infrastructure, tailored to meet the requirements of the COBRAS/SAMBA mission. In particular:

- The Flight Control System used for spacecraft monitoring and control (all telemetry and command processing) will be based on the second generation Spacecraft and Operations Control System (SCOS II) infrastructure, with specific extensions for COBRAS/SAMBA mission planning.

- The Flight Dynamics Facility will use the Orbit and Attitude Operations System (ORATOS) infrastructure. The operations will be performed by the team of specialists which has prepared the related facility.

- Elements of the existing ESA Ground Stations and Communications Network will be shared with other users in the required time frame.

- The computer configuration in the control centre will be derived from existing structures. A distributed system of workstations will be tailored to the specific needs of the COBRAS/SAMBA mission.

- The external connection to the DPCs and the PS will use dedicated commercial lines. All payload telemetry data augmented by auxiliary data on orbit, attitude and spacecraft status will be accessible on a data server. Command requests will be processed from the same data server.

- The Spacecraft Software Simulator used for Flight Control system and operations procedures validation and staff training will be based on the existing SIMSat infrastructure.

Before launch all dedicated COBRAS/SAMBA hardware and software will be procured, installed, developed and verified. General purpose facilities will be configured and scheduled for COBRAS/-SAMBA . All documentation required for operations will be prepared and the operations staff will be trained. The different elements, and the ground system as a whole, will be verified in a sequence of Validation Tests and Rehearsals. The Ground Segment will be prepared under the responsibility of the Ground Segment Manager according to the Mission Implementation Requirements Document (MIRD) issued under the Directorate of Scientific Programs responsibility.

# Chapter 5

# The Spacecraft

## 5.1 Requirements and Constraints

The main requirements and constraints that determine the design of the spacecraft have been discussed in the previous chapters, and are summarized in Table 5.1. In the following sections we describe the technical characteristics of the COBRAS/SAMBA spacecraft which allow to fulfill these requirements.

## 5.2 System Engineering

### 5.2.1 Spacecraft Configuration

Two separate modules, the payload module (PLM) and the service module (SVM) have been conceived to keep simple and clear interfaces, thus optimizing the development, integration and testing activities (see Figure 5.1).

The PLM houses all the payload equipments requiring cryogenic temperatures : the detection units of the instruments, the telescope, the baffle and the outer flared shield. All this is mounted on a cold optical bench, together with a cryogenic radiator of nearly 3 m$^2$, fixed vertically onto the main mirror support. The optical bench is attached to the SVM top platform by means of glass fiber struts. Cryo coolers and cryogenic dilution system equipment are also mounted on this top platform, and the whole constitutes a mechanically and thermally autonomous assembly.

The SVM houses all the warm electronics of the payload, together with the subsystems of the spacecraft. It is a flat octagonal box, whose design is driven by the need to maximize inertia about the spin axis. All equipments are attached to lateral walls, which simplifies their passive thermal control (see Figure 5.2). Four fuel tanks are accommodated inside the central cylinder. The solar array is fixed, non deployable, and of annular shape. Its outer diameter is 4 m, the maximum allowable for the SILMA fairing (see Fig. 5.3). It is mounted at the base of the SVM, with the active side facing away from the SVM and PLM.

### 5.2.2 Spacecraft Functional Architecture

The spacecraft block-diagram is shown on Figure 5.3. It is organized around a centralized data management system and a centralized power distribution scheme. Attitude control sensors and actuators are monitored by a common electronic unit (the Attitude Sensor Electronics, or ASE), in charge in particular of attitude anomaly detection, and safe mode implementation. The payload computers are directly connected to the data bus, and managed by the spacecraft central computer. Power is distributed to all equipments (payload and service module) via one Power Distribution Unit (PDU), apart from the cryocoolers which are fed by dedicated lines, owing to their high power needs.

Table 5.1: Requirements on the COBRAS/SAMBA Spacecraft

| PLM Thermal Control | • LFI: T<100 K (achieved passively)<br>• HFI: Heat input to outer shield < 1.4 W; bolometer temperature (~0.1 K) achieved with active coolers<br>• Mirrors and Baffle: T<130 K (achieved passively)<br>• Shield: T<150 K (achieved passively) |
|---|---|
| PLM Thermal Stability | See Table 3.7 |
| PLM Structure | • Withstand launch loads and vibrations<br>• Accommodate both cryogenic (telescope, detector boxes, baffle, shield) and room-temperature elements (cryocoolers, dilution refrigerator, electronics)<br>• Support telescope and focal plane with minimum impact on optical quality and pointing req's<br>• Decouple cryocooler microvibration from focal plane |
| PLM Alignment | • Total optical misalignment (mirrors plus instruments) leading to WFE < 40 $\mu$m rms |
| PLM Pointing | • Spatially periodic line-of-sight (LOS) motion (period ~1 min.)<br>• Near-all-sky coverage (×2 minimum); 5′ basic step (±2′, achieved in less than 5 mins.)<br>• Solar Aspect Angle (Sun-S/C-LOS) > 100° at any time<br>• Anti-Sun attitude |
| PLM Pointing Stability ($2\sigma$ values) | • Absolute Pointing Error: 1°<br>• Pointing Stability over 30 mins.: 2′.5<br>• Pointing Stability over 24 hrs.: 10′<br>• A-posteriori Pointing Uncertainty: 2′.5 |
| RF Communications | • Instrument acquisition data rate ~195 kbit/s, or 16.8 Gbit/day<br>• Raw data compression ability: factor of ~8<br>→ Telemetry data rate (Science + HK): ~30 kbit/s, or 2.6 Gbit/day<br>• Telecommand: ~1 kbit/s |
| Power | • During Launch: 132 W (to lock coolers)<br>• During operations: 413 W<br>• Delivered at 28 V (±1%) |
| Mission Duration: | • >15 mos routine operations<br>• Consumables for 5 years |
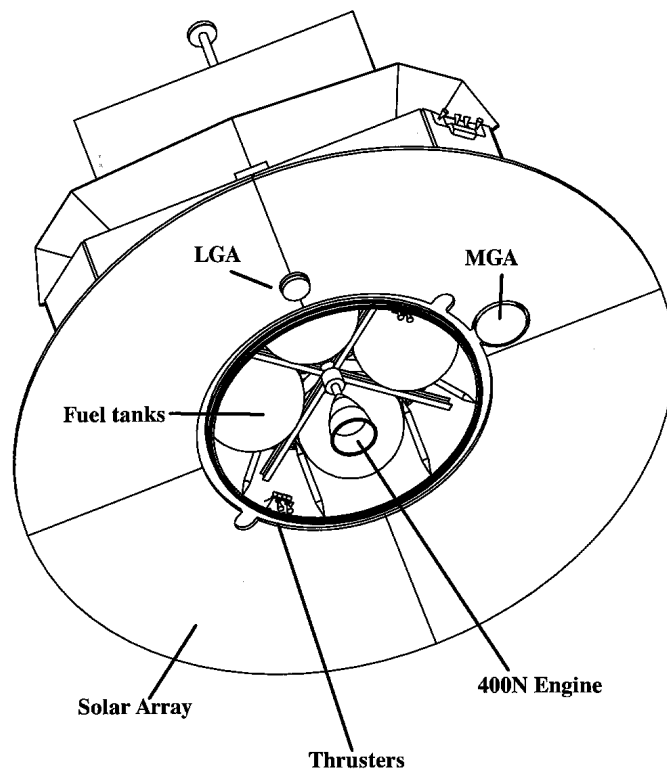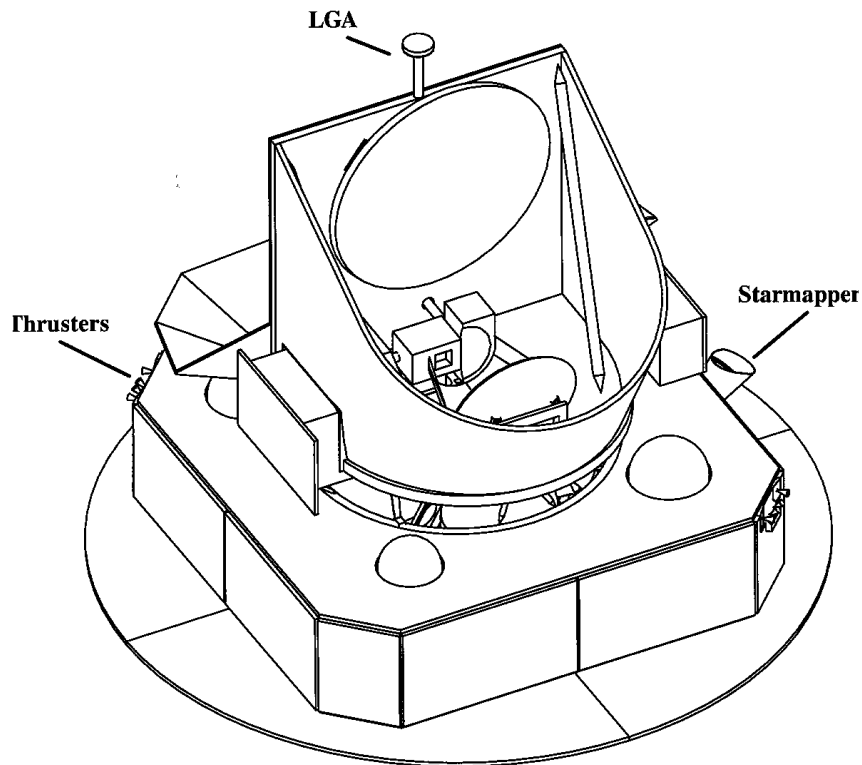
Figure 5.1: COBRAS/SAMBA in orbit configuration (MLI removed), showing the location of various elements (LGA = low gain antenna, MGA = medium gain antenna).
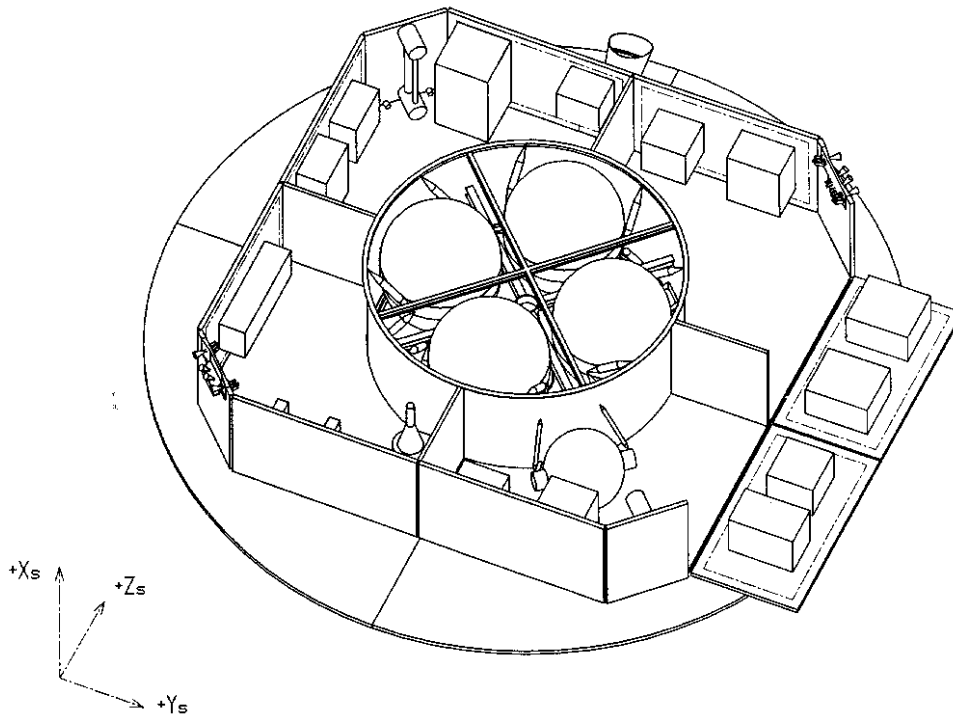
Figure 5.2: A view of the service module, with the top cover removed and one open side panel showing the arrangement of electronic boxes. The medium-gain horn antenna (MGA) is visible as the conical shape near the central SVM ring.
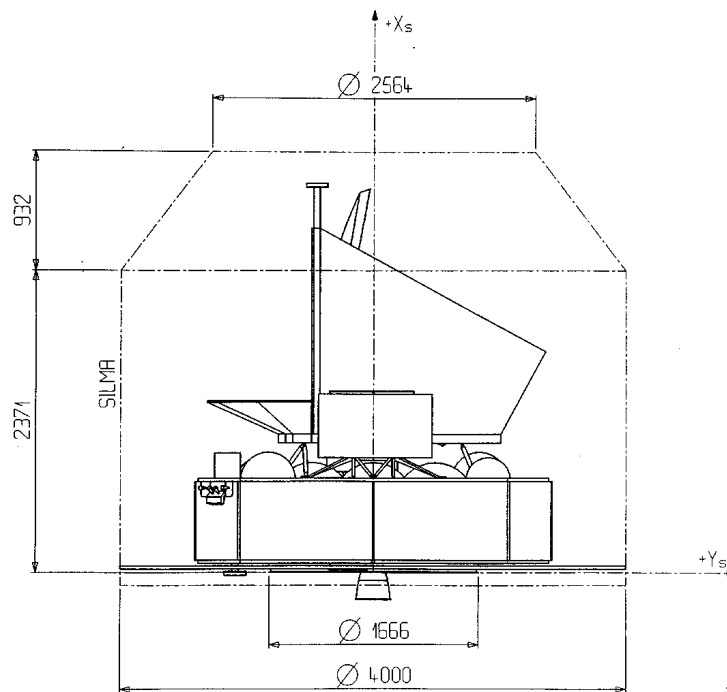


Figure 5.3: A view of COBRAS/SAMBA in the SILMA fairing, showing characteristic dimensions
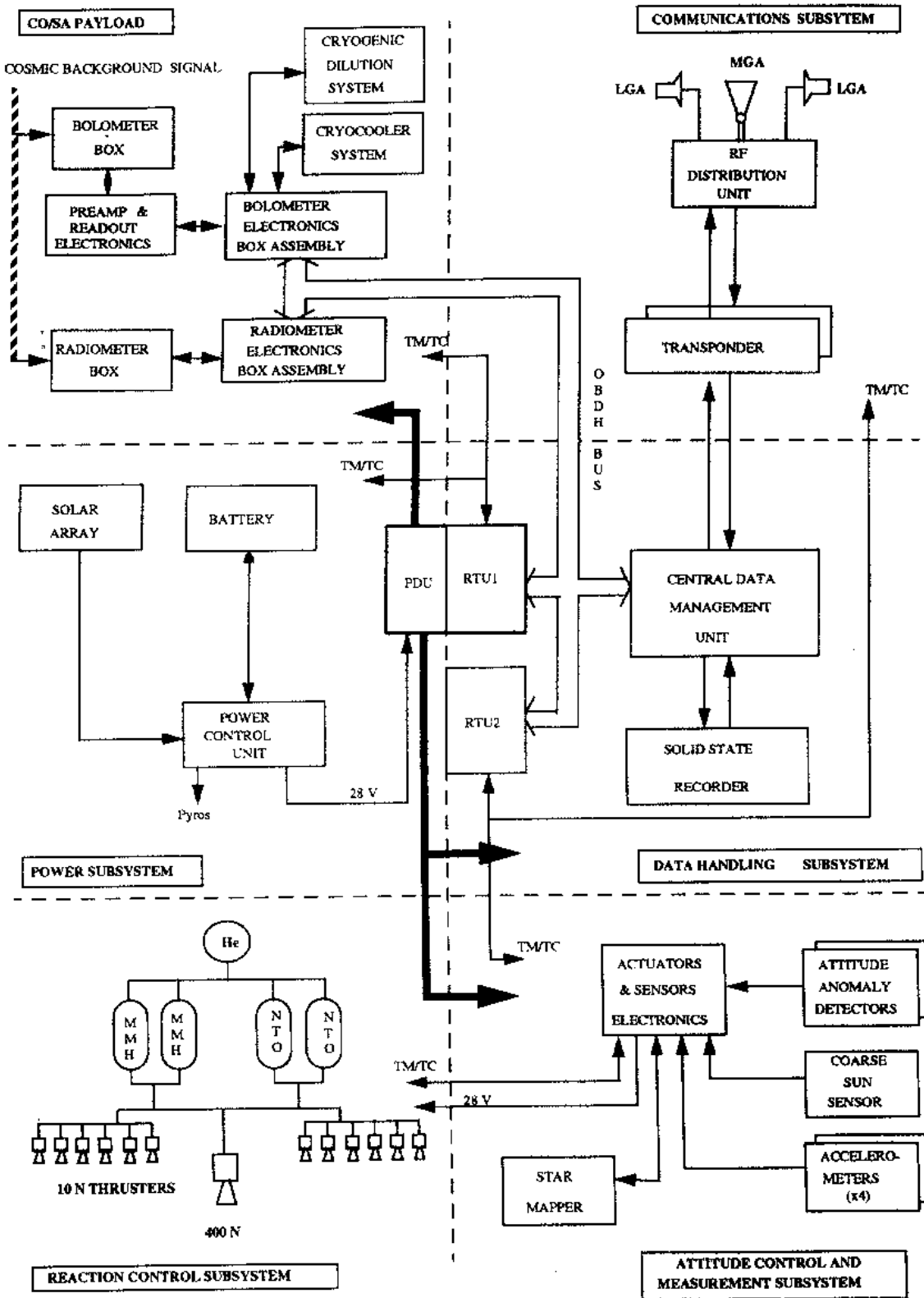
Figure 5.4: Satellite block-diagram.

## 5.3   Subsystem Design

### 5.3.1   Overview

A summary of the main characteristics of the COBRAS/SAMBA subsystems is presented in Table 5.2. Their design is driven by the satisfaction of the mission and payload requirements (see Table 5.1) at the lowest possible cost. Therefore, using well proven technologies and maximizing the reuse of existing units has been a permanent concern during the phase A study.

### 5.3.2   Attitude and Orbit Control System

The basic functions of the Attitude and Orbit Control System (AOCS) are to support the pre-operational transfer phase, to point the payload line of sight and scan the celestial sphere in accordance with the scientific requirements, to protect the payload from direct exposure to the Sun, and to provide the orbit maintenance. The spacecraft is spin-stabilized, the spin rate being set at 1 rpm for the observation strategy (5 rpm during transfer). This rate is sufficiently high for a pure passive attitude control : a simple star mapper permanently scans the sky, and star events are telemetered to the ground for attitude reconstruction. Manoeuvers are computed on ground, and corresponding nozzle commands uplinked accordingly. Nutation avoidance manoeuvers are required to fulfill the stability requirement of $2'5$; residual nutation is damped out thanks to fuel slosh, and Passive Nutation Dampers (PNDs). During scientific operations, a $5'$ spin axis slewing manoeuver is performed every two hours, which interrupts observations for less than 5 minutes.

An autonomous on-board protection system impedes the Sun from illuminating the payload module, a condition which would be damaging for the instruments. The solar aspect angle and the spin rate are monitored respectively by a sun sensor (the Attitude Anomaly Detector, or AAD) and a set of accelerometers : in case of anomaly, the survival mode is entered, and the satellite attitude is forced to anti-solar. This is achieved by means of an on-board control loop, using a Coarse Sun Sensor (CSS) and the redundant thruster branch as actuators. All AOCS equipments are flight proven, except for the PNDs and ASE which have to be adapted from existing hardware (CLUSTER).

### 5.3.3   Propulsion

A unified bipropellant Reaction Control System (RCS) is baselined owing to the large transfer $\Delta V$. The perigee boosts are performed with a 400 N main engine, whereas subsequent transfer $\Delta V$ manoeuvers are performed with a nominal set of six 10 N thrusters, used also for station keeping and attitude control. The blow-down mode is entered as soon as the perigee boosts with the 400 N engine are completed.

The set of 10 N thrusters offers pure (in average) torquing and $\Delta V$ capabilities along the 3 axes. For the fine scanning manoeuvers (with nutation avoidance), a minimum torque impulse bit of 0.06 Nms is required, with a reproducibility better than 0.02 Nms.

A typical fuel budget for a 5 year mission requires a total of $\sim$545 kg (or $\sim$500 liters of bipropellant), broken down as follows :

- perigee boosts using the 400 N engine (800 m/s): 350 kg

- other $\Delta V$ manoeuvers using the 10 N thrusters (400 m/s): 180 kg

- attitude control using the 10 N thrusters: 15 kg

The RCS equipment is mainly reused from the Eurostar platform, except for the fuel tanks, which are based on the XMM design.

Table 5.2: Main Characteristics of COBRAS/SAMBA Subsystems

| | |
|---|---|
| PLM Cryogenic Thermal Control | Passive, with high insulation from SVM (MLI, glass fibre bipods) and cryogenic radiators connected to radiometers via a copper braid. |
| PLM Structure | Low CTE carbon fibre with aluminum honeycomb. Isostatic mountings for optical bench and telescope. |
| SVM Thermal Control | Passive : MLI, heaters, black-painted radiators. Heat pipes for coolers radiators. |
| SVM Structure | All aluminum : central cylinder (1666 mm diam.), 4 shear walls, upper and lower platforms, 4 side walls supporting equipments and 4 corner panels. |
| Attitude Control | Passive spinner (1 rpm) with star mapper and passive nutation dampers. Manoeuvers computed by ground. Autonomous on-board protection (safe attitude) against accidental solar heating of payload. |
| Propulsion | Unified biliquid, with 400 N engine and 12 x 10 N thrusters. Four tanks (550 kg fuel). |
| Data Handling | Centralized architecture, with CDMU, 2 RTU's, OBDH bus. Payload interface via DBU, with RBI protocol. Solid State Recorder for non-visibility service (3 Gbit). Full packet standard (TM + TC) |
| RF Communications | S-band transponders (10 W RF emitted). Two low gain antennae for transfer ; one medium gain antenna for science phase (14 dBi within $\pm 15°$ cone) |
| Power | 28 V regulated power bus with PCU, PDU. One 13 Ah NiCd battery for launch and GTO eclipses. Fixed, non-deployable annular solar array (4 m diameter, 10 m2 physical area). Silicon high-eta BSFR cells (7.1 m2), for 700 W EOL power. |

### 5.3.4   Structure

The PLM structure makes use of low CTE materials (carbon fibre honeycomb with aluminum core) and of high thermally insulating struts (glass fibre, epoxy).

The structural core of the PLM is the optical bench, supporting the focal plane assembly, and the two mirrors of the telescope. Isostatic fixations are used for these mirrors, as well as for the mounting of the optical bench onto the SVM upper ring.

The SVM structure is based on a central cylinder with shear walls, top and bottom platforms and side walls; the latter are used to support equipments. All these elements are made in aluminum. The central cylinder interfaces with the launcher adapter, and supports the PLM. The four fuel tanks and the 400 N engine are attached to the inside of the SVM by means of struts.

### 5.3.5   Thermal Control

The cryogenic temperature of 100 K required for the payload is obtained passively. Indeed, thanks to the limited solar aspect angle excursion (of up to 15° from the anti-spin direction), the payload module only sees cold space and the service module. Thus, the thermal control is based on a highly efficient insulation between the PLM and the SVM (using MLI and glass fibre bipods) and a vertical

radiator in carbon fibre. The main heat input into the payload enclosure is due to dissipation in the LFI ($<6$ W), and is evacuated to the radiator by means of a copper braid.

The thermal stability, and especially the thermal modulation of detectors or mirrors at the spin frequency, are well within the specifications thanks to the absence of external modulation at L2, and because of the very large time constant associated with the heat transfer between SVM and PLM.

The cryocooler assembly is thermally decoupled from the cryogenic enclosure by means of an intermediate radiator (at 170 K) and several layers of MLI. The 170 W of heat dissipated by the coolers are rejected to free space by a dedicated radiator accommodating heat pipes.

The thermal control of the SVM is also passive, based on the use of the lateral panels as radiators and MLI elsewhere. No heaters are required during the operational phase, and only 30 W heating power is needed in GTO when the spacecraft is not sun-pointed (SAA = 120° ). The solar array is thermally insulated from the bottom of the SVM. All radiators are black painted.

### 5.3.6   Power Supply and Solar Array

A 28 V regulated bus distributes the power to the payload and service modules. The power is produced by 7.1 m$^2$ of hi-$\eta$ BSFR Silicon cells. For launch and GTO eclipses, a 13 Ah NiCd battery is used.

The power subsystem makes use of a Power Control Unit (PCU) providing power regulation, battery charge and discharge regulation and firing pulses for pyrotechnic devices. The PCU feeds the cryocooler electronics directly, and offers safe lines for essential loads (TC reception, safe mode). One Power Distribution Unit (PDU) feeds all other PLM or SVM units and heaters via switchable protected lines.

The power subsystem equipments will be reused from the XMM program.

The Solar Array is fixed, body-mounted at the bottom of the service module. It is of annular shape (external diameter is 4 m, internal diameter is 1.8 m).

### 5.3.7   Data Handling

The data handling is based on an On-Board Data Handling bus (OBDH) with a main computer, in a centralized architecture. Each of the payload instruments contains its own computer, and communicates with the central computer through the OBDH bus via Remote Bus Interface protocol. Full packet standard is used for telemetry (TM) and telecommand (TC), providing maximum flexibility and versatility for accommodation of several payload data rates. During non visibility periods ($\sim$13 hours per day), payload and housekeeping data are stored in a 3 Gbit solid state recorder, and downlinked at the next visibility period, multiplexed with real time data. The data handling system schedules autonomously all the spacecraft operations (e.g. spin-axis reorientation manoeuvers) during non visibility periods, thus providing 100% of time availability for scientific operations.

The subsystem comprises a Central Data Management Unit (CDMU) in charge of TM acquisition and formatting, TC decoding, spacecraft monitoring and possibly reconfiguration, OBDH management and on-board time generation and distribution. In particular, it acquires from the AOCS a spin synchronization signal and transmits it to the payload.

Two Remote Terminal Units (RTUs) are connected to the data bus, to enable TM and TC exchanges with spacecraft subsystems (and with the payload when it is turned off).

Again, it is planned that XMM or INTEGRAL equipments will be reused for the COBRAS/-SAMBA data handling system.

### 5.3.8   Telecommunications

A telemetry data rate of 60 kbit/s is required in order to download the equivalent of 24 hours of compressed payload and housekeeping data in one visibility pass of minimum 10 h. This is achieved thanks to a Medium Gain Antenna (MGA) having a 3 dB opening angle of 30° , fixed and aligned with

Table 5.3: RF Link Budget

|  | Low Gain Antennas (transfer) | Medium Gain Antenna (operations) |
|---|---|---|
| Assumed Earth dist./angle | 1.2 Mkm, 60° | 1.7 Mkm, 15° |
| Required data rate | 1 kb/s TC<br>1 kb/s TM | 2 kb/s TC<br>60 kb/s TM |
| TC Margin | 9.0 dB | 18.0 dB |
| TM Margin (w/ ranging)<br>TM Margin (no ranging) | 7.6 dB<br>7.9 dB | 3 dB<br>4 dB |
| Ranging Margin (w/ TM)<br>Ranging Margin (no TM) | 4.1 dB<br>10.5 dB | 10.5 dB<br>– |

the spin axis. The directivity of the MGA enables ±15° depointing of the spin axis from the direction of the Earth, as required by the combination of orbital motion and anti-Sun pointing. The MGA will be implemented as a horn. Omnidirectional coverage, based on 2 Low Gain Antennae (LGAs), is also available, and will be used during transfer mainly. The RF power output of the transmitter is 10 W.

Hot redundancy on TC is achieved thanks to two redundant transponders, linked either to the set of LGA's through a hybrid coupler, or to the dual polarization MGA. An RF Distribution Unit (RFDU) offers the switching capability to select either the active transponder or the active antennae system.

Recurrent hardware exists for all units, except for the medium gain horn for which the technology however is fully mature.

## 5.4   Mission Budgets

The RF link budget is summarized in Table 5.3, and assumes the use of the Kourou ground station (EIRP = 80 dBW; G/T = 29.9 dB/K) for at least 10 hours per day. The worst case margin on the TM is 3 dB (TM and ranging at furthest distance, and 15° Earth aspect angle).

The mass and power budgets for COBRAS/SAMBA are shown in Table 5.4. All payload elements include individual mass margins of 20%, as do those elements of the SVM which are not already developed in other programs (such as structure, thermal control, harness, the horn antenna, the solid state recorder, attitude electronics, and the PNDs). All other SVM elements have individual margins of either 5%, 10%, or 15%, depending on whether they are used as is or require some modification. In addition a system margin of 20% is applied on the dry mass. The total launch mass of 1523 kg is 127 kg below the mass threshold under which the cost of an Ariane 5 launch remains constant (i.e. 1650 kg).

The power budget includes 15% individual margin on each unit for uncertainty and lack of detailed definition. The distribution losses (3.5%) cover harness losses which are proportional to the power demand. At system level an additional margin of 10% is taken to cover the evolution of system definition, requirements or interfaces.

The fuel budget is shown in Table 5.5. The total bipropellant fuel required for 5 years of operation of COBRAS/SAMBA is 555 kg, occupying a volume of 505 liters. The volume of the tanks (617 l) would allow an additional 370 m/s of fuel to be loaded on COBRAS/SAMBA .

Table 5.4: Mass and Power Budget

| Subsystem | Mass (kg) | Power (W) | |
| --- | --- | --- | --- |
| | | Launch | Operations |
| LFI | 30 | 0.0 | 55.0 |
| HFI | 127 | 139.0 | 358.0 |
| Telescope+Shield+Baffle | 46 | | |
| Structure | 52 | | |
| Thermal Control | 40 | | |
| Harness | 10 | | |
| Total PLM | 304 | 139 | 413 |
| TM/TC | 10 | 11.6 | 82.9 |
| Data Handling | 39 | 41.4 | 51.8 |
| Attitude (ACMS) | 30 | 0.0 | 24.2 |
| Reaction Control System | 81 | | |
| Power | 87 | 17.5 | 31.9 |
| Structure | 116 | | |
| Thermal Control | 20 | 0.0 | 5.0 |
| Harness | 30 | | |
| Total SVM | 413 | 70.5 | 195.8 |
| Dry Mass (PLM+SVM) | 717 | | |
| System Margin (20%) | 143 | | |
| Ballast Mass | 16 | | |
| Total Dry Mass | 876 | | |
| Fuel | 555 | | |
| Launch Adaptor | 92 | | |
| **Total Launch Mass** | **1523 kg** | | |
| Power (PLM+SVM) | | 209.5 | 608.8 |
| Distribution Losses (3.5%) | | 7.3 | 21.3 |
| System Margin (10%) | | 21.7 | 63.0 |
| **Total Power Required** | | **239.0 W** | **693.0 W** |

Table 5.5: Fuel budget

| Phase | Requirement | Margin | Fuel Mass (kg) |
| --- | --- | --- | --- |
| Perigee Boosts | 800 m/s | 10% | 350 |
| Cruise | 380 m/s | 10% | 165 |
| Total Transfer | | | 515 |
| Spin Axis Orientation | 17800 Ns | 50% | 11 |
| Spin Rate Control | 5250 Ns | 50% | 4 |
| Station Keeping | 25 m/s | 50% | 14 |
| Total Attitude and Orbit Control | | | 29 |
| Total | | | 544 |
| 2% Residuals | | | 11 |
| 5% Ullage | | | 24 |
| **Total** | | | **555 kg** |

# Chapter 6

# Project Management

## 6.1    Introduction

The procurement schedule and model philosophy shown in the following sections is provided for illustrative purposes only as this was the basis of the cost estimate made by industry. However new and probably different approaches to the procurement will apply to the M3 mission as this has been selected to be a "pilot project" with the purpose of verifying the cost effectiveness of new procurement methods.

Several options, ranging from complete delegation to industry to more control by ESA, can be envisaged. These options are being assessed currently. The roles of the Agency; the Industrial companies; the ESA Delegate bodies; the PI's and their respective funding agencies will all be subject to review. The precise approach to be applied to M3 will depend on the actual mission selected and on the willingness of all participants to accept the changes that may be necessary.

To quantify the new approach, the selected M3 mission will be subjected to a detailed assessment of the procurement philosophy proposed during Phase A; alternatives will be evaluated; changes will be proposed and discussed within the Agency and with Delegations. Where needed, the approval of the IPC and Council will be sought.

Particular attention will be given to:

- the relationship between industry, the Agency and the PI's;

- questions of industrial policy;

- PI/Agency funding agreements;

- Industrial management philosophy and

- ESA internal constraints.

The following sections describe a possible procurement approach for the COBRAS/SAMBA spacecraft.

## 6.2    Procurement Philosophy

The proposed procurement scheme of COBRAS/SAMBA is based on the concept that the Payload Module (PLM) consists of a Telescope Assembly (TA), two instruments (constituting the Focal Plane Assembly) and their associated electronics, and the PLM Mechanical and Thermal Works (MTW), including mirror support structures, thermal radiators and dissipative paths, optical bench and telescope shielding. The FPA instruments and electronics are assumed to be provided by Principal Investigators (PIs) with funding from ESA's member states. The same PIs will be responsible for the scientific Data

Processing Centres (DPCs) (two in principle). The TA is also assumed to be supplied to ESA by an international collaborator, identified at present as the Danish Space Research Organization.

ESA would be responsible for

- the overall spacecraft and mission design, including the PLM MTW

- instrument integration into the MTW of the Telescope Assembly and the two FPA instruments, to form the PLM

- integration of the PLM onto the spacecraft bus

- system testing

- spacecraft launch and operations

- acquisition and distribution of data to the DPCs.

## 6.3 Scientific Management and Instrument Selection

After the approval of the mission, the Agency would issue an Announcement of Opportunity (AO) calling for proposals for the payload instruments, including the DPCs. The AO would be explicit in terms of the spacecraft mission and resources, technical interfaces, schedule, deliverable items, responsibilities of the parties, etc.

The AO would contain a description of the model payload and would request proposals for the supply of the complete packages as defined here above and for the COBRAS/SAMBA scientific operations concept (see Section 4.6). These proposals should describe in detail the scientific objectives and the design and development of the envisaged instrumentation and its associated software. They should also describe the management structure within the collaboration and show how the responsibilities for the scientific, technical, operational and analysis aspects are discharged.

Selection of the COBRAS/SAMBA experiments would take place via the normal procedure which includes a technical evaluation by the ESA Executive, a scientific evaluation by ESA's scientific advisory bodies and approval by the Science Programme Committee (SPC).

The selected PI's would be responsible for obtaining the necessary funding from the appropriate national authorities.

Following selection, refined resource allocations and instrument interfaces would be negotiated with the PI's prior to the start of the spacecraft Phase B. These resources and interfaces would be frozen at the end of Phase B. Special items of mechanical ground support equipment and electrical check-out equipment would also have to be supplied by the COBRAS/SAMBA collaboration.

During the development phase of the instruments, the project team would conduct, with the COBRAS/SAMBA collaboration, a preliminary design review, a critical design review and a flight model review.

A COBRAS/SAMBA Science Team comprising scientists from the collaboration, discipline scientists (see Section 4.6) and the ESA project scientist would be established to support the project.

## 6.4 Industrial Management

It is proposed that the COBRAS/SAMBA spacecraft procurement is carried out by an industrial prime contractor, who is responsible for the development of the service module and of a satellite system which satisfies the COBRAS/SAMBA requirements. The development of the PLM is assumed to be the task of a separate contractor. Therefore, the prime contractor would have responsibility for the integration and tests of the COBRAS/SAMBA payload assembly and the overall spacecraft.

These industrial contracts would be placed and funded by ESA. The responsibility for control and monitoring the contracts and provision for liaison between partners, contractors and PI groups would be with the ESA project team.

## 6.5   Development Philosophy and Schedule

### 6.5.1   General

The spacecraft development will follow the ESA PFM approach. The first system level test at spacecraft level would be conducted on a STM (Structural Thermal Model), to establish the structural and thermal characteristics and compatibility at the system level. Then, the PLM and SVM would be assembled and tested on the EM (Electrical Model) to qualify the electrical system and the EMC approach (partially) at spacecraft level.

The final testing would be performed on the PFM (Protoflight Model).

### 6.5.2   Payload Model Philosophy

The model philosophy chosen is based on the requirement for single flight instruments supported by adequate spares.

As already mentioned, to meet the early system level test a STM would be built, fitted with at least one active unit of the instrument detectors, the rest being representative dummies. This would allow a full verification of the thermo-mechanical design of the payload. For electrical and functional testing an EM would be required. All payload elements would undergo qualification testing, if necessary, prior to delivery for AIT.

It is assumed that only system level testing will be under ESA responsibility, while performance testing at instrument/subassembly level will be under responsibility of the PI's.

### 6.5.3   Bus Model Philosophy

A protoflight approach is proposed where only one model (the PFM) is built at flight standard with Hi-Rel components. However, to perform the early system level tests with the payload, STM (Structural Thermal Model) and EM (Electrical Model) models of the bus would be utilized, using dummies and commercially available parts.

The STM spacecraft structure would be at flight standard. Since this structure would be designed for a total spacecraft lift-off mass with more than 159 kg as system margin (20%) and ballast mass (16 kg) and since the proposed design of the structure is very mature, it is reasonable to assume that the same structure can be used for the STM and for the FM models.

The STM and the EM would be subjected to an extensive test programme which would allow verification of the design concept and interfaces.

It is expected that most of the units would have been qualified on previous programmes. However those units which would be especially developed or significantly modified, would be subject to a qualification programme. After refurbishment, they would be used as flight spare units.

### 6.5.4   Schedule

The schedule of the COBRAS/SAMBA programme is given in Fig. 6.1. The expected launch date at the beginning of this study was towards the end of the year 2003. However, new programmatic considerations may delay the program and launch by 1 to 1.5 years.
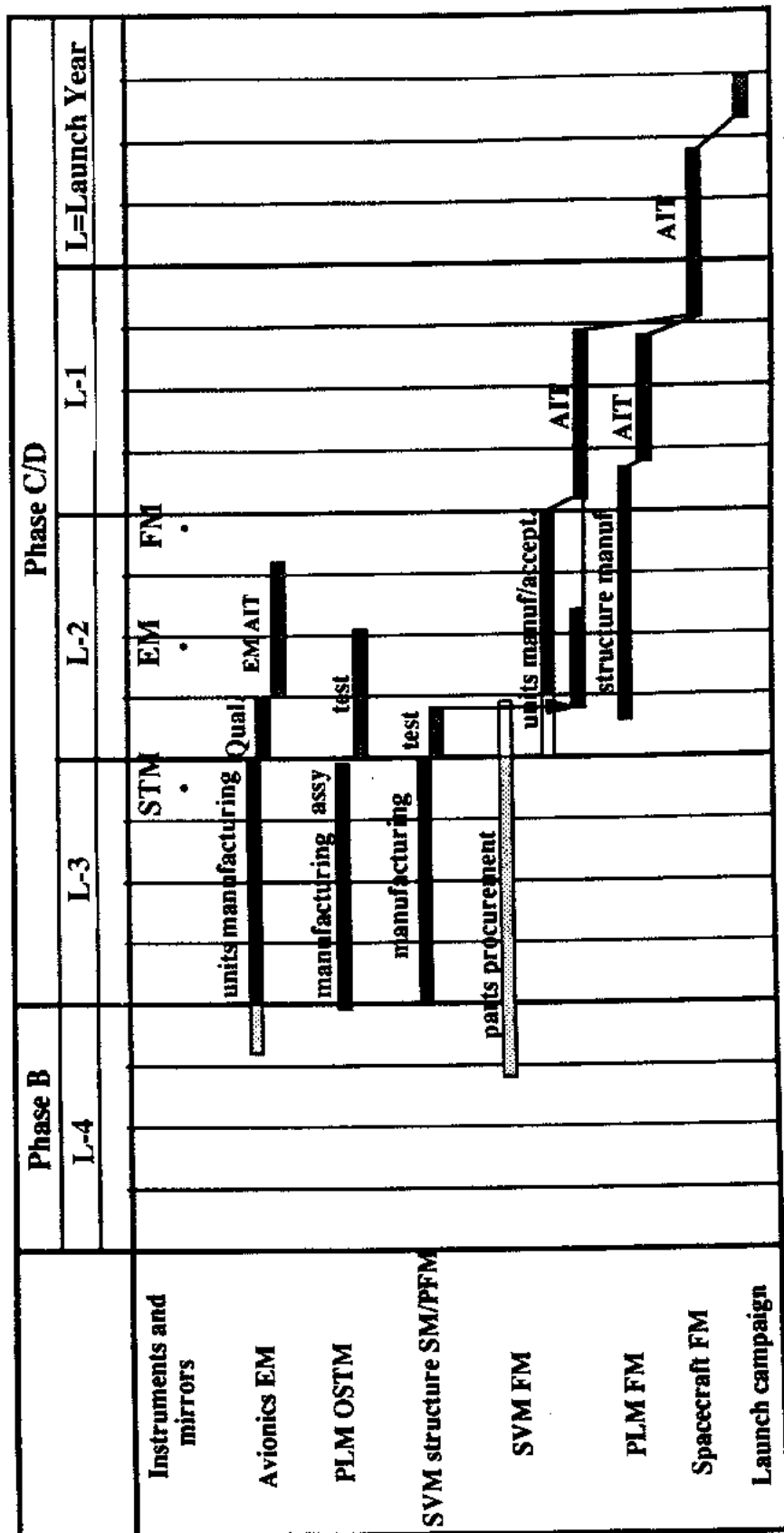
Figure 6.1: The COBRAS/SAMBA project schedule. L stands for the year of launch.

# Chapter 7

# References

Aghanim, N., De Luca, A., Bouchet, F.R., Gispert, R. & Puget, J.L. 1996, in preparation.

Alcock C. *et al.* , 1995, Phys. Rev. Lett, **74**, 2867.

Bahcall, N. A. & Cen, R. 1993, ApJ, **407**, L49.

Banday A., *et al.* , 1994, ApJ., **436**, L99.

Banday, A.J., & Lubin, P. 1996, ApJ, submitted.

Bardeen J.M., Steinhardt P.J. & Turner M.S., 1983, Phys Rev. D, **28**, 679.

Bartlett, J. & Silk, J. 1994, ApJ, **423**, 12.

Bennett C. *et al.* , 1994, ApJ, **436**, 423.

Bennett, C.L., *et al.* 1994, ApJ, **436**, 423.

Bennett, et al. 1992, ApJ, **391**, 466.

Benoit, A., Bradshaw, T., Orlowska, A., Jewell, C., Maciaszek, T., & Pujol, S. 1994, SAE Technical
    Paper Series 941276

Bersanelli, M., Mandolesi, N., Weinreb, S., Ambrosini, R., & Smoot, G., 1995, ITESRE Report 177/95

Bersanelli, M., Muciaccia, F., Natoli, P., N.Vittorio, N.Mandolesi, 1996, in preparation

Bock, J.J., Chen, D., Mauskopf, P.D., & Lange, A.E. 1995, Space Science Reviews, **74**, 229.

Bond J.R. & Efstathiou G., 1987, MNRAS, **226**, 655.

Bond J.R., 1995, PRL, **74**, 4369.

Bond J.R., 1996, *Les Houches Lectures*, ed. R. Schaefer, Elsevier Science Publishers, Netherlands, in
    press.

Bond, J.R. & Myers, S.M. 1996, ApJ Supp, in press

Bouchet, F.R., Bennett, D.P., & Stebbins, A. 1988, Nature, **335**, 410.

Bouchet, F.R., Gispert, R., Aghanim, N., Bond. J.R., De Luca, A., Hivon, E. & Maffei, B., 1995a,
    Space Science Review, **74**, 37-43.

Bouchet, F.R., Gispert, R. & Puget, J.L., 1995b, Proceedings of the $30^{th}$ Moriond meeting "Clustering
    in the Universe", Les Arcs, France, Editions Frontières (preprint SISSA astro-ph/9507032).

Bouchet, F.R., Gispert, R. & Puget, J.L., 1995c, Proceedings of the COBE Workshop "Unveiling the
    Cosmic Infrared Background", Baltimore, Maryland, USA, Ed. E. Dwek.

Bouchet, F.R., Gispert, R. & Puget, J.L., 1996, in preparation.

Boulanger, F., Falgarone, E., Puget, J.L., & Helou, G. 1990, ApJ, **364**, 136.

Boulanger, F., *et al.* 1996, in preparation.

Cheng E.S. *et al.* , 1994, ApJ, **422**, L37.

Clark, F.O. 1991, BAAS, **23**, 887.

Colafrancesco, S., Mazzota, P., Rephaeli, Y. & Vittorio, N. 1994, ApJ, **433**, 454.

Condon, J.J. & Mitchell, K.J. 1984, AJ, **89**, 610.

Condon, J.J., Broderick, J.J., & Seielstad, G. 1989, AJ, **97**, 1064.

Coulson D. *et al.* , 1994, Nature, **368**, 27.

Crittenden R.G. & Turok N., 1995, PRL, **75**, 2642.

Crittenden R.G. *et al.* , 1993, PRL, **71**, 324.

Désert, X., *et al.* , 1996, in preparation.

Danese, L., Franceschini, A., Toffolatti, L., & De Zotti, G. 1987, ApJ, **318**, L15.

Davis M., Summers F. & Schlegel D., 1992, Nature, **359**, 393.

Davis R.L. *et al.* , 1992, PRL, **69**, 1856.

De Bernadis P., *et al.* , 1994, ApJ, **422**, L33.

De Bernardis, P., Melchiorri, F., Melchiorri, B. and Vittorio, N. 1992, ApJ, **396**, L57.

Dekel A., 1994, ARA&A, **32**, 371.

Delabrouille, J. 1996, in preparation.

Desert, F.X., Boulanger, F., & Puget, J.L. 1990, A& A, **237**, 215.

De Luca, A., Desert, F. X. & Puget, J. L. 1995, A & A, **300**, 335.

De Pater, I. 1990, Ann. Rev. Astron. Astrophys., **28**, 347.

De Pater, I. & Matisse, S.T. 1985, Icarus, **62**, 143

De Pater, I., et al. 1989, Icarus, **79**, 190.

Dodelson S., Gates E. & Stebbins A., 1996, preprint.

Dodelson, S. 1995, ApJ, submitted (preprint SISSA astro-ph/9512021).

Dowling, T.E., Muhleman, D.O. & Berge, G.L. 1987, Icarus, **70**, 506.

Efstathiou G., 1996, *Les Houches Lectures*, ed. R. Schaefer, Elsevier Science Publishers, Netherlands, in press.

Ellis J., 1990, in *Physics of the Early Universe*, eds

Epstein et al. 1980, Icarus, **41**, 103.

Falgarone, E., Puget, J.L., & Pérault, M. 1992, ApJ, **257**, 715.

Fischer M. L., Clapp, A., Devlin, M., Gunderssen, J. O., Lubin, P. M., Meinhold, P. R., Richards, P. L. and Smoot, G. F., 1995, ApJ, **444**, 226.

Fischer M. *et al.* , 1992, ApJ, **388**, 242.

Fomalont, E.B., Kellerman, K.I., Windhorst, R., & Kristian, J.A. 1991, AJ, **102**, 1258.

Fomalont, E.B., Kellermann, K.I., Anderson, M.C., Weistrop, D., & Wall, J.V. 1988, AJ, **96**, 1187.

Franceschini, A., Mazzei, P., De Zotti, G., & Danese, L. 1994, ApJ, **427**, 140.

Franceschini, A., Toffolatti, L., Danese, L., & De Zotti, G. 1989, ApJ, **344**, 35.

Franceschini, A., & Andreani, P. 1995, ApJ, **440**, L5.

Freedman W.L. *et al.* , 1994, Nature, **371**, 757.

Gaier T., *et al.* , 1992, ApJ, **398**, L1.

Ganga K. *et al.* , 1993, ApJ, **410**, L57.

Gautier, T.N., Boulanger, F., Perault, M., & Puget, J.L. 1992, AJ, **103**, 1313.

Gear, W.K., & Cunningham, C.R., 1995, in "Multi-feed systems for Radio Telescopes" ASP Conference series, vol 75, D.T. Emerson and J.M. Payne (eds), pp215-221.

Gorski K. *et al.* , 1994, ApJ, **430**, L89.

Griffin et al. 1986, Icarus, **65**, 244.

Grossman, A.W., Muhleman, D.O., & Berge, G.L. 1989, Science, **245**, 1211.

Guiderdoni, B. *et al.* 1996, in preparation.

Gulkis, S. et al. 1983, Science, **221**, 453.

Gundersen J.O., *et al.* , 1995, ApJ, **443**, L57.

Gunn J.E. & Weinberg D., 1995, in *Wide Field Spectroscopy and the Distant Universe*, 35th Herstmonceux Conference, eds. S.J. Maddox and A. Aragon-Salamanca,World Scientific Press, Singapore, p3.

Gunn, J.E., 1978, *Observational Cosmology*, Sauverny, Geneva Observatories, p1.

Guth A. & Pi S-Y., 1982, Phys Rev D., **23**, 347.

Gutierrez de la Cruz, C.M., Davies, R.D., Rebolo, R., Watson, R.A. Hancock,& Lasenby, A.N. 1995, ApJ, **442**, 10.

Hacking, P., & Houck, J.R. 1987, ApJS, **63**, 311.

Haehnelt M.G. & Tegmark M., 1996, MNRAS, in press.

Haslam C.G.T., Quigley M.J.S., Salter C.J., 1970, MNRAS, **147**, 405.

Haslam, C.G.T., Stoffel, H., Salter, C.J., & Wilson, W.E. 1982, A& A Supp., **47**, 1.

Hawking S., 1982, Phys. Lett., **115B**, 295.

Hu W. & Sugiyama N., 1995, Phys Rev D, **51**, 2599.

J.A. Peacock, A.F. Heavens and A.T. Davies, Scottish Universities Summer Schools in Physics, Edin-
    burgh.

Janssen, M.A., *et al.* 1996, submitted to ApJ (preprint SISSA astro-ph/9602009)

Jones *et al.* 1996, in preparation.

Jungman G., Kamionkowski M., Kosowsky A. & Spergel D.N., 1996, Phys Rev D, submitted.

Kaiser N. & Stebbins A., 1984, *Nature*, **310**, 391.

Kibble T., 1976, J Phys A: Math Gen. **9**, 1387.

Klypin A., Holtzman J., Primack J. & Regos E., 1993, ApJ, **416**, 1.

Knox L., 1995, Phys Rev D, **52**, 4307.

Kogut A., *et al.* , 1995, ApJ, **439**, L29.

Kogut, A., et al. 1993, ApJ, **419**, 1.

Kogut, A.J. Banday, C.L. Bennett, K.M. Gorski, G. Hinshaw, & W.T. Reach 1996, ApJ, in press
    (preprint SISSA astro-ph/9509151).

Kolb E.W. & Turner M.S., 1990, *The Early Universe*, Addison-Wesley Publishing Co.

Kowitt M.S. *et al.* , 1995, Astrophys. Lett., in press.

Kowitt, M.S. *et al.* 1995, *Proceedings of the 1993 Capri Workshop*, Astrophysics Letters.

Lauer, T.R. & Postman M., 1994, ApJ., **425**, 418.

Laureijs, R.J., Helou, G., Fukui, Y., Mizuno, A., Imaoka, K., &

Lawson, K.D., Mayer, C.J., Osborne, J.L.,& Parkinson, M. 1987, MNRAS, **225**, 307.

Linde A., 1990, *Particle Physics and Inflationary Cosmology*, Harwood Academic Publishers.

Lineweaver, C., Tenorio, L., Smoot, G.F., Keegstra, P., Banday, A.J.& P. Lubin 1996, ApjL submitted
    (preprint SISSA astro-ph/9601151).

Maddox S.J., Efstathiou G. & Sutherland W.J., 1990, MNRAS, **242**, 43p.

Maffei, B. 1995, in preparation.

Magueijo J, 1996, preprint.

Magueijo J., Albrecht A., Coulson D., Ferreira P., 1996, preprint.

Meinhold P.R. *et al.* , 1993, ApJ, **409**, L1.

Mezger, P.G. 1994, Astrophysics and Space Science, **212**, 197.

Muhleman, D.O., & Berge, G.L. 1991, Icarus, **92**, 263.

O'Sullivan C. *et al.* , 1995, MNRAS, **274**, 861.

Park C., Vogeley M.S., Geller M.J. & Huchra J.P., 1994, ApJ, **431**, 569.

Partridge, R.B., Hilldrup, K.C., & Ratner, M.I. 1986, ApJ, **308**, 46.

Peacock, J.A., & Gull, S.F. 1981, MNRAS, **196**, 611.

Peacock, J.A., & Nicholson, D. 1991, MNRAS, **253**, 307.

Peebles P.J.E., 1990, *Physical Cosmology*, Princeton University Press, Princeton.

Pen U., Spergel D. & Turok N., Phys Rev D., 1994, **49**, 692.

Penzias A.A. & Wilson R.W., 1965, ApJ, **142**, 419.

Press W.H. & Schechter P., 1974, ApJ, **187**, 425.

Puget, J.L., *et al.* 1995, submitted to ApJ.

Reach W., *et al.* 1995, ApJ, **451**, 188.

Reich, P., & Reich, W. 1988, A& A Suppl, **74**, 7.

Rephaeli Y., 1995, ARA&A, **33**, 541.

Reynolds, R.J. 1990, ApJ, **349**, L17

Reynolds, R.J., Tufte, S.L., Kung, D.T., McCullough, P.R., & Heiles,C. 1995, ApJ, 448, 715.

Reynolds, S.P. 1992, ApJ,**392**, L35.

Riess A.G., Press W.H. & Kirshner R.P., 1995, ApJ, **438**, L17.

Ristorcelli, I. 1996, in preparation.

Rudy, D.J. et al. 1987, Icarus, **71**, 159

Ruhl J.E. *et al.* , 1995 ApJ, **453**, L1.

Schloerb, F.P, et al. 1980, Icarus, **42**, 125

Schuster J. *et al.* , 1993, ApJ, **412**, L47.

Shectman S. *et al.* , 1995, in *Wide Field Spectroscopy and the Distant Universe*, 35th Herstmonceux
    Conference, eds. S.J. Maddox and A. Aragon-Salamanca, World Scientific Press, Singapore, p98.

Silk, J., & White, S.D.M. 1978, ApJ, **226**, L103.

Smith P.F. & Lwein J.D., 1990, Phys. Rep., **187**, 203.

Smoot G. *et al.* , 1992, ApJ, **396**, L1.

Starobinsky A.A., 1995, Sov Astr. Lett., **11**, 133.

Steinhardt P.J., 1995, preprint.

Tagger, M., Falgarone, E. & Shukurov, A. 1995, A& A, **299**, 940

Tegmark M., 1996, ApJ, in press.

Tegmark, M. & Eftstathiou, G. 1995, MNRAS, submitted (preprint SISSA astro-ph/9507009).

Toffolatti, L., 1996, private communication.

Turok N, 1989, PRL, **63**, 2625.

Ulich B.L. 1981, AJ, **86**, 1619

Ulich B.L. *et al.* 1980, IEEE Trans. Antennas Propagat., **AP-28**, 367

Vittorio, N. & Mandolesi R. 1996, A&A, in preparation.

Walker T.P. *et al.* , 1991, ApJ, **376**, 51.

Watson R.A. *et al.* , 1994, Nature, **357**, 660.

White M., Scott D. & Silk J., 1994, ARAA, **32**, 319.

White S.D.M. & Silk J., 1980, ApJ, **241**, 864.

Wilbanks T.M., Ade P.A.R., Fischer M.L., Holzapfel W.L., Lange A.E., 1994, ApJ, **427**, L75.

Wilbanks, T. *et al.* , 1990, IEEE transactions on nuclear science, **37**, 566

Windhorst, R.A., Fomalont, E.B., Partridge, R.B., & Lowenthal, J.D. 1993, ApJ, **405**, 498.

Windhorst, R.A., *et al.* 1995, Nature, **375**, 471.

Wollack E., *et al.* , 1993, ApJ, **419**, L49.

Wright, E.L. *et al.* 1991, ApJ, **381**, 200.

Zeldovich Y.B. & Sunyaev R.A., 1969, Astr. Sp. Sci., **4**, 301.

# Appendix A

# Foreground Inventory

Here we briefly review the current knowledge of the galactic foregrounds, and describe our models for extragalactic radio-sources and infrared galaxies.

## A.1 Our Galaxy

### A.1.1 Dust emission

The spectrum of the dust emission in the wavelength range of interest has been measured by the FIRAS instrument aboard COBE with a 7° beam (Wright *et al.* 1991, Reach *et al.* 1995, Boulanger *et al.* 1996). In addition, several balloon experiments have detected the dust emission at high galactic latitude in a few photometric bands with angular resolution between 30 arcminutes and 1 degree (see for example Fischer *et al.* 1995 and De Bernardis 1992 for recent results). The average spectrum *at low galactic latitudes and in molecular clouds* exhibits a cold dust component which can be fitted with a dust temperature of 21.3 K, and an emissivity which varies as $\nu^{1.4}$. *At high latitudes*, Reach *et al.* (1995) also interpret the observed excess at long wavelengths as a cold dust component. Nevertheless Boulanger *et al.* (1996) have shown that this excess is not correlated with the emission at $\lambda = 21$cm, which traces the HI gas, and is isotropic. It thus appears that the high latitude excess is either an extragalactic background or an instrumental component. The residual can be well fitted with a single temperature dust component at 18 K, and an emissivity which varies as $\nu^2$ .

Furthermore Kogut *et al.* (1995) have found a correlation at high latitudes (those of interest for precise determinations of the CMB anisotropies) between the DMR and the DIRBE data, as can be seen in figure A.1.a. The observed change of slope of the correlation coefficients at 90 GHz is just what is expected from the contribution of the free-free emission as predicted by Bennett *et al.* 1994. Although this data alone do not formally exclude a very cold dust component which would mimic free-free emission in the 30 and 53 GHz channels, this explanation is very unlikely. There is thus converging evidence that: (1) the interstellar cold dust component is concentrated in the higher column density lines of sight of the ISM (i.e. the galactic plane mostly); and (2) the dust emission in thin cirrus clouds (most of the sky above 30 degrees latitude) can be well approximated with a single dust temperature and $\nu^2$ emissivity.

Concerning the scale dependence of the amplitude of the fluctuations, we have verified that the power spectrum of the DIRBE fluctuations is decreasing approximately as the $3^{rd}$ power of the spatial frequency, $\ell$, in agreement with the determination of Gautier *et al.* (1992), who base their findings on 100 $\mu m$ IRAS (which has a better resolution of 4 arcminutes). Gautier *et al.* (1992) have also determined that the amplitude of the fluctuations increases faster than the average brightness: the relative fluctuations in thin cirrus clouds are smaller than in denser interstellar clouds.

## A.1.2   Free-free emission

The ionized gas in the interstellar medium can be traced in several ways, e.g. through its $H_\alpha$ emission (Reynolds 1992), the N-II fine structure line at $205\mu m$ seen in the FIRAS data, or pulsar dispersion measures. Nevertheless, the line intensities are proportional to the emission measure and thus do not yield directly an estimate of the column density.

As mentioned above, Kogut *et al.* (1995) have shown that the amplitude of the dust emission-correlated free-free emission is in good agreement with the earlier estimate by Bennett *et al.* (1992). In fact, comparisons with other tracers of the free-free emission show that the H-I correlated free-free emission accounts for most (at least 50%), and maybe all, of that component. To be conservative, one may assume that there is a second, uncorrelated, component accounting for 50% of the free-free emission. In both cases, the spectrum of the free-free emission may be described by $I_\nu \propto \nu^{-0.16}$ (the index being the best fit value of Kogut *et al.* 1995, see fig. A.1.a).
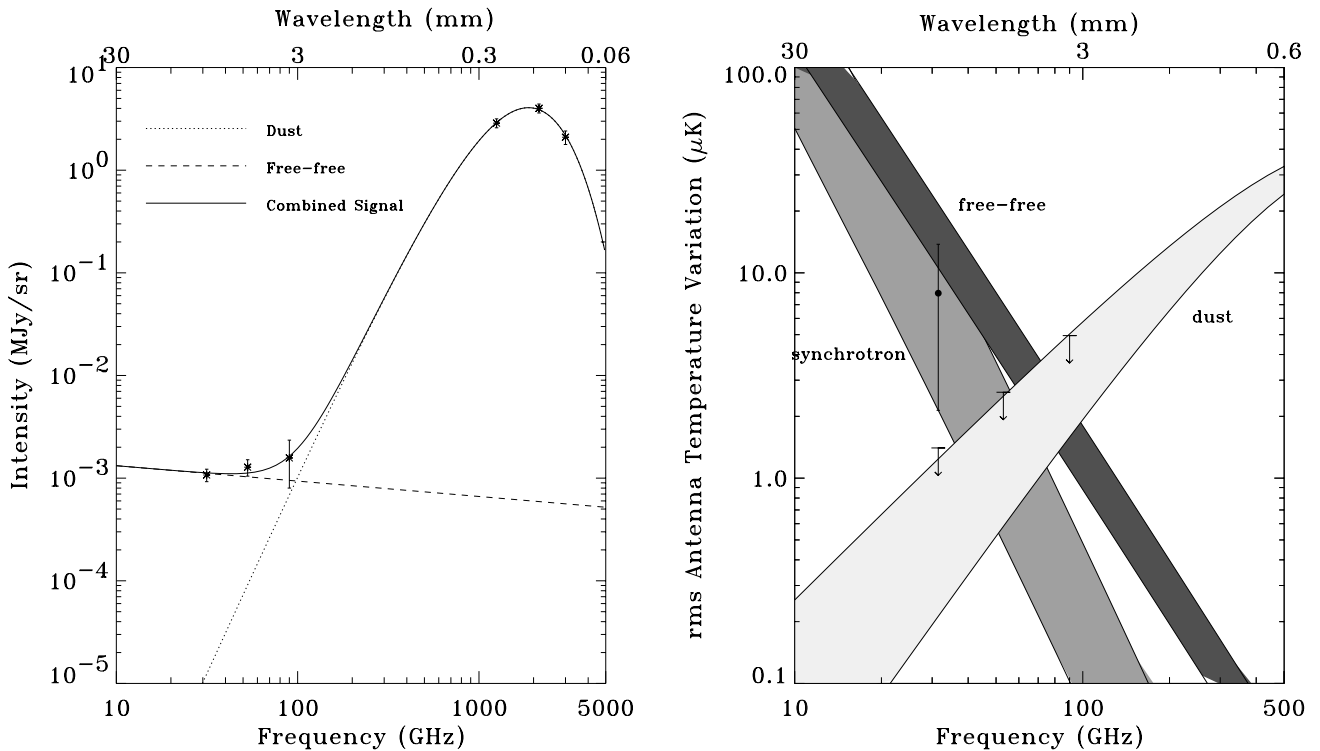


Figure A.1: (Left) Spectrum of the correlated intensity fluctuations in the COBE data at $|b| > 20°$ after subtracting a fitted monopole, dipole and quadrupole component from the data (Kogut *et al.* 1995). (Right) Amplitude of the galactic *rms* fluctuations at latitudes $|b| > 30°$ as a function of frequency, for a 7° FWHM beam (Kogut *et al.* 1995). The dipole and the quadrupole components have been subtracted out. This figure summarizes the information extracted from the DMR-DIRBE and DMR-Haslam cross-correlations. The arrows show upper limits on the dust derived from the DMR analysis only. More recent analysis (see text) indicates that the spectrum of dust at high galactic latitudes is close to that delineated by the *lower* edge of the shaded area.

In addition, Kogut *et al.* (1995) have found that the power spectrum of the spatial distribution of the free-free emission is very similar to the one obtained by Gautier *et al.* (1992) for the dust emission. It predicts *rms* fluctuations (excluding the dipole and quadrupole components) of $5.3\mu K$ at 53 GHz for a mean dust emission of 2.45 MJy/sr at $240\mu m$ (average values at $|b| > 30$ degrees).

## A.1.3  Synchrotron emission

Away from the Galactic plane region, synchrotron emission is the dominant signal at frequencies below ~5 GHz, and it has become standard practice to use the low frequency surveys of Haslam *et al.* 1982 (408 MHz) and Reich and Reich 1988 (1420 MHz) to estimate by extrapolation the level of synchrotron emission at the higher CMB frequencies. This technique is complicated by a number of factors. The synchrotron spectral index varies spatially due to the varying magnetic field strength in the Galaxy (Lawson *et al.* 1987). It also steepens with frequency due to the increasing energy losses of the electrons. Although the former can be accounted for by deducing a spatially variable index from a comparison of the temperature at each point in the two low frequency surveys, there is no satisfactory information on the steepening of the spectrum at higher frequencies. As detailed by Gutierrez *et al.* (1995), techniques that involve using the 408 and 1420 MHz maps are subject to many uncertainties, including errors in the zero levels of the surveys, scanning errors in the maps, residual point sources and the basic difficulty of requiring a very large spectral extrapolation (over a decade in frequency) to characterize useful CMB observing frequencies. Moreover, the spatial information is limited by the finite resolution of the surveys: 0.85° FWHM in the case of the 408 MHz map and 0.6° FWHM in the case of the 1420 MHz one.

Additional information is available from existing CMB observing programmes in the frequency range 5-15 GHz on ~ 7° and ~ 1° angular scales. Using data at frequencies higher than 408 or 1420 MHz improves the spectral leverage, and allows us to test the extrapolation methods used in Section 2.2. For instance, the Jodrell Bank 5 GHz interferometer has been used to make a high sensitivity survey of the northern sky in the declination range $35° − 45°$ on a scale of ~ 2°. A full analysis of the data has been undertaken by Jones *et al.* (1996), and we consider here the results for the quietest region of the sky as identified from the 1420 MHz map and from the Green Bank discrete source catalogue (Condon *et al.* 1989). A comparison of the (Jodrell Bank) observed *rms* signal levels and those at 1420 MHz yields a best fit spectral index between 1.4 and 5 GHz: over the 800 square degrees of sky included in the analysis, the best fit spectral index is $α = −0.9 ± 0.3$.

In the frequency range 10-33 GHz the best information comes from the Tenerife CMB project (Gutierrez *et al.* 1995), which has observed a large fraction of the northern sky with high sensitivity. At 10.4 GHz and 14.9 GHz the window from RA $161° − 230°$, Dec $35.0° − 45.0°$ considered above is fully covered, while at the higher 33 GHz frequency only data at declination $+40°$ have been analyzed. At these frequencies this sky area is free from significant discrete source contribution. The most accurate figures are obtained from the signal levels derived from a joint likelihood analysis of all of the sky area, which implies a residual *rms* signal of $24μK$ at 10 GHz and $20μK$ at 15 GHz. The confidence bounds on these figures have yet to be calculated, but assuming that these best fit values are correct, one can derive spectral indices of $α = −1.4$ between 1.4 and 10.4 GHz and $α = −1.0$ between 1.4 and 14.9 GHz. These values, which apply on scales of order 5°, are in agreement with those obtained from the 5 GHz observations on ~ 2° scales.

Finally, the lack of detectable cross-correlation between the Haslam data and the DMR data leads Kogut *et al.* (1995) to impose an upper limit of $α = −0.9$ for any extrapolation of the Haslam data in the millimetre wavelength range at scales larger than ~ 7°. In view of the other constraints at higher frequencies, it seems reasonable to assume that this spectral behavior keep holding at smaller scales.

The spatial power spectrum of the synchrotron emission is not well known and despite the problems associated with the 408 and 1420 MHz maps it is best estimated from these. We have computed the power spectrum of the 1420 MHz map for the sky region discussed above. The results show that at $ℓ \gtrsim 100$ the power spectrum falls off roughly as $ℓ^{-3}$ (i.e. with the same behavior as the dust and free–free emission).

The information above, partly summarized in Table 2.1, was the basis of the galactic model described in Section 2.2.1, which we later (Section 2.3.1) use to assess the level of the contamination problem.

## A.2    Radio-sources and infrared galaxies

In the extragalactic radio domain it is now possible, thanks to very deep VLA surveys of radio sources (Condon & Mitchell 1984; Partridge *et al.* 1986; Fomalont *et al.* 1988, 1991; Windhorst *et al.* 1993, 1995), to derive essentially model independent estimates of Poisson fluctuations at centimetric wavelengths down to scales $\simeq 30''$. The basic uncertainties of predictions at shorter wavelengths are due to the rather large spectral extrapolation required for the radio source counts (which are directly measured up to $\lambda \simeq 3$ cm), and to the possible contribution of unknown source populations with spectra peaking at millimetre wavelengths.

At $\nu \geq 100$ GHz, dust-dominated far-IR galaxies start to contribute. Until ISO long-$\lambda$ observations are analyzed, our knowledge of the counts of extragalactic far–IR sources must mainly rely on the $60 \mu$m IRAS survey, and on the upper limits for weak sources derived from millimetre and sub-millimetre observations using large ground-base antennas. An additional difficulty arises from the fact that galaxy spectra in the mm and sub-mm wavelength range are poorly known.

Despite these uncertainties, one can extrapolate the radio and IRAS counts into the mm and sub-mm domain by exploiting sound astrophysical arguments. This we outline in the rest of this section. However, the results can be summarized briefly by saying that, on angular scales $\theta \geq 10$' (or $l \leq 1000$), these extragalactic sources yield anisotropies at a level of or below $\Delta T/T \sim 2.10^{-6}$ in the range between $\lambda = 1$ and $\lambda = 6$ mm, even taking into account source clustering.

### A.2.1    Radio sources

Our predictions are based on a model developed by Danese *et al.* (1987) and Franceschini *et al.* (1989), hereafter referred to as RG. It uses the radio local luminosity functions for (1) four classes of *low–luminosity* sources: (normal ellipticals and S0 galaxies, spirals and classical irregulars, Seyfert galaxies, and Actively Star Forming -ASF- galaxies, the latter including non–Seyfert Markarians and galaxies displaying strong morphological peculiarities); and (2) *powerful* "flat"– and steep–spectrum radiogalaxies and QSOs. The definition of the latter two subclasses follows from the classical distinction between sources with radio spectra characterized in the centimetre region by spectral indices $\alpha_R > 0.5$ (steep) and $\leq 0.5$ (flat) $(S_\nu \propto \nu^{-\alpha_R})$.

We have applied the following evolutionary scheme to these source populations. *(1)* Radio–loud steep– and flat–spectrum elliptical + S0 galaxies and quasars are characterized by a luminosity evolution $P(z) = P(z = 0) \cdot e^{\tau(z) \cdot \kappa}$, $\tau$ being the look-back time and $\kappa$ the inverse of the evolution time scale in units of the Hubble time ($\kappa \simeq 4$ for the steep-spectrum and $\simeq 3.4$ for the flat-spectrum sources); *(2)* low luminosity ellipticals + S0 and spirals + irregular galaxies do not evolve; *(3)* ASF galaxies and Seyferts undergo pure luminosity evolution on time scales $\sim 20$ to 25% of the Hubble time (i.e. $\kappa \sim 4$ to 5). Finally, we have assumed, for flat–spectrum sources, $\alpha = 0$ up to $\nu = 100$ GHz and a break to $\alpha = 0.7$ above. For the steep spectrum sources, we have adopted the radio power – spectral index relation determined by Peacock and Gull (1981).

For extragalactic radio galaxies, even in the presence of substantial clustering as suggested by Peacock & Nicholson (1991) the non–Poisson contribution to fluctuations, although difficult to estimate, is smaller than the Poissonian ones on relevant angular scales.

### A.2.2    Infrared galaxies

For infrared galaxies we have considered two extreme evolutionary models. Both are consistent with currently available data (IRAS), but they strongly differ in their predictions at high redshift. The cosmological parameters are assumed to be $\Omega_0 = 1$ and $H_0 = 50$ km s$^{-1}$ Mpc$^{-1}$.

1. The first scheme is *pure luminosity evolution*, or PLE (Franceschini *et al.* 1994). It assumes a constant mass function, from the formation at redshift $z_{for} = 5$ to the present epoch. The

number density of galaxies is conserved. The luminosity evolution is modeled in the standard way[1]. In this "maximal" model, the 1.25 mm observations by Franceschini & Andreani (1995) are fitted with a very cold dust component (at temperature $\sim 7$ K). Early–formed dust is thus assumed to hide the expected bright star–formation phase of spheroidal galaxies from optical searches. The corresponding dust re–radiation in the far–IR during the early phases may have been orders of magnitude larger than today. Some hints in favor of this could be found in ultraluminous IRAS galaxies, high–redshift radio-galaxies and quasars.

2. The second scheme is *density and luminosity evolution* (hereafter DLE, Guiderdoni *et al.* 1995). Galaxies form in dark matter halos after their collapse, in the hierarchical growth of structures which is schematically described by the Press–Schechter prescription. A CDM, $b = 2.5$ standard model is assumed. Consequently, there is no unique $z_{for}$ and galaxy formation is a continuous process, with typical galaxies forming at $z \sim 2$. The baryonic gas cools in dark matter halos and collapses dissipatively until rotational equilibrium is reached. The star formation timescale is determined from the dynamical timescale of the disk. The luminosity evolution in the optical and FIR/submm/mm ranges is followed as in the previous model. In this "minimal" model, there is no cold dust and the submm emission is only the extrapolation of the warmer dust observed by IRAS ($T \sim 20$ K).

Other crucial parameters for the sub–mm evolution are the history of metal enrichment and the evolution of the average galactic radiation field due to the relative geometric distributions of dust and stars, which determines the dust temperature and millimetre emission. Both models rely on the same reasonable assumptions about these parameters. We expect the PLE and DLE scheme to bracket the real level of fluctuations contributed by infrared galaxies, and have used these models to estimate the level of the unresolved background due to the point sources, see Section 2.2.2.

---

[1] A standard initial mass function is assumed, with star formation rates proportional to the gas content, according to the object type. The evolution of the stellar populations is followed according to theoretical stellar tracks and the synthetic optical spectra are computed consistently; the re–emission in the FIR/submm/mm range is computed given dust properties scaled according to the gas content and metallicity, with simple assumptions on the geometry.

# Appendix B

# Acronyms

| | |
|---|---|
| AAD | Attitude Anomaly Detector |
| AGN | Active Galactic Nucleus |
| AIT | Assembly, Integration, and Testing |
| AIV | Assembly, Integration, and Verification |
| AO | Announcement of Opportunity |
| AOCS | Attitude and Orbit Control System |
| ASE | Attitude Sensor Electronics |
| ASF | Actively Star-Forming (galaxies) |
| AWG | Astronomy Working Group |
| BCIU | Bolometer Computer & Instrument Control Interface Unit |
| BEBA | Bolometer Electronics Box Assembly |
| BOB | Bolometer Box |
| BSFR | Back Surface Field Reflector |
| CCA | Cryogenic Cooler Assembly |
| CCS | Cryocooler System |
| CD-ROM | Compact Disc - Read Only Memory |
| CDM | Cold Dark Matter |
| CDMU | Central Data Management Unit |
| CDS | Cryogenic Dilution System |
| CE1 | Cryocooler Electronics 1 |
| CE2 | Cryocooler Electronics 2 |
| CE3 | Cryocooler Electronics 3 |
| CERN | Centre Européen pour la Recherche Nucléaire |
| CFRP | Carbon Fibre Resin Polymer |
| CLUSTER | ESA's Mission to explore the Earth's Magnetosphere |
| CMB | Cosmic Microwave Background |
| CNR | Centro Nazionale della Ricerca |
| CNRS | Centre National de la Recherche Scientifique |
| COBE | Cosmic Background Explorer |
| COBRAS | Cosmic Background Anisotropy Satellite |
| CRTBT | Centre de Recherches des Très Basses Temperatures |
| CSS | Coarse Sun Sensor |
| CTE | Coefficient of Thermal Expansion |
| DIRBE | Diffuse Infrared Background Experiment (on COBE) |
| DLE | Density and Luminosity Evolution (model) |
| DMR | Differential Microwave Radiometer (on COBE) |
| DPC | Data Processing Centre |

| | |
|---|---|
| EIRP | Equivalent Isotropic Radiated Power |
| EM | Electromagnetic |
| EMC | Electromagnetic Compatibility |
| EOL | End-of-Life |
| EPIC | The Prime Focus Camera of the XMM Observatory |
| ESA | European Space Agency |
| ESOC | European Space Operations Centre |
| EXOSAT | An ESA X-Ray Observatory |
| FCA | Flow Control Assembly |
| FIR | Far Infrared |
| FIRAS | Far Infrared Absolute Spectrophotometer (on COBE) |
| FIRST | ESA's Far Infrared and Submillimetre Telescope |
| FOV | Field of View |
| FPA | Focal Plane Assembly |
| FWHM | Full Width at Half Maximum |
| G/T | Gain over Temperature (factor of merit) |
| GTO | Geostationary Transfer Orbit |
| HEMT | High Electron Mobility Transistor |
| HFI | High Frequency Instrument |
| HK | Housekeeping (data) |
| HST | Hubble Space Telescope |
| IPC | ESA's Industrial Policy Committee |
| IRAS | Infrared Astronomical Telescope |
| ISAMS | Improved Stratospheric and Mesospheric Sounder (inst. on UARS) |
| ISE-C | NASA's International Space Explorer |
| ISM | Interstellar Medium |
| ISO | ESA's Infrared Space Observatory |
| L2 | The L2 Lagrangian Point of the Earth-Sun System |
| L4 | The L4 Lagrangian Point of the Earth-Moon System |
| L5 | The L5 Lagrangian Point of the Earth-Moon System |
| LEOP | Low Earth Orbit Phase |
| LFI | Low Frequency Instrument |
| LGA | Low Gain Antenna |
| LOS | Line of Sight |
| MCC | Mission Control Centre |
| MDM | Mixed Dark Matter |
| MGA | Medium Gain Antenna |
| MIRD | Mission Implementation Requirements Document |
| MLI | Multi Layer Insulation |
| MMIC | Monolithic Microwave Integrated Circuit |
| MMS | Matra Marconi Space |
| MOC | Mission Operations Center |
| MTW | Mechanical and Thermal Works |
| NASA | National Air and Space Administration (U.S.A.) |
| NEP | Noise Equivalent Power |
| NIR | Near Infrared |
| OBDH | On-Board Data Handling |
| ORATOS | Orbit and Attitude Operations System |
| PCU | Power Control Unit |
| PDU | Power Distribution Unit |

| | |
|---|---|
| PFM | Protoflight Model |
| PI | Principal Investigator |
| PLE | Pure Luminosity Evolution (model) |
| PLM | Payload Module |
| PND | Passive Nutation Damper |
| PRE | Preamp/Readout Electronics |
| PS | Project Scientist |
| QSO | Quasar |
| RAB | Radiometer Box |
| RAL | Rutherford Appleton Laboratories |
| RBI | Remote Bus Interface |
| RCIU | Radiometer Computer & Instrument Control Interface Unit |
| RCS | Reaction Control System |
| REBA | Radiometer Electronics Box Assembly |
| RF | Radio Frequency |
| RFDU | Radio Frequency Distribution Unit |
| RG | Danese et al. (1987) and Franceschini et al. (1989) model |
| ROSAT | Röntgen Observatory |
| RTU | Remote Terminal Unit |
| SAMBA | Satellite for the Measurement of Background Anisotropies |
| SCOSII | Spacecraft and Operations Control System |
| SILMA | Structure Interne Lancement Multiple Ariane |
| SIMSat | Satellite Simulation |
| SOC | Science Operations Center |
| SOHO | ESA's Solar and Heliospheric Observatory |
| SPC | ESA's Science Programme Council |
| SSAC | Space Science Advisory Committee |
| SSR | Solid State Recorder |
| ST | Science Team |
| STM | Structural and Thermal Model |
| SVM | Service Module |
| SZ | Sunyaev Zeldovich (effect) |
| TA | Telescope Assembly |
| TC | Telecommand |
| TM | Telemetry |
| TSS | Tank Subsystem |
| UARS | NASA's Upper Atmosphere Research Satellite |
| UT | Universal Time |
| WFE | Wavefront Error |
| XMM | ESA's X-Ray MultiMirror Observatory |